The Dissertation Committee for Kan Wu Certifies that this is the approved version of the following dissertation:

Numerical Modeling of Complex Hydraulic Fracture Development in Unconventional Reservoirs

Committee:

Jon E. Olson, Supervisor

Matthew T. Balhoff, Co-Supervisor

Mark E. Mear

Mukul Sharma

Kamy Sepehrnoori

Numerical Modeling of Complex Hydraulic Fracture Development in Unconventional Reservoirs

by

Kan Wu, B.E.; M.E.

Dissertation

Presented to the Faculty of the Graduate School of

The University of Texas at Austin

in Partial Fulfillment

of the Requirements

for the Degree of

Doctor of Philosophy

The University of Texas at Austin

December 2014

Dedication

To my parents, Guilao Wu and Chunyun Tang,

To my sister, Yanrong Wu,

To my brothers, Biyi Wu and Qifei Wu,

for their endless love, support and encouragement.

Acknowledgements

I would like to thank all those individuals who helped and encouraged me to make this dissertation work possible. First of all, I would like to express my sincerest gratitude to my supervisor, Dr. Jon E. Olson, for his guidance and encouragement throughout my study at The University of Texas at Austin. He is always very patient to discussing research problems with me. He guided me to the right track of research, suggesting valuable and critical ideas. His ingenious perspectives into the research as well as optimistic and friendly characters have set up an example that I wish to follow in my future career. I also want to extend my sincerest appreciation to my co-advisor, Dr. Matthew T. Balhoff for his guidance and support. I would like also to thank for my dissertation committee: Dr. Mark Mear, Dr. Mukul Sharma, and Dr. Kamy Sepehrnoori for their time and effort reviewing my dissertation and for giving insightful comments. The help and support from the rest of the PGE department faculty were also greatly appreciated, especially Dr. Masa Prodanovic and Dr. David Dicarlo.

I am also extremely grateful to the Fracture Research and Application Consortium (FRAC) for providing the financial support and the opportunities to present this research work to industry sponsors. Furthermore, I want to thank Dori L. Coy for helping me deal with tuition fee and insurance every semester, thank Frankie Hart for answering all my questions about course selection and graduation affairs, thank John Cassibry and Roger Terzian for computer technical support.

I would like to thank my officemates for discussing research questions with me and making a great deal of fun in my spare time. I cannot imagine having a more wonderful and happier life during my Ph.D. study. Many thanks go to my officemates,

Farrokh Sheibani, Precious Williams, Li Ji, Ben Bahorich, Farrukh Hamaza, Abdul Khan, Kashif Naseem, Hunjoo Lee, Weiwei Wang, Valerie Gono, Kaimin Yue, Javad Rashidi. I also want to thank all my friends and roommates for their tolerance and support. They helped me stay in good standing and gave me a great time in the United States, especially during the first year of my Ph.D. study.

Finally, I would like to extend my sincere appreciation to my parents and siblings for their endless love and support. My family has been a source of motivation to me to pursuit my long educational career and puts up with me this far. I also owe special thanks to my future husband, Wei Yu, for helping me and encouraging me all the time in my life. He provided me with an enormous source of optimistic energy, and is an adviser in my life. He deserves my warmest thanks from the bottom of my heart.

Numerical Modeling of Complex Hydraulic Fracture Development in Unconventional Reservoirs

Kan Wu, Ph.D.

The University of Texas at Austin, 2014

Supervisor: Jon E. Olson

Co-Supervisor: Matthew T. Balhoff

Successful creations of multiple hydraulic fractures in horizontal wells are critical for economic development of unconventional reservoirs. The recent advances in diagnostic techniques suggest that multi-fracturing stimulation in unconventional reservoirs has often caused complex fracture geometry. The most important factors that might be responsible for the fracture complexity are fracture interaction and the intersection of the hydraulic and natural fracture. The complexity of fracture geometry results in significant uncertainty in fracturing treatment designs and production optimization. Modeling complex fracture propagation can provide a vital link between fracture geometry and stimulation treatments and play a significant role in economically developing unconventional reservoirs.

In this research, a novel fracture propagation model was developed to simulate complex hydraulic fracture propagation in unconventional reservoirs. The model coupled rock deformation with fluid flow in the fractures and the horizontal wellbore. A Simplified Three Dimensional Displacement Discontinuity Method (S3D DDM) was proposed to describe rock deformation, calculating fracture opening and shearing as well as fracture interaction. This simplified 3D method is much more accurate than faster

pseudo-3D methods for describing multiple fracture propagation but requires significantly less computational effort than fully three-dimensional methods. The mechanical interaction can enhance opening or induce closing of certain crack elements or non-planar propagation. Fluid flow in the fracture and the associated pressure drop were based on the lubrication theory. Fluid flow in the horizontal wellbore was treated as an electrical circuit network to compute the partition of flow rate between multiple fractures and maintain pressure compatibility between the horizontal wellbore and multiple fractures. Iteratively and fully coupled procedures were employed to couple rock deformation and fluid flow by the Newton-Raphson method and the Picard iteration method.

The numerical model was applied to understand physical mechanisms of complex fracture geometry and offer insights for operators to design fracturing treatments and optimize the production. Modeling results suggested that non-planar fracture geometry could be generated by an initial fracture with an angle deviating from the direction of the maximum horizontal stress, or by multiple fracture propagation in closed spacing. Stress shadow effects are induced by opening fractures and affect multiple fracture propagation. For closely spaced multiple fractures growing simultaneously, width of the interior fractures are usually significantly restricted, and length of the exterior fractures are much longer than that of the interior fractures. The exterior fractures receive most of fluid and dominate propagation, resulting in immature development of the interior fractures.

Natural fractures could further complicate fracture geometry. When a hydraulic fracture encounters a natural fracture and propagates along the pre-existing path of the natural fracture, fracture width on the natural fracture segment will be restricted and injection pressure will increase, as a result of stress shadow effects from hydraulic fracture segments and additional closing stresses from in-situ stress field. When multiple

fractures propagate in naturally fracture reservoirs, complex fracture networks could be induced, which are affected by perforation cluster spacing, differential stress and natural fracture patterns. Combination of our numerical model and diagnostic methods (e.g. Microseismicity, DTS and DAS) is an effective approach to accurately characterize the complex fracture geometry. Furthermore, the physics-based complex fracture geometry provided by our model can be imported into reservoir simulation models for production analysis.

Table of Contents

List of Tables

List of Figures

CHAPTER 1: GENERAL INTRODUCTION

In this doctoral dissertation, a complex hydraulic fracture development model is introduced to simulate single non-planar fracture and multiple fracture propagation in naturally fractured reservoirs from horizontal wellbores. First, a Simplified Three Dimensional Displacement Discontinuity Method (S3D DDM) is presented to model fracture deformation. The Finite Difference Method (FDM) is used to model fluid flow in the fractures. The model incorporates physical mechanisms that are important for predicting the geometry of induced complex fracture networks such as stress shadow effects, fluid rate distribution among multiple fractures, crossing of simultaneous multiple fractures and interaction between hydraulic and natural fractures. Second, the model is applied to simulate different cases of complex hydraulic fracture propagation to examine fracture geometry, stress distribution as well as injection pressure.

This chapter introduces the background and literature review related to the research and then the main objectives are presented. The current state of hydraulic fracture modeling is discussed to put the current modeling in context. Finally, the organization of this dissertation is provided.

1.1 BACKGROUND

In recent years, production of tight oil and shale gas has increased exponentially in the United States. Based on estimations from U.S. Energy Information Administration (EIA), U.S. tight oil production in the fourth quarter of 2013 contributed to 4.3% of overall crude oil production and pushed it to more than 10% of total world production, up from 9% in the fourth quarter of 2012 (Figure 1.1). Shale gas production is also becoming increasingly vital to gas production in the United States and contributed more than 30% of total gas production in 2011 (U.S. Energy Information Administration (EIA)). The U.S. EIA forecasts that shale gas production will continue to increase for the next thirty years and may account for half of U.S. dry gas production in 2040 (Figure 1.2). Consequently, tight oil and shale gas will continue to play an important role in meeting the U.S.'s energy demands.

Furthermore, a recent study indicates that tight oil and shale gas basins continue to be found throughout the world (Figures 1.3 and 1.4). The United States is one of the largest tight oil and shale gas reserves in the world. Tight oil resources are primarily concentrated in Russia and the United States. The technically recoverable tight oil resource in Russia is about 75 billion barrels, and the United State is about 60 billion barrels. The estimated shale gas reserve in United States is 861.7 Tcft (trillion cubic feet), China is estimated to have 1274.3 Tcft, and Argentina 773.1 Tcft.

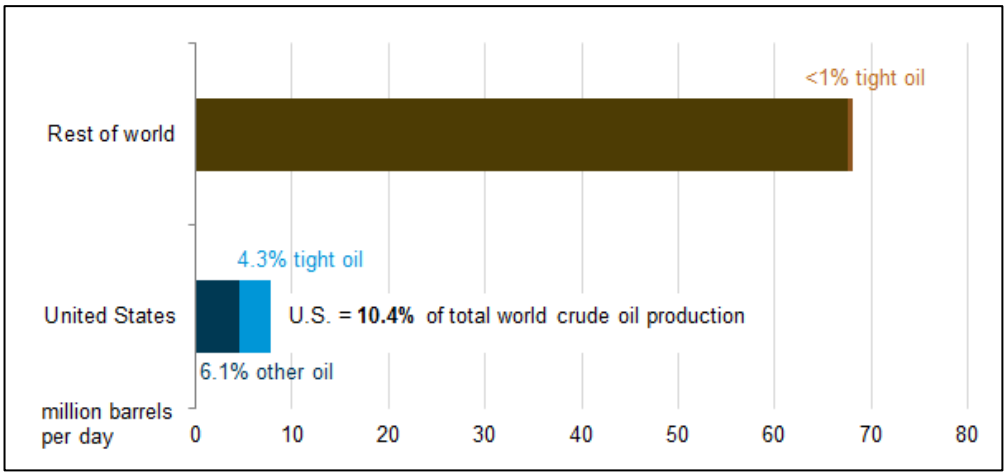

Figure 1.1: Estimated crude oil production in the fourth quarter of 2013 in the United States and rest of the world (U.S. Energy Information Administration, 2014 Short-Term Energy Outlook). (http://www.eia.gov/todayinenergy/detail.cfm?id=15571).

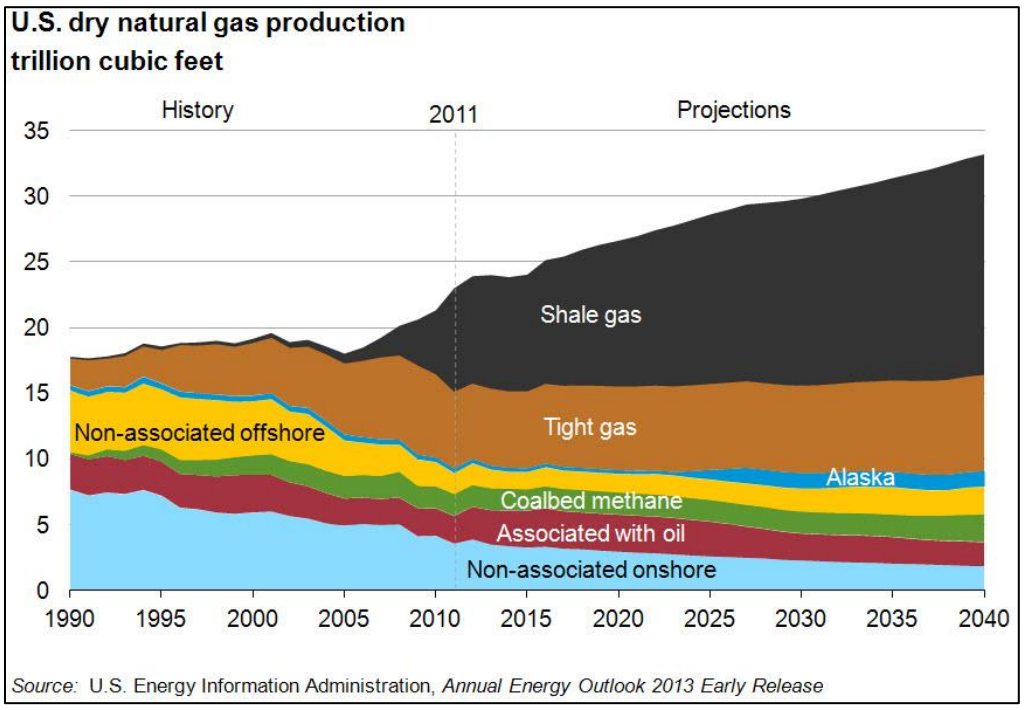

Figure1.2: US dry natural gas production, Trillion cubic feet (U.S. Energy Information Administration, Annual Energy Outlook 2013 Early Release). (http://www.eia.gov/forecasts/aeo/er/pdf/0383er%282013%29.pdf).

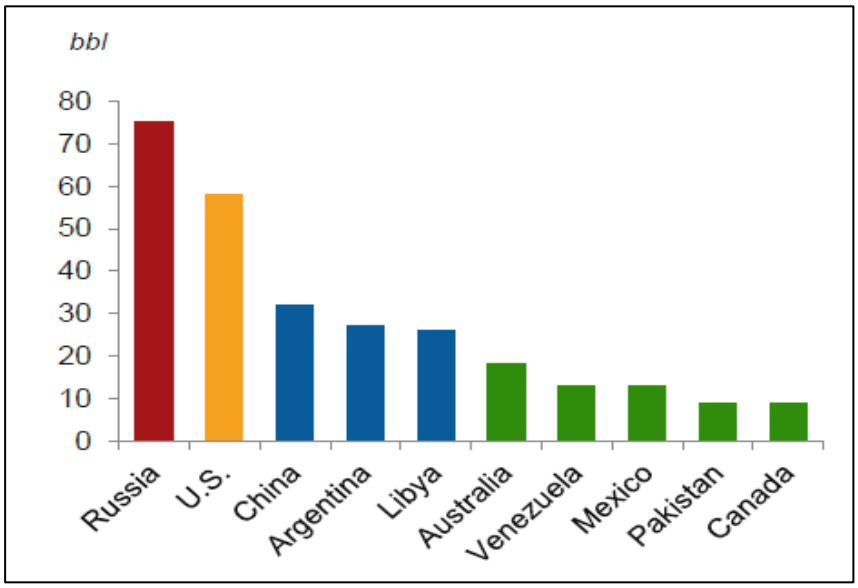

Figure 1.3: Top 10 Contries by technically recoverable shale oil resources (U.S. Energy Information Administration, 2013). (http://www.eia.gov/conference/2014/pdf/presentations/webster.pdf).

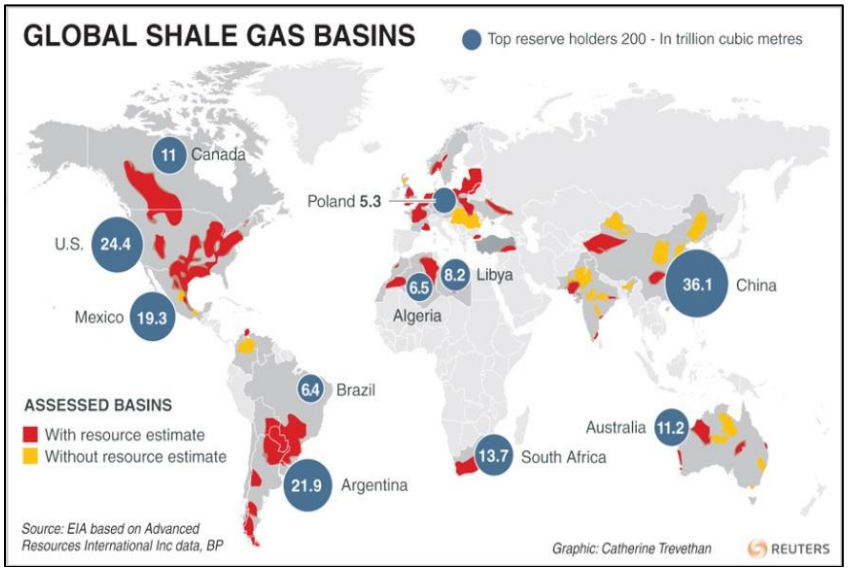

Figure1.4: Map of global shale gas resource distribution in the world (U.S. Energy Information Administration based on Advanced Resources International Inc data, BP).

Both tight oil and shale gas are found within reservoirs with ultra-low permeability, primarily shale formations. Compared with conventional gas formations, shale formations have some distinct properties, such as nano-Darcy permeability (Cipolla, 2009) and natural fracture distribution (Barton and Zoback, 2002; Gale et al., 2007; Gale and Holder, 2008; King, 2010). Two key technologies that enable economic viability of shale gas development are horizontal drilling (Fisher et al., 2004; Wiley et al., 2004) and hydraulic fracturing (Britt et al., 2006; Watson et al., 2008; Waters et al., 2009). Hydraulic fracturing of ultra-low permeability shale reservoirs is required to establish commercial productivity, which is one of the most important technologies used widely by the petroleum industry as an effective stimulation strategy to enhance oil and gas recovery. In order to increase fracture contact area with the formation for improving recovery in shale reservoirs, ten to twenty or more fracture stages are employed in a horizontal wellbore (Figure 1.5) and each stage includes three to six fractures (Durst et al., 2008; Grieser, 2009). Sequential and simultaneous fracturing methods are implemented in shale reservoirs with the goal of improving well performance and enhancing operation efficiency (Mutalik and Gibson, 2008; Roussel and Sharma, 2011).

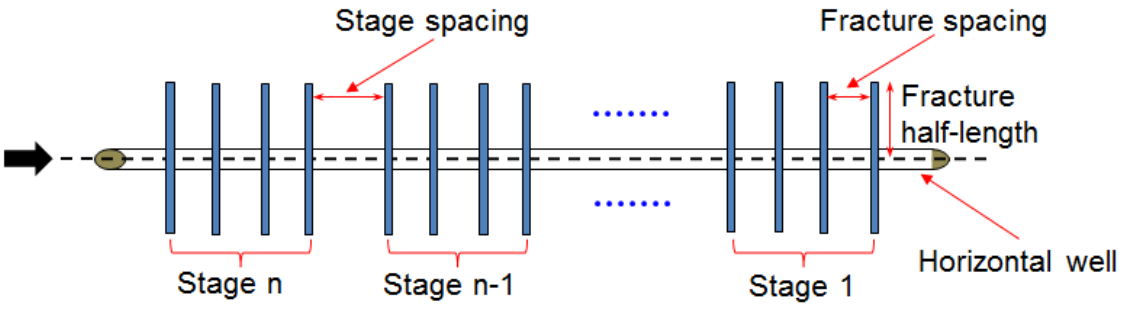

Figure 1.5: Illustration of multiple hydraulic fracturing in shale gas reservoirs.

1.2 STATEMENT OF THE PROBLEM

In shale reservoirs, multiple hydraulic fractures are closely spaced along horizontal wellbores, which has been demonstrated as a very highly effective method for stimulation (Burger et al. 2012). However, fracture interaction between growing fractures can occur within a stage, between adjacent stages and between different horizontal wells, resulting in a complex fracture network instead of a simple bi-wing planar fracture (Olson, 2008; Cheng, 2009; Roussel and Sharma, 2011; Wu and Olson, 2013, 2014). In addition, pre-existing natural fractures in shale reservoirs further complicate fracture geometry, providing opportunities for complexity to arise (Olson et al., 2009; Dahi-Taleghani et al., 2009; Kresse et al., 2013; Wu and Olson, 2014). Knowledge of fracture geometry, such as fracture trajectory, fracture width, and fracture height, is crucial for determining fracture coverage of reservoirs as well as for optimizing stage and well spacing for tight oil or shale gas production. However, the geometry of complex fracture networks is challenging to measure directly and completely by fracture diagnostic techniques (Cipolla, 2000). Therefore, modeling complex hydraulic fracture propagation can lead to significant contributions for economic development of shale reservoirs.

Conventional hydraulic fracture propagation models simulate single bi-wing planar fracture with opening-mode extending away from the wellbore. These traditional models are still used in hydraulic fracturing design for conventional settings. However, in shale reservoirs with complex fracture geometry, the conventional fracture models might fail to capture some key physical mechanisms of complex fracture propagation. For multiple fracture propagation in shale reservoirs, the stress shadow produced induces fracture tortuosity and width restriction. The propagation direction and internal driving pressure of the hydraulic fracture are affected by mechanical interaction with other hydraulic fractures as well as with pre-existing natural fractures. Fluid flow in the

wellbore and in the complex fracture networks must satisfy pressure equilibrium and material balance. The complete model requires coupling rock mechanics and fluid mechanics. Conventional hydraulic fracture models used in the industry do not take into account all this processes together, which prompts engineers to develop new methods to overcome limitations of the conventional models.

1.3 RESEARCH OBJECTIVES

The primary objective of this dissertation is to construct a computationally efficient fracture propagation model that is realistic enough to incorporate most of the important physical mechanisms that control complex fracture propagation in shale reservoirs. The unifying theme is to study fundamental physical laws of hydraulic fracturing to predict and optimize fracture geometry at the field scale.

This dissertation focuses on (1) developing a complex hydraulic fracture development model, and (2) quantifying the physical mechanisms through studying different cases. The specific objectives of this dissertation are to:

i. Develop a coupled complex hydraulic fracture development model, incorporating stress shadow effects, fluid rate distribution among multiple fractures, crossing of simultaneous multiple fractures and interaction of hydraulic and natural fractures.
ii. Derive a novel three-dimensional displacement discontinuity method for complex fracture geometry that is significantly more accurate than faster pseudo-3d methods but requires significantly less computational effort than currently available fully three-dimensional methodologies.

iii. Study the physical mechanisms of multiple fracture propagation and investigate the effects of fracture interaction on fracture geometry through using the complex fracture development model.
iv. Analyze hydraulic fracture interaction with natural fractures as exhibited through fracture geometry and injection pressure.

1.4 LITERATURE REVIEW

Hydraulic fracturing is a common and effective stimulation method to enhance production in the oil and gas industry. It is a technique that uses a large amount of special fluid that is injected into the reservoir and builds up pressure in the wellbore to create a fracture. The fracture is then supported by proppants to form conductive conduits which may greatly enhance production rates and extend the life of production wells. From the aspect of economics, various hydraulic fracturing models have been developed to simulate hydraulic fracturing and serve as guidance for optimizing job design to maximize production of oil and gas over the past 60 years (Zhang et al., 2005). The fracture models primarily focus on describing single fracture propagation extending from two-dimension to pseudo three-dimension and then to fully three dimensions.

An acceptable working model should at least be capable to capture major physical processes taking place during hydraulic fracturing. The basic processes of hydraulic fracturing include: (1) fracture deformation induced by internal pressure in the fracture; (2) fluid flow in the fracture; (3) fluid leak-off into the formation and (4) fracture propagation (Veatch et al., 1986; Adachi et al., 2007). Fracture deformation is generally computed using linear elasticity, and the elasticity equations can be solved using the displacement discontinuity method or discretizing 3D partial differential equations via the

finite element or finite difference methods. Fracturing fluid flow is idealized as laminar flow through a narrow and parallel-sided slot (Geertsma et al., 1969). Fluid leak-off is typically modeled as one-dimensional Darcy flow. According to the conventional LEFM criterion, fractures start propagating when the stress intensity factor approaches the rock toughness (Valko et al., 1995). Fracture propagation direction is usually determined by one of three different criteria: maximum circumferential stress (Erdogan and Sih, 1963), maximum strain energy density (Sih, 1974) or maximum energy release rate (Nuismer, 1975).

1.4.1 Review of single fracture propagation models

Hydraulic fracturing models have greatly evolved from simple two-dimensional models to three-dimensional models. Typical two-dimensional models are Khristianovich-Geertsma-DeKlerk (KGD) (Khristianovich and Zheltov, 1955; Geertsma and de Klerk, 1969) and Perkins-Kern-Nordgren (PKN) (Perkins et al., 1961; Nordgren et al., 1972). Both KGD and PKN models assume plane strain deformation with constant fracture height constrained to the pay zone thickness and calculate fracture width based on analytical solution for a crack (Sneddon, 1951),

$$w(x) = \frac{4(1-v^2)p}{E}(b^2 - x^2)^{0.5} \quad , \tag{1.1}$$

where w is the width along the crack, v is Possion ratio of rock, E is Young's Modulus of the rock, p is the constant net pressure within the crack, b is the crack half-length.

The KGD model presumes plane strain for a fracture in the horizontal plane and assumes no variation of fracture width in the vertical direction (Figure 1.6). The fracture has an elliptical shape in the horizontal plane, and the maximum fracture width at the wellbore can be calculated from

$$w_w = \frac{4(1-\nu^2)\, p_{n,avg} L}{E}, \tag{1.2}$$

where $p_{\mathrm{n,avg}}$ is the average net pressure in the fracture and L is fracture half-length. Fracture width is a function of fracture length. The model has a vertical rectangular cross-section perpendicular to fracture propagation direction, and pressure varying from wellbore to the fracture tip can be given by

$$p_{n,w} - p_{n,tip} = \frac{12\mu i L}{h}\left(\frac{1}{L}\int_0^L \frac{1}{w(x)^3}\, dx\right), \tag{1.3}$$

where $p_{n,w}$ is net pressure at the wellbore, $p_{n,tip}$ is net pressure at the fracture tip, μ is viscosity of injection fluid, i is the half of injection rate, $w(x)$ is fracture width.

The PKN model assumes plane strain for a fracture in a vertical plane, normal to the fracture propagation direction, and the vertical cross section of the fracture is elliptical in shape (Figure 1.7). The fracture width can be calculated from

$$w = \frac{2(1-\nu^2) h p_n}{E}, \tag{1.4}$$

where p_{n} is net pressure in the fracture, h is fracture height. Fracture width is a function of fracture height, instead of fracture length. Each vertical cross section is independent from each other and pressure drop along the fracture in an elliptical cross section is provided by

$$p_{n,w}^4 - p_{n,tip}^4 = \frac{32 E^3 \mu i L}{\pi(1-\nu^2)^3 h^4}, \tag{1.5}$$

where $p_{n,w}$ is net pressure at the wellbore, $p_{n,tip}$ is net pressure at the fracture tip, u is viscosity of injection fluid, i is the half of injection rate, L is fracture half-length, h is fracture height.

These two models are approximations and have been shown to be useful, but they have limits to their accuracy and over-simplify the problem in most cases. The KGD

model might be more suitable for fracture propagation at the early injection time when fracture height is much greater than fracture length, while the PKN model might be more reasonable at late injection time when fracture length exceeds fracture height. Now these two classic two-dimensional models are rarely used for fracture designs in the field because they have been replaced by pseudo-3d models, but still serve as verification with numerical models and providing insights for understanding the fracturing process.

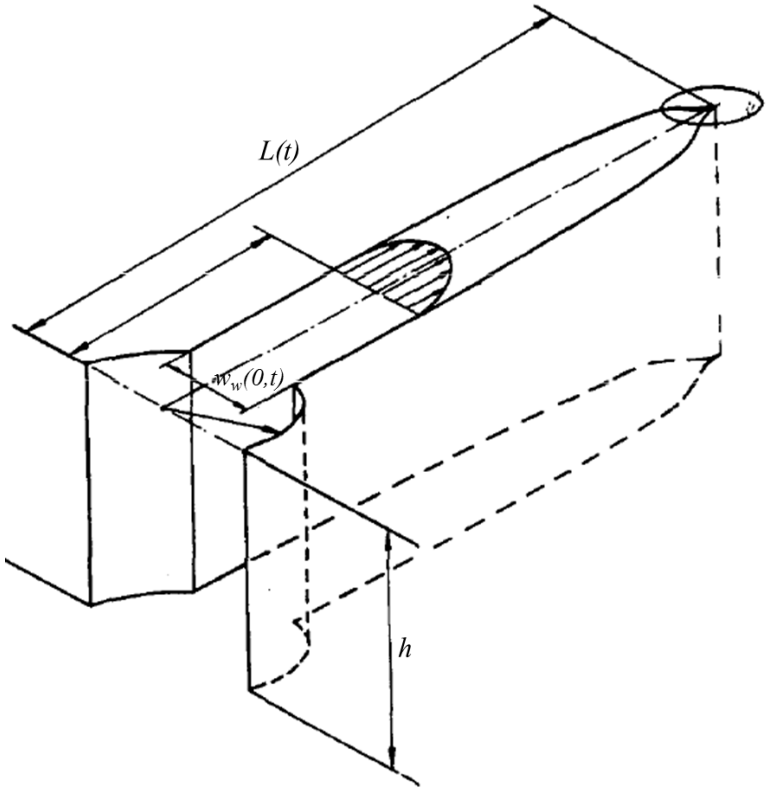

Figure 1.6: Schematic view of a KGD fracture model (from Geertsma and de Klerk, 1969). $L(t)$, h and $w_w(0, t)$ are fracture length, height and width at the wellbore, respectively.

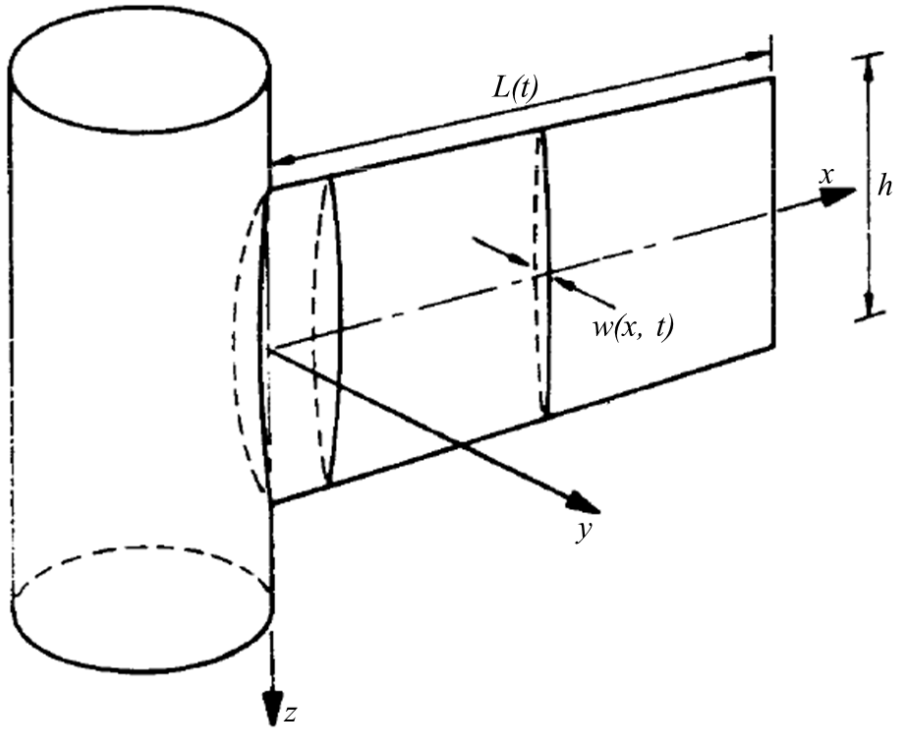

Figure 1.7: Schematic view of a PKN fracture model (from Nordgren et al., 1972). $L(t)$, h and $w(x, t)$ are fracture length, height and width, respectively.

Following the development of two-dimensional models, pseudo-3D (Simonson et al., 1978; Advani et al., 1982; Settari et al., 1982; Fung et al., 1987) and true 3D models (Clifton et al., 1981; Settari et al., 1984; Abou-Sayed et al., 1984) were developed to account for fracture height growth and to describe the hydraulic fracturing process with better accuracy. All models allow fractures to grow into layers adjoining the pay zone, and the depth of penetration is determined by differences in stiffness and horizontal in-situ stresses between the pay zone and adjoining layers (Van Eekelen, 1982). Simonson et al. (1978) developed a pseudo-3D model to simulate height growth in a symmetric three-layer formation and investigated the effects of different material properties and in-situ stresses as well as pressure gradients for the pay zone and the barrier formations on

fracture containment. Fung et al. (1982) extended Simonson et al.'s work to multi-layer, asymmetrical formations using a semi-analytic technique. Settari et al. (1982) also developed a pseudo-three-dimensional model by describing lateral fluid flow and crack opening for the fracture and coupling with an efficient scheme to deal with vertical fracture growth. Pseudo-3D models are approximate but efficient to capture the behavior of fracture height growth by employing special schemes. Most pseudo-3D models do not take into account fluid flow in the vertical direction (Valko et al., 1995). For true 3D models, movement of fluid is modeled not only in the lateral direction but also in the vertical direction, whereas the computational cost of the models is too excessive to be widely applied. The general approach for true 3D models is based on analysis of three-dimensional rock deformation and two-dimensional fluid flow through the fractures (Clifton et al., 1981; Abou-Sayed et al., 1984).

The conventional hydraulic fracturing models discussed above only simulate propagation of single bi-wing planar fracture. However, in highly deviated or horizontal wellbores, a tortuous fracture shape is often created when fractures initiate in a non-preferred orientation (Figure 1.8). As such, some experiments and models have been developed to understand the non-planar fracture shape. Weijers and de Pater (1992, 1994) performed some experiments and two-dimensional numerical simulations to investigate the near-wellbore fracture geometry for deviated and horizontal wells. The results indicated that several starter fractures were created along the perforations and then gradually reoriented with the same curvature towards to the preferred fracture plane. Olson (1995) proposed a two-dimensional model to analyze the effect of non-planar fractures with different wellbore angles, differential stress and injection parameters. Numerical simulations showed that non-planar fracture geometry at the wellbore causes fracture width restriction and the increment of treating pressure. Rungamornrat et al.

(2005) also developed a model to simulate non-planar fracture growth utilizing a symmetric Galerkin boundary element method to treat the elasticity problem and a Galerkin finite element method to describe fluid flow within fractures.

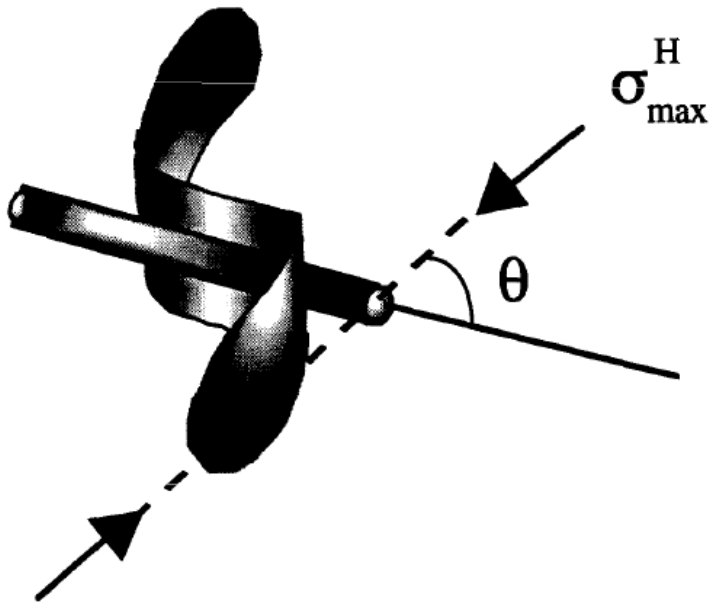

Figure 1.8: Schematic view of non-planar fracture geometry (from Olson, 1995). σ_{max}^{H} is maximum horizontal stress, θ is the angle between fracture and σ_{max}^{H}.

1.4.2 Review of multiple fracture propagation models

Multiple fractures in horizontal wells are often used to develop shale gas economically (Warpiniski et al., 1991; Sato et al., 1999). There are two main causes for multi-frac propagation (Weijers et al., 2000). One is multiple fracture initiation points provided by a long perforated interval with numerous perforations; the other is bifurcation of hydraulic fractures due to intersection with natural fractures in the naturally fractured formation. Recent efforts to model multi-frac propagation have taken various forms. There are generally three types of multi-frac models:

i. Mechanical interaction between multiple fractures is ignored, but fluid flow in the fracture and wellbore are considered (Siriwardane et al., 1991; Elbel et al., 1992; Mack et al., 1992).

ii. Mechanical interaction is modeled explicitly, but fluid flow is simply described by assuming constant internal pressure in the fracture pattern (Dong et al., 2001; Olson, 2008; Cheng, 2009; Roussel, 2011).

iii. Both mechanical interaction and fluid flow are taken into account (Yamamoto et al., 2004; Wong and Xu, 2013; Castonguay et al., 2013; Shin and Sharma, 2014).

The multi-frac models without mechanical interaction usually consist of two components, an analytical fracture propagation model which simulates the growth of a single fracture and a fluid flow model for the fracture and wellbore (Mack et al., 1992). Analytical models have been published based on the PKN model (Elbel et al., 1992), the KGD model (Siriwardane et al., 1991) and a pseudo three-dimensional model (Mack et al., 1992). Fractures extend independently and are not affected by the stress shadow induced by other fractures. The fracture geometry is planar and symmetric with respect to the wellbore. An electrical analogue is used to relate fluid flow in the wellbore to individual fractures (Elbel et al., 1992; Mack et al., 1992). Based on an electrical current analogue for the fluid flow, Kirchoff's first law states that pumping rate is equal to summation of injection rates of each fracture. It is presumed that fluid exchange between fractures occurs only via the wellbore and wellbore storage effects are ignored.

The models of the first type were generally applied for vertical wells and for zones that were separated by zones not expected to fracture. It was the advent of closely spaced hydraulic fractures in horizontal wells that was the driver for a better model. Elastic interaction between fractures is an important factor affecting fracture aperture and

trajectory. Based on this effect, the second type model of multiple fracture propagation is developed with various forms. The fracture interaction is often modeled by analytical and numerical methods. Sneddon and Elliot (1946) derived an analytical model to calculate stress field around an infinitely long two-dimensional crack. Numerical methods primarily include displacement discontinuity methods (Dong et al., 2001; Yamamoto et al., 2004; Olson et al., 2009; Cheng, 2009), finite difference method (Roussel, 2011) and finite element method (Shin and Sharma, 2014).

The second type of model that incorporated fracture mechanical interaction usually assumed constant internal pressure. Dong et al. (2001) modeled a two dimensional elastic fracture with constant internal pressure using a quadratic displacement discontinuity method. Olson (2008) employed a pseudo-3D approach using the constant displacement discontinuity method for vertical but laterally non-planar fractures, assuming zero viscosity fluid injection to reduce computation time for multi-fracture problems. Cheng (2009) used a two-dimensional displacement discontinuity method to describe stress distribution around multiple static fractures for analysis of fracture interaction. Fluid pressure within static fractures varies along the fracture length. Roussel (2011) used a three-dimensional finite difference, explicit numerical method to model stress perturbation for a static fracture by fixing the opening along pre-existing fractures as if they were propped open and predict that the static fracture would follow stress trajectories dictated by the pre-existing fractures.

The third type of model couples fluid flow and rock deformation. Yamamoto et al. (2004) iteratively coupled fluid flow and rock deformation in multiple fractures including consideration of fracture interaction through respectively using the finite element method and the three-dimensional displacement discontinuity method. Wong and Xu (2013) modeled multiple fracture propagation in horizontal wells through the

boundary integral formulation, considering both mechanical interaction and fluid flow but in two dimensions. Castonguay et al. (2013) implemented a weakly-singular, symmetric Galerkin boundary element method to calculate fracture geometry, where flow in the fracture is modeled as power-law fluid flow in the arbitrary curved channels. Shin and Sharma (2014) investigated the effect of factors such as perforation cluster spacing, fracture height, fracturing fluid viscosity, and pumping rate on simultaneous propagation of multiple fractures in a horizontal well by using ABAQUS, which is a three-dimensional geomechanical model utilizing the finite element method.

1.4.3 Review of hydraulic fracturing in naturally fractured reservoirs

It is believed that natural fractures are present in most shale reservoirs and act as weak planes for fracture growth (Gale et al., 2007). Complex fracture networks might be induced when hydraulic fractures are propagated in the naturally fractured reservoirs (Dahi-taleghani et al., 2009; Warpiniski, 1987). There are three possibilities that might occur when hydraulic fractures intersect with natural fractures (Figure 1.9). First, the hydraulic fracture crosses the natural fracture and continues to propagate along the original direction without any influence. Second, the hydraulic fracture is diverted along the pre-existing path of the natural fracture, and then creates a new fracture path again starting at the end of the natural fracture. Third, the hydraulic fracture is also diverted along the pre-existing path of the natural fracture, and then kinks out at some weak point along the natural fracture (Dahi-Taleghani and Olson, 2013).

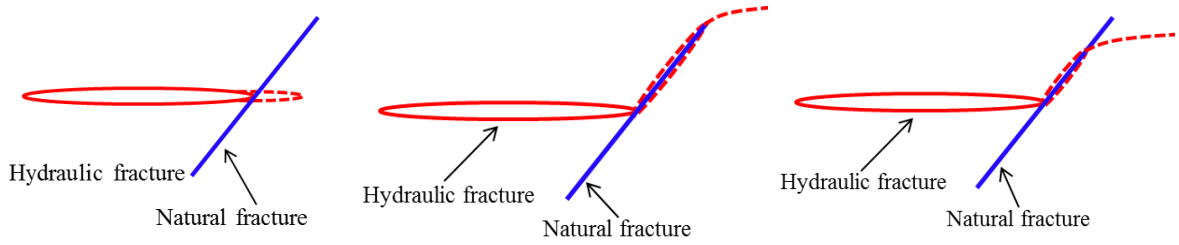

(a) (b) (c)

Figure 1.9: Three possible scenarios at intersection of hydraulic and natural fractures: (a) the hydraulic fracture crosses the natural fracture; (b) the hydraulic fracture is diverted along the pre-existing path of the natural fracture, and then creates a new fracture path again starting at the end of the natural fracture; (c) the hydraulic fracture is also diverted along the pre-existing path of the natural fracture, and then kinks out at some weak point along the natural fracture.

Recent efforts to study the interaction between natural and hydraulic fractures have taken various forms. Extensive theoretical and experimental works have been conducted (Blanton, 1986; Warpiniski and Teufel, 1987; Renshaw and Pollard, 1995; Beugelsdijk et al., 2000; Dahi-Taleghani and Olson, 2009; Gu and Weng, 2010; Gu et al., 2011; Bahorich et al., 2012; Olson et al., 2012; Chuprakov et al., 2013; Wang et al., 2013). Various criteria have been developed to predict the interaction and were validated by laboratory experiments which are very important approaches to investigate the physics of hydraulic fracture complexity with the advantage of complete observation of fracture geometry. Blanton (1986) reported scaled laboratory experiments using hydrostone to study interactions between induced and pre-existing fractures under different angles of approach and differential stresses. Based on the laboratory results, a criterion for interactions was developed to provide a basis for extrapolating the laboratory results to field cases. The criterion determines whether the hydraulic fracture deviates into or crosses the natural fracture. If the pressure required for reinitiating is greater than the

opening pressure, the natural fracture will open and take fluid, otherwise crossing will occur.

Warpinski and Teufel (1987) performed mineback experiments and laboratory tests on Coconino sandstone under tri-axial conditions to study the effect of geologic discontinuities on hydraulic fracture propagation under different joint orientations and stress states. A simple analysis was developed to estimate whether the induced fracture will propagate across, activate (shear), or dilate the joint based on local stress field. Additional stresses induced by the hydraulic fracture and fluid leak-off are taken into account.

Renshaw and Pollard (1995) proposed a criterion to predict a fracture propagating across a frictional interface orthogonal to the approaching fracture. Based on Linear Elastic Fracture Mechanics (LEFM), the stresses near the fracture tip were studied to determine whether fracture slip occurs along the interface, diverting fracture propagation, or the fracture crosses the interface. The criterion was validated by experiments works using three molded layers of brittle materials. Since the intersection angle between hydraulic and natural fractures is not always 90^o and has a great impact on crossing, Gu and Weng (2010) extended the criterion to intersection at non-orthogonal angles.

The criteria summarized above concentrate on the mechanical interaction when a hydraulic fracture encounters a natural fracture. Chuprakov et al. (2013) developed a new analytical crossing model, which analyzes the crossing/arresting behavior of hydraulic and natural fractures including the effect of flow rate and fluid viscosity. The method uses an elasticity solution to analyze the fracture contact problem and a stress-energy criterion to study the crack initiation. The new model was validated with some laboratory experiments, two crossing criteria and numerical simulations.

Most of criteria and experimental works focus on frictional interfaces. However, core observations indicate that natural fractures in Barnet and other shale plays are largely sealed with minerals, such as calcite or quartz (Gale, 2007). Dahi-Taleghani and Olson (2009) proposed a new crossing criterion to determine whether a hydraulic fracture will cross or deflect into a fully cemented natural fracture based on energy release rates of the reservoir rock and the cements in the natural fracture. Laboratory work was also conducted to determine the impact of cemented natural fractures on hydraulic fracture propagation. Bahorich et al. (2012) performed multiple hydraulic fracturing experiments using gypsum cement blocks with different cemented natural fracture proxies, including glass, Berea sandstone and gypsum plaster. The results included bypass, separation of weakly bounded interfaces, diversion, and mixed mode propagation depending strongly on the angle of intersection, the ratio of hydraulic fracture height to natural fracture height, and the differential stress. Wang et al. (2013) employed semi-circular bending tests to assess the effects of pre-existing cemented fractures with different approach angles, cement strengths and natural fracture thicknesses on hydraulic fracture propagation. From the experiment results, the authors concluded that natural fracture cement thickness might not affect the crossing/diverting behavior of hydraulic fractures, but it changes the jog distance along the natural fracture. The hydraulic fracture tends to cross natural fractures with high approach angle and deflect into natural fractures with low approach angle.

To analyze complex fracture networks in naturally fractured reservoirs, various models have been developed incorporating interaction between hydraulic and natural fractures. Two practical engineering design approaches are embodied in the so-called wire-mesh model (Xu et al., 2009) and the discrete fracture network model (DFN) (Meyer et al., 2011), where hydraulic fractures are presumed to form an orthogonal grid

pattern. These two models calculate opening displacement discontinuity based on the relationship of crack aperture and net pressure (Meyer et al., 2011), and use analytical methods (Olson et al., 2004; Meyer et al., 2011) to describe fracture mechanical interaction, without explicit treatment of individual fracture influence on propagation path and interaction between induced fractures and pre-existing fractures.

Olson et al. (2009) presented a model to describe multiple, non-planar, pseudo-3D fracture propagation in naturally fractured reservoirs. The model describes mechanical interaction between pressurized fractures and the effect of pre-existing fractures on fracture pattern complexity, showing the influence of in-situ horizontal differential stress and fracture propagation velocity exponent on network geometry. However, this model assumes constant internal pressure along fracture length.

Dahi-Taleghani et al. (2009) incorporated fluid flow into this an eXtended Finite Element Method (XFEM) model to analyze hydraulic fracture interaction with natural fractures, but this model is limited in that it is a two dimensional. Budyn et al. (2004) and Keshavarzi et al. (2012) also modeled hydraulic fracture propagation applying two-dimensional XFEM to analyze the interaction between hydraulic and natural fractures under plane strain and quasi-static conditions.

Weng et al. (2011) and Wu et al. (2012) described a model for simulating multiple hydraulic fractures in naturally fractured reservoirs combining standard pseudo-3D equations for fracture width calculations, explicitly applying the displacement discontinuity approach of Olson (2004) to account for the stress interaction effects between fractures.

Two parallel but very different approaches were proposed based on discrete element method (DEM). One approach is 3DEC model (Nagel et al., 2011), which uses a discrete fracture network (DFN) to subdivide deformable blocks into a mesh in three

dimensions. Injected fluid can open pre-existing fractures in the DFN as dictated by the pressure and stresses acting on the model or these discontinuities can shear, but no new fracture propagation is allowed beyond the original included set of natural fractures. The other approach is a DEM model made of bonded particles that have inter-granular pore space (Zhao et al., 2009). An injected fluid raises the pressure to break the bonds between particles, enabling fracture growth. Pre-existing fractures are modeled as zones of initially broken or weak bonds, but new fractures can form following the stress state by breaking additional bonds. This approach can also simulate induced microseismic energy, but large problems are difficult to solve because of computational intensity of the method.

McClure (2012) developed a discrete fracture network model to simulate hydraulic fracture propagating in naturally fractured reservoirs, coupling fluid flow with the stresses induced by fracture deformation. The induced stresses are computed by the displacement discontinuity method with a three-dimensional correction factor (Olson, 2004). The model is able to simulate hydraulic fracture intersecting with natural fractures and investigate the induced seismicity during injection, but it requires that the location of new fractures must be specified in advance.

1.5 ORGANIZATION OF THE DISSERTATION

The dissertation is divided into eight chapters. Chapters 2 and 4 introduce the methodology of modeling and analyze physical sub-processes incorporated into the model. Chapters 3, 5, 6 and 7 are validation, testing, and application of the model, investigating the physical mechanisms of complex hydraulic fracture development.

Following this chapter, Chapter 2 describes the details of the stimulation model and presents results from validation tests. The mathematical and numerical methodologies are described. The Two-Dimensional Displacement Discontinuity Method (2D DDM) with a three dimensional elastic correction factor G is used to represent the rock deformation. Non-linear fluid mechanics is solved by the Finite Different Method. Iterative and fully coupled procedures are implemented to couple rock mechanics and fluid mechanics together. Finally, comparison with the analytical solutions and Unconventional Fracture Model are presented to validate our model.

In Chapter 3, the model developed in Chapter 2 is applied to simulate single non-planar fracture and multiple fracture propagation. The single non-planar fracture propagation is simulated by both iteratively and fully coupling procedures given in Chapter 2. We also investigate a sensitivity study for the non-planar propagation. Two different stimulation methods (simultaneous and sequential) are then simulated for the same case of multiple fractures, showing the difference on fracture geometry and injection pressure.

Chapter 4 presents Three-Dimensional Displacement Discontinuity Method (3D DDM) and an analytical solution for plane strain problems. Based on 3D DDM and the analytical solution, a novel Simplified Three-Dimensional Displacement Discontinuity Method (S3D DDM) is proposed and derived, which is able to calculate displacements and induced stresses not only for single fracture but also for multiple fractures, especially complex fracture networks in three dimensions. The computational efficiency of S3D DDM is improved by more than one thousand times compared with 3D DDM.

The objectives of Chapter 5 are to test, validate and apply the S3D DDM derived in Chapter 4 for rock deformation. First, the S3D DDM is used to calculate rock deformation for static single and multiple fractures to validate the accuracy and efficiency

of the method. This method is then incorporated into our fracture propagation model given in Chapter 2. The new model is used to discover the physical mechanisms controlling simultaneous multiple fracture propagation through analysis of static and dynamic fracture.

Chapter 6 primarily studies the interaction between natural and hydraulic fractures that is the most important factor that might be responsible for the fracture complexity. Two crossing criteria are presented to determine the intersection of hydraulic and natural fractures. Based on our complex hydraulic fracture development model incorporating S3D DDM and the crossing criteria, we describe a sensitivity study for fracture geometry and injection pressure, examining the influence of geometric configuration of hydraulic and natural fractures and in-situ differential stress.

Chapter 7 shows the results of hydraulic fracture propagating in naturally fractured reservoirs. Natural fracture distribution is characterized by a stochastic realization method. The impacts of reservoir and operation parameters on fracture complexity were investigated through our model.

Finally, Chapter 8 draws the conclusions of the research stemming from this dissertation and gives some pertinent recommendations for future research.

CHAPTER 2: MODELING AND VERIFICATION[1]

In this chapter, a complex hydraulic fracture development model is developed to simulate single and multiple non-planar fracture propagation from horizontal wellbore in shale reservoirs. The numerical model can be used to explore the physical mechanisms of complex fracture geometry generation. The model also can be used to simulate multiple fracture propagation sequentially and simultaneously.

The model couples rock mechanics and fluid mechanics. A displacement discontinuity method is used to describe shear and normal displacement discontinuities and stress shadow effects between closely spaced fractures. Fluid flow in the fracture and the associated pressure drop are based on the lubrication theory, assuming the fracture is analogous to a slot between parallel plates and the fluid is non-Newtonian. The pressure equilibrium is maintained based on Kirchooff's first and second laws. Flow rate distribution into multiple perforation clusters is a dynamic process and a function of pressure loss along the wellbore and pressure within the hydraulic fractures. The rock mechanics and fluid mechanics can be coupled together numerically through an iteratively coupled solution procedure or a fully coupled solution procedure. In addition, a variety of validation methods to ensure accurate model behavior are implemented.

[1]Parts of this chapter have been published in SPE Journal: Wu, K. and Olson, J. E. 2014. Simultaneous multi-frac treatments: fully coupled fluid flow and fracture mechanics for horizontal wells. SPE 167626-PA. SPE Journal. http://dx.doi.org/10.2118/167626-PA. This paper was supervised by Jon Olson.

2.1 INTRODUCTION

Computational modeling of fracture propagation in shale reservoirs has proven to be a very important tool for exploring fundamental mechanisms and optimizing stimulation. However, fracture propagation is a very complex physical process, involving several co-existing and codependent sub-processes. The modeling is further complicated by fracture interference and the presence of heterogeneities (e.g. pre-existing natural fractures) in the shale formations. In this chapter, dominated sub-processes (e.g. fluid mechanics, rock deformation, fracture mechanics, and leak-off) are taken into account to comprehensively analyze complex fracture propagation.

Before deriving the governing equations of rock mechanics and fluid flow in Sections 2.2, 2.3 and 2.4, the following assumption are introduced:

For rock mechanics:

i. Linear elastic material properties;
ii. A homogeneous and isothermal medium;
iii. Vertical fractures with constant height;
iv. Only Mode I (Opening) and Mode II (Shearing) propagation.

For fluid mechanics:

i. Incompressible fluid;
ii. No proppant transport;
iii. Fluid flow within the fractures obeys Poiseuille flow;
iv. Fracture is fully filled with fluid, and there are no dry tips.

This chapter describes the development and validation of a fracture propagation model that has been used specifically to handle with complex hydraulic fracture propagation. In Section 2.2, governing equations and numerical methods for rock

deformation are described in detail. Section 2.3 describes fracture propagation based on fracture mechanics. In Section 2.4, the mathematical model of the fluid flow in the fracture system is reviewed. After obtaining numerical expressions of the rock deformation and the fluid flow, two numerical strategies are discussed for solving this coupled problem in Section 2.5. Finally, in Section 2.6, the results of model validation are presented and discussed. The results verify the accuracy of the model to solve three-dimensional problems and calculate mechanical interaction.

2.2 THE ELASTIC DISPLACEMENT DISCONTINUITY METHOD

The elastic rock deformation theory is used to solve for fracture opening and shearing given prescribed traction boundary conditions. These tractions are provided by a fluid mechanics model that computes the distribution of pressure along the fracture path. The fracture opening generates fracture aperture which allows fluid to flow. The shearing controls the fracture propagation direction, inducing non-planar propagation.

The two-dimensional displacement discontinuity method, a special boundary element method, was developed by Crouch (1976) and designed for handling problems with crack-like geometries. The boundary $S^{\pm}$ is divided into N planar elements. Based on the analytical solution of a constant displacement discontinuity element in an infinite elastic solid, stresses at arbitrary points can be calculated according to the principle of superposition, by linear combination of the displacement discontinuities at all elements.

Stresses at a point ξ within an elastic region are integrals of displacement discontinuities Δu_i over the boundary $S^{\pm}$ of the region (Figure 2.1),

$$\sigma_{jk}(\xi) = \int_S E_{ijk}(\xi,\eta)\Delta u_i(\eta)dS(\eta) \quad \Delta u_i = u_i^- - u_i^+, \tag{2.1}$$

where the quantity $E_{ijk}(\xi,\eta)$ is tensor field that represents the influences of a concentrated force at the point ξ on displacements at the point η.

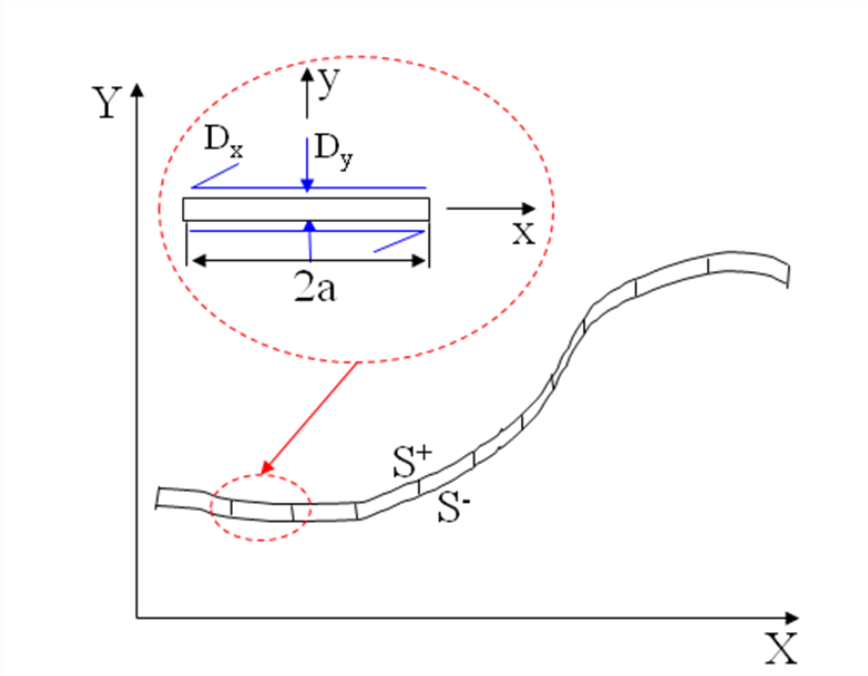

Figure 2.1: Illustration of a two-dimensional boundary with crack-like geometry.

Since analytical solutions for Eq. 2.1 are very hard to obtain, a numerical solution was applied to deal with this problem. There are two main types of numerical methods to solve the elasticity equations: (1) the domain type, (2) the boundary type. The details about these methods will be discussed in Chapter 4. We choose to discretize on the boundary of the domain to handle the problem via displacement discontinuity method. In this chapter, we only introduce the two-Dimensional Displacement Discontinuity Method (2D DDM).

The analytical solution $f(x,y)$ to the problem of a constant displacement discontinuity is obtained based on the solution of Kelvin's problem, expressed as (Crouch, 1983),

$$f(x,y)=\frac{-1}{4\pi(1-\nu)}[y(\arctan\frac{y}{x-a}-\arctan\frac{y}{x+a})-(x-a)\ln\sqrt{(x-a)^2+y^2} + (x+a)\ln\sqrt{(x+a)^2+y^2}] \quad , (2.2)$$

where ν is possion's ratio and a is half length of an element (Figure 2.1).

The general solution of stresses on a displacement discontinuity element is a function of $f(x,y)$, given as,

$$\begin{aligned}\sigma_{xx}&=2GD_x[2f_{,xy}+yf_{,xyy}]+2GD_y[f_{,yy}+yf_{,yyy}]\\ \sigma_{yy}&=2GD_x[-yf_{,xyy}]+2GD_y[f_{,yy}-yf_{,yyy}]\\ \sigma_{xy}&=2GD_x[f_{,yy}+yf_{,yyy}]+2GD_y[-yf_{,xyy}]\end{aligned} \quad , \quad (2.3)$$

$$\begin{aligned}f_{,xy}&=\frac{1}{4\pi(1-\nu)}[\frac{y}{(x-a)^2+y^2}-\frac{y}{(x+a)^2+y^2}]\\ f_{,yy}&=\frac{-1}{4\pi(1-\nu)}[\frac{x-a}{(x-a)^2+y^2}-\frac{x+a}{(x+a)^2+y^2}]\\ f_{,xyy}&=\frac{1}{4\pi(1-\nu)}[\frac{(x-a)^2-y^2}{\{(x-a)^2+y^2\}^2}-\frac{(x+a)^2-y^2}{\{(x+a)^2+y^2\}^2}]\\ f_{,yyy}&=\frac{2y}{4\pi(1-\nu)}[\frac{x-a}{\{(x-a)^2+y^2\}^2}-\frac{x+a}{\{(x+a)^2+y^2\}^2}]\end{aligned} \quad , \quad (2.4)$$

where G is shear modulus, D_x and D_y are displacement discontinuities in x and y direction, respectively.

The positions and directions of elements are generally different with each other, causing the solutions of stresses and displacement discontinuities of each element are written with respect to their own local coordinate system. Eq. 2.3 gives stress components for each element in local coordinates. In order to add the contributions of all N elements together, we must recast stresses from each local coordinate to global coordinate or local coordinate of element i, and then summarize contributions of all individual elements to

get stresses at a point. The details about this derivation will be discussed in Chapter 4.2.1. The coordinate transform is given in Appendix A.1.

For fracture problems, displacement or stress boundary conditions are generally defined on the crack surfaces with remote boundary conditions. Additionally, the simultaneous solution of the system of equations accounts for stresses caused by the mechanical interaction with other nearby elements (Crouch and Starfield, 1983). The remote and local stress boundary conditions are summarized by the following equations (Olson, 2007):

$$\begin{aligned} \Delta\sigma_n &= P_{net} = P_{frac} - \sigma_n^{remote} \\ \Delta\sigma_s &= \sigma_s^{local} - \sigma_s^{remote} \end{aligned}, \tag{2.5}$$

where P_{frac} is the internal fluid pressure, σ_n^{remote} is the normal stress acting on the element due to the remote boundary conditions, σ_s^{local} is locally applied shear traction acting on the element (typically a frictional resistance when the crack surfaces are in contact or zero if the crack is open), and σ_s^{remote} is the remote boundary shear stress. $\Delta\sigma_n$ is equivalent to the net pressure if the fracture is perpendicular to the least principal stress. Based on given normal and shear stresses (σ_n^i and σ_s^i) imposed on an i^{th} boundary element, the shear and normal displacement discontinuities, D_s^j and D_n^j, at any element j, can be computed by solving the following system of equations for i = 1 to N,

$$\begin{aligned} \sigma_n^i &= \sum_{j=1}^{N} G^{ij} C_{ns}^{ij} D_s^j + \sum_{j=1}^{N} G^{ij} C_{nn}^{ij} D_n^j \\ \sigma_s^i &= \sum_{j=1}^{N} G^{ij} C_{ss}^{ij} D_s^j + \sum_{j=1}^{N} G^{ij} C_{sn}^{ij} D_n^j \end{aligned}, \tag{2.6}$$

where C_{ns}^{ij} is the plane-strain, elastic influence coefficient matrix representing the normal stress at element i induced by a shear displacement discontinuity at element j, and C_{nn}^{ij} gives the normal stress at element i due to an opening displacement discontinuity at

element *j*. Analogous meanings can be attributed to C_{ss}^{ij} and C_{sn}^{ij}. The detailed derivation of C is given by Crouch and Starfield (1983).

This two-dimensional displacement discontinuity method assumes plane strain where the out of plane direction is vertical, implying a crack with infinite height. However, fracture height is typically finite relative to fracture length in the reservoirs. Therefore, to account for the 3D aspects of displacement discontinuities of finite height fractures, we employ a 3D correction factor G^{ij} derived by Olson (2004),

$$G^{ij} = 1 - \frac{d_{ij}^{\beta}}{[d_{ij}^2 + (h/\alpha)^2]^{\beta/2}}, \tag{2.7}$$

where d_{ij} is the distance between the center of elements *i* and *j*, *h* is the fracture height, and α and β are empirically determined constants, where $\alpha = 1$ and $\beta = 2.3$.

2.3 FRACTURE PROPAGATION

The fracture propagation process can be treated as the length incremental process (Yew, 1997). At every time step, pumping fluid is injected into the fracture and increases pressure inside of fracture, fracture width and stress intensity factor before propagation. When deformation at the fracture tips reaches a critical point in terms of the material strength, the fracture front will move forward a certain distance. During this propagation process, the critical condition of fracture propagation, the propagation direction, and propagation velocity need to be determined.

2.3.1 Fracture propagation criterion

The propagation criterion for a hydraulic fracture is dependent on the propagation regime (Detournay, 2004; Adachi et al., 2007). The viscosity-dominated regime represents that energy dissipated in creating new fracture surfaces is much smaller than

that dissipated in fluid flow. The toughness-dominated regime is when the energy dissipated in the fracture tips is larger than the energy consumed by viscous flow. Generally, the criterion for propagation in the toughness-dominated regime is described by conventional linear elastic fracture mechanics (LEFM). A fracture starts growing if $K_I = K_{IC}$, where K_I is stress intensity factor at fracture tips and K_{IC} is the toughness of rock (an assigned value). For the viscosity-dominated regime, toughness plays a negligible role in fracture propagation and the rock can be assumed as zero-toughness.

In small-scale hydraulic fracturing (e.g. laboratory tests with block volume of 1 cubic foot), toughness might dominate the fracture growth. The fracture propagates when the stress intensity factor reaches rock toughness. However, in field-scale treatments, most of energy is dissipated in fluid flow along the fracture, and viscosity controls fracture propagation.

2.3.2 Maximum circumferential stress criterion

When propagation of the fracture occurs, the propagation direction needs to be determined. In cases where non-planar propagation is expected, propagation is usually controlled by both Mode I (shearing) and Mode II (opening) loadings. Erdogan and Sih (1963) formulated the first mixed-mode fracture propagation theory, the maximum circumferential stress criterion. The criterion is based on the stress state near fracture tips, expressed in polar coordinates (Figure 2.2) as,

$$\begin{aligned}
\sigma_r &= \frac{1}{\sqrt{2\pi r}}\cos\frac{\theta}{2}[K_I(1+\sin^2\frac{\theta}{2}) + \frac{3}{2}K_{II}\sin\theta - 2K_{II}\tan\theta] \\
\sigma_\theta &= \frac{1}{\sqrt{2\pi r}}\cos\frac{\theta}{2}[K_I\cos\frac{\theta}{2} - \frac{3}{2}K_{II}\sin\theta] \qquad , \qquad (2.8) \\
\tau_{r\theta} &= \frac{1}{\sqrt{2\pi r}}\cos\frac{\theta}{2}[K_I\sin\theta + K_{II}(3\cos\theta - 1)]
\end{aligned}$$

where K_I is the stress intensity factor of mode I (opening), K_{II} is the stress intensity factor of mode II (shearing), r, θ are the polar coordinate system with origin at the crack tip, θ is the counterclockwise positive angle from the direction of in-plane propagation.

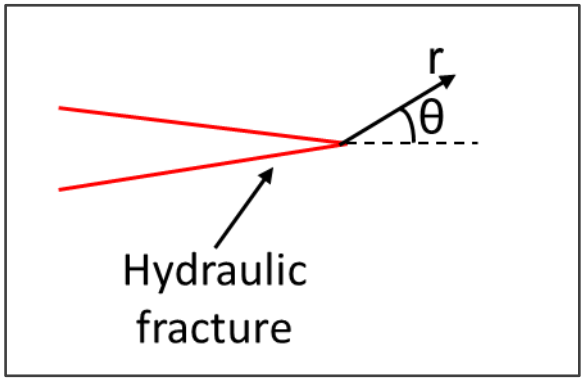

Figure 2.2: Illustration of fracture propagation direction.

The criterion states that a fracture starts propagating in the plane perpendicular to the direction of greatest tension (or least compression) when the stress reaches a critical material constant. This also necessitates that the fracture propagates in the plane where $\tau_{r\theta}$ is 0. According to the Eq. 2.8, the direction θ can be solved by setting the shear stress to zero as

$$\frac{1}{\sqrt{2\pi r}}\cos\frac{\theta}{2}[K_I \sin\theta + K_{II}(3\cos\theta - 1)] = 0 . \tag{2.9}$$

The Eq. 2.9 has two solutions,

$$\begin{matrix} \cos\dfrac{\theta}{2} = 0 \\ K_I \sin\theta + K_{II}(3\cos\theta - 1) = 0 \end{matrix} . \tag{2.10}$$

The first solution is trivial. Consequently, the fracture propagation direction is based on the second solution, where

$$\tan\frac{\theta}{2} = \frac{1}{4}\frac{K_I}{K_{II}} \pm \frac{1}{4}\sqrt{(\frac{K_I}{K_{II}})^2 + 8} . \tag{2.11}$$

When $K_I > 0$ and $K_{II} = 0$, planar crack propagation should proceed along $\theta = 0^o$. When $K_I = 0$ and $K_{II} \neq 0$, a pure shear in mode, the result is the strongest possible kink in fracture direction along $\theta = \pm 70.5°$ for positive or negative K_{II}, respectively.

To obtain propagation direction from Eq. 2.11, the stress intensity factors (K_I and K_{II}) must be calculated, which are functions of shear and normal displacement discontinuities at the crack tips computed by the displacement discontinuity method discussed in Section 2.2.1. Olson (1990, 2007) gave expressions of the stress intensity factors as

$$\begin{aligned} K_I &= \frac{0.806E\sqrt{\pi}}{4(1-\nu^2)\sqrt{2a}} D_n \\ K_{II} &= \frac{0.806E\sqrt{\pi}}{4(1-\nu^2)\sqrt{2a}} D_s \end{aligned}, \tag{2.12}$$

where E is the young's modulus, D_n is the normal displacement discontinuity, D_s is the shear displacement discontinuity, a is the half element length, ν is the possion's ratio.

2.3.3 Fracture propagation velocity

Fracture propagation velocity is affected by many factors, such as the generation of a plastic zone at fracture tips, micro cracks and cavities, and fluid velocity and pressure at fracture tips (Yamamoto et al., 2004). Desroches et al. (1994, 1998) stated that fluid velocity might be the most important factor controlling advance of the fracture front. Therefore, in our model the propagation velocity is calculated based on injection rate within each fracture.

2.4 FLUID MECHANICS

Fracture propagation is driven by an incompressible and non-Newtonian fluid. For single fracture propagation, only fluid flow within the fracture needs to be

considered. For multiple fractures, fluid flow consists of three parts: fluid flow in the fracture, fluid flow in the horizontal wellbore, and the total material balance of all fractures.

2.4.1 Fluid flow within the fracture

Fluid flow through a rock fracture is modeled by the Navier-Stokes equations of fluid mechanics (Schlichting, 1968). When assuming a uniform pressure gradient in the channel between two parallel and smooth fracture surfaces, the Navier-Stokes equations can be simplified as (Valko and Economides, 1995)

$$\frac{\partial p}{\partial s} = C_f h^{-n'} w^{-(2n'+1)} q^{n'}, \tag{2.13}$$

where $C_f = 2^{n'+1} k' (\frac{1+2n'}{n'})^{n'}$, p is the fluid pressure, q is the fluid flow rate in the fracture, h is the fracture height, w is the fracture width, s is the distance along the fracture, and n' and k' are the fluid power-law index and consistency index, respectively.

From Eq. 2.13, we can obtain the relationship between pressure drop and fluid properties, fracture geometry and flow rate. Pressure drop increases with increasing flow rate, q, and decreases with increasing fracture width, w. When n' = 1, the fluid is Newtonian with a viscosity of k'. When a hydraulic fracture intersects with a natural fracture and creates two branches (Figure 2.3), material balance of flow rate is satisfied at the intersection point ($Q_{in} = Q_{out}^1 + Q_{out}^2$), and pressure is continuous. Spence and Sharp (1985) and Zimmerman et al. (1991) discussed the validation of the lubrication theory for modeling fluid flow inside the fractures. According to their analysis, fracture aperture cannot change too abruptly and should be small in comparison to the other dimensions of the fractures, and fluid flow should be laminar.

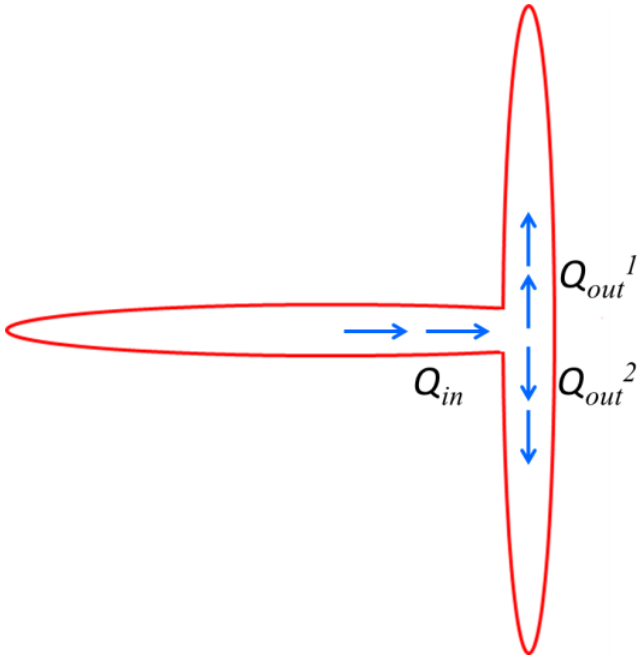

Figure 2.3: Illustration of fluid flow at an intersection point.

The material balance within the fracture can be written as:

$$\frac{\partial q(s,t)}{\partial s} - q_l(s,t) - \frac{\partial A(s,t)}{\partial t} = 0\,. \tag{2.14}$$

The leak-off volume is described by Carter leak-off model (Carter, 1957), which is expressed as

$$q_l(s,t) = \frac{2hC_L}{\sqrt{t-\tau(s)}}\,, \tag{2.15}$$

where $q(s, t)$ is flow rate through the fracture cross section, $A(s, t)$ is the cross-sectional area of the fracture, $q_l(s, t)$ is volume rate of fluid loss to the formation per unit length of fracture, C_L is the fluid loss coefficient, and $\tau(s)$ is the time at which fracture reaches position s. The Carter leak-off model assumes that leak-off is one dimension in the direction perpendicular to the fracture plane.

2.4.2 Fluid flow in horizontal wellbore

A numerical model for multilayer fracturing treatments in vertical wells was presented by Siriwardane et al. (1991), Mack et al. (1992) and Elbel et al. (1992). The model described the conservation of volume and continuity of pressure by using a set of constraints, such as hydrostatic pressure change, perforation friction pressure drop, and friction pressure loss in each casing interval. Fluid flow in the horizontal wellbore is similar to fluid flow in the vertical wellbore with multiple layers. The only difference is that we assume no hydrostatic pressure change in the horizontal wellbore.

Fluid flow in the wellbore is analogous to the flow of electric current through an electrical circuit network, applying Kirchoff's first and second laws to obtain the flow rate distribution of multiple fractures (Siriwardane et al., 1991; Mack et al., 1992; Elbel et al., 1992). Our model assumes multiple transverse fractures are initiated perpendicular to the horizontal wellbore at perforation cluster locations. The total injection rate, Q_T, is divided into injection rates of each fracture, Q_{fi}. The flow rate distribution is a dynamic process, and diversion of the fluid into various perforation clusters is a function of wellbore friction, perforation friction and the fluid pressure within the fractures (Figure 2.4).

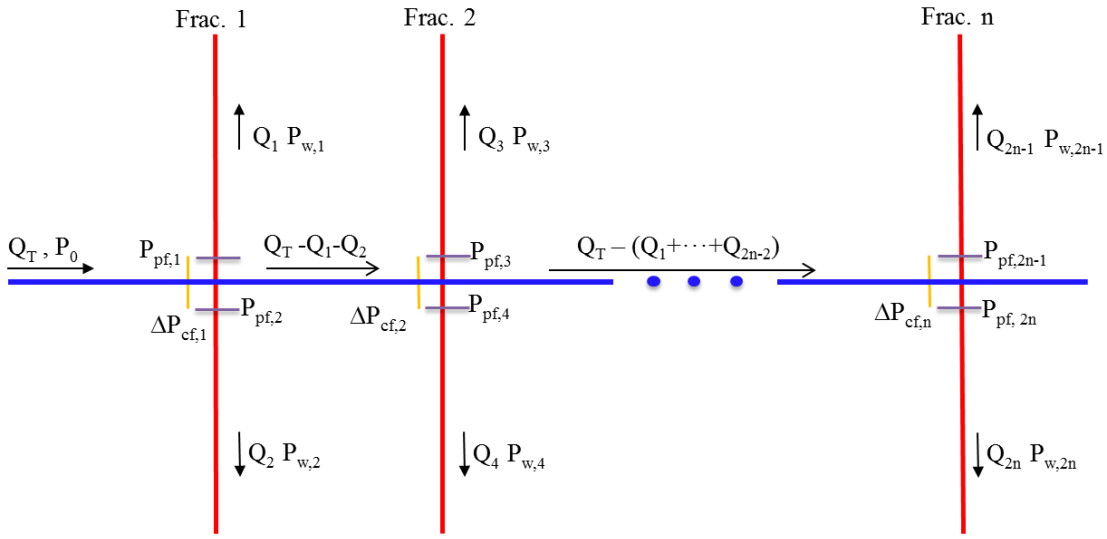

Figure 2.4: Illustration of flow rate partition and pressure drop.

Ignoring wellbore storage effects, total injection rate should be the sum of the injection rates of all fractures,

$$Q_T = \sum_{fi=1}^{N_f} Q_{fi}\,, \tag{2.16}$$

where Q_T is total injection rate, Q_{fi} is injection rates of fi^{th} fracture.

Kirchoff's second law describes the continuity of pressure, where the pressure in the wellbore heel is equal to the sum of wellbore friction pressure drop, perforation friction pressure drop and pressure in the first element of fracture as (Elbel et al.,1992)

$$p_o = p_{w,fi} + p_{pf,fi} + p_{cf,fi}\,, \tag{2.17}$$

where p_o is the total pressure at the wellbore heel, $p_{w,fi}$ is pressure in the first element of fi^{th} fracture, which is calculated by Eq. 2.13, $p_{pf,fi}$ is the perforation friction pressure loss which is proportional to the square of flow rate, estimated by (Crump and Conway, 1988; Economides and Nolte, 2000; Bunger et al., 2014; Lecampion and Desroches, 2014)

$$p_{pf,fi} = \frac{0.2369\rho_s}{n_{p,fi}^{\,2} d_{p,fi}^{\,4} K_d^{\,2}} Q_{fi}^{\,2}\,, \tag{2.18}$$

where ρ_s *is* density of slurry, $n_{p,fi}$ *is* the number of perforations of fi^{th} fracture, $d_{p,fi}$ is diameter of perforation of fi^{th} fracture, K_d is the discharge coefficient, ranging from 0.56 to 0.89, 0.2369 is a coefficient for field unit.

$P_{cf,fi}$ is pressure loss in the horizontal wellbore given by (Valko and Economides, 1995)

$$\begin{aligned} p_{cf,fi} &= C_{cf} \sum_{j=1}^{i} (x_j - x_{j-1}) Q_{wj}{}^{n'} \\ Q_{wj} &= Q_T - \sum_{k=1}^{2(j-1)} Q_k \\ Q_{wj} &= Q_T \quad at\ j = 1 \\ C_{cf} &= 2^{3n'+2} \pi^{-n'} k' \left(\frac{1+3n'}{n'}\right)^{n'} D^{-(3n'+1)} \end{aligned} \quad , \tag{2.19}$$

where D is the diameter of wellbore.

The pressure drop between the wellbore intervals is a function of distance between two neighboring fractures and flow rate Q_{wj} in the wellbore intervals. The longer the distance between two neighboring fractures, the larger the pressure drop.

Material balance must be satisfied in the whole fluid flow system. The total volume of fluid pumped during the injection time is equal to the fluid volume preserved in the multiple fractures and the volume leaking into the surrounding porous medium. The global volume balance is

$$\int_0^t Q_T(t)dt = \sum_1^{N_f} \int_0^{L_i(t)} hwds + \sum_1^{N_f} \int_0^{L_i(t)} \int_0^t q_l(s,t)dtds\,, \tag{2.20}$$

where N_f is the number of fractures, $L_i(t)$ is the total fracture length of i^{th} fracture at time t.

2.4.3 Boundary conditions

Boundary condition at the wellbore for single fracture and multiple fracture propagation is different. For single fracture propagation, the boundary condition at the wellbore is

$$q(t,0) = \left(\frac{1}{C_f} h^{n'} w^{(2n'+1)} \frac{\partial p}{\partial s}\right)^{\frac{1}{n'}}\Bigg|_{s=0} = Q, \tag{2.21}$$

where Q is the injection rate at the wellbore.

However, for multiple fracture propagation, the boundary condition at the wellbore is

$$Q_T = Q. \tag{2.22}$$

At the fracture tip, the boundary condition is that fracture propagation criterion is satisfied.

2.5 NUMERICAL STRATEGIES FOR THE COUPLED MODEL

In the Sections 2.3 and 2.4, the mathematical models of rock deformation and fluid mechanics are presented. Rock deformation is a set of linear algebraic equations (Eq. 2.6). The Finite Difference Method (FDM) is used to discretize the fluid flow governing equations (Eqs. 2.13 and 2.14) which are a set of nonlinear algebraic equations. Generally, two kinds of solution procedure can be used to solve the coupled model: an iteratively coupled solution procedure and a fully coupled solution procedure (Pan, 2009). The iteratively coupled solution procedure is based on the Picard iterative method. Linear rock deformation equations are first solved, and then non-linear fluid flow equations are solved using the Newton-Raphson method (Figure 2.6 (a)). The fully coupled solution procedure solves rock deformation and fluid flow simultaneously through the Newton-Raphson method (Figure 2.6 (b)). In our model, the fully coupled

solution procedure is employed to simulate non-planar single fracture propagation, and the iteratively coupled solution procedure is applied to solve multiple fracture propagation.

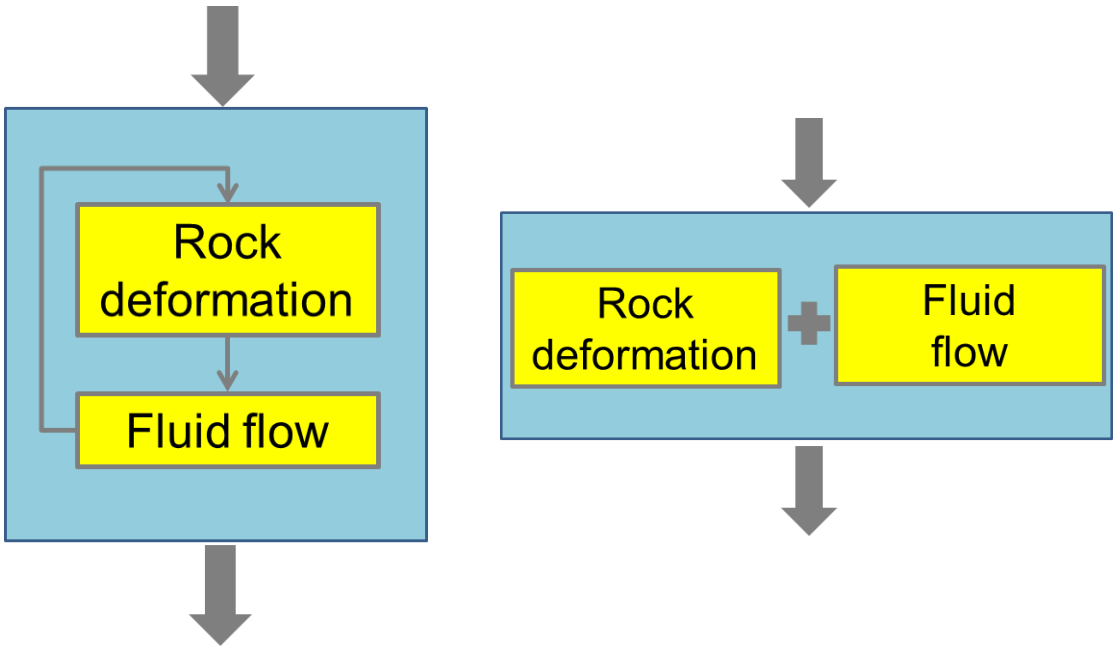

(a) Iteratively coupled rock deformation and fluid flow

(b) Fully coupled rock deformation and fluid flow

Figure 2.5: Comparison of the implementation of the iteratively coupled solution procedure and the fully coupled solution procedure.

2.5.1 A fully coupled solution procedure: non-planar single fracture propagation

For single non-planar fracture, we only need to consider fluid flow inside of fracture (Eqs. 2.13 and 2.14). The coupled rock deformation and fluid flow, Eqs. 2.6, 2.13, and 2.14 were solved using the fully coupled solution procedure which utilizes the Newton-Raphson iterative method. This method is widely used in numerical calculation, which can effectively solve nonlinear problems and has very high quadratic convergence speed. But this method also has some disadvantages. It is very sensitive to an initial

guess. When the initial guess is very far from the solution, the method does not converge very well. The formulation of this method is

$$\begin{aligned} x_{k+1} &= x_k + dx_k \\ dx_k &= -M^{-1} f(x) \end{aligned}, \tag{2.23}$$

where x_k is the solution at k time step, and x_{k+1} is the solution at $k+1$ time step, M is the Jacobian matrix, $f(x)$ is the residual term. The algorithm of the Newton-Raphson iterative method is shown in Figure 2.6.

Algorithm **Newton-Raphson iterative method**

Step 1: Initially guess x_k

Step 2: Compute Jacobian matrix M **and residual term** $f(x)$

Step 3: Get dx_k **through solving the linear system** $dx_k = -M^{-1} f(x)$

Step 4: Update $x_{k+1} = x_k + dx_k$

Step 5: Check convergence criterion. If satisfied, stop; otherwise go back to step 1

Figure 2.6: Algorithm of the Newton-Raphson iterative method.

Fluid flow and rock deformation are both discretized on the same grids of boundary elements. If the hydraulic fracture is divided into N elements, the total unknown variable is $4N$. The unknown variables can be described in the following vector form:

$$x^T = [D_n, D_s, q_i, dt, p_i]. \tag{2.24}$$

Also, we have $4N$ equations to solve the variables. Based on Eqs. 2.6, 2.13 and 2.14, a residual function vector can be written as

$$f_I = \sigma_n^i - \sum_{j=1}^{N} G^{ij} C_{ns}^{ij} D_s^j - \sum_{j=1}^{N} G^{ij} C_{nn}^{ij} D_n^j, \tag{2.25}$$

$$f_{II} = \sigma_s^i - \sum_{j=1}^{N} G^{ij} C_{ss}^{ij} D_s^j - \sum_{j=1}^{N} G^{ij} C_{sn}^{ij} D_n^j , \tag{2.26}$$

$$f_{III} = \frac{\partial p}{\partial s} - C_f h^{-n'} w^{-(2n'+1)} q^{n'} , \tag{2.27}$$

$$f_{IV} = \frac{\partial q(s,t)}{\partial s} - \frac{2hC_L}{\sqrt{t-\tau(s)}} - \frac{\partial A(s,t)}{dt} . \tag{2.28}$$

This nonlinear equation system can be solved by the Newton-Raphson iterative method. After deriving the partial derivatives of Eqs. 2.25 through 2.28 with respective to 4N unknown variables, a linear fully coupled system is obtained. The Jacobian matrix M, dx_k and residual term $f(x)$ can be expressed as

$$M = \begin{bmatrix} \frac{\partial f_I}{\partial D_{ni}} & \frac{\partial f_I}{\partial D_{si}} & \frac{\partial f_I}{\partial q_i} & \frac{\partial f_I}{\partial dt} & \frac{\partial f_I}{\partial p_i} \\ \frac{\partial f_{II}}{\partial D_{ni}} & \frac{\partial f_{II}}{\partial D_{si}} & \frac{\partial f_{II}}{\partial q_i} & \frac{\partial f_{II}}{\partial dt} & \frac{\partial f_{II}}{\partial p_i} \\ \frac{\partial f_{III}}{\partial D_{ni}} & \frac{\partial f_{III}}{\partial D_{si}} & \frac{\partial f_{III}}{\partial q_i} & \frac{\partial f_{III}}{\partial dt} & \frac{\partial f_{III}}{\partial p_i} \\ \frac{\partial f_{IV}}{\partial D_{ni}} & \frac{\partial f_{IV}}{\partial D_{si}} & \frac{\partial f_{IV}}{\partial q_i} & \frac{\partial f_{IV}}{\partial dt} & \frac{\partial f_{IV}}{\partial p_i} \end{bmatrix}, \tag{2.29}$$

$$dx_k = \begin{bmatrix} dD_n \\ dD_s \\ dq_i \\ ddt \\ dp_i \end{bmatrix} \qquad f(x) = \begin{bmatrix} f_I \\ f_{II} \\ f_{III} \\ f_{IV} \end{bmatrix}. \tag{2.30}$$

The linear equation system includes two parts, rock deformation (RD) and fluid flow (FF). Eqs. 2.29 and 2.30 can be simplified as

$$\begin{bmatrix} M_{11}^{RD} & M_{12}^{RD \leftarrow FF} \\ M_{21}^{FF \leftarrow RD} & M_{22}^{FF} \end{bmatrix} \begin{bmatrix} dx_k^{RD} \\ dx_k^{FF} \end{bmatrix} = \begin{bmatrix} f^{RD} \\ f^{FF} \end{bmatrix}, \tag{2.31}$$

where M_{11}, M_{12}, dx_1, and f_1 are matrices and vectors from the rock deformation, while M_{21}, M_{22}, dx_2, and f_2 are matrices and vectors from the fluid flow. M_{12} and M_{21} are the

coupling matrices contributed from the coupling of the fluid flow and the rock deformation.

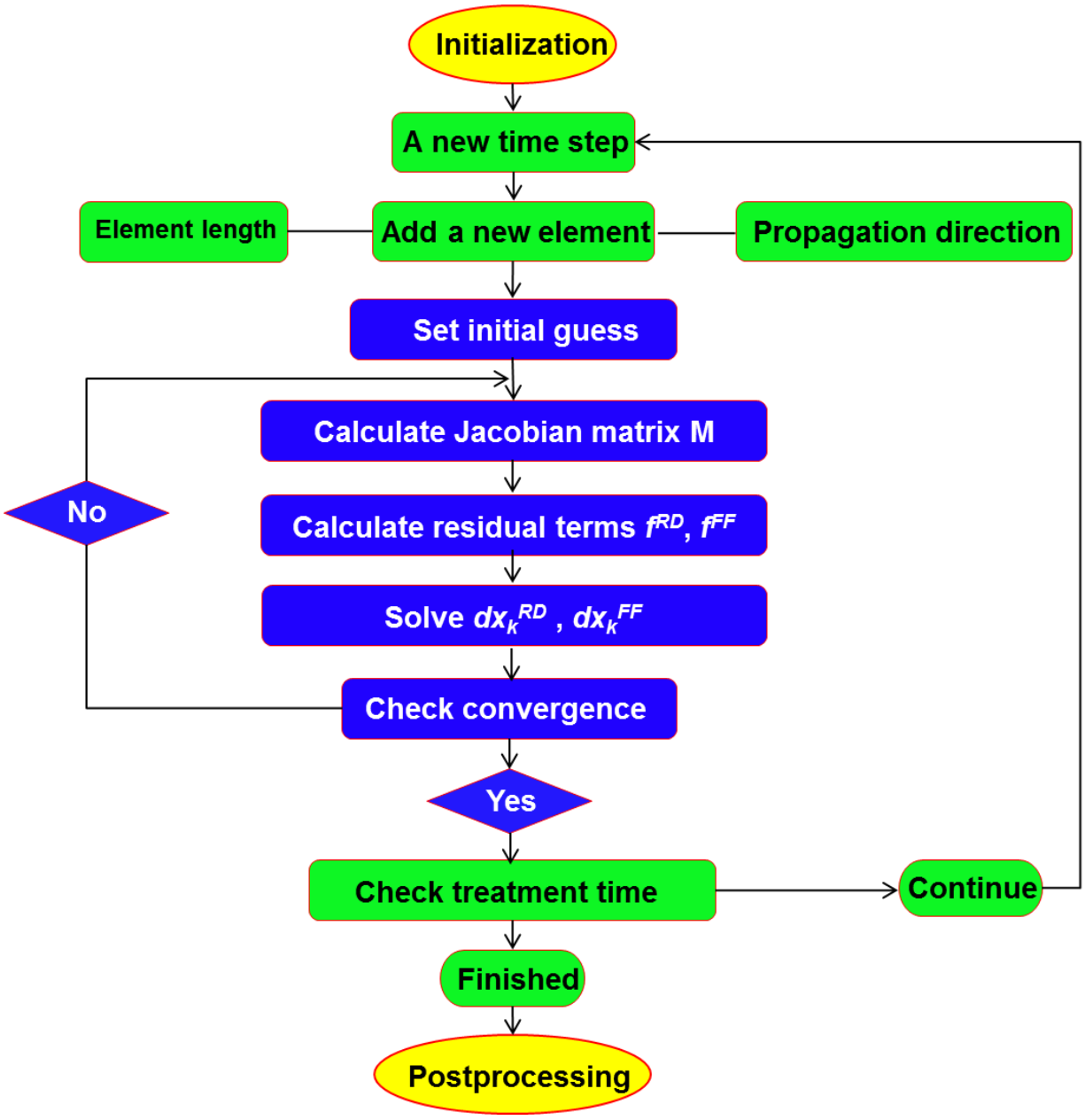

Figure 2.7: Flow chart of time-step loop of the fully coupled solution procedure.

A flowchart that explains the fully coupled procedure for non-planar single fracture propagation is shown in Figure 2.7. At each time step, a new fracture element is added based on fracture mechanics. Based on an initial guess of pressure, displacement discontinuities, flow rate and time interval are calculated. With a good initial guess, the Newton-Raphson iterative method can converge in only several steps.

2.5.2 An iteratively coupled solution procedure: multiple fracture propagation

For multiple fracture propagation, we need to consider fluid flow inside of fracture and horizontal wellbore (Eqs. 2.13, 2.14, 2.16 and 2.17). The fluid flow is still solved by the Newton-Raphson iterative method discussed in Section 2.4.1, and the coupled rock deformation and fluid flow, Eqs. 2.6, 2.13, 2.14, 2.16 and 2.17, are solved using the iteratively coupled solution procedure through the Picard iterative method.

The Picard coupling (Li, 1991; Adachi et al., 2007) also can be used to solve a system of nonlinear algebraic equations (in vector notation):

$$X = F(X)\,. \tag{2.32}$$

The iterative process can be expressed by the following formula:

$$X_{k+1} = \alpha_r F(X_k) + (1-\alpha_r) X_k\,, \tag{2.33}$$

where α_r is a retardation coefficient ranging from 0 to 1 that dampens variations to avoid X jumps and extreme changes in $F(X)$. If the convergence criterion cannot be satisfied, decreasing α_r is an approach to improve convergence. Smaller α_r can cause convergence to be too slow, while a large α_r can result in diverging oscillations. If α_r = 1, Eq. 2.33 becomes:

$$X_{k+1} = F(X_k)\,. \tag{2.34}$$

The advantage of this method is very easy to achieve and does not require complicated calculations. The shortcoming is that convergence is very slow. The algorithm of the Picard iterative method is shown in Figure 2.8.

Algorithm **Picard iterative method**

Step 1: Initially guess X_0

Step 2: Compute $F(X_k)$

Step 3: Update X_{k+1} using Eq. 2.33

Step 4: Check convergence criterion. If satisfied, stop; otherwise go back to step 2

Figure 2.8: Algorithm of the Picard iterative method.

For the fluid flow in multiple fractures, we simplified the fluid flow within the fracture. The flow rate gradient along the fracture is ignored in order to enhance convergence stability with little cost in accuracy. Therefore, governing equations of fluid flow (Eq. 2.13) becomes

$$\frac{\partial p}{\partial s} = C_f h^{-n'} w^{-(2n'+1)} Q_{fi}^{\ n'}. \tag{2.35}$$

If the number of hydraulic fracture is N_f, and each hydraulic fracture is divided into N elements, the total unknown variable is N_f*N+N_f+1. The unknown variables can be described in the following vector form:

$$x^T = [p_i, Q_{fi}, p_o]. \tag{2.36}$$

We have N_f*N+N_f+1 equations to solve the variables. Based on Eqs. 2.35, 2.16 and 2.17, a residual function vector can be written as

$$f_I = \frac{\partial p}{\partial s} - C_f h^{-n'} w^{-(2n'+1)} Q_{fi}^{\ n'}, \tag{2.37}$$

$$f_{II} = p_o - p_{w,fi} - p_{pf,fi} - p_{cf,fi}, \tag{2.38}$$

$$f_{III} = Q_T - \sum_{fi=1}^{N_f} Q_{fi} \,. \tag{2.39}$$

Also, we derived the partial derivatives of Eqs. 2.37 through 2.39 with respective to unknown variables, and the Jacobian matrix and residual term are obtained. Hence the whole fluid flow system of multiple fractures can be solved.

A flowchart that explains the iteratively coupled procedure for multiple fracture propagation is shown in Figure 2.9. At each time step, a new fracture element is added based on fracture mechanics. An initial guess of pressure inside of fracture is set. Displacement discontinuities are calculated using the guessing pressure by Eq. 2.6. After obtaining fracture width from rock deformation, pressure distribution is calculated using the Newton-Raphson method. After that, the calculated pressure and guessing pressure is compared to check the convergence. If the convergence criterion is not satisfied, the pressure is modified as,

$$p_{k+1} = (1-\alpha_r)\, p_{k-1} + \alpha_r\, p_k \,. \tag{2.40}$$

After obtaining a new pressure, the whole process is repeated until the convergence criterion is satisfied. For this problem, we have found that α_r = 0.2 provides a reasonably stable convergence. If the convergence criterion is reached, based on total material balance the time increment *dt* is calculated using the equation:

$$Q_T(t)(t+dt) - \sum_{1}^{N_f}\sum_{i=1}^{N} hw_i s_i - \sum_{1}^{N_f}\sum_{i=1}^{N}\sum_{k=0}^{t} \frac{2hC_L s_i}{\sqrt{t-\tau_i^k}} = 0 \,, \tag{2.41}$$

where s_i is the length of each element.

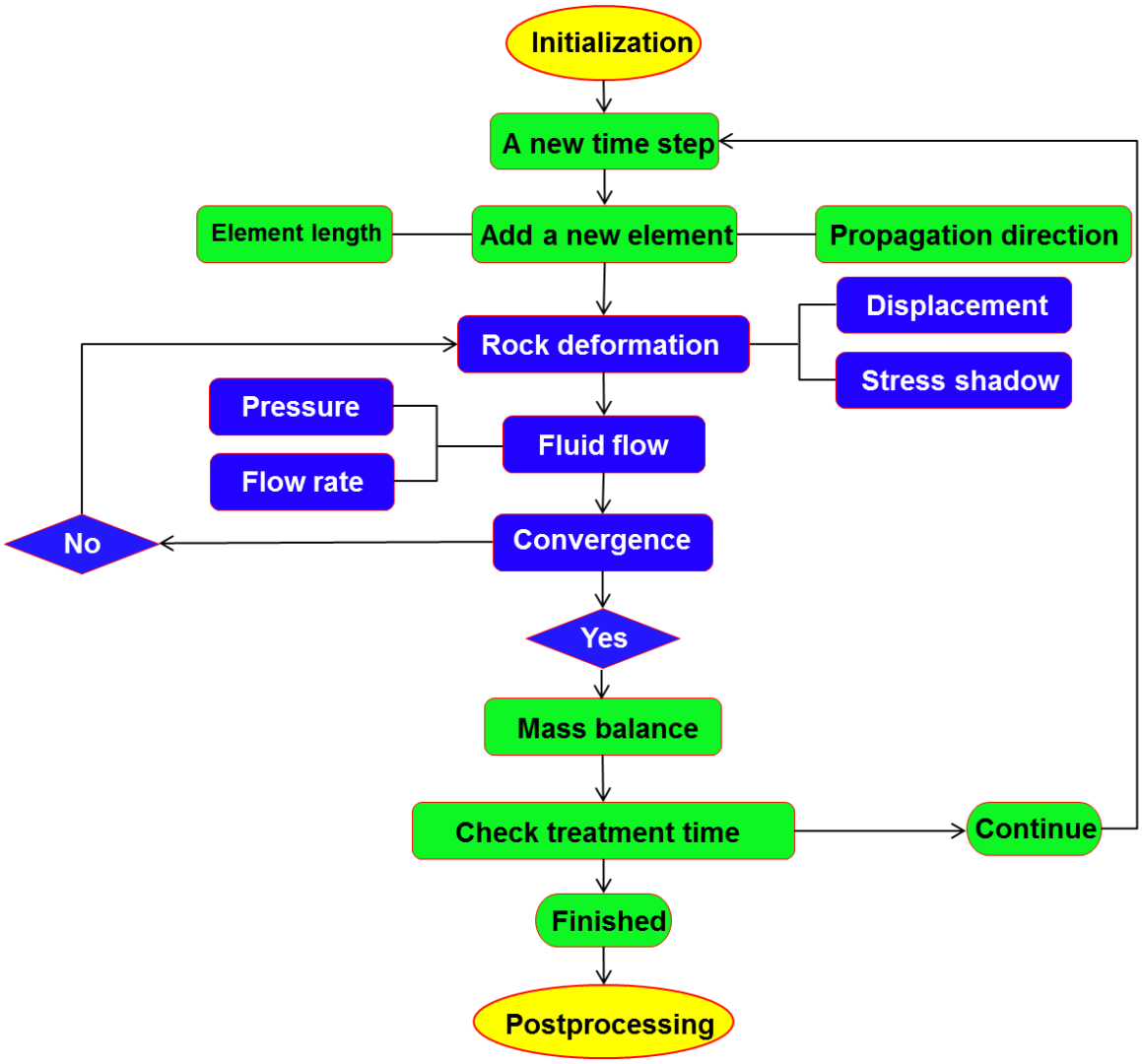

Figure 2.9: Flow chart of time-step loop of the iteratively coupled solution procedure.

2.6 VERIFICATION

Verification is another important task for fracture modeling, because there is very little direct data on fracture geometry we can access to compare with modeling results. Most fracture diagnostic technologies cannot provide enough information to completely

describe fracture geometry. Hence, we will validate our model through comparing with analytical solutions and another numerical model (Unconventional Fracture Model).

2.6.1 Comparison with analytical solutions

Our complex hydraulic fracture development model is a three-dimensional model, which can simulate fracture propagation with constant height. We compare our model to the classical analytical solutions of Khristianovich-Geertsma-Deklerk (KGD) and Perkins-Kern-Nordgren (PKN) (Table 2.1). The detailed descriptions of these two models are given in Section 1.4.1. For dynamic propagation fracture with constant height, at very early time KGD model can accurately simulate the process because fracture height is much greater than fracture length. As fracture grows longer, the assumption of KGD model is violated. When fracture length is much greater than height, the PKN model can give accurate results. Hence, to validate our three-dimensional model, fracture geometry at the early time is compared with results calculated by the KGD model, and the PKN model is used to compare with the results of late time.

We simulate a case with a fracture height 200 ft. The fracture geometry calculated by KGD is much wider and shorter with very low net pressure that climbs with time, compared with PKN model. The other input parameters are listed in the Table 2.2.

A comparison of results is plotted for fracture length (Figure 2.10), fracture width at the wellbore (Figure 2.11), and net injection pressure (Figure 2.12). As shown, our model gives very good agreement with the KGD model in the earlier time and tends to match the PKN analytical solution as the fracture grows longer, consistent with our expectations.

	Fracture half-length	Wellbore width	Injection pressure
KGD	$0.539(\frac{i^3E'}{\mu h^3})^{1/6}t^{2/3}$	$2.36(\frac{\mu i^3}{E'h^3})^{1/6}t^{1/3}$	$S_{h\min}+1.09(E'^2\mu)^{1/3}t^{-1/3}$
PKN	$0.524(\frac{i^3E'}{\mu h^4})^{1/5}t^{4/5}$	$3.04(\frac{\mu i^2}{E'h})^{1/5}t^{1/5}$	$S_{h\min}+1.52(\frac{E'^4\mu i^2}{h^6})^{1/5}t^{1/5}$

Table 2.1: Analytical solutions of KGD and PKN (Valko and Economides, 1995).

μ	100 cp
Injection rate	20 bpm
Young's modulus	6,530,000 psi
Poisson's ratio	0.2
Height	200 ft
Minimum horizontal stress	4,450 psi

Table 2.2: Input parameters for validation with analytical solutions.

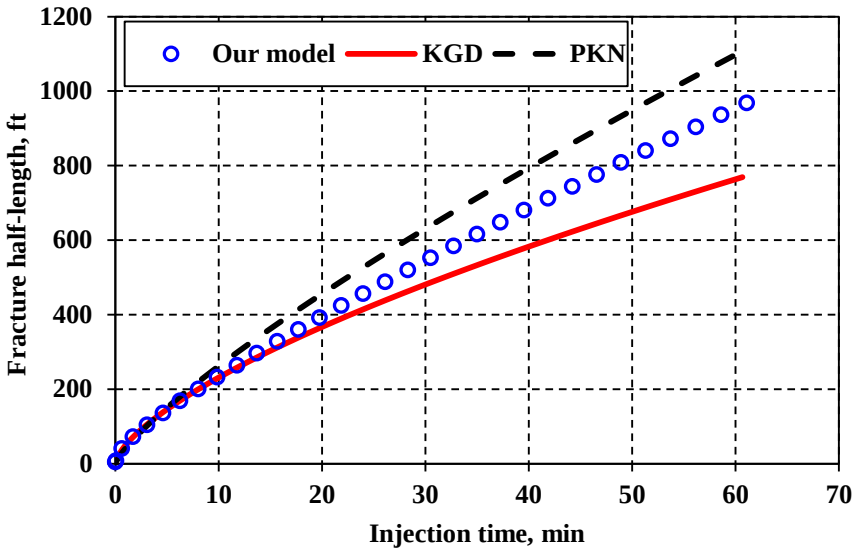

Figure 2.10: Comparison of fracture half-length versus injection time between the KGD, PKN models and our model.

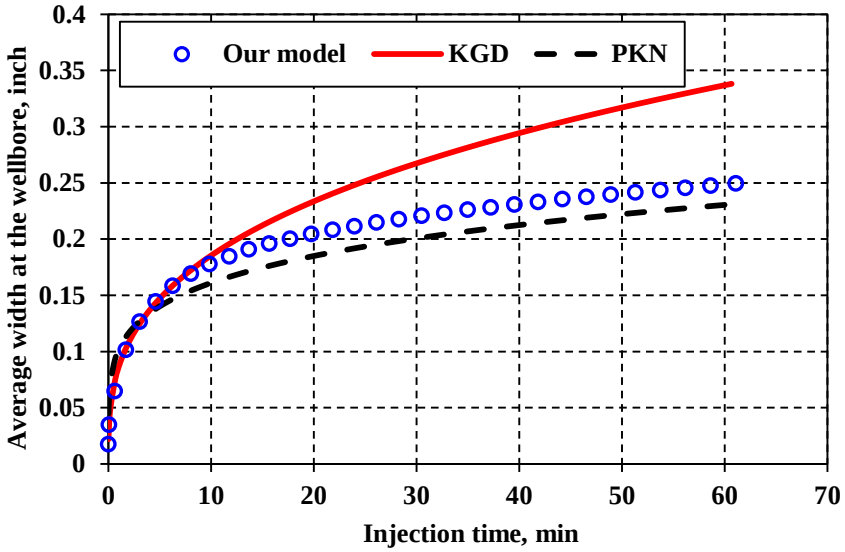

Figure 2.11: Comparison of fracture width at the wellbore between the KGD, PKN models and our model.

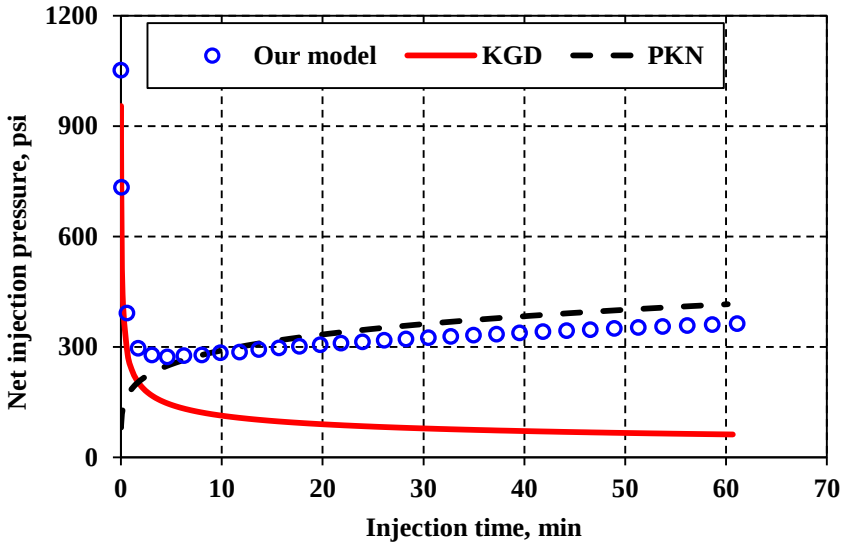

Figure 2.12: Comparison of fracture pressure at the wellbore between the KGD, PKN models and our model.

2.6.2 Comparison with the Unconventional Fracture Model (UFM)

For multiple fracture propagation, fracture interaction plays an important role in fracture geometry. To validate fracture interaction, we compare with the Unconventional Fracture Model (Weng et al., 2011; Wu et al., 2012) for the configurations of a single horizontal wellbore with two initial fractures (Figure 2.13 (a)) and two horizontal wellbores with one fracture each (Figure 2.13 (b)). We simulated these two configurations under isotropic and anisotropic in-situ stress conditions (see Table 2.3 for input parameters). The differential stress for the anisotropic stress reservoir is 130 psi with the maximum horizontal stress oriented in y-direction.

Two fractures, initiated parallel with each other in a horizontal wellbore for isotropic and anisotropic far-field stresses, are illustrated in Figure 2.14. The two fractures propagate away from each other due to the mechanical fracture interaction (i.e.,

stress shadow effects). An opening fracture exerts additional stresses on surrounding rock and adjacent fractures, which can result in a local change in the direction of maximum horizontal stress and deviation of the fracture path from a planar geometry. In addition, the fractures have larger curvature under the isotropic stress condition than that under the anisotropic condition. This is because the anisotropic far-field stresses tend to suppress fracture curving (Olson and Pollard, 1989). The stress shadow and the anisotropic far-field stresses compete with each other. To quantify the competition, Olson and Dahi-Taleghani (2009) defined a parameter called the relative net pressure, R_n,

$$R_n = \frac{(P_{frac} - S_{h\min})}{(S_{h\max} - S_{h\min})}, \tag{2.42}$$

where the numerator is the net pressure and the denominator is horizontal differential stress. Stress shadow effects strongly depend on the net pressure within the fractures (Pollard and Segall, 1987; Warpinski and Branagan, 1989). A larger net pressure will lead to stronger stress shadow effects. When R_n is much greater than 1, the net pressure is much greater than the differential stress, which suggests that stress shadow effects will dominate the fracture geometry. However, if the R_n is much less than 1, the fractures will propagate along a straight line under the domination of differential stress. However, this parameter only indicates whether a non-planar fracture propagation path is possible, which means that strong stress shadow effects still affect fracture width even if the fractures are perfectly straight in a strongly anisotropic stress field. As seen from Figure 2.14, we found that these two models give a very similar fracture propagation path with side by side configuration.

Injection rate	40 bbl/min
Stress anisotropy	130 psi
Poisson's ratio	0.35
Young's modulus	4.35e+6 psi
Fluid viscosity	1 cp
Fracture height	394 ft
Min horizontal stress	6,773 psi
Max horizontal stress	6,903 psi
Distance between initiation points	33 ft

Table 2.3: Input parameters for validation with the Unconventional Fracture Model (after Wu et al., 2012).

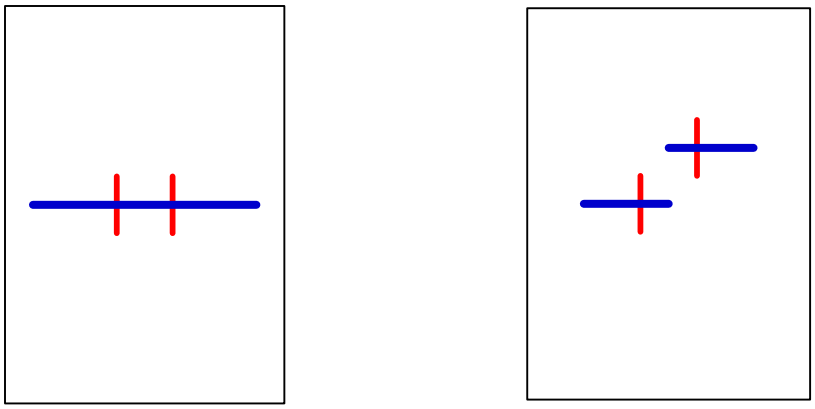

(a) (b)

Figure 2.13: Two initiation fractures in a horizontal wellbore (a) and two horizontal wellbores (b), blue lines represent horizontal wellbores; red lines represent initial fractures.

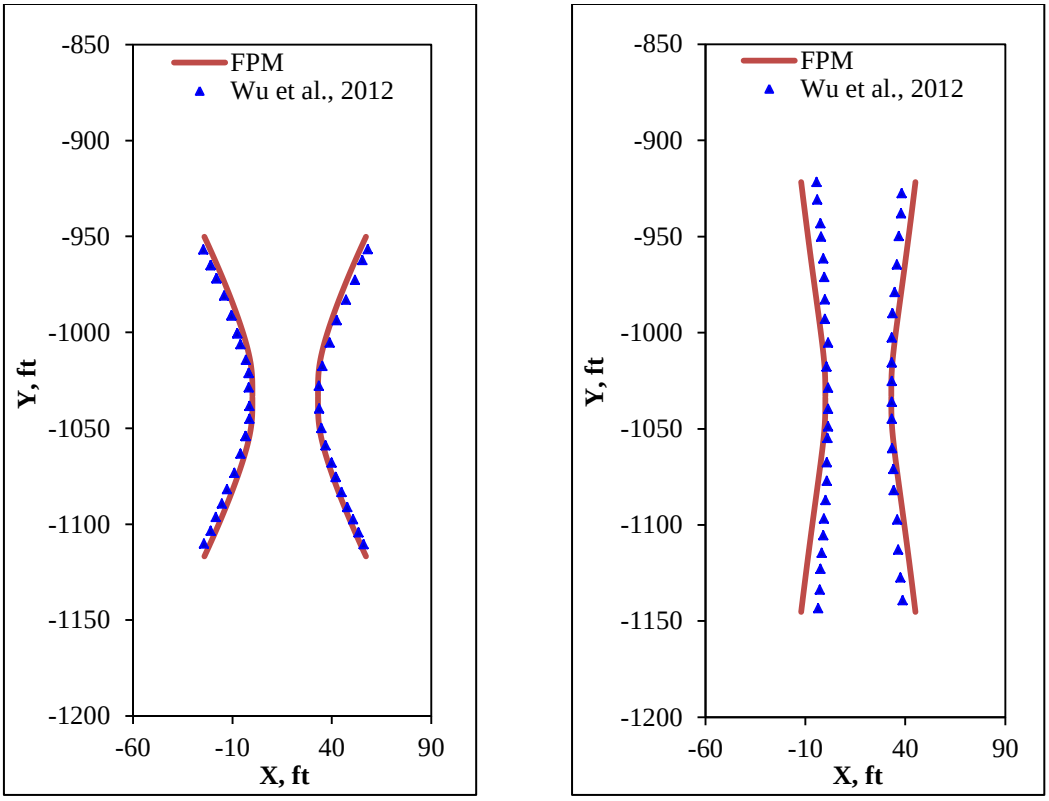

Figure 2.14: Comparison of propagation paths for two initially parallel fractures in isotropic and anisotropic stress fields; left figure refers to isotropic stress field, right one refers to anisotropic stress field.

Figure 2.15 shows two fractures in an en echelon arrangement from two adjacent horizontal wellbores under isotropic and anisotropic far-field stress conditions. The two fractures grow toward each other, because of induced shear stress at the fracture tips caused by mechanical interaction. In the anisotropic far-field case, there is reduced fracture path curvature as compared to the isotropic case. In summary, our model compares favorably with the non-planar results generated by Wu et al. (2012).

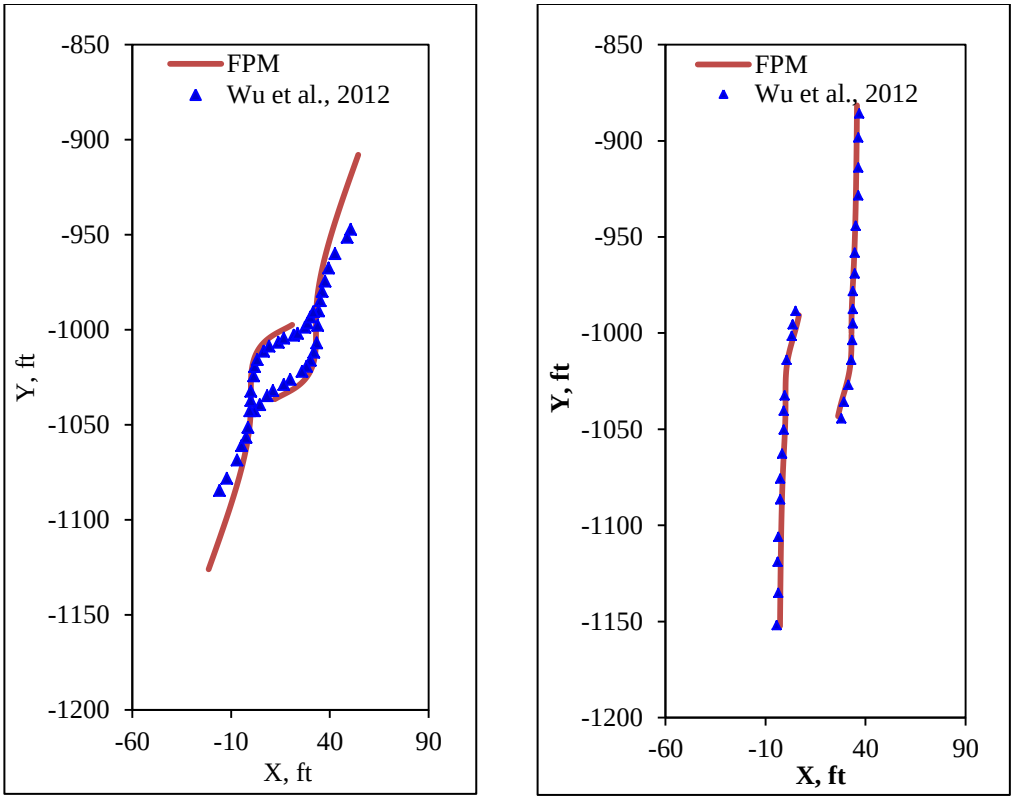

Figure 2.15: Comparison of propagation paths for two initially offset fractures in isotropic and anisotropic stress fields; left figure refers to isotropic stress field, right one refers to anisotropic stress field.

2.7 CONCLUSIONS

The methodology of modeling complex hydraulic fracture development was derived in this chapter. The rock deformation was described by the displacement discontinuity method generating a linear system of equations. The fluid flow in the fracture was described by the finite difference method (FDM) forming a non-linear equation system. The dominant sub-processes of hydraulic fracturing (rock deformation, fluid mechanics, fracture mechanics and leak-off) were coupled together through full or iterative coupled solutions. The model was validated with classic analytical solutions (PKN and KGD), demonstrating the accuracy of the model to solve fracture propagation

with constant height. Besides, another numerical model (Unconventional Fracture Model) was used to verify that the model also can accurately consider fracture interaction between multiple fractures. Simultaneous propagating fractures extend, attracting or repelling each other due to stress shadow effects. The non-planar fracture path curvature is dependent on the relative magnitude of stress shadow effects and differential stress. The model can be used to explore the behavior of non-planar fracture geometry, propagation of closely spaced fractures as well as the interaction between hydraulic and natural fractures.

CHAPTER 3: NON-PLANAR SINGLE AND MULTIPLE FRACTURE PROPAGATION[2]

In Chapter 2, a novel complex hydraulic fracture development model was developed to simulate non-planar fracture propagation in the horizontal wellbore. The model couples rock deformation and fluid mechanics together using two different coupling procedures.

In this chapter, the model is applied to simulate single non-planar and multiple fractures for simulation of simultaneous and sequential propagation. The purposes of these simulations are to test the accuracy and versatility of the model and to investigate the impact of key parameters on non-planar fracture geometry. In addition, some interesting physical insights are drawn from the results, demonstrating that stress shadow effects play an important role in multiple fracture propagation and result in complex fracture geometry. For the sequential and simultaneous cases, there is great deviation in fracture path due to different fracture interactions. Width restriction is induced on non-planar fracture geometry because of stress shadow effects and additional closing stresses from in-situ stress field.

[2]Parts of this chapter have been presented in the following conference: Olson, Jon E., Wu, K. 2012. Sequential versus Simultaneous Multi-zone Fracturing in Horizontal Wells: Insights from a Non-planar, Multi-frac Numerical Model, SPE 152602, presented at the SPE Hydraulic Fracturing Technology Conference in The Woodlands, Texas, USA 6-8 February. This paper was supervised by Jon Olson.

3.1 INTRODUCTION

An important aspect of hydraulic fracturing from horizontal wells in naturally fracture reservoirs is the prospect of non-planar propagation paths. The experimental work of El Rabaa (1989) and Abass et al. (1996) indicated that well deviation from a principal stress direction and perforated interval length dominate fracture geometry near the wellbore. Similar results were also obtained in numerical studies where non-planar propagation is influenced by wellbore orientation and stress shadow effects of nearby hydraulic fractures (Warpinski and Branagan, 1989; Weijers and de Pater, 1994; Rungamornrat et al., 2005; Olson, 2008; Bunger et al., 2011) or by interacting with natural fractures (Olson, 2008; Xue and Ghassemi, 2009; Min et al, 2010). Non-planar fracture propagation can have negative influences on fracture operation, for example, extremely high treating pressure (Owens et al., 1992; Weijers et al., 1992), reduction in the fracture width near the wellbore (Owens et al., 1992; Olson, 1995), and screen-out of the proppant.

Using multiple hydraulic fractures in combination with horizontal drilling significantly improves well productivity in shale reservoirs. One fracturing technique, limited entry, is widely employed to create multiple perforation clusters for fracturing (Daneshy, 2011). In a single fracturing stage, three to six perforation clusters are designed based on the limited-entry technique. Generally, there are about 20-40 stages in a horizontal well. In comparison with modeling single fracture propagation, a key difference in modeling multi-frac propagation is to consider fracture interaction which is subject to a process of subsurface geomechanical stress changes induced by fracturing treatments. The significant consequences of multi-frac treatments are potentially fracture width restriction and complex fracture trajectory as a result of stress shadow effects. Weijers et al. (2000) listed the impact of simultaneous multiple hydraulic fractures as

resulting in shorter and narrower fractures which increases the risk of proppant screen-out. Observations from multi-fracturing experiments show that generally only one or two dominant fractures are created and accept most of injected fluid (EI Rabaa, 1989; Abass et al., 2009). Based on field data from multiple fracture treatments in shale reservoirs, Fisher et al. (2004), Ketter et al. (2006) and Daneshy (2011) reported that the growth of middle fractures can be restricted by stress shadow effects when perforation cluster spacing is tight.

3.2 SINGLE NON-PLANAR FRACTURE PROPAGATION

3.2.1 Comparison of different coupling procedures

In Section 2.4, two different coupled solution procedures were introduced to simulate fracture propagation. The fully coupled solution procedure (procedure 1) is used to solve single non-planar fracture propagation, while the iteratively coupled solution procedure (procedure 2) is used to simulate multiple fracture propagation. For the second procedure, except changing the coupling method, we also relaxed the assumption and presumed that injection rate within the fracture is constant to enhance the calculation stability. In this section, we employ these two methods to simulate single non-planar fracture propagation and verify the accuracy of the second procedure. The input data of case study is listed in Table 3.1.

Fractures from horizontal wellbores may not start parallel to S_{Hmax}, either because of initial wellbore guiding of the fracture or initiation along an unfavorably oriented natural fracture that the wellbore intersects. For this case study, we assume the angle of initial hydraulic fracture is 45^{o} with respective to the maximum horizontal stress (S_{Hmax}). Non-planar fracture geometry is created, as shown in Figure 3.1, which illustrates that

although orientation of an initial fracture is misaligned, the fracture gradually reorients to the favorable propagation direction (the direction of S_{Hmax}). Figure 3.2 displays the fracture width change along the fracture and indicates that width at the non-planar segment is reduced. Figures 3.1 through 3.4 give comparisons of non-planar fracture geometry and injection pressure calculated by two different coupling procedures. The iteratively coupled procedure predicts slightly greater width and injection pressure but a shorter fracture length, compared with fully coupled procedure. The reason for this observation is probably due to the assumption of constant flow rate within the fracture. Overall, the iteratively coupled procedure shows good agreement with the fully coupled procedure.

Fluid leak-off coefficient	0.0001 ft/min$^{0.5}$
n'	0.7
K'	0.02 lbf-sec^n/ft^2
Injection rate	20 bmp
Young's modulus	6530000 psi
Poisson's ratio	0.2
Height	100 ft
Misaligned angle	45^o
Minimum horizontal stress	4450 psi
Maximum horizontal stress	4550 psi

Table 3.1: Input parameters for single non-planar fracture propagation with a 45^o misaligned angle.

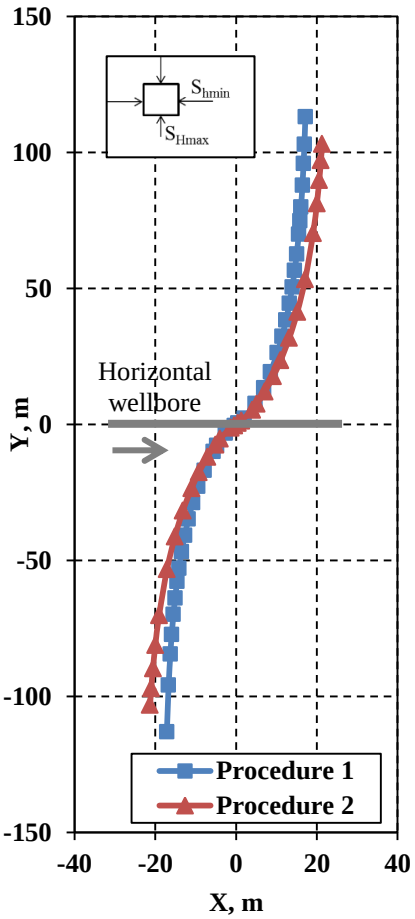

Figure 3.1: Non-planar fracture trajectories for the coupling procedures 1 and 2.

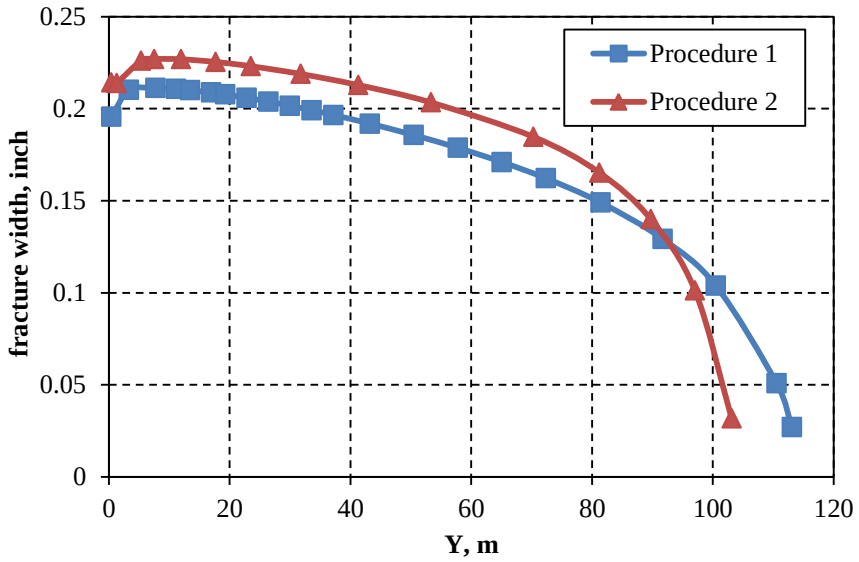

Figure 3.2: Width distribution along fracture for coupling procedures 1 and 2.

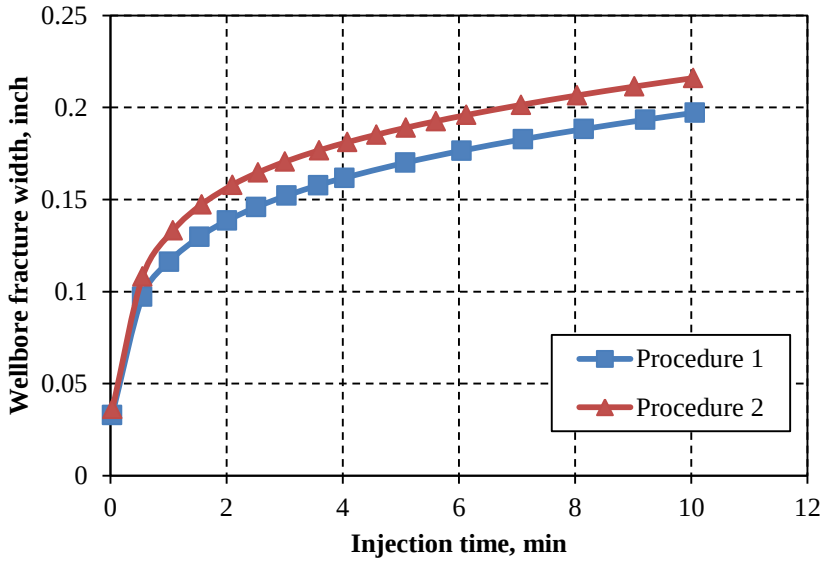

Figure 3.3: Fracture width at the wellbore vs. injection time for coupling procedures 1 and 2.

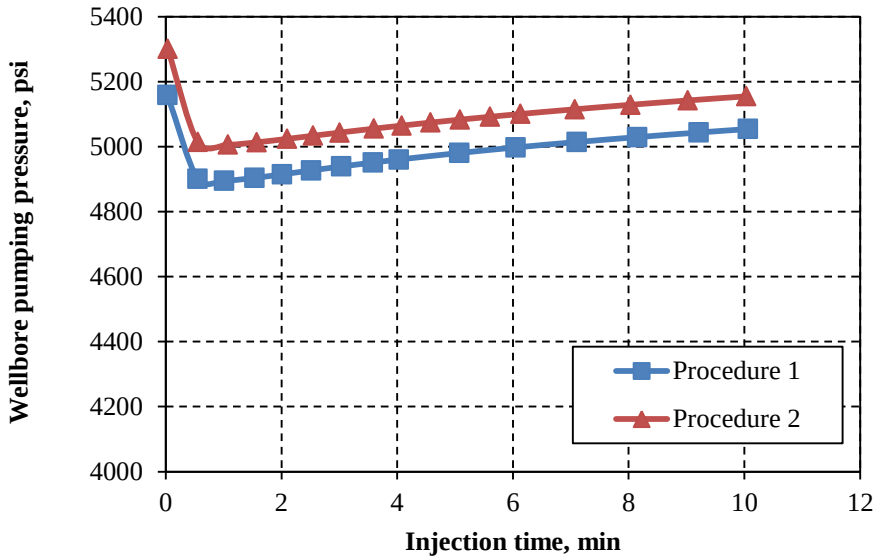

Figure 3.4: Pumping pressure at the wellbore vs. injection time for coupling procedures 1 and 2.

3.2.2 Sensitivity analysis of non-planar propagation

Non-planar fracture geometry can result in width restriction which greatly affects proppant transport and increases the risk of screen-out. Olson (1995) described a sensitivity study for non-planar propagation, examining the influence of initial fracture orientation relative to S_{Hmax} and in-situ differential stress on fracture width. We followed Olson's input parameters (Table 3.2), with the exception that we included a 100 ft fracture height (Olson (1995) was 2d plane strain). The initial fracture half-length in the simulation is 20 ft.

Fluid leak-off coefficient	0.001 ft/min$^{0.5}$
n'	0.7
K'	0.02 lbf-sec^n/ft^2
Injection rate	20 bmp
Young's modulus	4000000 psi
Poisson's ratio	0.25
Height	100 ft
Minimum stress	4450 psi
Maximum stress	4950 psi

Table 3.2: Input parameters for sensitivity analysis of non-planar propagation (after Olson, 1995).

3.2.2.1 Fracture misalignment angle

The width reduction on non-planar trajectory (Figure 3.5) also can be predicted analytically by the following relationship from Olson (1995),

$$R = 100\frac{(w_f - w_w)}{w_f} = 100(1-\cos\theta), \tag{3.1}$$

where R is percentage of width reduction, w_w is the width of restricted wellbore fracture segment at fracture angle striking θ from the S_{Hmax} direction, and w_f is the maximum width of planar fracture. The figure includes the analytical calculation as well as numerical simulation results. At $\theta = 0^o$, there is no fracture reorientation, and the width is that of a planar fracture. At $\theta = 45^o$, the width reduction at the wellbore reaches about 40%. At 70 degrees, the numerical and analytic results still match rather well at over 60% wellbore fracture segment width reduction. The numerical results show the most severe width reduction, matching the analytical result to almost $\theta = 80^o$, after which it reaches a maximum reduction, as the fluid must still be pumping through the fracture.

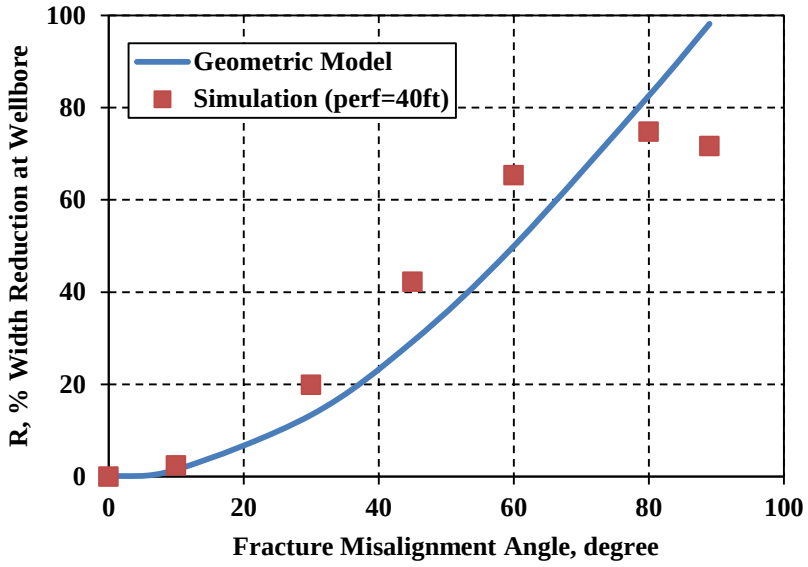

Figure 3.5: Non-planar fracture width reduction at the wellbore normalized to planar fracture results.

Figure 3.6 shows the wellbore fracture segment width through time for various initial misalignment angles ($\theta = 10^o$ to 89^o) at a differential stress of 500 psi. It is evident from this result that the wellbore width reduction can persist, particularly when the fracture reorientation is severe ($\theta > 45^o$). Going away from the wellbore, it is apparent the re-oriented fracture wing opens up more freely than the wellbore segment (Figure 3.7). For this differential stress case (500 psi), the severity of near wellbore restriction depends on misalignment angle, but once the fractures gets away from the wellbore, where it has turned to be more parallel to S_{Hmax}, the opening approaches that of a planar fracture (close to the $\theta = 10°$ case).

The width variation has a strong influence on the pressure in the fracture along its length (Figure 3.7). Near the wellbore, with the strong width reduction, the pressure is extremely high, but it drops rapidly as the fracture turns the corner and the width opens

up. Figure 3.8 displays the final treating pressure as a function of misalignment angle. Based on this example, the non-planar path can add another 600 psi to the net pressure.

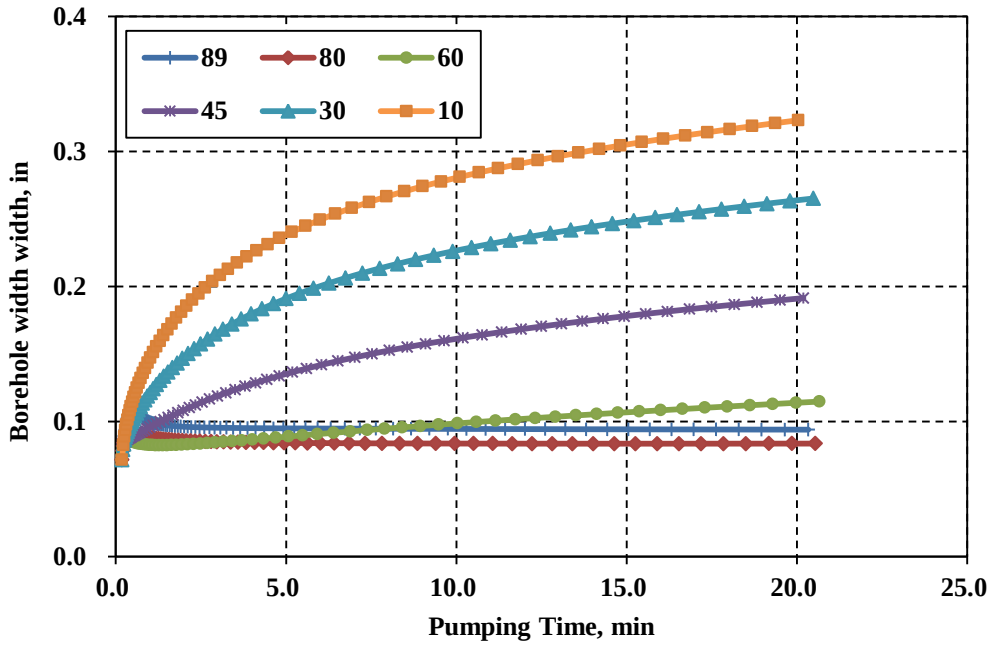

Figure 3.6: Borehole width vs. pumping time (injection rate = 20 bpm, initial x_f = 20 ft, differential stress = 500 psi).

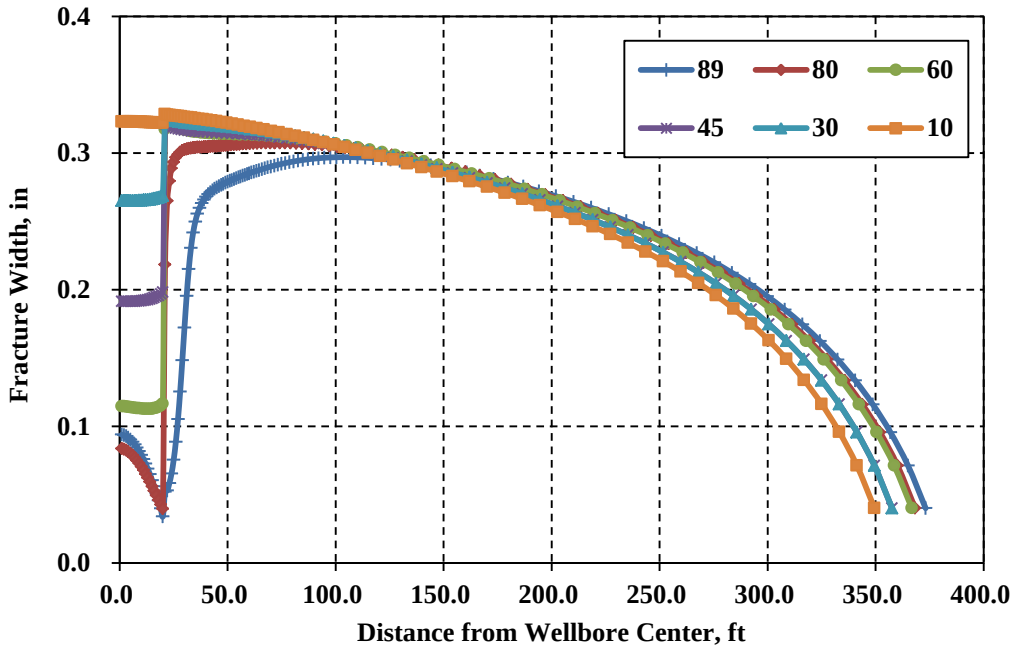

Figure 3.7: Final width profile (injection rate = 20 bpm, initial L_w = 20 ft, differential stress = 500 psi).

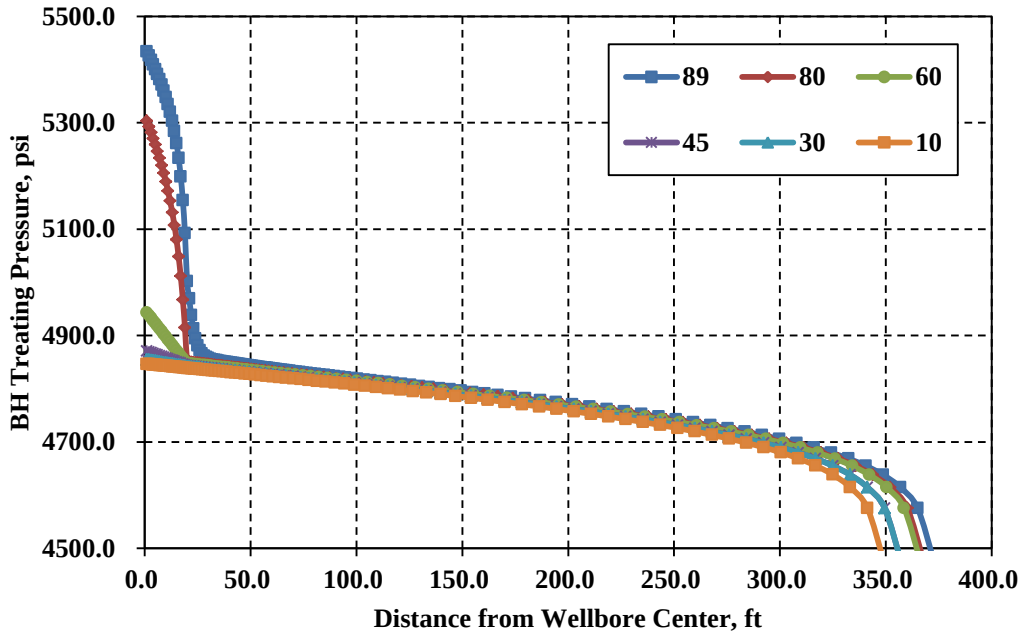

Figure 3.8: Impact of aligned angle on treating pressure (injection rate = 20 bpm, initial L_w = 20 ft, differential stress = 500 psi).

3.2.2.2 Differential stress

The severity of the near wellbore width restriction also depends on differential stress. Figure 3.9 shows the non-planar propagation paths for the case of 89° initial misalignment under various differential stresses ($S_{Hmax} - S_{hmin}$). It is clear from the figure that the more isotropic the stress, the wider the curve the fracture follows, but all cases are approaching ultimate alignment of the fracture plane with the S_{Hmax} direction. If we take the extreme case of $\theta = 89^o$ (Figure 3.10), we can see the influence of differential stress on width reduction. A differential stress of 100 psi for this case doesn't vary much from the base planar case. 200 psi of differential cuts the wellbore width by over 1/3. Higher differential stresses (500 and 1000 psi) cut the width by 2/3.

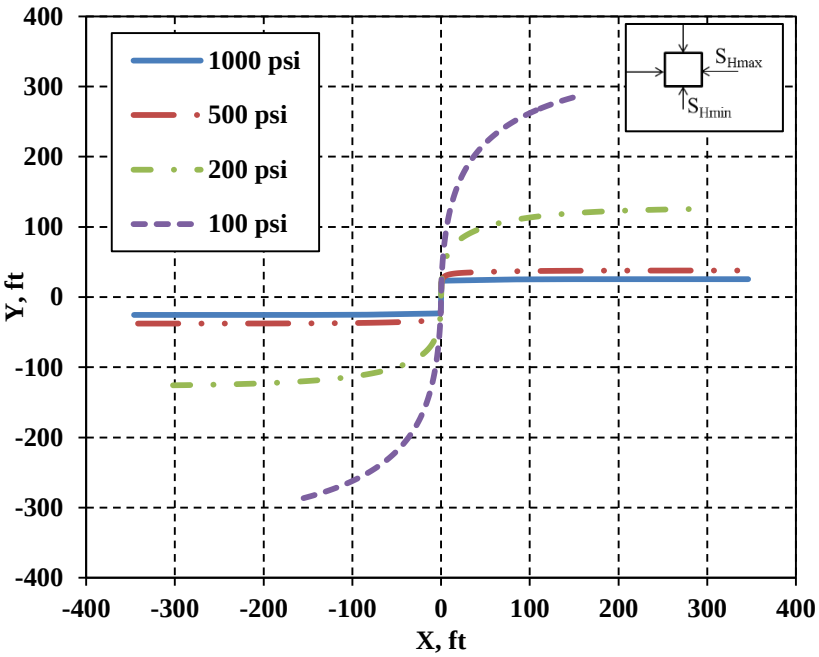

Figure 3.9: Non-planar fracture paths for varying differential stress (injection rate = 20 bpm, initial x_f = 20 ft, misaligned angle = 89°).

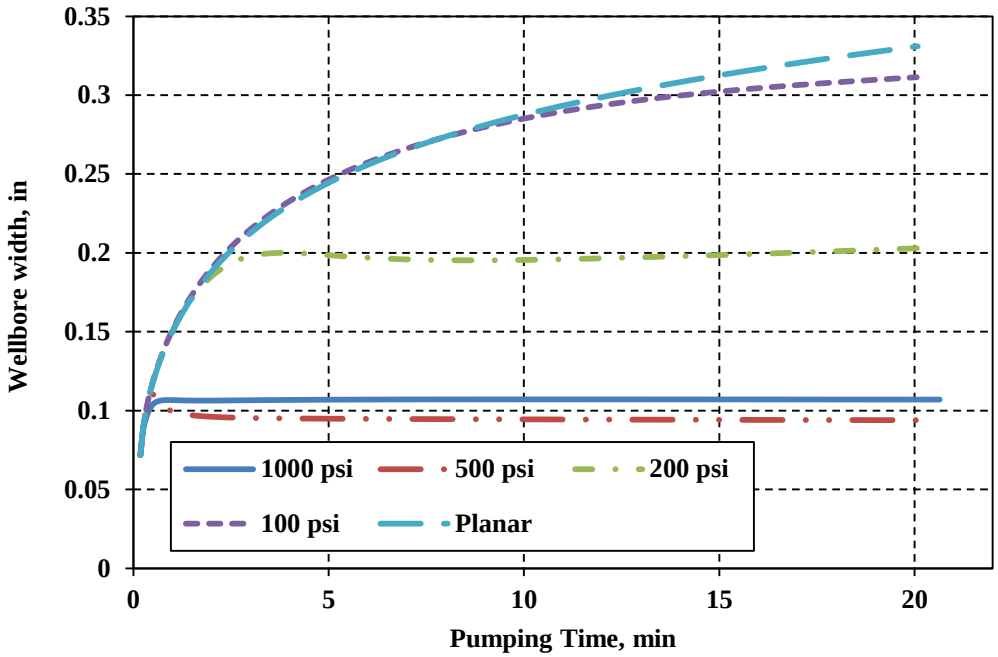

Figure 3.10: Fracture width of wellbore segment for varying differential stress (injection rate = 20 bpm, initial L_w = 20 ft, misaligned angle = 89°).

3.3 MULTIPLE FRACTURE PROPAGATION

3.3.1 Simultaneous multiple fracture propagation

To develop shale reservoirs, simultaneous multiple fracture propagation in a stage is treated as a very efficient and economic method of stimulation. For example, in the Barnett Shale, some horizontal wells were drilled with six perforation clusters spaced 50 feet apart in each stage (Vermylen, 2011). It is very important for engineers to understand the fracture geometry of multiple fractures to optimize fracturing treatment design. Therefore, to represent the real fracturing in a single fracturing stage, a case of six initial fractures is studied using our model to investigate fracture geometry, pressure distribution

and stress shadow effects (Figure 3.11). The input parameters for the Barnett Shale based on the available data in the literature are shown in Table 3.3.

Fracture spacing	50 ft
Layer height	100 ft
Minimum horizontal stress	4450 psi
Maximum horizontal stress	4550 psi
Fluid Leak-off Coefficient	0.00001 $ft/min^{0.5}$
Injection Rate	60 bpm
n'	0.7
K'	0.02 $lbf\text{-}sec^n/ft^2$
Young's Modulus	6.53×10^6 psi
Poisson's Ratio	0.2
No. of Perforations	60
Density of Slurry	1.2 g/cm^3
Diameter of Perforations	15 mm
Diameter of Wellbore	0.1 m

Table 3.3: Input parameters for case study.

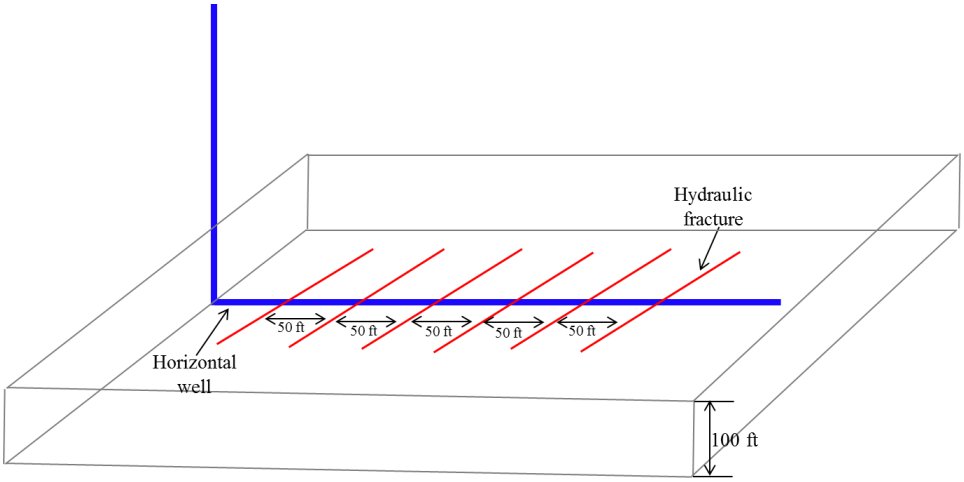

Figure 3.11: Six fractures propagating orthogonally from a horizontal wellbore.

Figure 3.12 displays the fracture trajectory and fracture width at the end of 12 minutes of injection time. This fracture geometry is dominated by two factors: distance from the injection point and mechanical interaction between fractures. To clearly illustrate the fracture aperture distribution for each fracture, we enlarge the aperture 500 times in Figure 3.12 (b). The injection point is at the heel of horizontal wellbore (-200, 0). Fractures close to the heel obtain more fluid due to viscous dissipative flow through the wellbore from earlier fractures. Fractures obtaining more fluid have greater length and aperture. Fractures 1 and 6 are under the same stress shadow position being on the outside of the array, but fracture 1 is closer to the injection point. Therefore, fracture 1 has higher net pressure and grows longer with larger width compared with fracture 6. All of the interior fractures 2, 3, 4 and 5 have similar trends. Fractures spaced with 50 ft apart in this case are within the region of stress shadow influence, which results in strong mechanical interaction between them. Fractures 2 and 5 are close to the exterior fractures 1 and 6 and are strongly affected by the induced stresses of the fractures, which make fractures 2 and 5 gradually slow down the growth and deviate from their original

propagation path (Figure 3.12). Fractures 3 and 4 are less affected by the two exterior fractures. Fracture apertures are illustrated in Figures 3.12 (b) and 3.13, which show that the interior fractures are much narrower and shorter compared with the exterior fractures. Hence, interior fractures have less ability to accept proppant during fracturing and present a greater risk of proppant screen-out. In summary, the key features for the multiple fracture geometry are that the interior fractures are shorter, narrower and more non-planar, while the exterior fractures are longer, wider and grow roughly along a straight line.

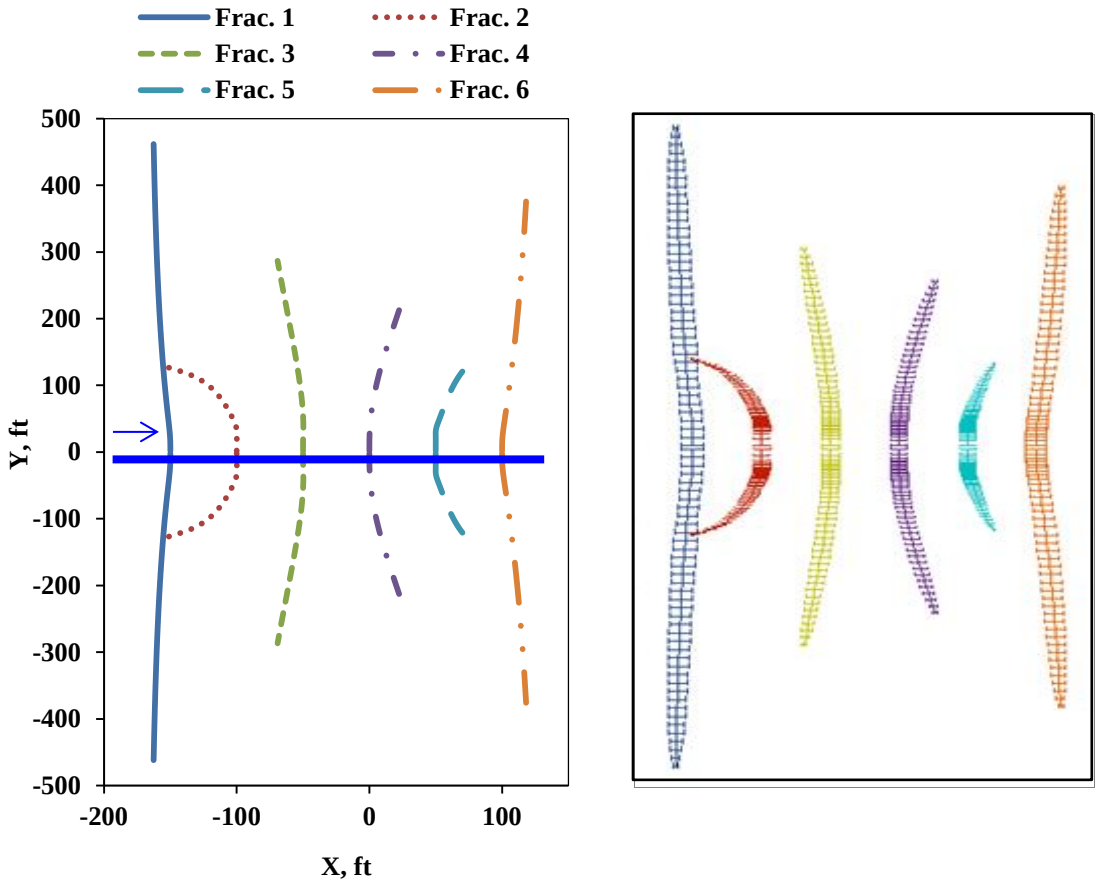

(a) Fracture trajectory (b) Fracture width distribution

Figure 3.12: Fracture trajectory and aperture distribution after simultaneous fracturing (map view), twice X exaggeration.

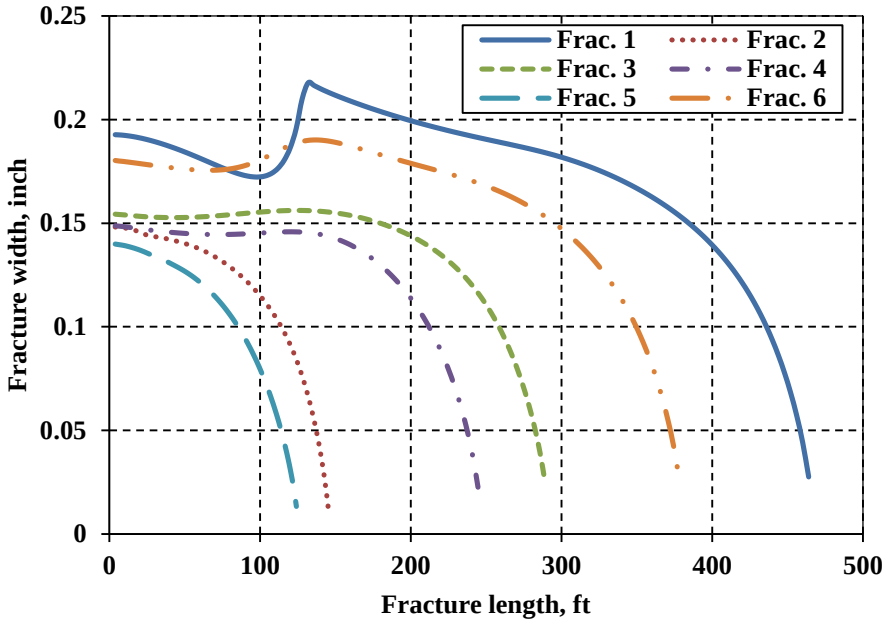

Figure 3.13: Fracture width vs. fracture length.

Before fracturing, the minimum horizontal stress of σ_{xx} is oriented parallel to the x direction, and the maximum horizontal stress is the σ_{yy}. Fractures grow along the y direction initially against the least resistance. As the fractures grow, the stresses around them are dynamically changed. In Figures 3.14 and 3.15, red colors indicate an increase of compression, and blue colors represent a decrease of compression. Nearby and ahead of the fracture tips, compressions in the σ_{xx} and σ_{yy} direction both decrease due to the near tip field. In contrast, rock behind the tips is compressed due to fracture opening.

Comparing the change in σ_{xx} and σ_{yy} at the end of injection (Figures 3.14 and 3.15), the area of stress change for σ_{xx} is much larger than that for σ_{yy}, because y-parallel fractures open against the rock and directly squeeze it in the x direction, whereas y direction effects are reduced by Poisson ratio effects. Hence, at some specific points the change in σ_{xx} is greater than the change in σ_{yy}. At these points, σ_{xx} might become larger

than σ_{yy}, and the orientation of the maximum horizontal stress rotates away from the y direction, which explains why interior fractures change their propagation directions to seek the path with the least resistance.

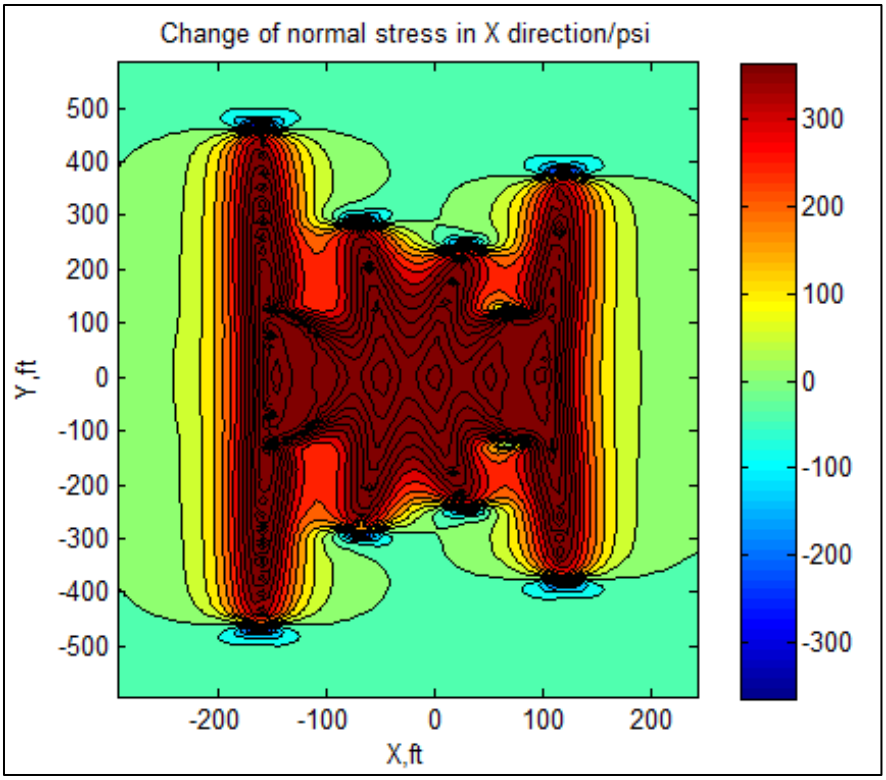

Figure 3.14: Stress change of normal stress σ_{xx} (map view); twice X exaggeration.

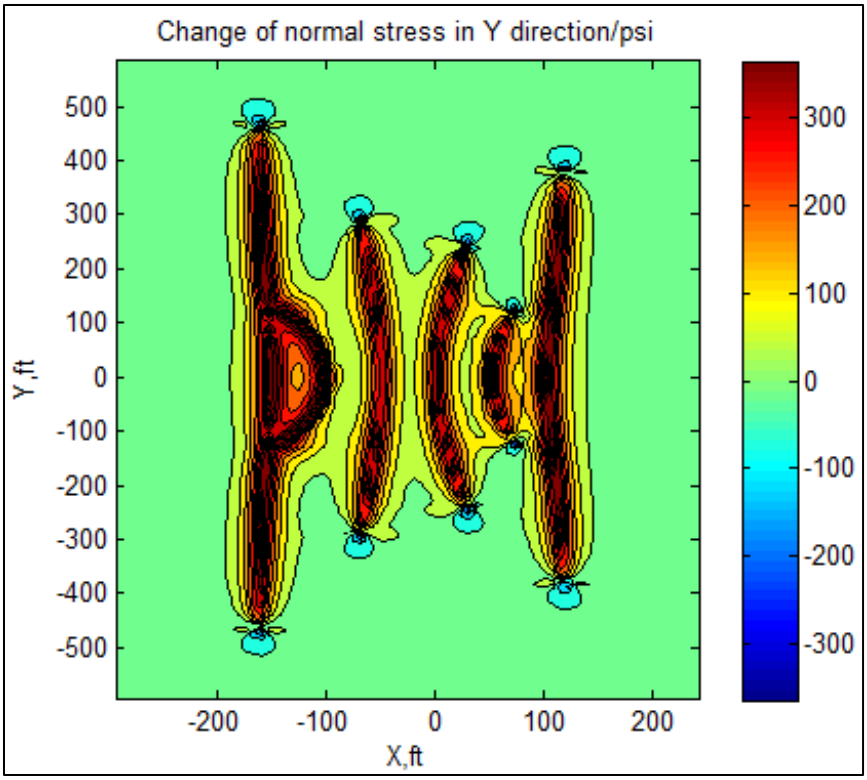

Figure 3.15: Stress change of normal stress σ_{yy} (map view); twice X exaggeration.

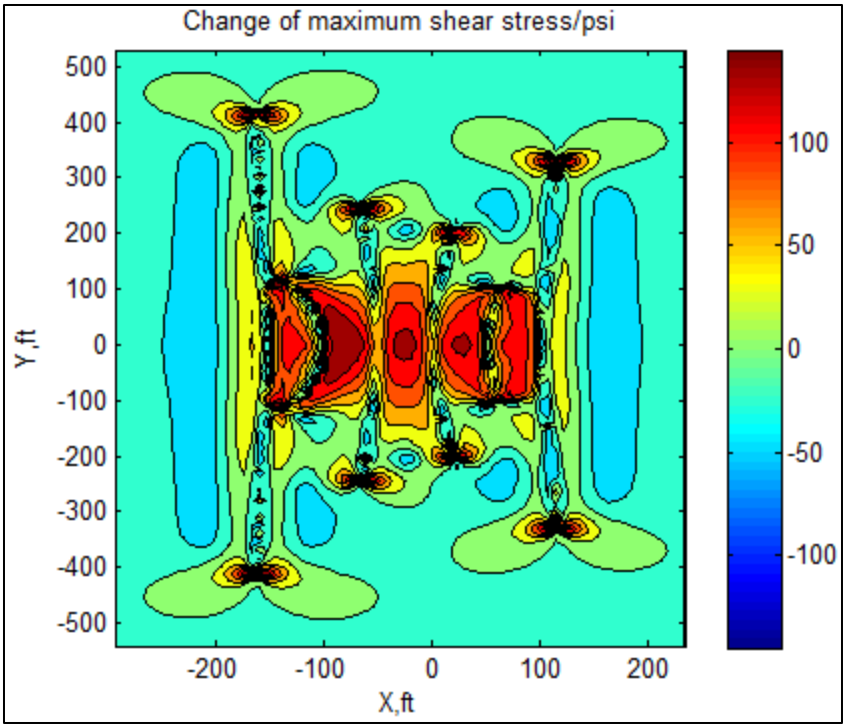

Figure 3.16: The change of maximum shear stress (map view); twice *X* exaggeration.

Microseismic events are induced by changes in stresses and pore pressure caused by hydraulic fracturing (Warpinski et al., 2001; Vulgamore et al., 2007), and the events are often used to estimate fracture geometry. The stress change generated by opening fractures might lead to shear failure of pre-existing fractures. Figure 3.16 shows the change of the maximum shear stress at the end of fracturing. Red colors mean an increase in the maximum shear stress; while blue colors indicate a decrease. The initial maximum shear stress is 50 psi before fracturing since the maximum shear stress is half of the differential stress (S_{Hmax} - S_{hmin}). A larger maximum shear stress suggests a greater likelihood to induce shear failure. Figure 3.16 illustrates that the large increase of the shear stress primarily occurs around fracture tips and the region between two fractures. Accordingly, these areas have a greater possibility of induced shear failure and microseismic activity. Additionally, Figure 3.16 shows that the maximum shear stress

decreases just outside the two exterior fractures, which implies that if the fracturing reduces the shear stress, areas where is a reduction are less likely to have microseismic. Warpinski et al. (2001) reported that the induced shear stress near fracture tips provides a mechanism for microseisms to accurately determine the length and height of fractures, and pore pressure change due to fluid leak-off is an important factor in microseismic development behind the tip. Although leak-off is included in the material balance equation for the propagating hydraulic fractures, we do not model how that fluid moves into the formation and might increase pore pressure around pre-existing fractures. Consequently, all the microseisms implied by the shear stresses in Figure 3.16 are what would be called "dry", meaning they come from shear stress changes induced by mechanical rock interaction, not pore pressure increase caused by leak-off.

3.3.2 Sequential multiple fracture propagation

Sequential propagation has been proposed by Roussel et al. (2012) as a way to better control fracture propagation path. In this section, we used the same input parameters as the simultaneous case (Table 3.3). The only difference of sequential case is to separate the 6 fractures into two stages, as shown Figure 3.17. Three fractures in stage 1 were propagated simultaneously and are held open assuming that two thirds of their created width is propped, which results in exerting additional stresses on adjacent fractures. After finishing fracturing treatments in the stage 1, stage 2 followed with its fractures extending simultaneously as well. In the simultaneous case, all the fractures start out small and grow at the same time, competing with each other. The fractures are subject to the dynamic process of subsurface geomechanical stress changes. For the sequential case, the first three fractures are competing in simultaneous propagation, but for the next three fractures, there are already some fully grown fractures perturbing the

stress field even before they start propagating. These fractures are subject to not only the dynamic stress change, but also the static additional stresses induced by opening fractures in stage 1. This section examined the sequential propagation to show the difference of fracture geometry with the simultaneous propagation.

Figures 3.18, 3.19, and 3.20 show fracture geometry at the end of injection for the sequential injection with identical input parameters with simultaneous injection. Fractures in stage 1 display a symmetric pattern (Figure 3.18) because pressure drop due to wellbore friction in stage 1 is very small and can be ignored. The fractures in stage 2 do not propagate symmetrically because each fracture is unsymmetrically affected by opening fractures in stage 1. If there were no additional pre-existing stresses from stage 1, the fractures in stage 2 would have the same geometry with as the fractures in stage 1. It is evident from this result that fractures 4 and 5 are most strongly affected by the interaction stresses, resulting in immature growth and width restriction (Figures 3.18 and 3.20). Figure 3.18 also shows that fractures 4 and 5 curve toward to the pre-existing fractures because the exterior fracture 6 has very strong stress shadow effects, repelling the fractures 4 and 5. This does not always happen for the fractures 4 and 5, which depend on the competition of stress shadow effects from the fracture 6 and the pre-existing fractures. If the fracture 6 has stronger stress shadow effects, the fractures 4 and 5 will extend toward the pre-existing fractures, as shown in Figure 3.18; otherwise, they will turn to the fracture 6.

Figure 3.21 displays the net injection pressure of stage 1 and 2, illustrating that the later stage (stage 2) requires a higher injection pressure than the previous stage (stage 1). This is because the mechanical interaction limits the opening of the later stage, so that increases the friction pressure drop in the fractures.

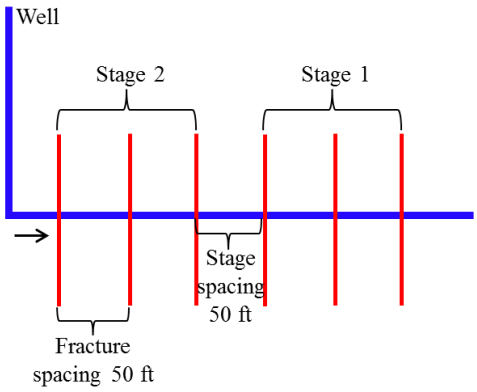

Figure 3.17: Two stages with three fractures each in a horizontal wellbore.

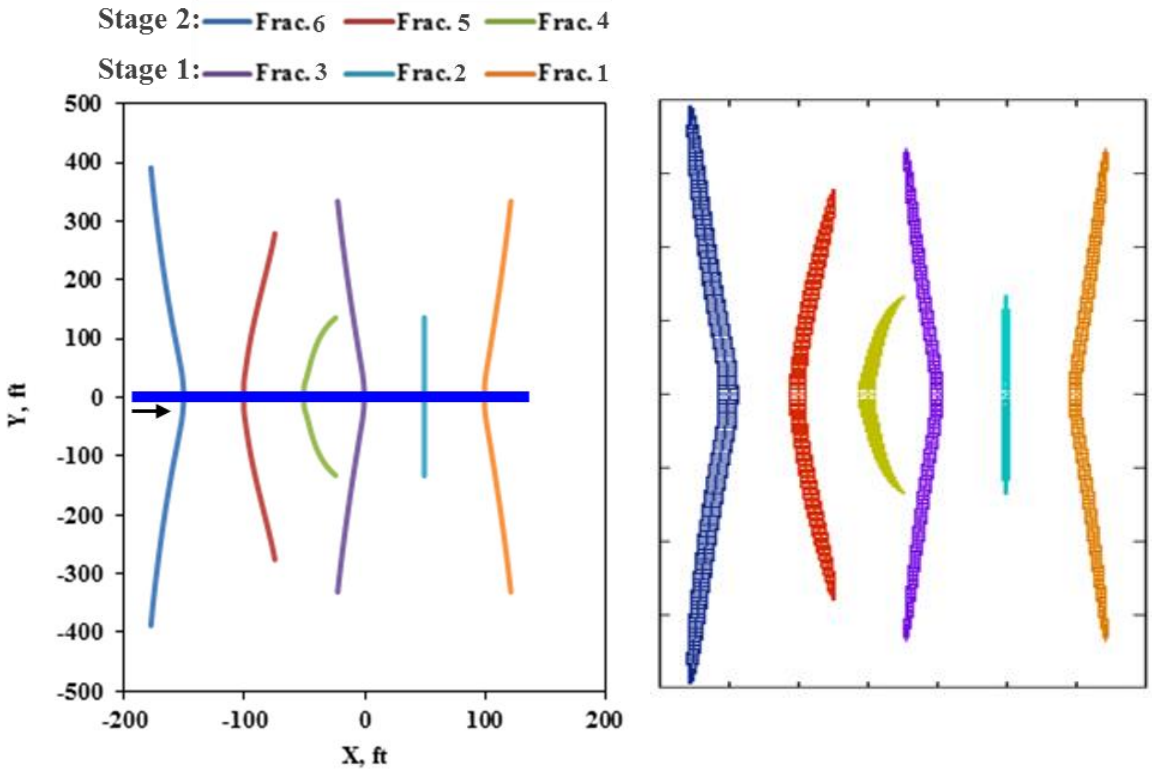

(a) Fracture trajectory (b) Fracture width distribution

Figure 3.18: Fracture trajectory and width distribution after sequential fracturing (map view), twice *X* exaggeration.

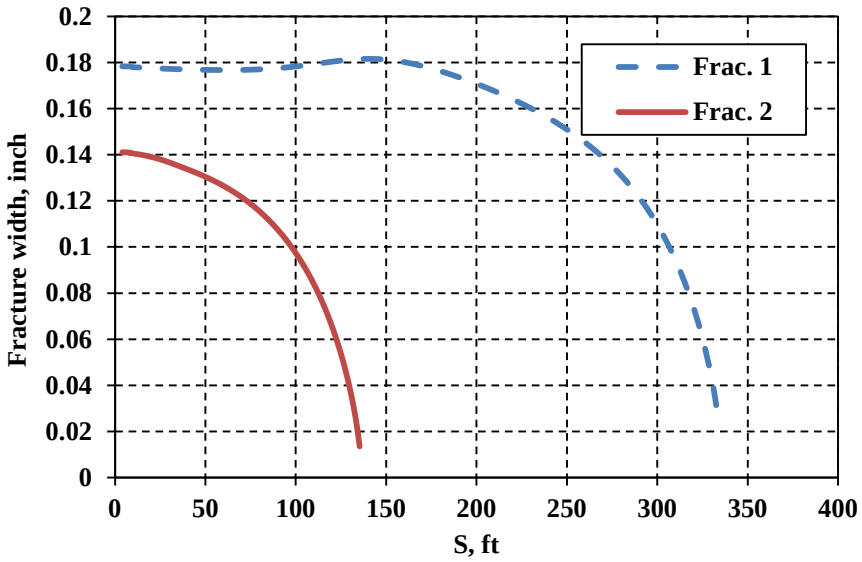

Figure 3.19: Fracture width vs. fracture length for stage 1.

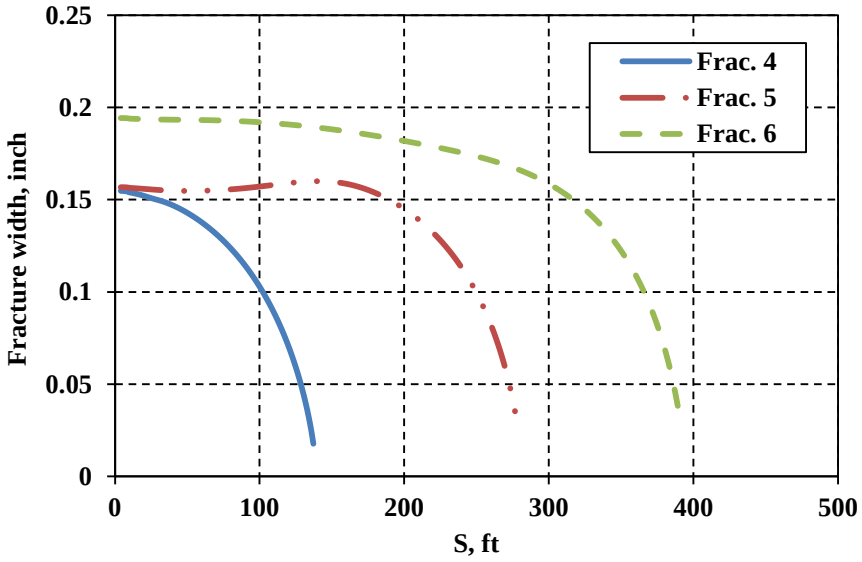

Figure 3.20: Fracture width vs. fracture length for stage 2.

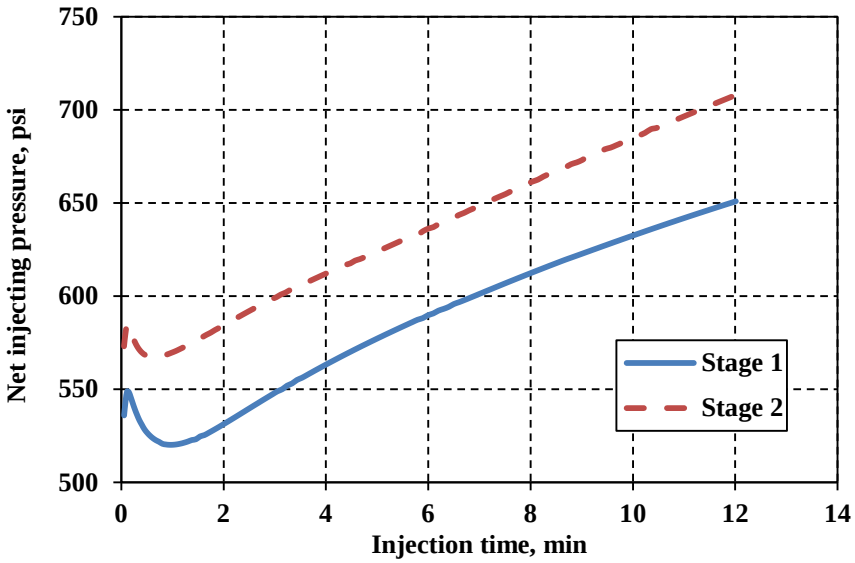

Figure 3.21: Net injection pressure for stage 1 and stage 2.

Before fracturing, the in-situ stress state of the sequential case is the same as that of the simultaneous case. The minimum horizontal stress is σ_{xx}, and the maximum horizontal stress is σ_{yy}. After fracturing in stage 1, the stress distribution in the reservoir is changed, as shown in Figures 3.22 and 3.23. Red colors indicate an increase in compression, and blue colors represent a decrease. The stress perturbation of the first stage (the light green) covers much of the space that the second stage must propagate into. This should make the local S_{hmin} (S_{xx}) higher, causing elevation of treatment pressure and width reduction. Fractures in stage 2 were propagated along the y direction initially against compressional stress of σ_{xx}, which is increased in the whole reservoir except the areas near fracture tips (Figure 3.23). The final stress distribution is displayed in Figures 3.24 and 3.25 after fracturing both stages 1 and 2. It is evident from Figures 3.14, 3.15, 3.24 and 3.25 that the sequential and simultaneous injections induce different stress distributions by different sequence of fracturing, resulting in distinct fracture geometries.

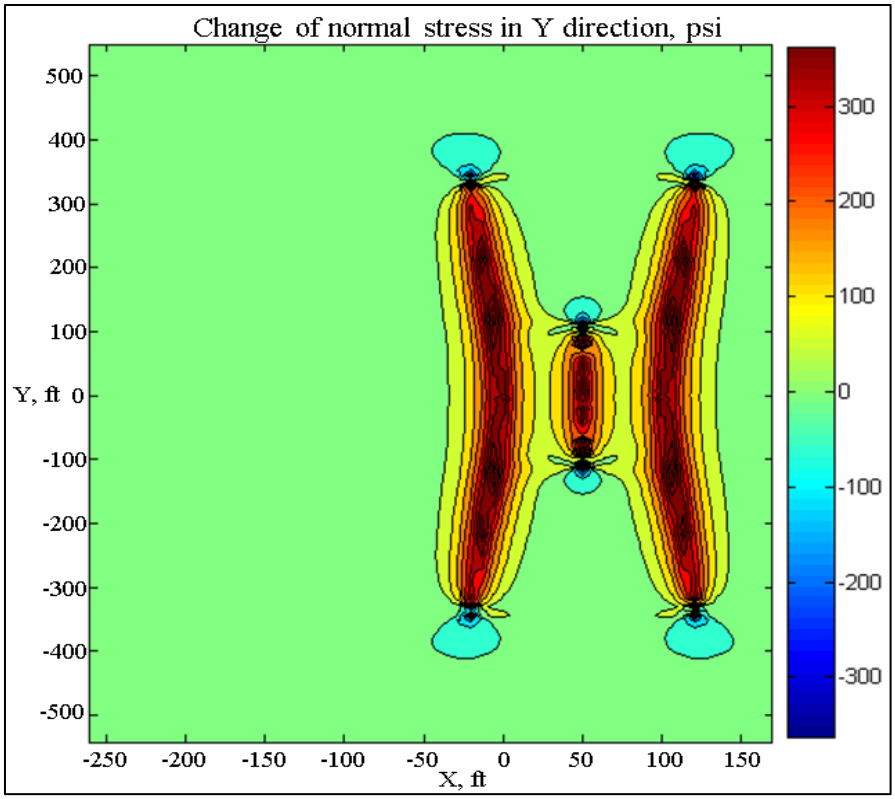

Figure 3.22: Stress change of normal stress σ_{yy} after stage 1 (map view); twice X exaggeration.

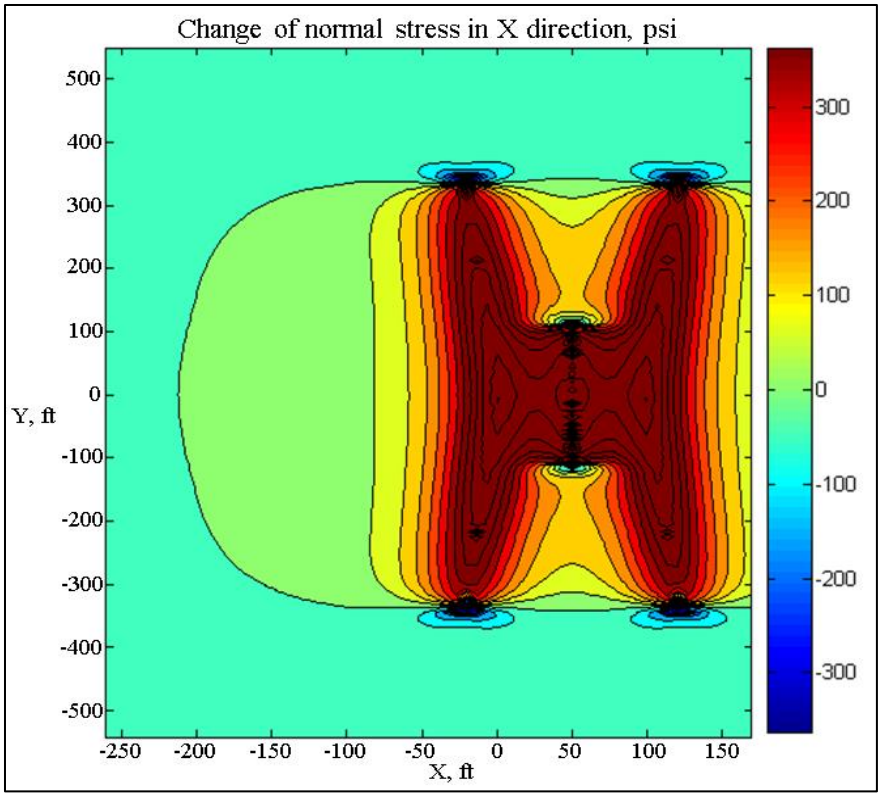

Figure 3.23: Stress change of normal stress σ_{xx} after stage 1 (map view); twice X exaggeration.

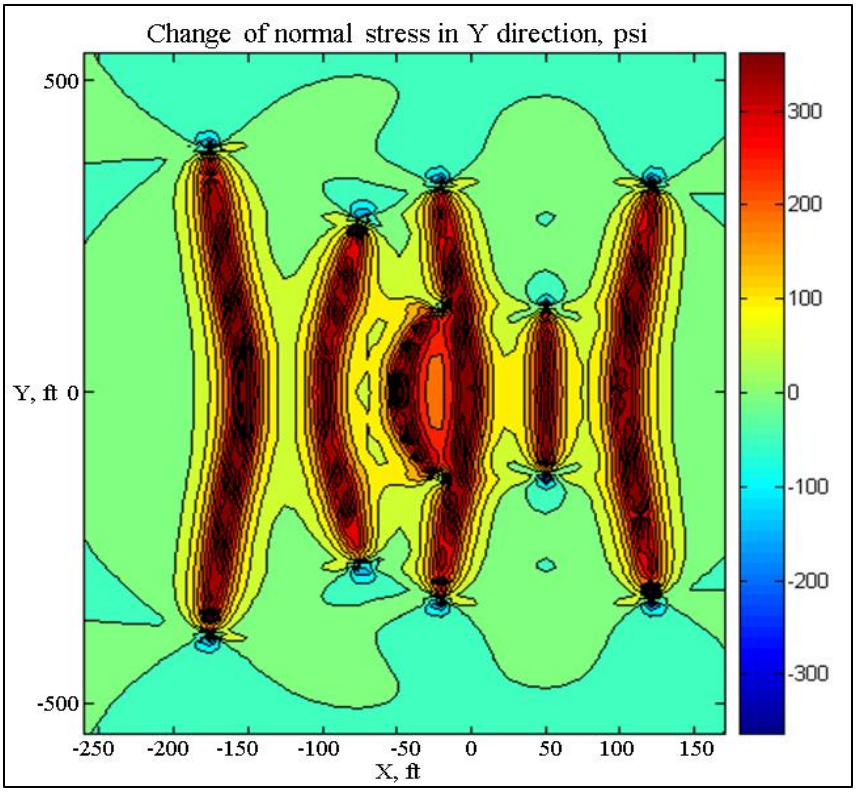

Figure 3.24: Stress change of normal stress σ_{yy} after stage 2 (map view); twice X exaggeration.

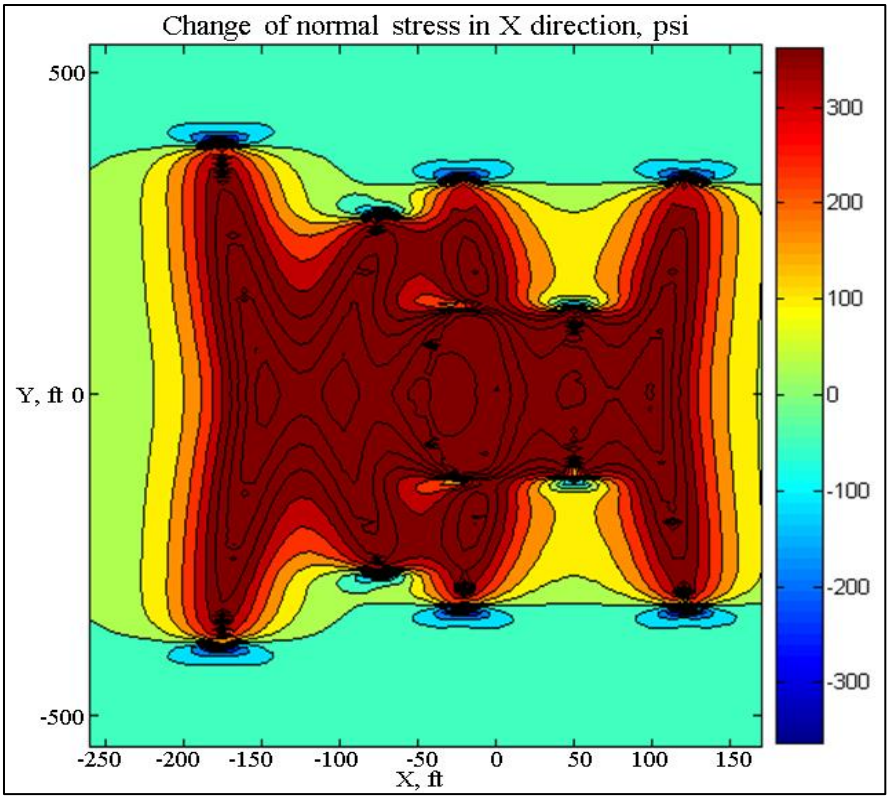

Figure 3.25: Stress change of normal stress σ_{xx} after stage 2 (map view); twice *X* exaggeration.

Through comparing the fracture geometry of sequential and simultaneous cases (Figures 3.12 and 3.18), it is apparent that there is great deviation in fracture geometry due to different mechanisms of mechanical interaction. For the simultaneous case, four interior fractures were immaturely propagated, while only three fractures have immature growth for the sequential case. From this point, the sequential case might be able to create better fracture geometry. In addition, the results of the sequential case also reveal that fracture geometries in two stages are also very distinct, which consequently implies that stage spacing also needs to be considered for crack interaction and stress shadow effects, not just the perforation spacing within a given stage.

3.4 CONCLUSIONS

The complex hydraulic fracture development model was applied to simulate single non-planar and multiple fracture propagation. Both iteratively and fully coupling procedures were used to calculate fracture geometry of single non-planar fracture, indicating that iteratively coupling method is sufficient for coupling rock mechanics and fluid mechanics. The effects of fracture misalignment and in-situ differential stress on non-planar propagation are studied, revealing that fracture width restriction is more pronounced with the larger misalignment angle. The fracture follows the wider curve with the more isotropic stress condition, but finally the fracture is approaching the orientation of maximum horizontal stress. Furthermore, simultaneous and sequential multiple fracture propagation are investigated, showing the two stimulation methods create distinct fracture geometries because of different mechanisms of mechanical interaction. Stresses are induced by opening fractures, resulting in orientation and magnitude change of minimum and maximum horizontal principal stresses. Non-planar geometry of interior fractures causes restriction of fracture aperture and length reduction. The significant fracture width restriction might increase the likelihood of proppant screen-out.

CHAPTER 4: SIMPLIFIED THREE-DIMENSIONAL DISPLACEMENT DISCONTINUITY METHOD (S3D DDM)

The Displacement Discontinuity Method (DDM) is widely used to describe rock deformation for hydraulic fracture propagation in oil and gas industry. However, the two-dimensional DDM with plane strain assumption cannot accurately simulate fracture propagation in the finite height formations. Olson (2004) proposed a three-dimensional correction factor to combine with the two-dimensional DDM to account for fractures with limited height, which was presented and applied in Chapter 2 and Chapter 3.

In this chapter, to further improve the accuracy of displacement discontinuity and stress calculation for three-dimensional fractures, we propose a new displacement discontinuity method, which is simplified a fully 3D solution by Shou (1993). This new method is able to calculate displacement discontinuities and induced stresses not only for single fracture but also for multiple fractures in three dimensions. Computational efficiency is significantly improved compared to the fully 3D approach.

4.1 INTRODUCTION

In the oil and gas industry, hydraulic fractures are often created to obtain economic production rate. In general, there are two types of numerical methods for solving the fracture problems, (1) the domain type, discretization through the domain, (2) the boundary type, only discretization on the boundary of domain (Shou, 1993). An example of the first type is the Finite Element Method (FEM); The Boundary Element Method (BEM) is one of the second type. For FEM, fracture tips require special elements to handle asymptotic stress fields, and it is very computationally expensive and difficult to mesh cracks with complex geometries (Pathak et al., 2013). BEM applies an analytical solution of displacement discontinuities integrated over a boundary element, which easily accommodates complex boundary geometries and is suitable for modeling regions with rapidly stress change (Becker, 1992).

Comparing these two methods, the advantages of the boundary element method are as follows:

i. BEM reduces the dimension of the problem by one, since only boundary of the domain is required to discretize. Less data preparation time is needed for BEM.

ii. BEM is inherently more accurate than FEM, because the numerical solution is based on the integration of exact analytical solution throughout the domain. This makes BEM very suitable for modeling fracture problems with rapid stress change.

iii. Compared with FEM, less computer time and memory is needed for BEM to obtain the same level of accuracy.

Some of the limitations of BEM are:

i. For heterogeneous problems, BEM loses the main advantage of reduction in dimensionality for modeling interior domain.

ii. The solution matrix formed by BEM is nonsymmetric and fully populated; while, the solution matrix for FEM is usually larger in size but sparsely populated.

The Displacement Discontinuity Method (DDM) is a special direct boundary element method, which solves unknown boundary stresses or displacements in terms of the given boundary conditions, based on the Somigliana's formula (Shou, 1993; Love, 1994),

$$u_j(\xi) = \int_S U_{ij}(\xi,\eta) t_i(\eta) dS(\eta) - \int_S T_{ij}(\xi,\eta) u_i(\eta) dS(\eta), \tag{4.1}$$

$$\sigma_{jk}(\xi) = \int_S D_{ijk}(\xi,\eta) t_i(\eta) dS(\eta) - \int_S E_{ijk}(\xi,\eta) u_i(\eta) dS(\eta), \tag{4.2}$$

where, $u_j(\xi)$ are displacement components at a point ξ , $\sigma_{jk}(\xi)$ is stress state at a point ξ, $t_j(\eta)$ are tractions over the boundary S of the region, as shown in Figure 4.1(a), and $u_i(\eta)$ are displacements over the boundary S of the region. The quantities $U_{ij}(\eta,\xi)$, $T_{ij}(\eta,\xi)$, $D_{ijk}(\eta,\xi)$ and $E_{ijk}(\eta,\xi)$ are tensor fields that represent the influences of a concentrated force at point η on the tractions and displacements on point ξ.

For crack-like geometries, the thickness of the opening compared with its lateral extent is so small that it can be ignored. Therefore, the boundary S of the region can be idealized as two surfaces, $S^{\pm}$, in an infinite body, as shown in Figure 4.1(b). For this crack-like geometry, the tensors have properties, $U_{ij}^{+} = U_{ij}^{-}$, $T_{ij}^{+} = -T_{ij}^{-}$, $D_{ijk}^{+} = D_{ijk}^{-}$, $E_{ijk}^{+} = -E_{ijk}^{-}$, and the traction equilibrium condition is $t_j^{+} = -t_j^{-}$. Therefore, Eqs. 4.1 and 4.2 can be simplified as

$$u_j(\xi) = \int_S T_{ij}^{+}(\xi,\eta) \Delta u_i(\eta) dS(\eta) \quad \Delta u_i = u_i^{-} - u_i^{+}, \tag{4.3}$$

$$\sigma_{jk}(\xi) = \int_S E_{ijk}^{+}(\xi,\eta) \Delta u_i(\eta) dS(\eta) \quad \Delta u_i = u_i^{-} - u_i^{+}, \tag{4.4}$$

Since analytical solutions are very hard to obtain for Eqs. 4.3 and 4.4, numerical solutions are generally sought. The boundary $S^{\pm}$ can be divided into N planar elements with assumption of constant or certain variation of the tractions and displacements over each element, as shown in Figure 4.2. Constant tractions and displacements distribution for each element are assumed for clarity and brevity. Eqs. 4.3 and 4.4 can be reduced to

$$\begin{aligned} u_j(\xi_n) &= \sum_{m=1}^{N} T_{ij}^{*}(\xi_n, \eta_m)\Delta u_i(\eta_m) \\ T_{ij}^{*}(\xi_n, \eta_m) &= \int_{\Delta S_m} T_{ij}^{+}(\xi_n, \eta) dS(\eta) \end{aligned}, \tag{4.5}$$

$$\begin{aligned} \sigma_{jk}(\xi_n) &= \sum_{m=1}^{N} E_{ijk}^{*}(\xi_n, \eta_m)\Delta u_i(\eta_m) \\ E_{ijk}^{*}(\xi_n, \eta_m) &= \int_{\Delta S_m} E_{ijk}^{+}(\xi_n, \eta) dS(\eta) \end{aligned}. \tag{4.6}$$

Based on Eqs. 4.5 and 4.6, unknown displacement discontinuities can be calculated for specific boundary conditions of the domain. After that, the displacements and stresses at arbitrary point ξ in the field can be obtained.

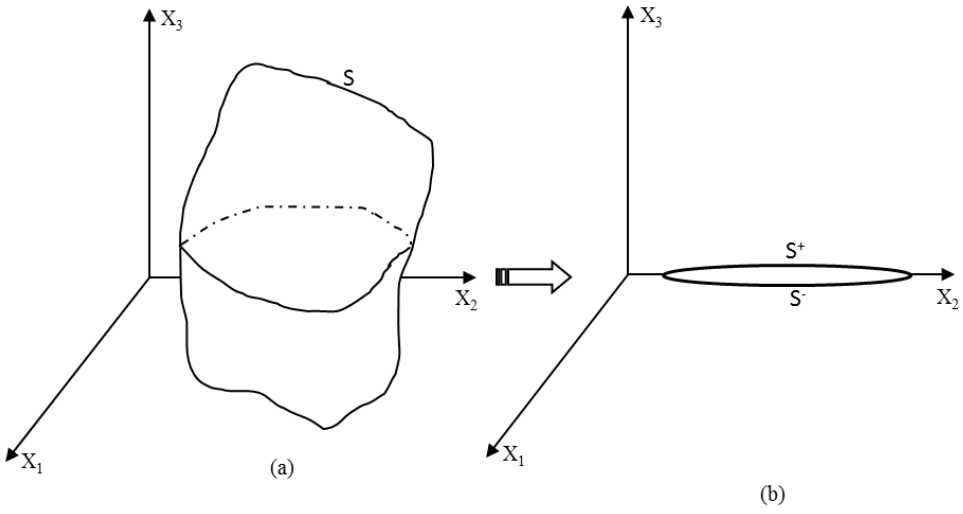

Figure 4.1: Arbitrary three-dimensional cracks with (a) general domain and (b) crack-like domain.

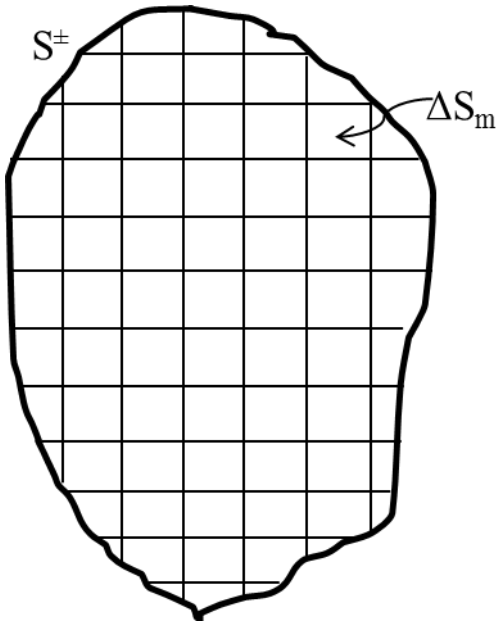

Figure 4.2: Discrete boundary of the crack.

In chapters 2 and 3, a method for fracture propagation modeling in pseudo-3D for single and multiple non-planar fracture problems is described based on two-dimensional displacement discontinuity method with correction factor G proposed by Olson (2004). Wu and Olson (2013) discovered that although the correction factor of Olson (2004) is very accurate for single fracture problems, this method underestimates the crack interaction between nearby cracks and thus the computed apertures are too large for multiple fractures that are closely spaced. Consequently, this demonstrates a need for a better way to represent 3D problems. In order to find a better way, we have gone to the fully 3D solutions of Shou (1993).

4.2 THREE-DIMENSIONAL DISPLACEMENT DISCONTINUITY METHOD (3D DDM)

An analytical solution of 3D DDM for elements with constant displacement discontinuities was documented by Shou (1993). In this section, the analytical solution is outlined in brief and then numerical implementation for vertical fractures is derived.

4.2.1 Formula derivation

A three-dimensional crack in an infinite elastic medium can be described as a collection of rectangular elements (Figure 4.3). The global coordinate is X, Y, Z. Each rectangular element has its own local coordinate system x_1, x_2, x_3. Each element has a positive ($x_3 = 0^+$) side and a negative ($x_3 = 0^-$) side. There are three displacement discontinuities for each element, $D_i = (D_1, D_2, D_3)$, given by

$$\begin{aligned} D_1(x_1, x_2, 0) &= u_1(x_1, x_2, 0^-) - u_1(x_1, x_2, 0^+) \\ D_2(x_1, x_2, 0) &= u_2(x_1, x_2, 0^-) - u_2(x_1, x_2, 0^+), \\ D_3(x_1, x_2, 0) &= u_3(x_1, x_2, 0^-) - u_3(x_1, x_2, 0^+) \end{aligned} \tag{4.7}$$

where u_1, u_2, u_3 are displacements in the x_1, x_2, x_3 direction, respectively.

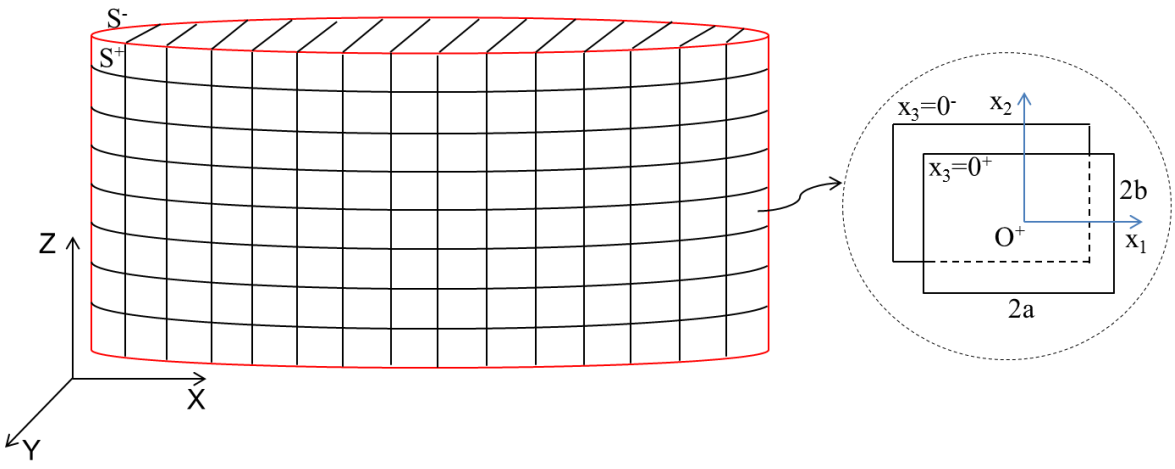

Figure 4.3: A three-dimensional crack in an infinite elastic solid.

The analytical solution for the stresses, σ_{ij}, caused by a displacement discontinuity element can be given in terms of the local coordinate system x_1, x_2, x_3, as (Rongved, 1957; Salamon, 1964):

$$\begin{aligned}
\sigma_{11} &= C_r D_1[2I_{,13} - x_3 I_{,111}] + C_r D_2[2\nu I_{,23} - x_3 I_{,211}] + C_r D_3[I_{,33} + (1-2\nu) I_{,22} - x_3 I_{,311}] \\
\sigma_{22} &= C_r D_1[2\nu I_{,13} - x_3 I_{,122}] + C_r D_2[2I_{,23} - x_3 I_{,222}] + C_r D_3[I_{,33} + (1-2\nu) I_{,11} - x_3 I_{,322}] \\
\sigma_{33} &= C_r D_1[-x_3 I_{,133}] + C_r D_2[-x_3 I_{,233}] + C_r D_3[I_{,33} - x_3 I_{,333}] \\
\sigma_{12} &= C_r D_1[(1-\nu) I_{,23} - x_3 I_{,112}] + C_r D_2[(1-\nu) I_{,13} - x_3 I_{,212}] + C_r D_3[-(1-2\nu) I_{,12} - x_3 I_{,312}] \\
\sigma_{13} &= C_r D_1[I_{,33} + \nu I_{,22} - x_3 I_{,113}] + C_r D_2[-\nu I_{,12} - x_3 I_{,213}] + C_r D_3[-x_3 I_{,313}] \\
\sigma_{23} &= C_r D_1[-\nu I_{,21} - x_3 I_{,123}] + C_r D_2[I_{,33} + \nu I_{,11} - x_3 I_{,223}] + C_r D_3[-x_3 I_{,323}]
\end{aligned} \qquad \text{(4.8)}$$

in which

$$C_r = \frac{G}{4\pi(1-\nu)}, \qquad (4.9)$$

where G is shear modulus, and ν is the Poisson's ratio. The notation '$,i$' (where i = 1, 2, 3) represents the partial derivative with respect to x_i. Shou (1993) presented the kernel analytical solution I to the problem of a constant displacement D_i over an arbitrarily oriented, rectangular element in an infinite elastic medium solved by employing the Green's function approach,

$$I(x_1, x_2, x_3) = \int_{-b}^{b}\int_{-a}^{a} \frac{1}{\sqrt{(x_1-\xi_1)^2 + (x_2-\xi_2)^2 + x_3^{\,2}}} d\xi_1 d\xi_2 . \qquad (4.10)$$

After integration, $I(x_1, x_2, x_3)$ can be written as

$$I(x_1, x_2, x_3) = [\bar{x}_1 \ln(r + \bar{x}_2) + \bar{x}_2 \ln(r + \bar{x}_1) - x_3\theta]\Big|_{\xi_1=-a}^{\xi_1=a}\Big|_{\xi_2=-b}^{\xi_2=b}, \qquad (4.11)$$

where, $\bar{x}_1 = x_1 - \xi_1$, $\bar{x}_2 = x_2 - \xi_2$, $\theta = \tan^{-1}[\bar{x}_1 \bar{x}_2 / (r x_3)]$,

$r = \sqrt{(x_1-\xi_1)^2 + (x_2-\xi_2)^2 + x_3^{\,2}}$.

It is convenient to rename the derivatives of I to J, where the various J factors are defined as:

$$J_1 = I_{,1} = \ln(r + x_2 - \xi_2)\Big\|$$

$$J_2 = I_{,2} = \ln(r + x_1 - \xi_1)\Big\|$$

$$J_3 = I_{,3} = -\tan^{-1}\left(\frac{(x_1 - \xi_1)(x_2 - \xi_2)}{x_3 r}\right)\Big\|$$

$$J_4 = I_{,11} = \frac{(x_1 - \xi_1)}{r(r + x_2 - \xi_2)}\Big\|$$

$$J_5 = I_{,22} = \frac{x_2 - \xi_2}{r(r + x_1 - \xi_1)}\Big\|$$

$$J_6 = I_{,33} = \frac{(x_1 - \xi_1)(x_2 - \xi_2)({x_3}^2 + r^2)}{r({x_3}^2 + (x_1 - \xi_1)^2)({x_3}^2 + (x_2 - \xi_2)^2)}\Big\|$$

$$J_7 = I_{,12} = \frac{1}{r}\Big\|$$

$$J_8 = I_{,13} = \frac{x_3}{r(r + x_2 - \xi_2)}\Big\|$$

$$J_9 = I_{,23} = \frac{x_3}{r(r + x_1 - \xi_1)}\Big\|$$

$$J_{10} = I_{,111} = -\frac{(r + x_2 - \xi_2)((x_1 - \xi_1)^2 - r^2) + (x_1 - \xi_1)^2 r}{r^3(r + x_2 - \xi_2)^2}\Big\|$$

$$J_{11} = I_{,211} = \frac{-\bar{x}_1}{r^3}\Big\| = \frac{-(x_1 - \xi_1)}{r^3}\Big\|$$

$$J_{12} = I_{,311} = -\frac{(x_1 - \xi_1)x_3(2r + x_2 - \xi_2)}{r^3(r + x_2 - \xi_2)^2}\Big\|$$

$$J_{13} = I_{,122} = -\frac{(x_2 - \xi_2)}{r^3}\Big\|$$

$$J_{14} = I_{,222} = -\frac{(r + x_1 - \xi_1)((x_2 - \xi_2)^2 - r^2) + (x_2 - \xi_2)^2 r}{r^3(r + x_1 - \xi_1)^2}\Big\|$$

$$J_{15} = I_{,322} = -\frac{(x_2 - \xi_2)x_3(2r + x_1 - \xi_1)}{r^3(r + x_1 - \xi_1)^2}\Big\|$$

$$J_{16} = I_{,133} = -\frac{(r + x_2 - \xi_2)(x_3{}^2 - r^2) + x_3{}^2 r}{r^3 (r + x_2 - \xi_2)^2}\Bigg\|$$

$$J_{17} = I_{,233} = -\frac{(r + x_1 - \xi_1)(x_3{}^2 - r^2) + x_3{}^2 r}{r^3 (r + x_1 - \xi_1)^2}\Bigg\|$$

$$J_{18} = I_{,333} =$$

$$-x_3 \bar{x}_1 \bar{x}_2 \frac{(x_3{}^2 + (x_1 - \xi_1)^2)^2 (x_3{}^2 + (x_2 - \xi_2)^2 + 2r^2) + (x_3{}^2 + (x_2 - \xi_2)^2)^2 (x_3{}^2 + (x_1 - \xi_1)^2 + 2r^2)}{r^3 (x_3{}^2 + (x_2 - \xi_2)^2)^2 (x_3{}^2 + (x_1 - \xi_1)^2)^2}\Bigg\|$$

$$J_{19} = I_{,123} = -\frac{x_3}{r^3}\Bigg\|$$

…… (4.12)

The symbol $\|$ denotes Chinnery's notation to represent the substitution

$$J(\xi_1, \xi_2)\| = J(a,b) - J(a,-b) - J(-a,b) + J(-a,-b).$$

Substituting the various J's into Eqs. 4.8 results in

$$\sigma_{11} = C_r D_1[2J_8 - x_3 J_{10}] + C_r D_2[2\nu J_9 - x_3 J_{11}] + C_r D_3[J_6 + (1-2\nu)J_5 - x_3 J_{12}]$$
$$\sigma_{22} = C_r D_1[2\nu J_8 - x_3 J_{13}] + C_r D_2[2J_9 - x_3 J_{14}] + C_r D_3[J_6 + (1-2\nu)J_4 - x_3 J_{15}]$$
$$\sigma_{33} = C_r D_1[-x_3 J_{16}] + C_r D_2[-x_3 J_{17}] + C_r D_3[J_6 - x_3 J_{18}]$$
$$\sigma_{12} = C_r D_1[(1-\nu)J_9 - x_3 J_{11}] + C_r D_2[(1-\nu)J_8 - x_3 J_{13}] + C_r D_3[-(1-2\nu)J_7 - x_3 J_{19}]$$
$$\sigma_{13} = C_r D_1[J_6 + \nu J_5 - x_3 J_{12}] + C_r D_2[-\nu J_7 - x_3 J_{19}] + C_r D_3[-x_3 J_{16}]$$
$$\sigma_{23} = C_r D_1[-\nu J_7 - x_3 J_{19}] + C_r D_2[J_6 + \nu J_4 - x_3 J_{15}] + C_r D_3[-x_3 J_{17}]$$

…….... (4.13)

4.2.2 Numerical implementation

Eqs. 4.13 are developed from the analytical solution to the problem of a constant displacement discontinuity over an arbitrarily oriented, finite rectangular element in an infinite medium (Shou, 1993). The equations are relative to the local coordinate system of a given element. Based on these equations, we will solve displacement discontinuities and stress distribution for fractures through coordinate transformation.

When calculating stresses at a point (*X*, *Y*, *Z*) with respect to global coordinate system induced by displacement discontinuities of element *j*, the point (*X*, *Y*, *Z*) needs to be transformed to the local coordinate system of element *j*:

$$\begin{aligned} x_1 &= (X - \overset{j}{X})\cos\beta\cos\theta + (Y - \overset{j}{Y})\sin\beta\cos\theta - (Z - \overset{j}{Z})\sin\theta \\ x_2 &= (X - \overset{j}{X})\cos\beta\sin\theta + (Y - \overset{j}{Y})\sin\beta\sin\theta + (Z - \overset{j}{Z})\cos\theta, \\ x_3 &= -(X - \overset{j}{X})\sin\beta + (Y - \overset{j}{Y})\cos\beta \end{aligned} \tag{4.14}$$

where β is the angle of element *j* between x_1 and *X*, θ is the angle of element *j* between x_2 and *Z*. In cases where vertical stress much greater than horizontal stresses is expected, we can assume a special case of the 3-D crack that has a vertical dip. To solve this vertical fracture problem, we assumed that fracture element plane is the x_1-x_2 plane and the x_3 direction is perpendicular to the element (Figure 4.4). Hence, by setting θ = 0, Eqs. 4.14 can be simplified as

$$\begin{aligned} x_1 &= (X - \overset{j}{X})\cos\beta + (Y - \overset{j}{Y})\sin\beta \\ x_2 &= Z - \overset{j}{Z} \\ x_3 &= -(X - \overset{j}{X})\sin\beta + (Y - \overset{j}{Y})\cos\beta \end{aligned} \quad . \tag{4.15}$$

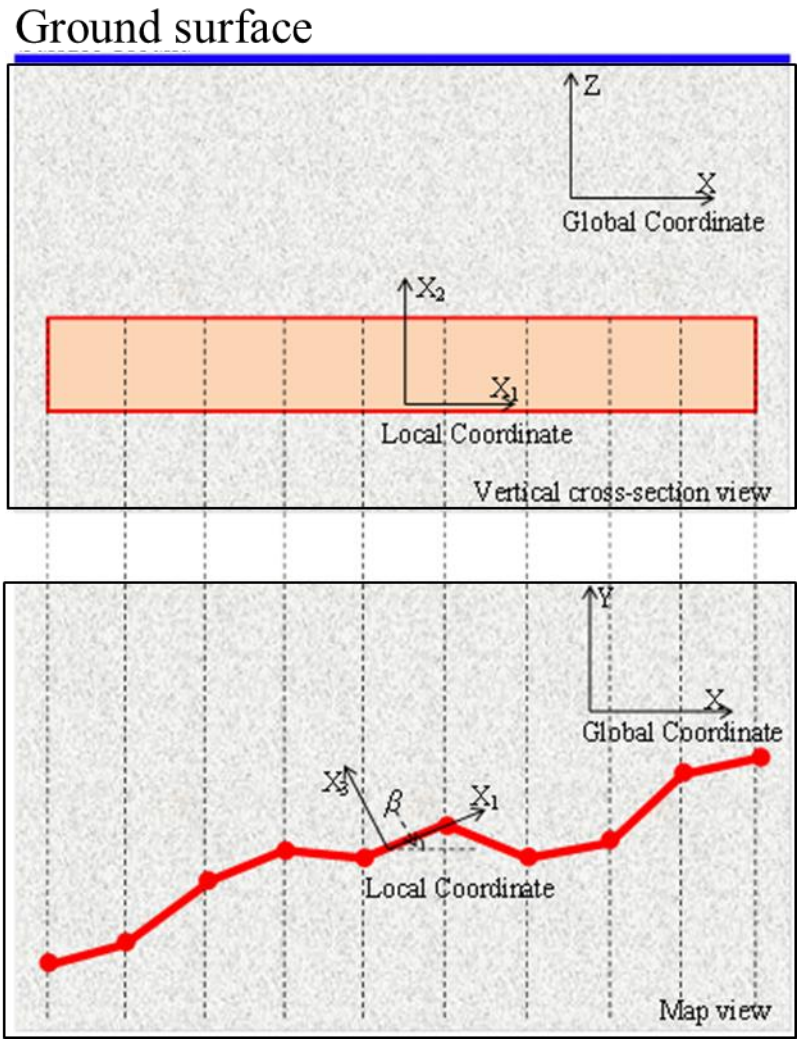

Figure 4.4: Crack elements on a vertical cross-section view and map view.

Displacement Discontinuity calculation

In order to develop a general method for simultaneously solving for the displacement discontinuities of a population of elements given the stress boundary conditions, the equations must be rewritten in terms of element *j*'s influence on the normal and shear stresses on element *i*. If calculating induced stresses at the midpoint of element *i*, the coordinate of element *i* ($\overset{i}{X}, \overset{i}{Y}, \overset{i}{Z}$) should substitute into Eqs. 4.15:

$$x_1 = (\overset{i}{X} - \overset{j}{X})\cos\beta + (\overset{i}{Y} - \overset{j}{Y})\sin\beta$$
$$x_2 = \overset{i}{Z} - \overset{j}{Z} \qquad . \qquad (4.16)$$
$$x_3 = -(\overset{i}{X} - \overset{j}{X})\sin\beta + (\overset{i}{Y} - \overset{j}{Y})\cos\beta$$

Stresses $\overset{j}{\sigma}_{11}, \overset{j}{\sigma}_{22}, \overset{j}{\sigma}_{33}, \overset{j}{\sigma}_{12}, \overset{j}{\sigma}_{13}, \overset{j}{\sigma}_{23}$ induced by displacement discontinuities of element *j* with respect to local coordinate system of element *j* can be calculated by substituting Eqs. 4.16 into Eqs. 4.13. To solve the displacement discontinuities on the elements, the coordinate of the stresses need to transform from the local reference frame of element *j* to that of element *i* based on coordination transformation (Appendix A.2.1),

$$\overset{i}{\sigma}_{33} = \sin^2\gamma\,\overset{j}{\sigma}_{11} - 2\sin\gamma\cos\gamma\,\overset{j}{\sigma}_{13} + \cos^2\gamma\,\overset{j}{\sigma}_{33}, \qquad (4.17)$$

$$\overset{i}{\tau}_{13} = -\sin\gamma\cos\gamma\,\overset{j}{\sigma}_{11} + \cos 2\gamma\,\overset{j}{\sigma}_{13} + \sin\gamma\cos\gamma\,\overset{j}{\sigma}_{33}, \qquad (4.18)$$

$$\overset{i}{\tau}_{23} = -\overset{j}{\sigma}_{12}\sin\gamma + \overset{j}{\sigma}_{23}\cos\gamma, \qquad (4.19)$$

where $\gamma = \overset{i}{\beta} - \overset{j}{\beta}$.

For a specific problem, *N* displacement discontinuity elements along the boundary *S* are placed (Figure 4.5). It is convenient to term the displacement discontinuities in terms of opening and shearing modes of deformation, using the terms $\overset{j}{D}_n, \overset{j}{D}_{sL}, \overset{j}{D}_{sH}$ to refer to D_3, D_1, D_2. $\overset{j}{D}_n$ is the normal displacement discontinuity of an element (opening); $\overset{j}{D}_{sL}$ is the shear displacement discontinuity in the element length direction (strike-slip); $\overset{j}{D}_{sH}$ is the shear displacement discontinuity in the element height direction (dip-slip). The normal and shear stresses of element *i* can then use $\overset{i}{\sigma}_n, \overset{i}{\sigma}_{sL}, \overset{i}{\sigma}_{sH}$ to substitute for $\overset{i}{\sigma}_{33}$, $\overset{i}{\sigma}_{13}, \overset{i}{\sigma}_{23}$. Applying this new terminology and substituting Eqs. 4.13 into Eqs. 4.17, 4.18 and 4.19 results in

$$\overset{i}{\sigma}_{sL} = C_r(-\sin\gamma\cos\gamma[2\overset{ij}{J}_8 - x_3\overset{ij}{J}_{10}] + \cos 2\gamma[\overset{ij}{J}_6 + \nu\overset{ij}{J}_5 - x_3\overset{ij}{J}_{12}] + \sin\gamma\cos\gamma[-x_3\overset{ij}{J}_{16}])\overset{j}{D}_{sL}$$
$$+C_r(-\sin\gamma\cos\gamma[2\nu\overset{ij}{J}_9 - x_3\overset{i,j}{J}_{11}] + \cos 2\gamma[-\nu\overset{ij}{J}_7 - x_3\overset{ij}{J}_{19}] + \sin\gamma\cos\gamma[-x_3\overset{ij}{J}_{17}])\overset{j}{D}_{sH} \quad ,$$
$$+C_r(-\sin\gamma\cos\gamma[\overset{ij}{J}_6 + (1-2\nu)\overset{ij}{J}_5 - x_3\overset{ij}{J}_{12}] + \cos 2\gamma[-x_3\overset{ij}{J}_{16}] + \sin\gamma\cos\gamma[\overset{ij}{J}_6 - x_3\overset{ij}{J}_{18}])\overset{j}{D}_n$$

…… (4.20)

$$\begin{aligned}\overset{i}{\sigma}_{sH} &= C_r(-\sin\gamma[(1-\nu)\overset{ij}{J}_9 - x_3\overset{ij}{J}_{11}] + \cos\gamma[-\nu\overset{ij}{J}_7 - x_3\overset{ij}{J}_{19}])\overset{j}{D}_{sL} \\ &+C_r(-\sin\gamma[(1-\nu)\overset{ij}{J}_8 - x_3\overset{ij}{J}_{13}] + \cos\gamma[\overset{ij}{J}_6 + \nu\overset{ij}{J}_4 - x_3\overset{ij}{J}_{15}])\overset{j}{D}_{sH} \quad , \\ &+C_r(-\sin\gamma[-(1-2\nu)\overset{ij}{J}_7 - x_3\overset{ij}{J}_{19}] + \cos\gamma[-x_3\overset{ij}{J}_{17}])\overset{j}{D}_n\end{aligned} \tag{4.21}$$

$$\overset{i}{\sigma}_{nn} = C_r(\sin^2\gamma[2\overset{ij}{J}_8 - x_3\overset{ij}{J}_{10}] - 2\sin\gamma\cos\gamma[\overset{ij}{J}_6 + \nu\overset{ij}{J}_5 - x_3\overset{ij}{J}_{12}] + \cos^2\gamma[-x_3\overset{ij}{J}_{16}])\overset{j}{D}_{sL}$$
$$+C_r(\sin^2\gamma[2\nu\overset{ij}{J}_9 - x_3\overset{ij}{J}_{11}] - 2\sin\gamma\cos\gamma[-\nu\overset{ij}{J}_7 - x_3\overset{ij}{J}_{19}] + \cos^2\gamma[-x_3\overset{ij}{J}_{17}])\overset{j}{D}_{sH} \quad .$$
$$+C_r(\sin^2\gamma[\overset{ij}{J}_6 + (1-2\nu)\overset{ij}{J}_5 - x_3\overset{ij}{J}_{12}] - 2\sin\gamma\cos\gamma[-x_3\overset{ij}{J}_{16}] + \cos^2\gamma[\overset{ij}{J}_6 - x_3\overset{ij}{J}_{18}])\overset{j}{D}_n$$

…… (4.22)

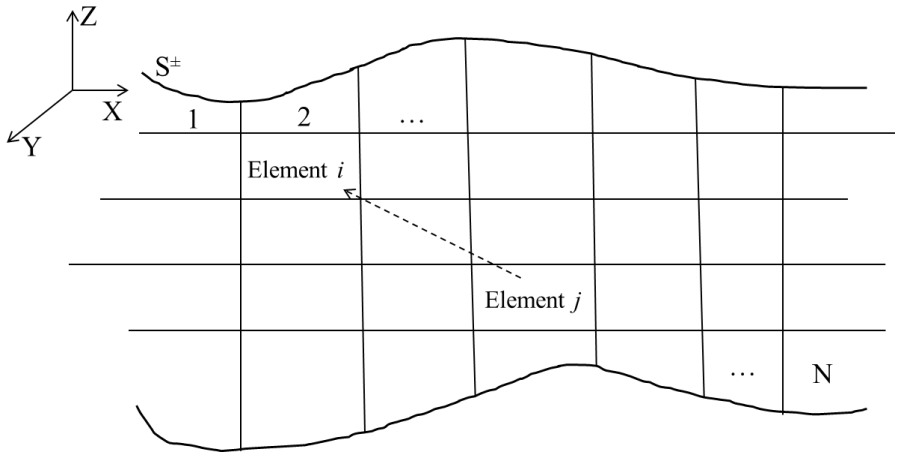

Figure 4.5: Boundary elements on a fracture of interest.

The normal and shear stresses at the midpoint of the element *i* induced by all *N* elements can then be written as

$$
\begin{aligned}
\overset{i}{\sigma}_{sL} &= \sum_{j=1}^{N} \overset{ij}{A}_{sL,sL}\, \overset{j}{D}_{sL} + \sum_{j=1}^{N} \overset{ij}{A}_{sL,sH}\, \overset{j}{D}_{sH} + \sum_{j=1}^{N} \overset{ij}{A}_{sL,nn}\, \overset{j}{D}_{n} \\
\overset{i}{\sigma}_{sH} &= \sum_{j=1}^{N} \overset{ij}{A}_{sH,sL}\, \overset{j}{D}_{sL} + \sum_{j=1}^{N} \overset{ij}{A}_{sH,sH}\, \overset{j}{D}_{sH} + \sum_{j=1}^{N} \overset{ij}{A}_{sH,nn}\, \overset{j}{D}_{n} \,, \\
\overset{i}{\sigma}_{nn} &= \sum_{j=1}^{N} \overset{ij}{A}_{nn,sL}\, \overset{j}{D}_{sL} + \sum_{j=1}^{N} \overset{ij}{A}_{nn,sH}\, \overset{j}{D}_{sH} + \sum_{j=1}^{N} \overset{ij}{A}_{nn,nn}\, \overset{j}{D}_{n}
\end{aligned}
\tag{4.23}
$$

where $\overset{ij}{A}_{sL,sL}$ are the boundary influence coefficients. For example, $\overset{ij}{A}_{sL,sL}$ represents induced shear stress in the fracture length direction of element *i* (i.e., $\overset{i}{\sigma}_{sL}$) resulting from shear displacement discontinuity in the fracture length direction of element *j* (i.e., $\overset{j}{D}_{sL}$).

For hydraulic fracturing problems, the stress boundary conditions on the elements are the combination of the local conditions (fracturing fluid pressure and zero shear stress) and the resolution of the remote stress state onto the elements. Hence, based on the given boundary conditions, the normal and shear displacement discontinuities can be solved using the system of 3N linear algebraic equations,

$$
\begin{bmatrix}
\overset{11}{A}_{sL,sL} & \cdots & \overset{1N}{A}_{sL,sL} & \overset{11}{A}_{sL,sH} & \cdots & \overset{1N}{A}_{sL,sH} & \overset{11}{A}_{sL,nn} & \cdots & \overset{1N}{A}_{sL,nn} \\
\vdots & & & & & & & & \\
\overset{N1}{A}_{sL,sL} & \cdots & \overset{NN}{A}_{sL,sL} & \overset{N1}{A}_{sL,sH} & \cdots & \overset{NN}{A}_{sL,sH} & \overset{N1}{A}_{sL,nn} & \cdots & \overset{NN}{A}_{sL,nn} \\
\overset{11}{A}_{sH,sL} & \cdots & \overset{1N}{A}_{sH,sL} & \overset{11}{A}_{sH,sH} & \cdots & \overset{1N}{A}_{sH,sH} & \overset{11}{A}_{sH,nn} & \cdots & \overset{1N}{A}_{sH,nn} \\
\vdots & & & & & & & & \\
\overset{N1}{A}_{sH,sL} & \cdots & \overset{NN}{A}_{sH,sL} & \overset{N1}{A}_{sH,sH} & \cdots & \overset{NN}{A}_{sH,sH} & \overset{N1}{A}_{sH,nn} & \cdots & \overset{NN}{A}_{sH,nn} \\
\overset{11}{A}_{nn,sL} & \cdots & \overset{1N}{A}_{nn,sL} & \overset{11}{A}_{nn,sH} & \cdots & \overset{1N}{A}_{nn,sH} & \overset{11}{A}_{nn,nn} & \cdots & \overset{1N}{A}_{nn,nn} \\
\vdots & & & & & & & & \\
\overset{N1}{A}_{nn,sL} & \cdots & \overset{NN}{A}_{nn,sL} & \overset{N1}{A}_{nn,sH} & \cdots & \overset{NN}{A}_{nn,sH} & \overset{N1}{A}_{nn,nn} & \cdots & \overset{NN}{A}_{nn,nn}
\end{bmatrix}
\begin{bmatrix}
\overset{1}{D}_{sL} \\ \vdots \\ \overset{N}{D}_{sL} \\ \overset{1}{D}_{sH} \\ \vdots \\ \overset{N}{D}_{sH} \\ \overset{1}{D}_{n} \\ \vdots \\ \overset{N}{D}_{n}
\end{bmatrix}
=
\begin{bmatrix}
\overset{1}{\sigma}_{sL} \\ \vdots \\ \overset{N}{\sigma}_{sL} \\ \overset{1}{\sigma}_{sH} \\ \vdots \\ \overset{N}{\sigma}_{sH} \\ \overset{1}{\sigma}_{n} \\ \vdots \\ \overset{N}{\sigma}_{n}
\end{bmatrix}.
\tag{4.24}
$$

Stress field Calculation

After obtaining the displacement discontinuity values of all boundary elements, additional calculations can be made. For instance, stresses at any point (e.g., Point *P*) in the body can be calculated by summing the induced stresses of all elements together. To do this, Eqs. 4.13 need to be transformed to the global coordinate system. The coordinate transformation from the local coordinate system to the global coordinate system is given in Appendix A.2.2. The stresses at point *P* induced by displacement discontinuities of element *j* can be written as

$$\overset{P}{\sigma}_{XX} = \cos^2\beta\,\overset{j}{\sigma}_{11} - \sin 2\beta\,\overset{j}{\sigma}_{31} + \sin^2\beta\,\overset{j}{\sigma}_{33} \ , \tag{4.25}$$

$$\overset{P}{\sigma}_{YY} = \sin^2\beta\,\overset{j}{\sigma}_{11} + \sin 2\beta\,\overset{j}{\sigma}_{31} + \cos^2\beta\,\overset{j}{\sigma}_{33} \ , \tag{4.26}$$

$$\overset{P}{\sigma}_{ZZ} = \overset{j}{\sigma}_{22} \ , \tag{4.27}$$

$$\overset{P}{\sigma}_{XY} = \sin\beta\cos\beta\,\overset{j}{\sigma}_{11} + \cos 2\beta\,\overset{j}{\sigma}_{13} - \sin\beta\cos\beta\,\overset{j}{\sigma}_{33} \ , \tag{4.28}$$

$$\overset{P}{\sigma}_{XZ} = \cos\beta\,\overset{j}{\sigma}_{12} - \sin\beta\,\overset{j}{\sigma}_{23} \ , \tag{4.29}$$

$$\overset{P}{\sigma}_{YZ} = \sin\beta\,\overset{j}{\sigma}_{12} + \cos\beta\,\overset{j}{\sigma}_{23} \ . \tag{4.30}$$

Substituting Eqs. 4.13 into Eqs. 4.25 to 4.30 results in

$$\begin{aligned}\overset{P}{\sigma}_{XX} &= C_r(\cos^2\beta\,\overset{j}{[}2\,\overset{Pj}{J}_8 - x_3\,\overset{Pj}{J}_{10}] - \sin 2\beta\,\overset{j}{[}\overset{Pj}{J}_6 + \nu\,\overset{Pj}{J}_5 - x_3\,\overset{Pj}{J}_{12}] + \sin^2\beta\,\overset{j}{[}-x_3\,\overset{Pj}{J}_{16}])\,\overset{j}{D}_{sL} \\ &+C_r(\cos^2\beta\,\overset{j}{[}2\nu\,\overset{Pj}{J}_9 - x_3\,\overset{Pj}{J}_{11}] - \sin 2\beta\,\overset{j}{[}-\nu\,\overset{Pj}{J}_7 - x_3\,\overset{Pj}{J}_{19}] + \sin^2\beta\,\overset{j}{[}-x_3\,\overset{Pj}{J}_{17}])\,\overset{j}{D}_{sH} \\ &+C_r(\cos^2\beta\,\overset{j}{[}\overset{Pj}{J}_6 + (1-2\nu)\,\overset{Pj}{J}_5 - x_3\,\overset{Pj}{J}_{12}] - \sin 2\beta\,\overset{j}{[}-x_3\,\overset{Pj}{J}_{16}] + \sin^2\beta\,\overset{j}{[}\overset{Pj}{J}_6 - x_3\,\overset{Pj}{J}_{18}])\,\overset{j}{D}_n\end{aligned} \ , \tag{4.31}$$

$$\begin{aligned}\overset{P}{\sigma}_{YY} &= C_r(\sin^2\beta\,\overset{j}{[}2\,\overset{Pj}{J}_8 - x_3\,\overset{Pj}{J}_{10}] + \sin 2\beta\,\overset{j}{[}\overset{Pj}{J}_6 + \nu\,\overset{Pj}{J}_5 - x_3\,\overset{Pj}{J}_{12}] + \cos^2\beta\,\overset{j}{[}-x_3\,\overset{Pj}{J}_{16}])\,\overset{j}{D}_{sL} \\ &+C_r(\sin^2\beta\,\overset{j}{[}2\nu\,\overset{Pj}{J}_9 - x_3\,\overset{Pj}{J}_{11}] + \sin 2\beta\,\overset{j}{[}-\nu\,\overset{Pj}{J}_7 - x_3\,\overset{Pj}{J}_{19}] + \cos^2\beta\,\overset{j}{[}-x_3\,\overset{Pj}{J}_{17}])\,\overset{j}{D}_{sH} \\ &+C_r(\sin^2\beta\,\overset{j}{[}\overset{Pj}{J}_6 + (1-2\nu)\,\overset{Pj}{J}_5 - x_3\,\overset{Pj}{J}_{12}] + \sin 2\beta\,\overset{j}{[}-x_3\,\overset{Pj}{J}_{16}] + \cos^2\beta\,\overset{j}{[}\overset{Pj}{J}_6 - x_3\,\overset{Pj}{J}_{18}])\,\overset{j}{D}_n\end{aligned} \ , \tag{4.32}$$

$$\overset{P}{\sigma}_{ZZ} = C_r[2\nu \overset{Pj}{J}_8 - x_3 \overset{Pj}{J}_{13}]\overset{j}{D}_{sL} + C_r[2\overset{Pj}{J}_9 - x_3 \overset{Pj}{J}_{14}]\overset{j}{D}_{sH} + C_r[\overset{Pj}{J}_6 + (1-2\nu)\overset{Pj}{J}_4 - x_3 \overset{Pj}{J}_{15}]\overset{j}{D}_n \ ,$$

..... (4.33)

$$\begin{aligned}\overset{P}{\sigma}_{XY} = \ & C_r(\sin\overset{j}{\beta}\cos\overset{j}{\beta}[2\overset{Pj}{J}_8 - x_3\overset{Pj}{J}_{10}] + \cos 2\overset{j}{\beta}[\overset{Pj}{J}_6 + \nu\overset{Pj}{J}_5 - x_3\overset{Pj}{J}_{12}] - \sin\overset{j}{\beta}\cos\overset{j}{\beta}[-x_3\overset{Pj}{J}_{16}])\overset{j}{D}_{sL} \\ & + C_r(\sin\overset{j}{\beta}\cos\overset{j}{\beta}[2\nu\overset{Pj}{J}_9 - x_3\overset{Pj}{J}_{11}] + \cos 2\overset{j}{\beta}[-\nu\overset{Pj}{J}_7 - x_3\overset{Pj}{J}_{19}] - \sin\overset{j}{\beta}\cos\overset{j}{\beta}[-x_3\overset{Pj}{J}_{17}])\overset{j}{D}_{sH} \\ & + C_r(\sin\overset{j}{\beta}\cos\overset{j}{\beta}[\overset{Pj}{J}_6 + (1-2\nu)\overset{Pj}{J}_5 - x_3\overset{Pj}{J}_{12}] + \cos 2\overset{j}{\beta}[-x_3\overset{Pj}{J}_{16}] - \sin\overset{j}{\beta}\cos\overset{j}{\beta}[\overset{Pj}{J}_6 - x_3\overset{Pj}{J}_{18}])\overset{j}{D}_n\end{aligned}$$

..... (4.34)

$$\begin{aligned}\overset{P}{\sigma}_{XZ} = \ & C_r(\cos\overset{j}{\beta}[(1-\nu)\overset{Pj}{J}_9 - x_3\overset{Pj}{J}_{11}] - \sin\overset{j}{\beta}[-\nu\overset{Pj}{J}_7 - x_3\overset{Pj}{J}_{19}])\overset{j}{D}_{sL} \\ & + C_r(\cos\overset{j}{\beta}[(1-\nu)\overset{Pj}{J}_8 - x_3\overset{Pj}{J}_{13}] - \sin\overset{j}{\beta}[\overset{Pj}{J}_6 + \nu\overset{Pj}{J}_4 - x_3\overset{Pj}{J}_{15}])\overset{j}{D}_{sH} \\ & + C_r(\cos\overset{j}{\beta}[-(1-2\nu)\overset{Pj}{J}_7 - x_3\overset{Pj}{J}_{19}] - \sin\overset{j}{\beta}[-x_3\overset{Pj}{J}_{17}])\overset{j}{D}_n\end{aligned} \quad , \qquad (4.35)$$

$$\begin{aligned}\overset{P}{\sigma}_{YZ} = \ & C_r(\sin\overset{j}{\beta}[(1-\nu)\overset{Pj}{J}_9 - x_3\overset{Pj}{J}_{11}] + \cos\overset{j}{\beta}[-\nu\overset{Pj}{J}_7 - x_3\overset{Pj}{J}_{19}])\overset{j}{D}_{sL} \\ & + C_r(\sin\overset{j}{\beta}[(1-\nu)\overset{Pj}{J}_8 - x_3\overset{Pj}{J}_{13}] + \cos\overset{j}{\beta}[\overset{Pj}{J}_6 + \nu\overset{Pj}{J}_4 - x_3\overset{Pj}{J}_{15}])\overset{j}{D}_{SH} \\ & + C_r(\sin\overset{j}{\beta}[-(1-2\nu)\overset{Pj}{J}_7 - x_3\overset{Pj}{J}_{19}]) + \cos\overset{j}{\beta}[-x_3\overset{Pj}{J}_{17}])\overset{j}{D}_n\end{aligned} \quad . \qquad (4.36)$$

Hence, the total induced stresses at the point P can be calculated by

$$\begin{aligned}\overset{P}{\sigma}_{XX} &= \sum_{j=1}^{N}\overset{Pj}{F}_{XX,sL}\overset{j}{D}_{sL} + \sum_{j=1}^{N}\overset{Pj}{F}_{XX,sH}\overset{j}{D}_{sH} + \sum_{j=1}^{N}\overset{Pj}{F}_{XX,nn}\overset{j}{D}_n \\ \overset{P}{\sigma}_{YY} &= \sum_{j=1}^{N}\overset{Pj}{F}_{YY,sL}\overset{j}{D}_{sL} + \sum_{j=1}^{N}\overset{Pj}{F}_{YY,sH}\overset{j}{D}_{sH} + \sum_{j=1}^{N}\overset{Pj}{F}_{YY,nn}\overset{j}{D}_n \\ \overset{P}{\sigma}_{ZZ} &= \sum_{j=1}^{N}\overset{Pj}{F}_{ZZ,sL}\overset{j}{D}_{sL} + \sum_{j=1}^{N}\overset{Pj}{F}_{ZZ,sH}\overset{j}{D}_{sH} + \sum_{j=1}^{N}\overset{Pj}{F}_{ZZ,nn}\overset{j}{D}_n \\ \overset{P}{\sigma}_{XY} &= \sum_{j=1}^{N}\overset{Pj}{F}_{XY,sL}\overset{j}{D}_{sL} + \sum_{j=1}^{N}\overset{Pj}{F}_{XY,sH}\overset{j}{D}_{sH} + \sum_{j=1}^{N}\overset{Pj}{F}_{XY,nn}\overset{j}{D}_n \\ \overset{P}{\sigma}_{XZ} &= \sum_{j=1}^{N}\overset{Pj}{F}_{XZ,sL}\overset{j}{D}_{sL} + \sum_{j=1}^{N}\overset{Pj}{F}_{XZ,sH}\overset{j}{D}_{sH} + \sum_{j=1}^{N}\overset{Pj}{F}_{XZ,nn}\overset{j}{D}_n \\ \overset{P}{\sigma}_{YZ} &= \sum_{j=1}^{N}\overset{Pj}{F}_{YZ,sL}\overset{j}{D}_{sL} + \sum_{j=1}^{N}\overset{Pj}{F}_{YZ,sH}\overset{j}{D}_{sH} + \sum_{j=1}^{N}\overset{Pj}{F}_{YZ,nn}\overset{j}{D}_n\end{aligned} \quad , \qquad (4.37)$$

where $F^{Pj}_{XX,sL}$ are also the influence coefficients. For example, $F^{Pj}_{XX,sL}$ represents induced stress in X direction at the point P (σ^{P}_{XX}) resulting from shear displacement discontinuity in the fracture length direction of element j (D^{j}_{sL}).

4.2.3 Comparison of different displacement discontinuity methods

2D DDM can efficiently and accurately solve fracture problems of two-dimensional plane strain that one dimension of cracks (e.g. crack length) has a much greater length than the other two dimensions. However, this two-dimensional method is inadequate when both the impact of height and length are required to incorporate into the solution. Figure 4.6 shows the aperture development with increasing length for a fixed height and constant pressure fracture. Fracture apertures are normalized by the aperture of a plane strain fracture of the same height (w_{ni}). For hydraulic fracture propagation problems, we focus on lateral propagation. Hence, both two-dimensional and three-dimensional methods are discretized in the fracture length direction. Figure 4.6 indicates that 2D DDM can give accurate results with a small L/H but start deviating from the reference 3D solution when the ratio of L/H is greater than 1.0.

To improve the accuracy and keep the computational efficiency of the two-dimensional method, Olson (2004) derived an approximate correction factor G to be included in 2D DDM that accounts for the three dimensional effects of limited-height fractures. This 3D approximation method is also used to calculate the fracture aperture development with increasing length for a fixed height and constant pressure fracture and compared with the fully 3D solution. Figure 4.7 illustrate that the two solutions are an almost perfect match. The computational cost of this method is exactly the same as 2D DDM because this method does not increase the size of coefficient matrix. However, this

method only can give accurate results for single 3-D crack problems and is limited to model multiple fractures and describe fracture interaction.

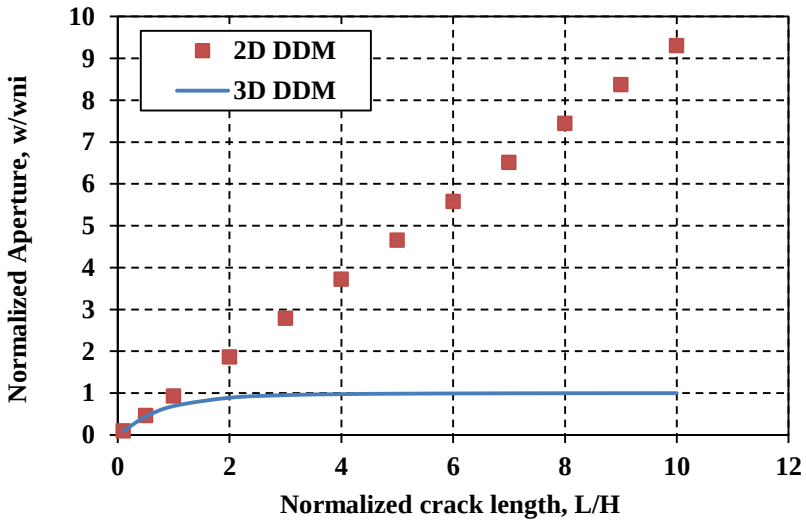

Figure 4.6: Normalized aperture vs. normalized length for non-interacting, isolated cracks of limited height and uniform internal pressure; Aperture is normalized by the results of the plane strain fracture with the fracture length much greater than the fracture height.

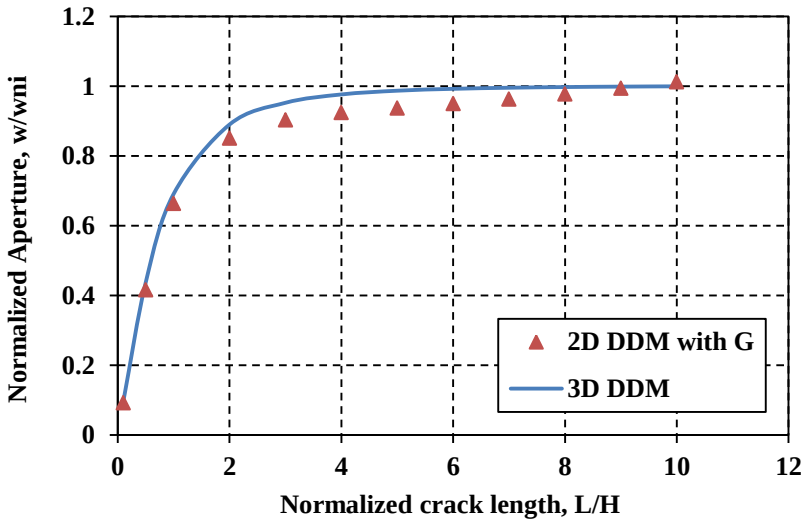

Figure 4.7: Normalized aperture vs. normalized length for non-interacting, isolated cracks of limited height and uniform internal pressure; Aperture is normalized by the results of the plane strain fracture with the fracture length much greater than the fracture height.

Figure 4.8 shows the impact of fracture interaction on fracture aperture for a 3 crack array with various spacing to height ratios, S/H. This calculation is for a three-dimensional fracture with $L/H = 4$. Fracture apertures are normalized by the aperture of a non-interaction, plane strain fracture of the same height (w_{ni}). Both exterior fractures have the same aperture due to symmetry, so only one curve is plotted for them. It is evident from the figure that the results from the 3D approximation method cannot match the fully 3D results (dashed and solid lines) at close spacing relative to fracture height because of the mechanical interaction. The aperture values can match the 3D solution when fracture spacing is three times greater than fracture height and the mechanical interaction is vanished.

Figure 4.9 demonstrates the dependence of mechanical interaction on fracture length for a 3 crack array with a normalized spacing of $S/H = 0.5$ and normalized lengths varying from $0.2 < L/H < 5.0$. The results are also normalized by the non-interacting

plane strain fracture of the same height and net pressure, so the general increase in aperture with increasing length reflects the increased compliance of a fixed height fracture as it grows in length. After a normalized length of L/H = 2 is reached, the mechanical interaction has nearly reached its maximum, and things don't change much for greater lengths. The figure further demonstrates that the aperture values given by the 3D approximation method cannot match the 3D solution, and this method underestimates the crack interaction between nearby cracks.

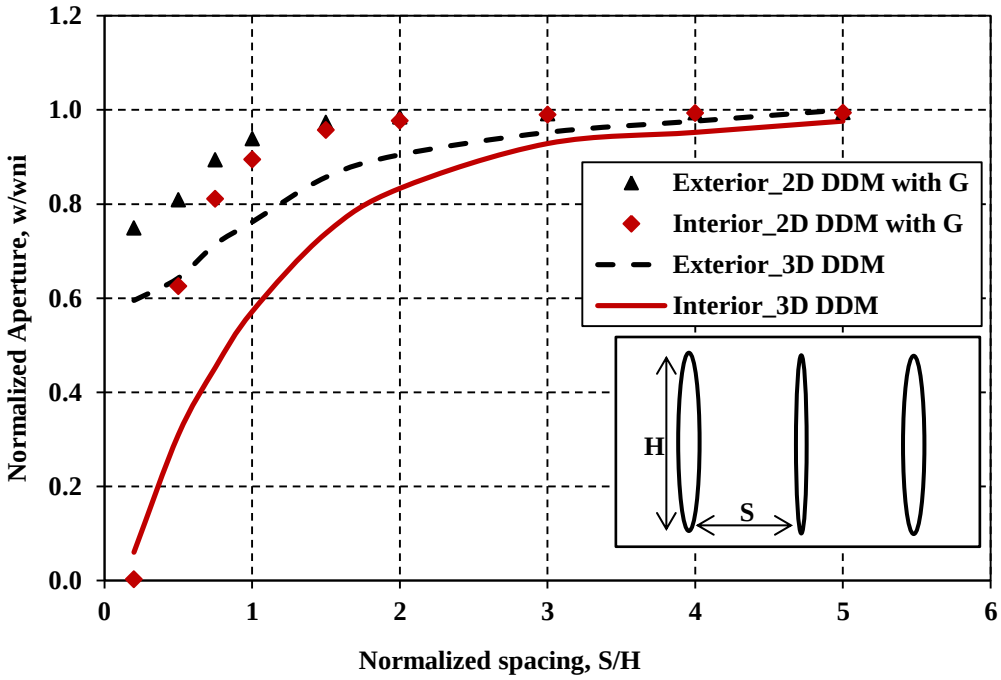

Figure 4.8: Normalized aperture vs. normalized spacing for a 3 crack array of parallel, equal length fractures (L/H = 4) with uniform internal pressure. Aperture is normalized by a non-interacting, isolated fracture of fixed height and uniform internal pressure.

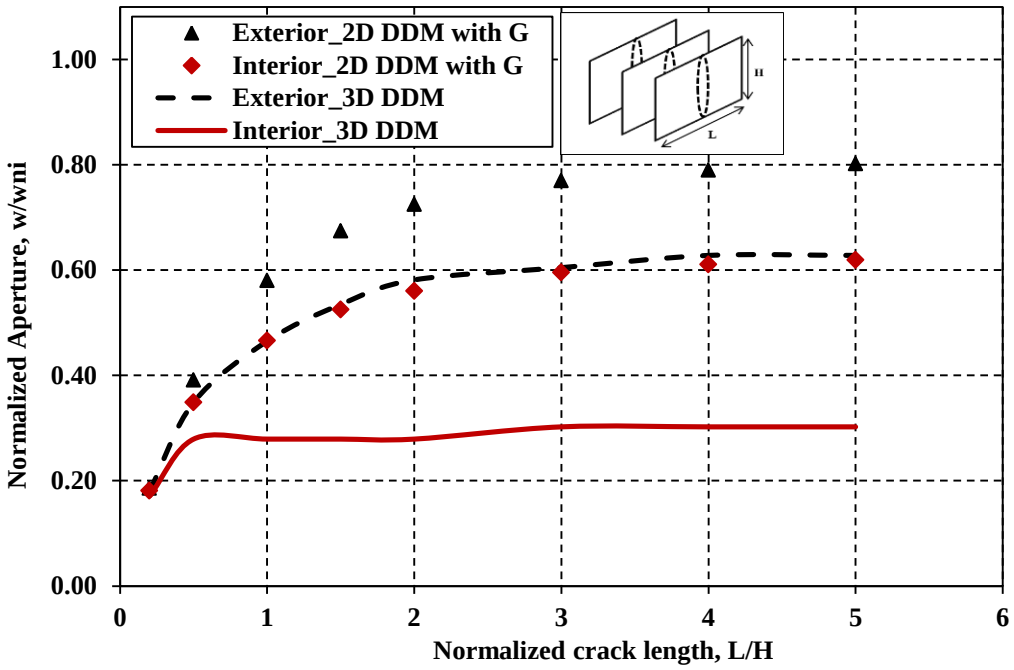

Figure 4.9: Normalized aperture vs. normalized length for a 3 crack array of parallel, equal length, uniformly pressurized fractures, with a normalized spacing of $S/H = 0.5$. Aperture is normalized by a non-interacting, isolated fracture of fixed height and uniform internal pressure.

2D DDM only has discretization in one direction, which we typically choose to be along the length for hydraulic fracturing. That means there is only one value for fracture width over the height. 3D DDM can improve on that be having discretization over both the length and height. Unfortunately, though, that means typically the 3D method will have more elements than the 2D method, and computation time is dependent on number of elements. Figure 4.10 shows this dependence of computation time with elements, indicating that for both the 2D and 3D methods, computation time increases with the square of element number. Thus, if using more elements, as would be expected in the 3D method, the computational cost will rise quickly. Another factor that is evident from Figure 4.10 is that the 3D equations are more complex, such that even for the same number of elements, the 3D method is still more than twenty times slower that the 2D

method. Although the 3D method can accurately solve fracture problems, excessive computational burden makes it hard to be widely used, particularly for multiple cracks. For other three-dimensional boundary element methods (Okada, 1985, 1992; Thomas, 1993), they also have very low computational efficiency, because these methods also require using more elements to discretize both the fracture height and length as expected in 3D DDM.

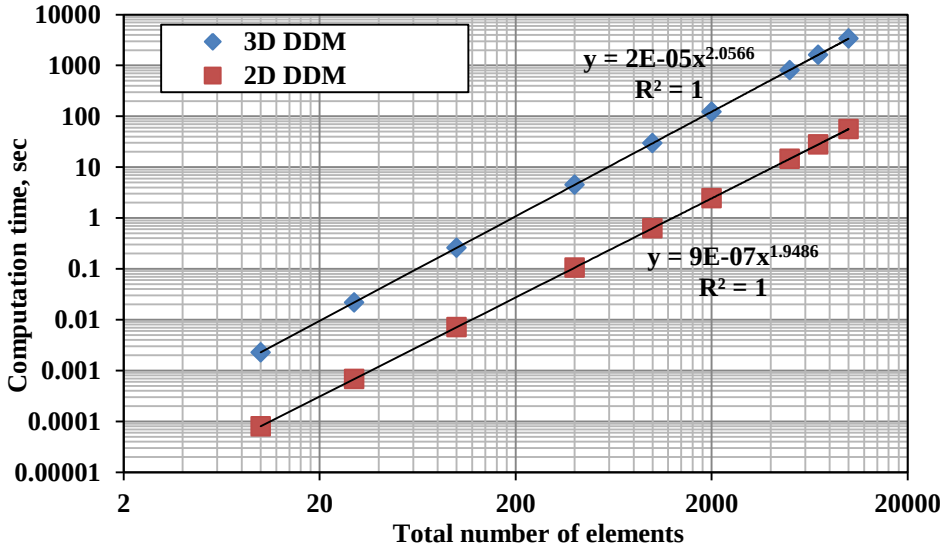

Figure 4.10: Computation time of 2D DDM and 3D DDM for different element number in the length direction.

If computational efficiency is important so that we can do large problems, two aspects require to be achieved. The first aspect is to reduce the number of extra elements that are inherent in the 3D method which is more similar to the discretization in 2D method. The second one is to simplify the 3D equations (neglect terms with small significance) so that they are more comparable in computational cost to the 2D solution. The challenge is to do this without sacrificing accuracy. Based on the fully 3D method,

we propose a new method and guarantee the accuracy with a smaller penalty in computation time.

4.3 Simplified Three-Dimensional Displacement Discontinuity Method (S3D DDM)

The standard approach in three-dimensional modeling utilizes a substantial number of elements in the height direction for the sake of accuracy. However, Olson (2004) demonstrated that a reasonable level of accuracy can be achieved using a pseudo-3D method having no discretization over the height (the 2D solution with a correction factor accounting for fracture height). The width value at any location along the length of the fracture represents the average width value for that location over the height. One drawback is that there is no information for computing stress intensity factor at the top or bottom of the fracture for height growth purposes, but knowing the average width of each element allows for accurate volumetric and mechanical interaction computations, which is sufficient if we are predominantly interested in the lateral propagation of a confined fracture. In this section, we follow Olson's method using only a single element in the height direction but derive our correction factor using the 3D model equations as our starting point. We also simplify the form of the base 3D equations by recognizing that for a problem with vertical fractures only, any stress component involving dip-silp shear can be ignored.

4.3.1 Formula derivation

In cases where the vertical stress is much greater than the horizontal stresses, fractures are likely to be restricted to vertical planes because the large vertical stress will prevent the crack from shearing in the dip-slip mode and suppress the curving out of

vertical plane. Thus, only two displacement discontinuities (D_1 and D_3, referred as to D_{sL} and D_n) are required to characterize the crack deformation, D_2 (D_{sH}) can be ignored. This simplification reduces the number of unknown variables from 3N to 2N. If we could also eliminate the discretization along the height direction (i.e., the element dimension in the dip direction is 1), we should be able to make the computation time more comparable to the faster 2D model. Based on the assumptions, normal and shear stresses from Eqs.4.13 can be simplified as

$$\begin{aligned}
\sigma_{11} &= C_{11}C_r D_1[2I_{,11} - x_3 I_{,111}] + C_{11}C_r D_3[I_{,33} + (1-2\nu)I_{,22} - x_3 I_{,311}] \\
\sigma_{33} &= C_{11}C_r D_1[-x_3 I_{,133}] + C_{11}C_r D_3[I_{,33} - x_3 I_{,333}] \\
\sigma_{22} &= C_{11}C_r D_1[2\nu I_{,13} - x_3 I_{,122}] + C_{11}C_r D_3[I_{,33} + (1-2\nu)I_{,11} - x_3 I_{,322}] \\
\sigma_{13} &= C_{13}C_r D_1[I_{,33} + \nu I_{,22} - x_3 I_{,113}] + C_{13}C_r D_3[-x_3 I_{,313}] \\
\sigma_{21} &= C_r D_1[(1-\nu)I_{,23} - x_3 I_{,112}] + C_r D_3[-(1-2\nu)I_{,12} - x_3 I_{,312}] \\
\sigma_{23} &= C_r D_1[-\nu I_{,21} - x_3 I_{,123}] + C_r D_3[-x_3 I_{,323}]
\end{aligned} \quad . \tag{4.38}$$

Note that two terms, C_{11} and C_{13}, have been added to the equations as correction factors to account for the lack of discretization in the height direction. Following the method of Olson (2004), C_{11} and C_{13} were based on the analytical expression for the normal and shear stress induced by a uniformly loaded plane strain crack as described by Pollard and Segall (1987)

$$\sigma_{11} = \nu(-2\Delta\sigma_I[(\left|x_3^3\right|(a^2 + x_3^2)^{-3/2} - 1) + \left|x_3\right| a^2 (a^2 + x_3^2)^{-3/2}]), \tag{4.39}$$

$$\sigma_{33} = -\Delta\sigma_I[\left|x_3^3\right|(a^2 + x_3^2)^{-3/2} - 1], \tag{4.40}$$

where σ_{11}, σ_{33} are induced stresses along the line $x_1 = 0$ and $|x_3| \geq 0$ in the x_1-x_3 plane, ν is poission's ratio, a is half-height in x_2 direction (H/2) (Figure 4.11). The key elements of these equations are spatial geometry terms involving x_3, the perpendicular distance away from the crack center, and a, the crack half-length. Following the method of Olson (2004), we recast x_3 as radial distance between centers of elements, D, and introduce

adjustable exponents for the powers in the analytical solution. Combining all these concepts, C_{11} and C_{13} can be written as

$$\begin{aligned} C_{11} &= 1 - \frac{D^{\beta_1}(H/\alpha)^{\beta_2}}{(D^2+(H/\alpha)^2)^{(\beta_1+\beta_2)/2}} \quad (\beta_1 = 1.5 \quad \beta_2 = 4 \quad \alpha = 1) \\ C_{13} &= 1 - \frac{D^{\beta_1}(H/\alpha)^{\beta_2}}{(D^2+(H/\alpha)^2)^{(\beta_1+\beta_2)/2}} \quad (\beta_1 = 1.8 \quad \beta_2 = 4 \quad \alpha = 1) \end{aligned} \quad , \tag{4.41}$$

where β_1, β_2 and α are adjustable parameters. Values of coefficients are empirically determined through comparing to the fully 3D solution.

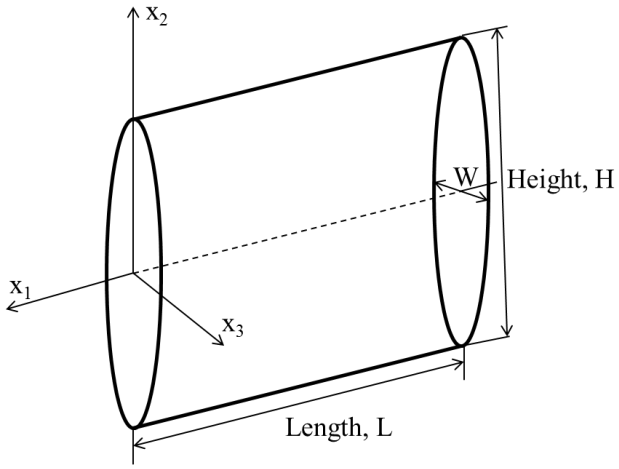

Figure 4.11: Idealized sketch of a crack where length in the x_1 direction is much larger than length in the x_2, x_3 directions.

4.3.2 Numerical implementation

Based on the analytical solution (Eqs. 4.38), similar to the numerical implementation described in the section 4.2.2, displacement discontinuities and stress field for a crack can be calculated.

Displacement Discontinuity calculation

To solve displacement discontinuities for a crack with N elements (Figure 4.11), we can simplify Eqs. 20 and 22 as

$$
\begin{aligned}
\overset{i}{\sigma}_{sL} &= C_r(-C_{11}\sin\gamma\cos\gamma[2\overset{ij}{J}_8 - x_3\overset{ij}{J}_{10}] + \\
&C_{13}\cos 2\gamma[\overset{ij}{J}_6 + \nu\overset{ij}{J}_5 - x_3\overset{ij}{J}_{12}] + C_{11}\sin\gamma\cos\gamma[-x_3\overset{ij}{J}_{16}])\overset{j}{D}_{sL} \\
&+C_r(-C_{11}\sin\gamma\cos\gamma[\overset{ij}{J}_6 + (1-2\nu)\overset{ij}{J}_5 - x_3\overset{ij}{J}_{12}] + \\
&C_{13}\cos 2\gamma[-x_3\overset{ij}{J}_{16}] + C_{11}\sin\gamma\cos\gamma[\overset{ij}{J}_6 - x_3\overset{ij}{J}_{18}])\overset{j}{D}_n \\
\overset{i}{\sigma}_{nn} &= C_r(C_{11}\sin^2\gamma[2\overset{ij}{J}_8 - x_3\overset{ij}{J}_{10}] - \\
&2C_{13}\sin\gamma\cos\gamma[\overset{ij}{J}_6 + \nu\overset{ij}{J}_5 - x_3\overset{ij}{J}_{12}] + C_{11}\cos^2\gamma[-x_3\overset{ij}{J}_{16}])\overset{j}{D}_{sL} \\
&+C_r(C_{11}\sin^2\gamma[\overset{ij}{J}_6 + (1-2\nu)\overset{ij}{J}_5 - x_3\overset{ij}{J}_{12}] - \\
&2\,C_{13}\sin\gamma\cos\gamma[-x_3\overset{ij}{J}_{16}] + C_{11}\cos^2\gamma[\overset{ij}{J}_6 - x_3\overset{ij}{J}_{18}])\overset{j}{D}_n
\end{aligned}
\quad . \qquad (4.42)\ (4.43)
$$

These equations can then be arranged in the summation presented in Eq. 4.23. Hence, the total induced stresses at the midpoint of the element *i* are as follows:

$$
\begin{aligned}
\overset{i}{\sigma}_{sL} &= \sum_{j=1}^{N}\overset{ij}{A}_{sL,sL}\overset{j}{D}_{sL} + \sum_{j=1}^{N}\overset{ij}{A}_{sL,nn}\overset{j}{D}_n \\
\overset{i}{\sigma}_{nn} &= \sum_{j=1}^{N}\overset{ij}{A}_{nn,sL}\overset{j}{D}_{sL} + \sum_{j=1}^{N}\overset{ij}{A}_{nn,nn}\overset{j}{D}_n
\end{aligned}
\quad , \qquad (4.44)
$$

Where $\overset{i}{\sigma}_{sL}$, $\overset{i}{\sigma}_{nn}$ are the shear and normal boundary stresses on the element *i*, $\overset{ij}{A}_{sL,sL}$, are also the boundary influence coefficients. Similar to Eq. 4.24, the unknown displacement discontinuity components can be solved by the system of 2*N* linear algebraic equations,

$$
\begin{bmatrix}
\overset{11}{A}_{sL,sL} & \cdots & \overset{1N}{A}_{sL,sL} & \overset{11}{A}_{sL,sH} & \cdots & \overset{1N}{A}_{sL,sH} & \overset{11}{A}_{sL,nn} & \cdots & \overset{1N}{A}_{sL,nn} \\
\vdots & & & & & & & & \\
\overset{N1}{A}_{sL,sL} & \cdots & \overset{NN}{A}_{sL,sL} & \overset{N1}{A}_{sL,sH} & \cdots & \overset{NN}{A}_{sL,sH} & \overset{N1}{A}_{sL,nn} & \cdots & \overset{NN}{A}_{sL,nn} \\
\overset{11}{A}_{nn,sL} & \cdots & \overset{1N}{A}_{nn,sL} & \overset{11}{A}_{nn,sH} & \cdots & \overset{1N}{A}_{nn,sH} & \overset{11}{A}_{nn,nn} & \cdots & \overset{1N}{A}_{nn,nn} \\
\vdots & & & & & & & & \\
\overset{N1}{A}_{nn,sL} & \cdots & \overset{NN}{A}_{nn,sL} & \overset{N1}{A}_{nn,sH} & \cdots & \overset{NN}{A}_{nn,sH} & \overset{N1}{A}_{nn,nn} & \cdots & \overset{NN}{A}_{nn,nn}
\end{bmatrix}
\begin{bmatrix}
\overset{1}{D}_{sL} \\ \vdots \\ \overset{N}{D}_{sL} \\ \overset{1}{D}_n \\ \vdots \\ \overset{N}{D}_n
\end{bmatrix}
=
\begin{bmatrix}
\overset{1}{\sigma}_{sL} \\ \vdots \\ \overset{N}{\sigma}_{sL} \\ \overset{1}{\sigma}_n \\ \vdots \\ \overset{N}{\sigma}_n
\end{bmatrix}
. \qquad (4.45)
$$

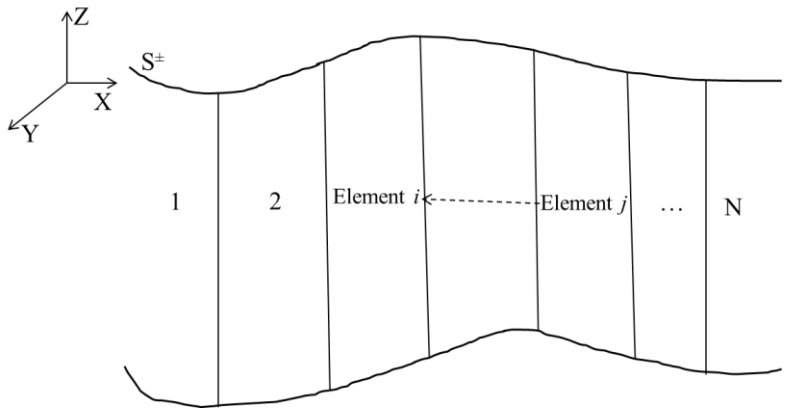

Figure 4.12: Boundary elements on a fracture of interest.

Stress field Calculation

Similarly, stresses at any point (e.g. Point *P*) in the body can be calculated by summing the induced stresses of all elements together. The stress calculation equations 4.31 to 4.34 can be rewritten as

$$\overset{P}{\sigma}_{XX} = C_r(C_{11}\cos^2\overset{j}{\beta}[2\overset{Pj}{J}_8 - x_3\overset{Pj}{J}_{10}] - C_{13}\sin 2\overset{j}{\beta}[\overset{Pj}{J}_6 + v\overset{Pj}{J}_5 - x_3\overset{Pj}{J}_{12}] + C_{11}\sin^2\overset{j}{\beta}[-x_3\overset{Pj}{J}_{16}])\overset{j}{D}_{sL}$$
$$+C_r(C_{11}\cos^2\overset{j}{\beta}[\overset{Pj}{J}_6 + (1-2v)\overset{Pj}{J}_5 - x_3\overset{Pj}{J}_{12}] - C_{13}\sin 2\overset{j}{\beta}[-x_3\overset{Pj}{J}_{16}] + C_{11}\sin^2\overset{j}{\beta}[\overset{Pj}{J}_6 - x_3\overset{Pj}{J}_{18}])\overset{j}{D}_n$$

…… (4.46)

$$\overset{P}{\sigma}_{YY} = C_r(C_{11}\sin^2\overset{j}{\beta}[2\overset{Pj}{J}_8 - x_3\overset{Pj}{J}_{10}] + C_{13}\sin 2\overset{j}{\beta}[\overset{Pj}{J}_6 + v\overset{Pj}{J}_5 - x_3\overset{Pj}{J}_{12}] + C_{11}\cos^2\overset{j}{\beta}[-x_3\overset{Pj}{J}_{16}])\overset{j}{D}_{sL}$$
$$+C_r(C_{11}\sin^2\overset{j}{\beta}[\overset{Pj}{J}_6 + (1-2v)\overset{Pj}{J}_5 - x_3\overset{Pj}{J}_{12}] + C_{13}\sin 2\overset{j}{\beta}[-x_3\overset{Pj}{J}_{16}] + C_{11}\cos^2\overset{j}{\beta}[\overset{Pj}{J}_6 - x_3\overset{Pj}{J}_{18}])\overset{j}{D}_n$$

…… (4.47)

$$\overset{P}{\sigma}_{ZZ} = C_rC_{11}[2v\overset{Pj}{J}_8 - x_3\overset{Pj}{J}_{13}]\overset{j}{D}_{sL} + C_rC_{11}[\overset{Pj}{J}_6 + (1-2v)\overset{Pj}{J}_4 - x_3\overset{Pj}{J}_{15}]\overset{j}{D}_n \qquad (4.48)$$

$$\overset{P}{\sigma}_{XY} = C_r(C_{11}\sin\overset{j}{\beta}\cos\overset{j}{\beta}[2\overset{Pj}{J}_8 - x_3\overset{Pj}{J}_{10}] + C_{13}\cos 2\overset{j}{\beta}[\overset{Pj}{J}_6 + v\overset{Pj}{J}_5 - x_3\overset{Pj}{J}_{12}] - C_{11}\sin\overset{j}{\beta}\cos\overset{j}{\beta}[-x_3\overset{Pj}{J}_{16}])\overset{j}{D}_{sL}$$
$$+C_r(C_{11}\sin\overset{j}{\beta}\cos\overset{j}{\beta}[\overset{Pj}{J}_6 + (1-2v)\overset{Pj}{J}_5 - x_3\overset{Pj}{J}_{12}] + C_{13}\cos 2\overset{j}{\beta}[-x_3\overset{Pj}{J}_{16}] - C_{11}\sin\overset{j}{\beta}\cos\overset{j}{\beta}[\overset{Pj}{J}_6 - x_3\overset{Pj}{J}_{18}])\overset{j}{D}_n$$

…… (4.49)

Total induced stresses at the point P can be calculated by

$$\begin{aligned}
\sigma_{XX}^{P} &= \sum_{j=1}^{N} F_{XX,sL}^{Pj} D_{sL}^{j} + \sum_{j=1}^{N} F_{XX,nn}^{Pj} D_{n}^{j} \\
\sigma_{YY}^{P} &= \sum_{j=1}^{N} F_{YY,sL}^{Pj} D_{sL}^{j} + \sum_{j=1}^{N} F_{YY,nn}^{Pj} D_{n}^{j} \\
\sigma_{ZZ}^{P} &= \sum_{j=1}^{N} F_{ZZ,sL}^{Pj} D_{sL}^{j} + \sum_{j=1}^{N} F_{ZZ,nn}^{Pj} D_{n}^{j} \\
\sigma_{XY}^{P} &= \sum_{j=1}^{N} F_{XY,sL}^{Pj} D_{sL}^{j} + \sum_{j=1}^{N} F_{XY,nn}^{Pj} D_{n}^{j}
\end{aligned} , \tag{4.50}$$

where $F_{XX,sL}^{Pj}$ are also the influence coefficients.

4.4 CONCLUSIONS

In this chapter, derivation of the fully 3D method was presented for calculating displacement discontinuities and stress field of vertical fractures. The excessive computational burden prevents the 3D method from widely applied. The two dimensional method only can efficiently and accurately solve fracture problems of two-dimensional plane strain. A 3D approximation correction factor proposed by Olson (2004) was incorporated into the 2D method to account for three-dimensional effect of a limited-height fracture. However, this correction factor is inadequate for describing fracture interaction. A simplified three-dimensional method was derived following Olson's method but based on the 3D model. The simplified 3D method consequently only considers mode I and II loading and improves the accuracy of the crack-induced stresses given there is only 1 row of elements with respect to crack height (along the x_2 direction). The method sacrifices displacement discontinuities in the height dimension of cracks to greatly reduce computation burden. This method can accurately and efficiently solve 3D

multiple fracture problems and model fracture interaction. The validation and application of this method will be discussed in next chapter.

CHAPTER 5: APPLICATION OF SIMPLIFIED THREE-DIMENSIONAL DISPLACEMENT DISCONTINUITY METHOD (S3D DDM)

In the Chapter 4, a Simplified Three-Dimensional Displacement Discontinuity Method (S3D DDM) is proposed to solve rock deformation for hydraulic fracture propagation with high computational efficiency and reasonable accuracy. This chapter is dedicated to the application of this method and primarily has two objectives. The first objective is to use the method to describe rock deformation for stationary cracks with constant internal pressure and test the mathematical accuracy of S3D DDM. The second objective is to use our complex hydraulic fracture development model (Chapter 2) to analyze the physical mechanisms of simultaneous multiple fracture propagation through incorporating S3D DDM into the model for calculating rock deformation induced by fluid pressure within the fracture, replacing the pseudo-three-dimensional model given in Section 2.2.1.

5.1 INTRODUCTION

Simultaneous multiple fracture treatments in horizontal wellbores are becoming a prevalent approach to economically develop shale reservoirs. A better understanding of the mechanisms of simultaneous multiple fracture growth is essential for accurately predicting fracture geometry. To properly predict multiple fracture geometry, most work in the literature has focused on the discussion of fracture mechanical interaction, also referred to as stress shadow effects, between multiple fractures (Warpinski and Teufel, 1987; Britt and Smitt, 2009; Olson, 2008; Cheng, 2009; Meyer and Bazan, 2011; Roussel and Sharma, 2011; Wu et al., 2012). When a facture is opened by injected fluid, it exerts additional stresses on the surrounding rock. The additional stresses are proportional to the net pressure within the fracture (fluid pressure minus closure stress normal to the fracture surface) and gradually decay with the distance from the fracture. At a distance greater than one fracture height, the additional stresses are only a small fraction of the net pressure (Warpinski and Branagan, 1989). If multiple fractures are closely spaced within the region of stress shadow influence, non-planar fracture geometry and width restriction might be induced, as discussed in Chapter 3.

For simultaneous multiple fracture propagation, the fluid rate distribution into the fractures is a dynamic process and is dependent on the resistance to flow within the fractures. In addition, the fractures are part of the same pressure system connected through the horizontal wellbore. Pressure equilibrium in the horizontal wellbore must be maintained as discussed in Chapter 2. Fluid pressure slightly decreases along the horizontal wellbore from one injection point to another injection point and the pressure declines within the fracture from injection point to the fracture tip. Fluid pressure drop within the fracture is a function of fracture width, and the width is affected by the net pressure and stress shadow effects. Hence, the flow distribution through horizontal

wellbore and into the fractures must be accounted for and fluid mechanics is an important parameter affecting simultaneous multiple fracture propagation. As shown in chapter 2, the two processes (fluid and solid mechanics) must be coupled to get a complete solution.

5.2 APPLICATION TO STATIONARY CRACKS

5.2.1 A single crack

Two different geometries of isolated cracks are chosen in order to examine how deformation changes from two-dimensional plane strain to a true three dimensional case. In both cases the fracture length is 400 ft but the height is varied between 100 ft and 4000 ft (Figure 5.1). The crack with 4000 ft height can be assumed as a plane strain problem because the crack height is much larger than the crack length. The net pressure of these two different geometry cases are specified at 290 psi and the minimum horizontal stress is 5809 psi, listed in Table 5.1. The cracks are perpendicular to the minimum horizontal stress. The analytical solution for the normal and shear displacement discontinuities (D_n and D_s, respectively) for a planar, uniformly loaded, plane strain crack is (Pollard and Segall, 1987)

$$\begin{Bmatrix} D_n \\ D_s \end{Bmatrix} = \begin{Bmatrix} \sigma_{33}^c - \sigma_{33}^r \\ (\sigma_{13}^c - \sigma_{13}^r) \end{Bmatrix} \frac{2(1-\nu)}{G} (a^2 - x_2^2)^{1/2}, \tag{5.1}$$

where $\sigma_{33}{}^r$ is the minimum horizontal stress acting perpendicular to the crack, $\sigma_{13}{}^r$ is shear stress in the remote stress field (no remote shear stress in this case), $\sigma_{33}{}^c$ and $\sigma_{13}{}^c$ are the normal and shear loads on the crack faces, G is the shear modulus, ν is Poisson's ratio, and a is the half-crack length.

Crack height	100 ft
Crack length	400 ft
Minimum horizontal stress	5806 psi
Maximum horizontal stress	7257 psi
Internal uniform normal stress	6096 psi
Internal shear stress	73 psi
Young's Modulus	4.0×10^{6} psi
Poisson's ratio	0.25

Table 5.1: Input parameters for case study of stationary cracks.

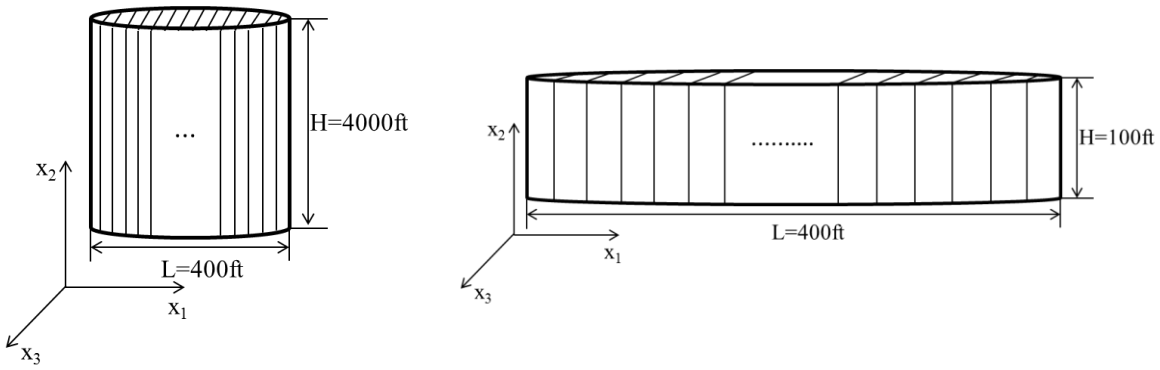

(a) (b)

Figure 5.1: A single crack with 100 ft height (a) and 4000 ft height (b) in infinite rock formation.

Figure 5.2 shows relative errors of different element numbers discretized in the fracture height direction for the fully 3D method. It is evident from the figure that discretizing 11 elements in the height direction is sufficient to obtain accurate results, while no discretization in the height direction would bring about 50% error of results.

Normal and shear displacement discontinuities for the plane strain crack and the crack with 100 ft limited height are plotted in Figures 5.3 and 5.4 along with analytical values and results from the fully 3D method with 11 height elements and 1 height element, respectively. From Figure 5.3, it is observed that numerical results from S3D DDM are very close to the analytical solution for the plane strain crack (Figure 5.1(a)). Also, it is evident from Figure 5.4 that the simplified 3D method gives very similar displacement discontinuities for the 3-D crack shown in Figure 5.1(b) with the fully 3D method with 11 height elements. The fully 3D method with only 1 element in the height direction gives too large displacement discontinuities, which again demonstrates that correction factors are required to account for no discretization in the height direction. Figure 5.5 illustrates aperture development with increasing length of cracks with 100 ft limited height. In this chapter, the term 'aperture' refers to the crack normal displacement discontinuity at the center. Crack aperture increases roughly linearly with length at $L/H \leq 0.5$, but grows more slowly after that. At $L/H = 4$, the curves is almost flat, and the aperture almost reaches 100% of plane strain amount at $L/H = 5$. Figures 5.3 through 5.5 show that the displacement discontinuities given by S3D DDM agree well with the results from the fully 3D method as well as with the analytical solution for the plane strain problems.

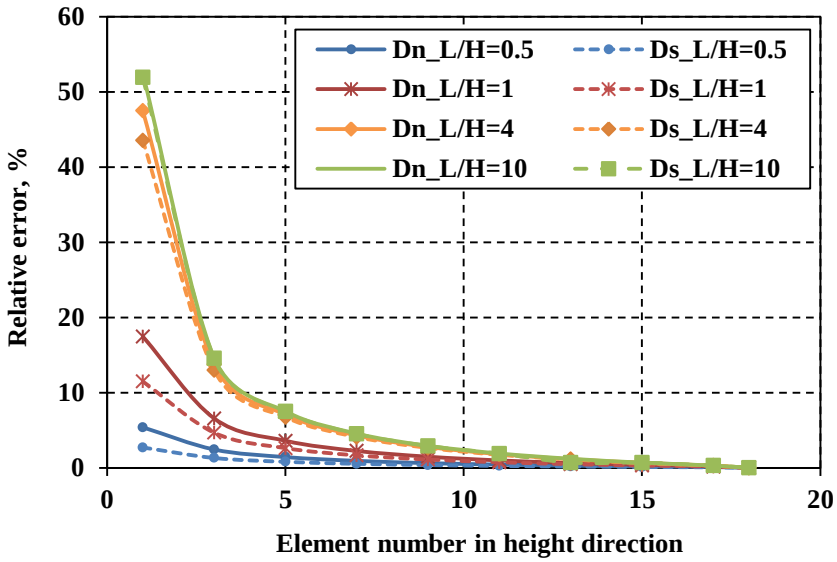

Figure 5.2: Relative error of normal and shear displacement discontinuities with different element number in the height direction for cracks with various lengths.

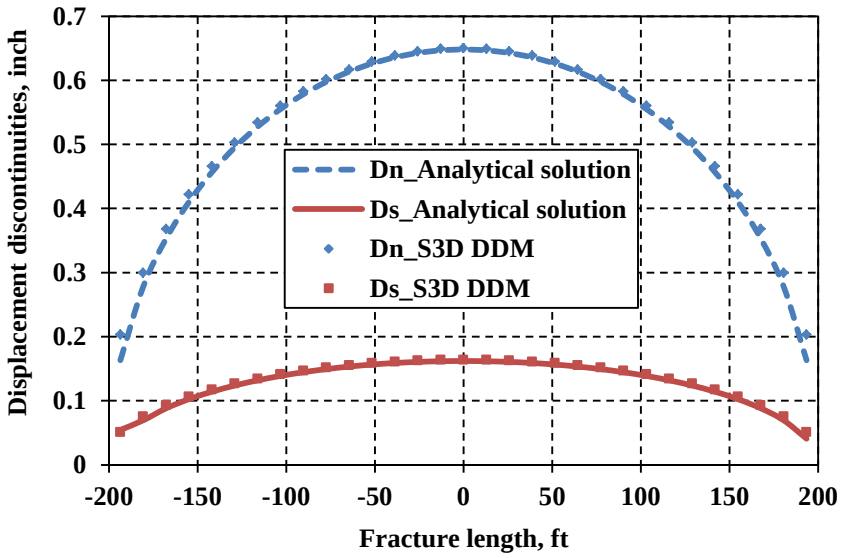

Figure 5.3: Normal and shear displacement discontinuities vs. length for the plane strain crack (Figure 5.2(a)).

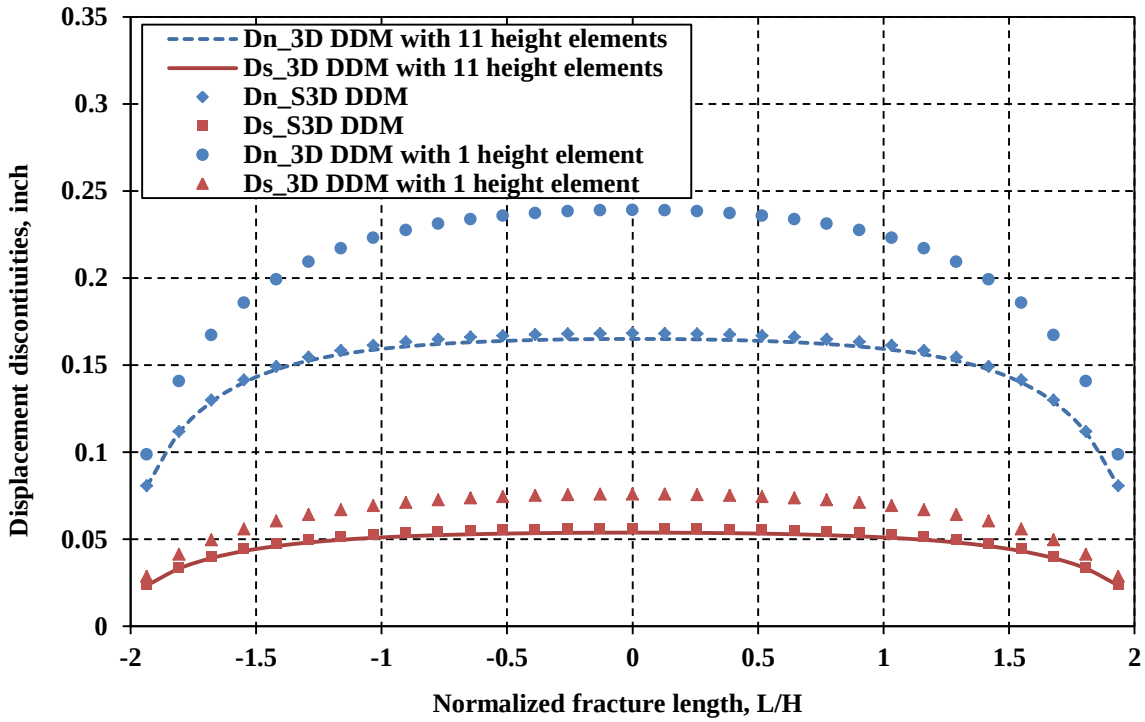

Figure 5.4: Normal and shear displacement discontinuities vs. normalized length for a non-interacting, isolated fracture of limited height and uniform internal pressure (Figure 5.2(b)).

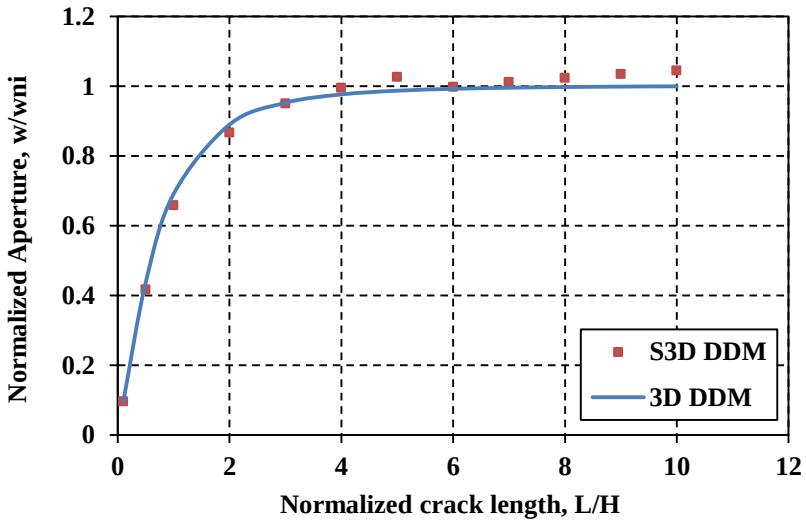

Figure 5.5: Normalized aperture vs. normalized length for non-interacting, isolated cracks of limited height and uniform internal pressure; aperture is normalized by the results of plane strain cracks.

The non-interacting, isolated crack with limited height is supported by internal load on crack faces. The medium around the opening crack is squeezed, and additional compression is imposed on the surrounding medium and vanishes gradually away from the crack. The crack is normal to the minimum horizontal principal stress, and the maximum value of crack-induced stresses is the difference between the internal load and the minimum horizontal stress. We focus our attention on the (x_1-x_3) plane (Figure 5.1) and investigate crack-induced stresses on this plane. Figure 5.6 illustrates crack-induced normal and shear stresses along the line $x_1 = 0$ and $x_3 \geq 0$, displaying that induced stresses calculated by the simplified 3D method have small deviation from the results provided by the fully 3D method when very close to the crack. Overall, S3D DDM gives a reasonably accurate approximation of the crack-induced stresses as compared to the fully 3D method.

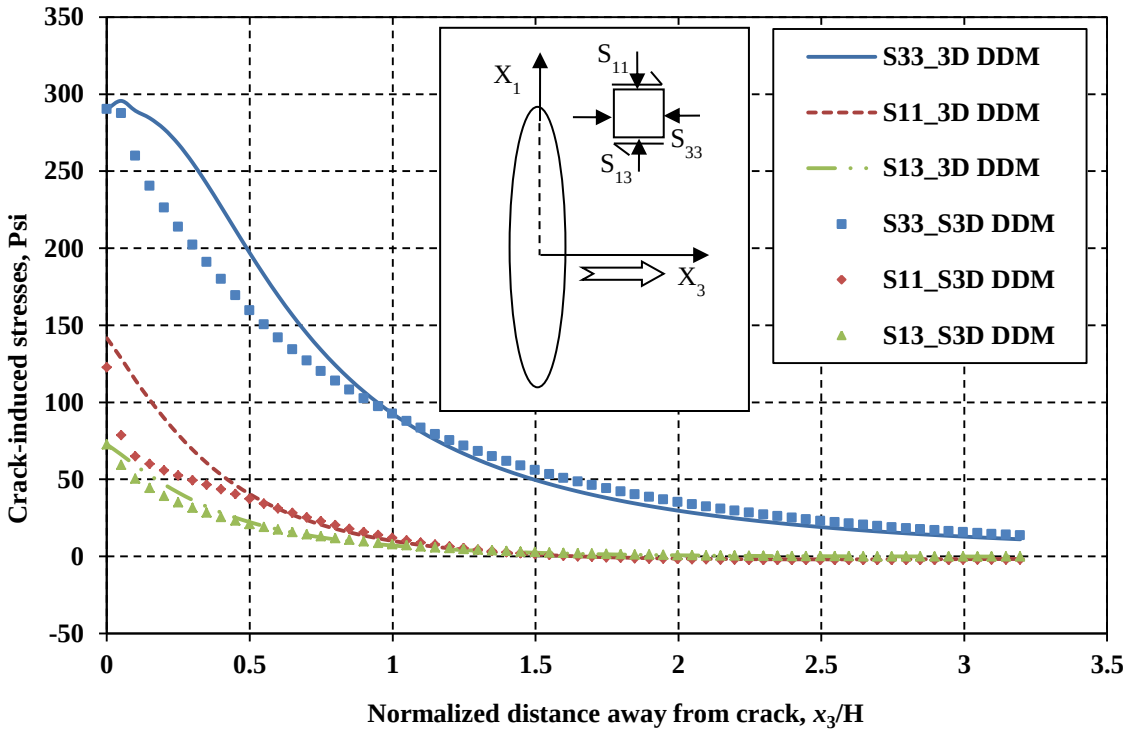

Figure 5.6: Crack-induced stress components vs. normalized distance, x_3/H.

Figures 5.3 through 5.6 show that S3D DDM can guarantee accuracy of modeling 3-D cracks. The computational time of S3D DDM and the fully 3D method are illustrated in Figure 5.7, which shows that the simplified 3D method is about seven times faster than the fully 3D method for the same number of elements (e.g. 2000). The computational time of the simplified 3D method increases with the number of elements to the power of 1.9, while the power coefficient of the fully 3D method is 2, which implies that the computational time for the fully 3D method will increase faster with the increasing number of elements. Furthermore, the simplified 3D method reduces the number of elements in 3D problems to the same number as required for the 2D method through having only one element in the height direction, which makes an additional, significant difference in computation time. Hence, combining these two enhancements of

computational time, for solving the same 3D problems, the simplified 3D method will be much faster than the fully 3D method to obtain the same level of accuracy. Computational time of S3D DDM and 3D DDM with 11 height elements with various element numbers in the fracture length direction are illustrated in Figure 5.8, which shows that S3D DDM is almost 10^3 times faster than 3D DDM with 11 height elements.

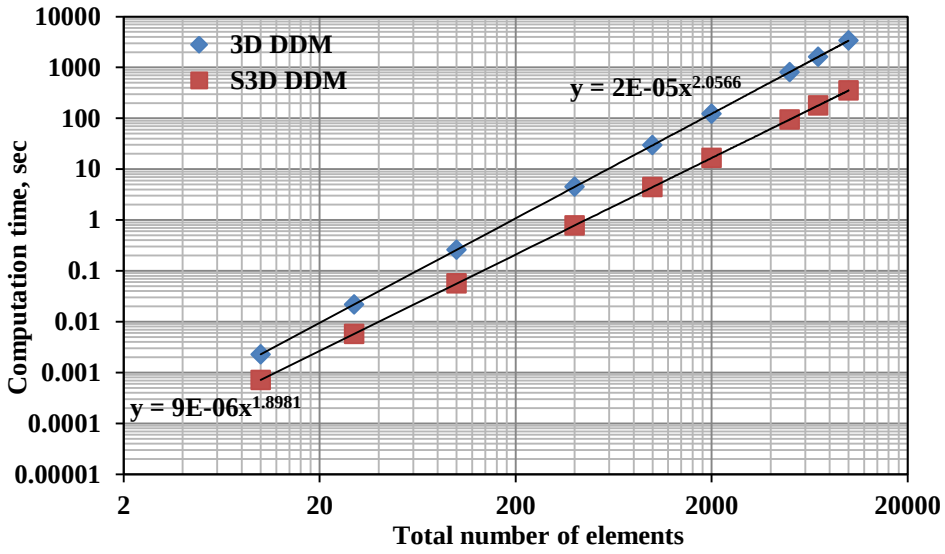

Figure 5.7: Calculation time vs. increasing element number in crack length direction for a non-interacting, isolated crack.

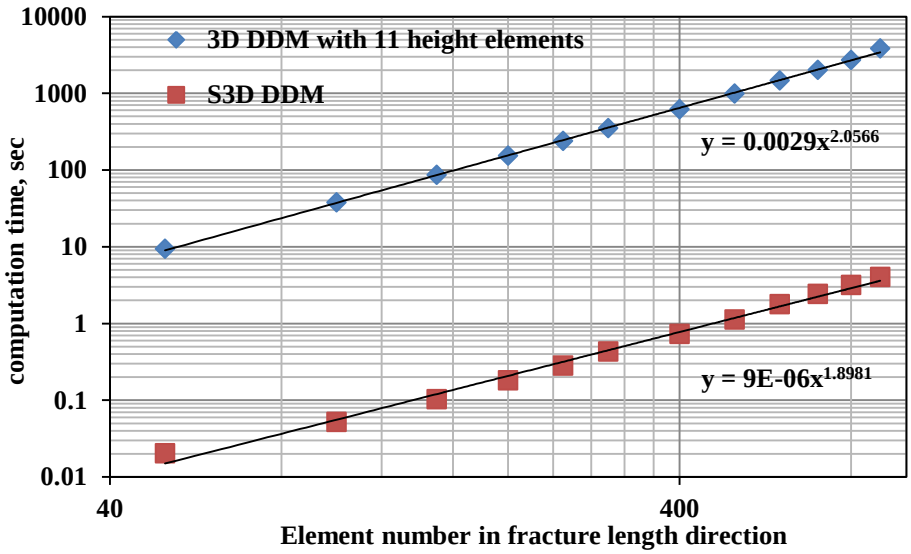

Figure 5.8: Calculation time vs. increasing element number in the fracture length direction for a non-interacting, isolated fracture.

5.2.2 Multiple cracks

Multiple parallel cracks interact with each other within certain crack spacing as a result from crack induced stresses. We ran three different cases to demonstrate that S3D DDM is able to describe fracture interaction and is also applicable for multiple 3-D cracks. The input parameters for the three cases are from Table 5.1. For multiple cracks, we assume no shear internal stress.

Figure 5.9 illustrates en echelon cracks spaced 50 ft apart (half of crack height) in an infinite elastic medium with uniform internal pressure. As the two cracks are symmetrical, Figure 5.10 shows shear and normal displacement discontinuities for only one crack and compares them with the results calculated by the fully 3D method. The wing with non-planar geometry has smaller normal displacement discontinuity and larger shear displacement discontinuity compared with the planar wing due to mechanical

interaction between two fractures. Figure 5.10 demonstrates that S3D DDM can accurately calculate displacement discontinuities for multiple non-planar fractures.

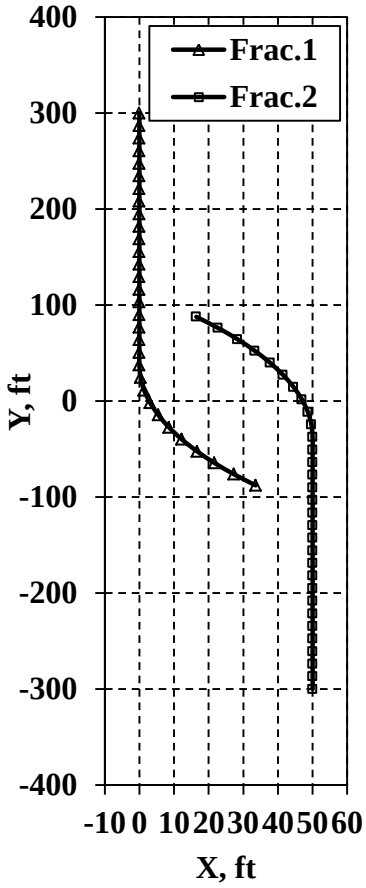

Figure 5.9: Geometry of en echelon cracks.

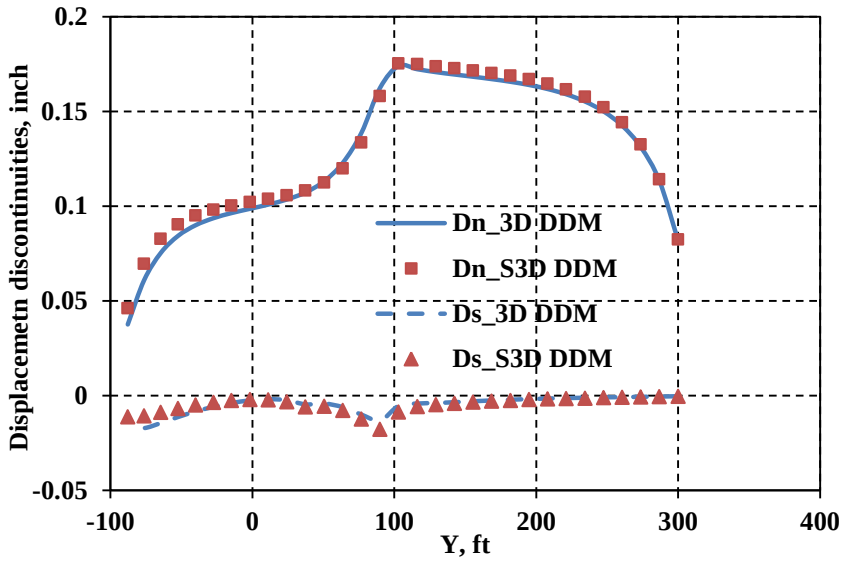

Figure 5.10: Crack displacement discontinuities of frac.1 along Y axis for en echelon cracks with uniform internal pressure.

Next, a case of three parallel cracks is simulated (Figure 5.11). Since the problem is symmetrical, only displacement discontinuities of one exterior crack are plotted. The normal displacement discontinuity of the cracks calculated by the fully 3D method and the simplified 3D method are illustrated in Figure 5.12, which shows that the fully 3D method and the simplified 3D method give very similar results.

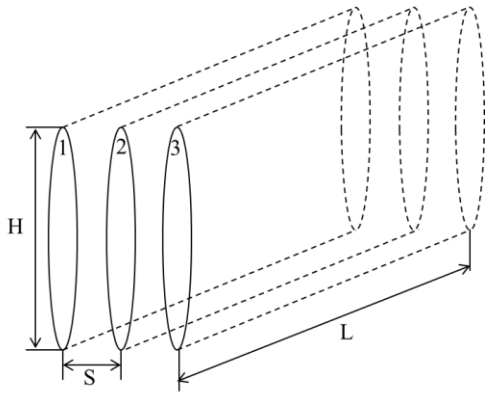

Figure 5.11: Three parallel cracks in an infinite elastic medium (S/H = 0.5, L/H = 4).

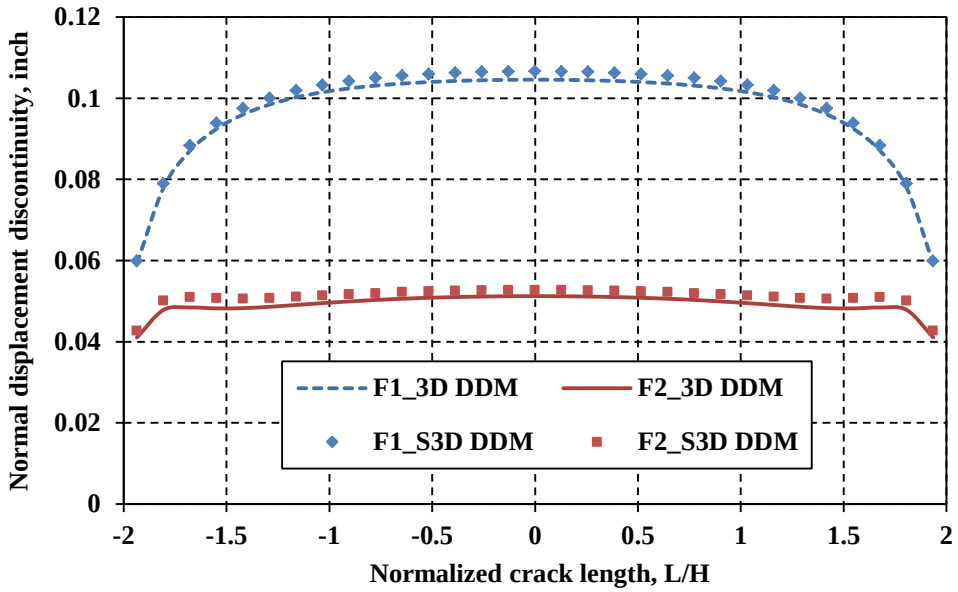

Figure 5.12: Crack normal displacement discontinuities vs. normalized length for three parallel cracks of limited height and $S/H = 0.5$.

Following the approach of analyzing fracture interaction in Wu and Olson (2013), the impact of fracture interaction on fracture aperture for the three fractures (Figure 5.11) given by the fully 3D method and the simplified 3D method is shown Figure 5.13. Spacing to height ratios, S/H, vary from 0.5 to 2. Fracture apertures are normalized by the aperture of a non-interacting crack of the same height and length (w_{ni}). The results given by the simplified 3D method (filled symbols) match exactly except for the very closest spaced interior fracture widths ($S/H < 0.2$). It is evident from the figure that both the interior and exterior fractures in an evenly spaced array of parallel fractures will lose width due to mechanical interaction at close spacing relative to fracture height. At a normalized spacing of $S/H = 2$ or greater, the effect is minimal, but at $S/H = 0.5$, for instance, the exterior fracture width is only 65% of the non-interacting case, and the interior fracture width is only 30% of the reference.

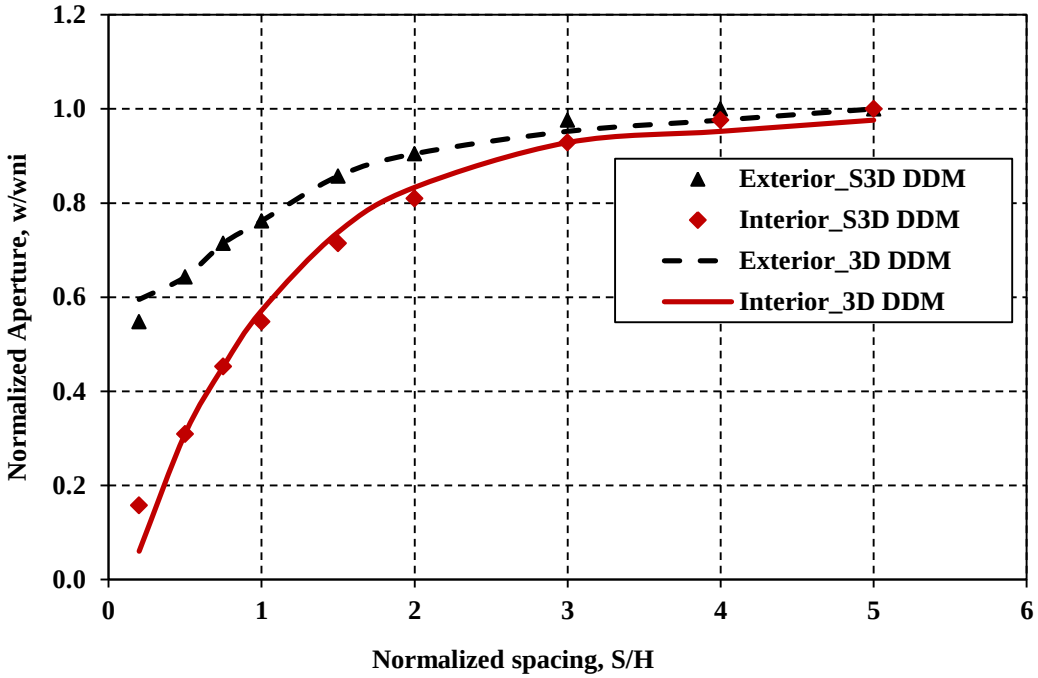

Figure 5.13: Normalized aperture vs. normalized spacing for a 3 fracture array of parallel, equal length fractures (L/H = 4) with uniform internal pressure. Aperture is normalized by a non-interacting, isolated fracture of fixed height and uniform internal pressure.

Figure 5.14 demonstrates this dependence of mechanical interaction on fracture length for the three fractures (Figure 5.9). Normalized length, L/H, is varied from 0.2 to 5.0. The aperture results are normalized by the aperture of a non-interacting plane strain fracture of the same height and net pressure. Mechanical interaction and stress shadow size depend on the shortest dimension of a crack (Olson, 1993, 2003). Consequently, at L/H = 0.2, the fracture spacing is large relative to the fracture length (which is the short dimension) and the widths of the interior and exterior fractures are the same, indicating mechanical interaction is minimal at this early stage. As fracture length increases (which would correspond to later pumping time), the curves for the interior and exterior fractures diverge, showing the increasing influence of mechanical interaction which favors

opening in the exterior fractures versus the interior fracture. After a normalized length of L/H = 2 is reached, the mechanical interaction has nearly reached its maximum and doesn't change much for greater lengths. The maximum apertures reached are 30% and 65% of the non-interacting reference value for the interior and exterior fractures, respectively.

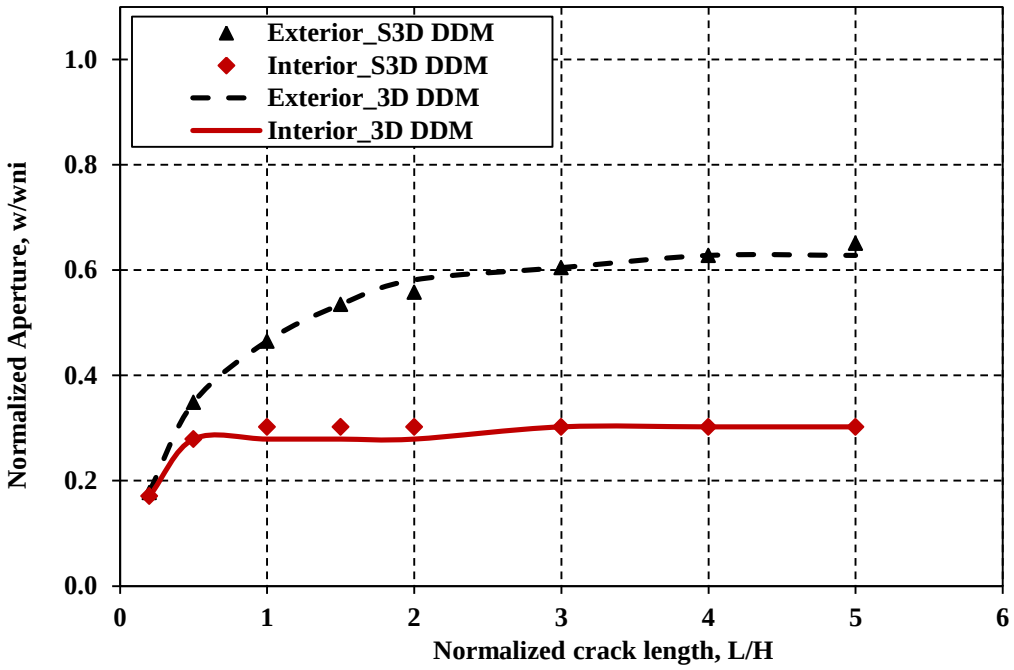

Figure 5.14: Normalized aperture vs. normalized length for a 3 crack array of parallel, equal length, uniformly pressurized fractures, with a normalized spacing of S/H = 0.5. Aperture is normalized by a non-interacting, isolated fracture of fixed height and uniform internal pressure.

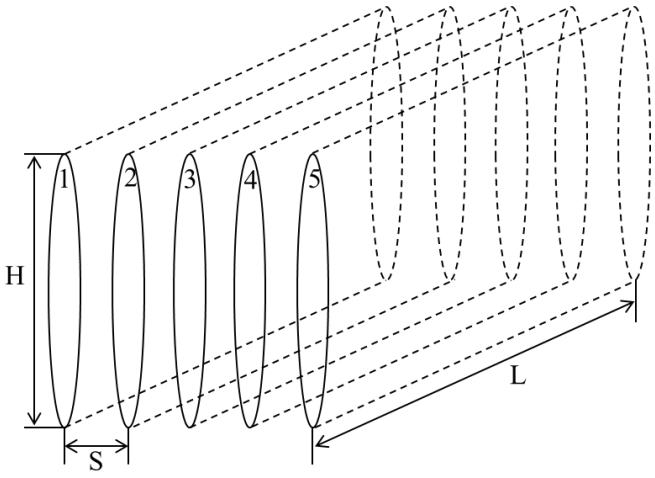

Figure 5.15: Five parallel cracks in an infinite elastic medium (S/H = 0.5).

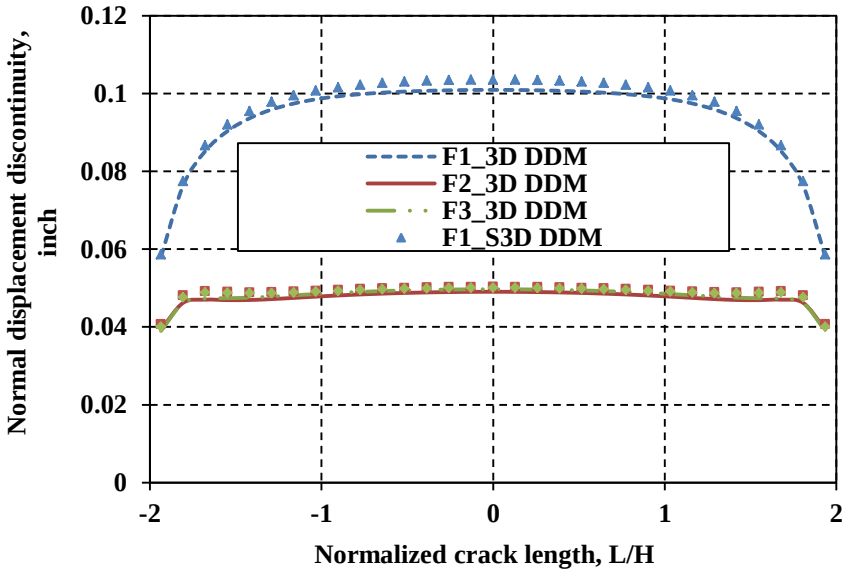

Figure 5.16: Crack normal displacement discontinuities vs. normalized length for five parallel cracks of fixed height and S/H = 0.5.

Five parallel cracks in an infinite elastic medium are shown in Figure 5.15, indicating that four edge cracks are symmetric with respective to middle crack 3. The normal displacement discontinuities of three cracks 1, 2, and 3, calculated by the

simplified 3D method and the fully 3D method, have a good match (Figure 5.16). Width of the interior fractures is greatly restricted because of mechanical interaction. Overall, Figures 5.3 through 5.16 demonstrate that S3D DDM is a highly efficient method for solving 3-D crack problems and is suitable for modeling multiple cracks.

5.3 PHYSICAL MECHANISMS OF SIMULTANEOUS MULTIPLE FRACTURE PROPAGATION

This section investigates the physical mechanisms of simultaneous multiple fracture propagation using our complex hydraulic fracture development model with S3D DDM, which can help us understand the process of multiple fracture propagation and the geometry of multiple fractures observed in the laboratory and in the field. Two mechanisms are identified: mechanical interaction and fluid flow interaction.

5.3.1 Stationary analysis

When opening fractures are closely spaced, the fractures will interact with each other by exerting additional stresses on adjacent fractures. Three stationary fractures with uniform internal pressure are simulated to analyze the effects of stress shadow, as shown in Figure 5.17. Fracture 3 is between two exterior fractures (Fractures 1 and 2) and orients toward the exterior fractures with a 45^{o} inclined angle. We ran four different cases by increasing the length of fracture 3 from approaching the exterior fractures to crossing them. The tips of fracture 3 just touch the exterior fractures for the case of Figure 5.17(b). The input parameters are listed in the Table 5.2. To eliminate the influence of differential stress, the four cases are simulated in an isotropic stress reservoir, which implies that there are no extra closing stresses from in-situ stress field acting on fracture 3. The three fractures are identical except for the relative positions. The distinct fracture geometry for the three fractures is primarily controlled by mechanical interaction. The shear and

normal displacement discontinuities of the fractures are induced by internal pressure. Here, we only discuss the normal displacement discontinuity which is fracture width.

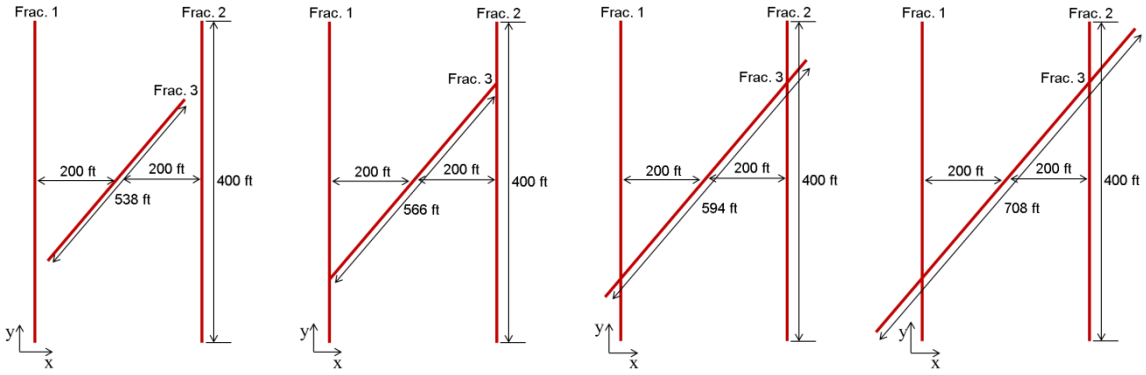

Figure 5.17: Illustration of relative positions of three stationary fractures.

Fracture spacing between Frac.1 and Frac.2	400 ft
Angle of Frac.3	45^{o}
Half-length of Frac.1 and Frac.2	300 ft
Half-length of Frac.3	269 ft, 283 ft, 297 ft, 354 ft
Layer height	100 ft
Minimum horizontal stress	4450 psi
Maximum horizontal stress	4450 psi
Young's Modulus	6.53×10^{6} psi
Poisson's Ratio	0.2
Internal pressure	300 psi

Table 5.2: Input parameters for static case study.

The fracture width distributions for four cases (Figure 5.17) are displayed in Figures 5.18, 5.19, 5.20 and 5.21, which illustrate that fracture geometries are very different with each case. For case (a), tips of fracture 3 do not touch the two exterior fractures but are close to the fractures. As discussed in Chapter 3, tensile stress is induced around fracture tips, which results in increased width on the exterior fractures at the points close to the tips of fracture 3. The exterior fractures conversely exert additional compressional stresses on fracture 3, causing width restriction its tips (Figure 5.18). As the tips of fracture 3 get closer to the exterior fractures, the width increase on the exterior fractures becomes more obvious, and the width restriction at the tips of fracture 3 becomes more serious. When the tips of fracture 3 touch the exterior fractures (Case (b)), fracture width at the intersection points on exterior fractures increases rapidly and reaches a maximum value. The width at the tips of fracture 3 becomes negative at this point (Figure 5.19). However, fracture width realistically cannot be negative. This indirectly reveals that the additional compressional stresses induced by the exterior fractures on fracture 3 are greater than the internal pressure, resulting in fracture closure. Avoiding fracture 3 closing would require a corresponding increase in internal pressure. Once fracture 3 crosses two exterior fractures (Case (c) and Case (d)), the width increase of the exterior fractures and the width restriction at tips of fracture 3 gradually vanish (Figures 5.20 and 5.21). For Case (c), the width increase at the intersection points of the exterior fractures still exists, as the tips of fracture 3 still induce tensile stresses on the intersection points. When fracture 3 crosses the two exterior fractures and the tips of fracture 3 are far away from the exterior fractures (Case (d)), fracture 3 starts exerting compressional stresses on exterior fractures. Meanwhile, the exterior fractures still induce compressional stresses on fracture 3. It is evident from Figure 5.21 that fracture width around the intersection points is reduced for all three fractures.

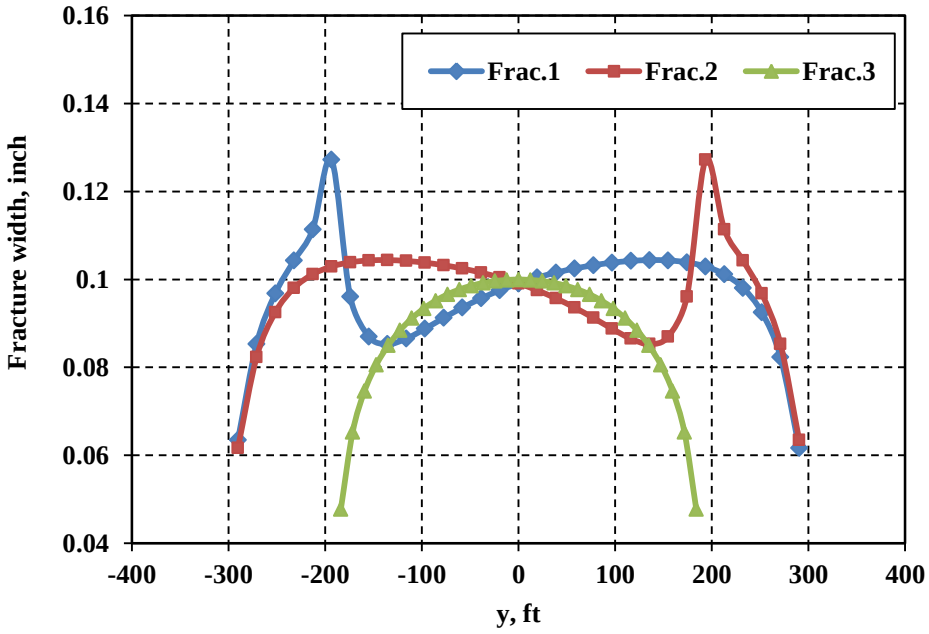

Figure 5.18: Fracture width distribution for case (a).

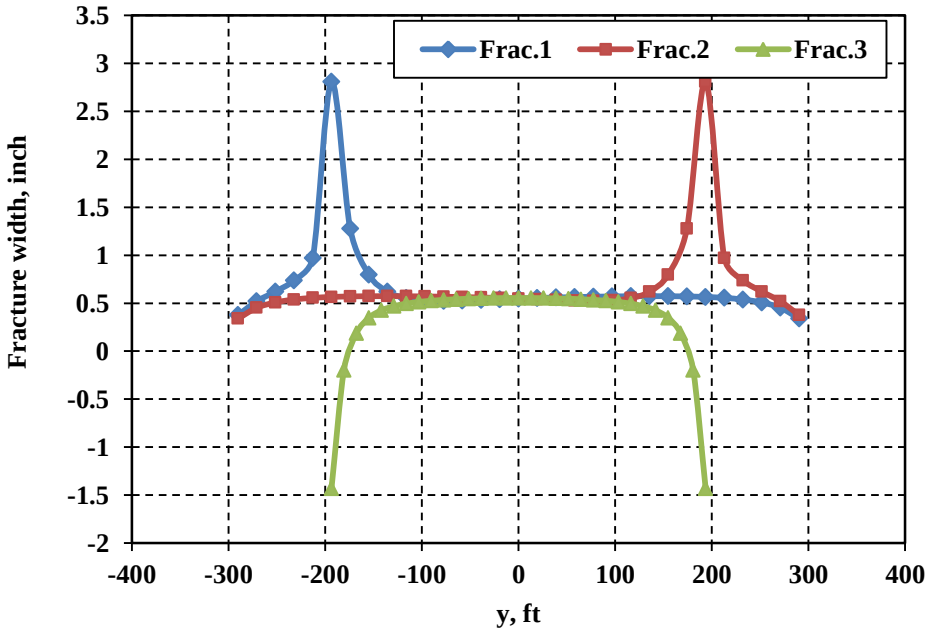

Figure 5.19: Fracture width distribution for case (b).

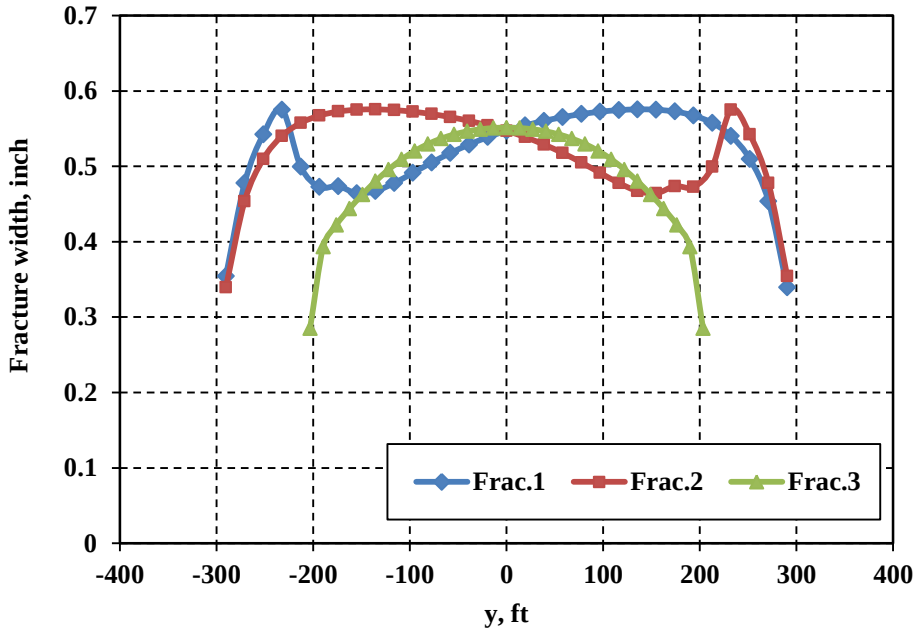

Figure 5.20: Fracture width distribution for case (c).

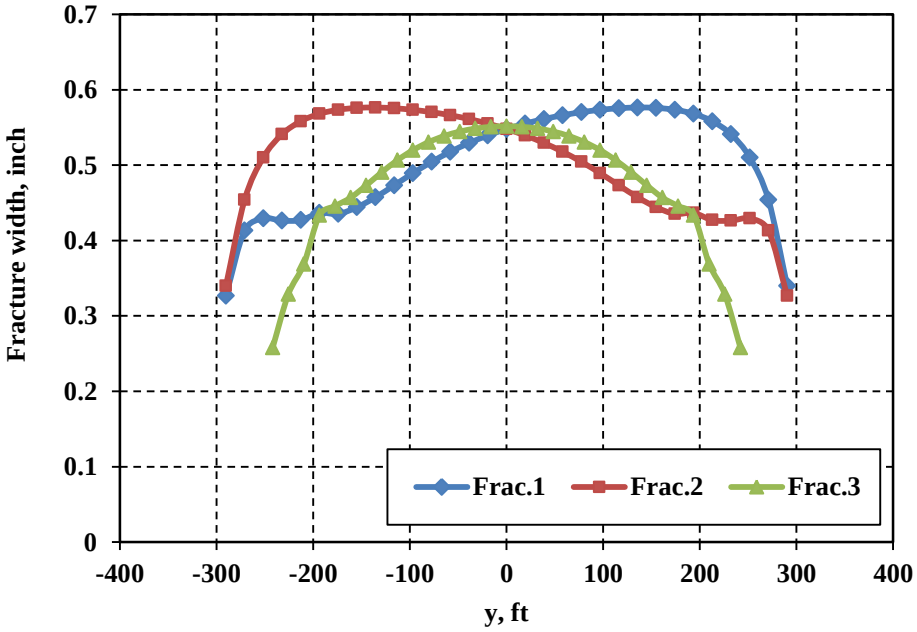

Figure 5.21: Fracture width distribution for case (d).

The results from this static analysis indicate that fractures mainly exert additional compressional stresses on surrounding rock and make it more difficult for other fractures to open, except ahead of their tips, where tensile stresses are induced. Hence, when a propagating fracture approaches another fracture, propagation will become more difficult and fracture width will be restricted because of the stress shadow effects from the approached fracture. A way to keep the fracture propagating is to increase the pumping pressure, which will be discussed in next section.

5.3.2 Dynamic analysis

In this section, simultaneous multiple fracture propagation is simulated to investigate the multiple fracture propagation process and discuss fracture mechanical interaction and pressure interaction together. Four parallel fractures with a spacing of 100 ft are propagated simultaneously (Figure 5.22). To eliminate the influence of differential stress, the case is simulated in an isotropic stress reservoir. The other input parameters are listed in Table 5.3. For this case, the friction pressure in the horizontal wellbore is ignored because distance between the perforation clusters is small (Figure 5.23). When multiple fractures propagate simultaneously, there are three stages for interior fractures (Frac.2 and Frac.3): before turning, after turning, and approaching the exterior fractures (Frac.1 and Frac.4).

Layer height	100 ft
Minimum and maximum horizontal stress	4450 psi
Injection rate for each fracture	20 bpm
n'	0.7
k'	0.02 lbf-sec^n/ft^2
Young's Modulus	6.53×10^6 psi
Poisson's ratio	0.2

Table 5.3: Input parameters for dynamic case study.

At the beginning of the propagation before fracture reorientation, the exterior fractures alter the stress distribution in the surrounding rock and exert additional stresses on interior fractures. As a result, a higher pressure is required to propagate interior fractures. However, fluid pressure within the interior fractures cannot be higher than the exterior fractures, as all the fractures are connected to the same pressure source, which is the horizontal wellbore. Hence, it is evident from Figure 5.24 that the fluid volume received by interior fractures decreases rapidly, and the propagation of the interior fractures is greatly retarded.

A fracture always seeks the orientation with the least resistance during propagation. Once the fracture is not against the least resistance, the fracture tends to re-orient and curve to the favorable direction. It is apparent from Figure 5.23 that the fractures tend to repel each other and curve outward, automatically adjusting their orientation to alleviate stress shadow effects. Figure 5.24 indicates that after turning, the interior fractures start receiving more fluid and the difference in fluid rate between exterior and interior fractures decreases, implying weaker mechanical interaction compared with the state before turning.

Additional stresses induced by an opening fracture are added to the in-situ stress field. The magnitude of additional stresses increases as close to the opening fracture. Hence, it is harder for the interior fractures to continue growing as they approach the exterior fractures. For the numerical model, one element is added to the fracture tips at every time step. Once the interior fractures intersect the exterior fractures, a negative flow rate is obtained, which implies that element length needs to shorten to gradually approach the exterior fractures. Figure 5.25 shows the element length of interior fracture tips, indicating that element length is greatly shortened at an injection time of 9 minutes to capture the intersection process of two hydraulic fractures. Figure 5.24 illustrates that the flow rate of the interior fractures drops rapidly as they approach intersection with the exterior fractures. The fluid pressure within the interior fractures is not high enough and cannot build up to overcome the additional stresses exerted on the interior fractures. Consequently, the interior fractures will stop before intersecting the exterior fractures.

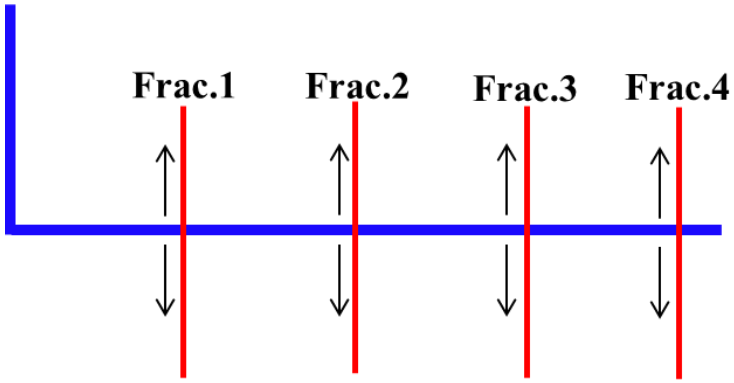

Figure 5.22: Illustration of four fractures propagating simultaneously.

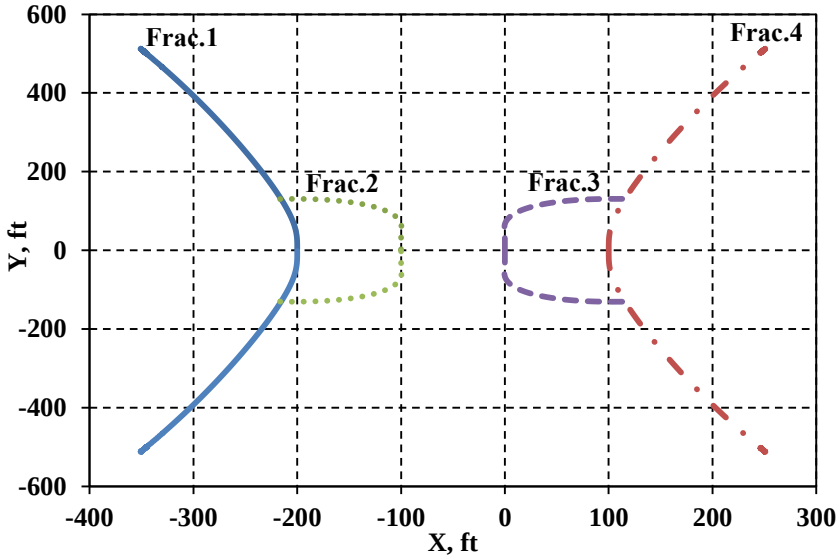

Figure 5.23: Fracture trajectory of four fractures growing simultaneously.

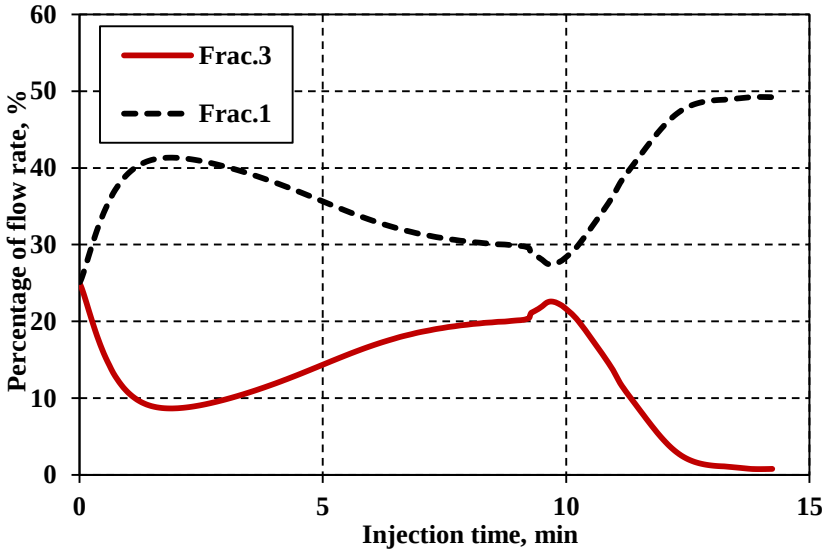

Figure 5.24: Flow rate distribution of Frac.3 and Frac.1.

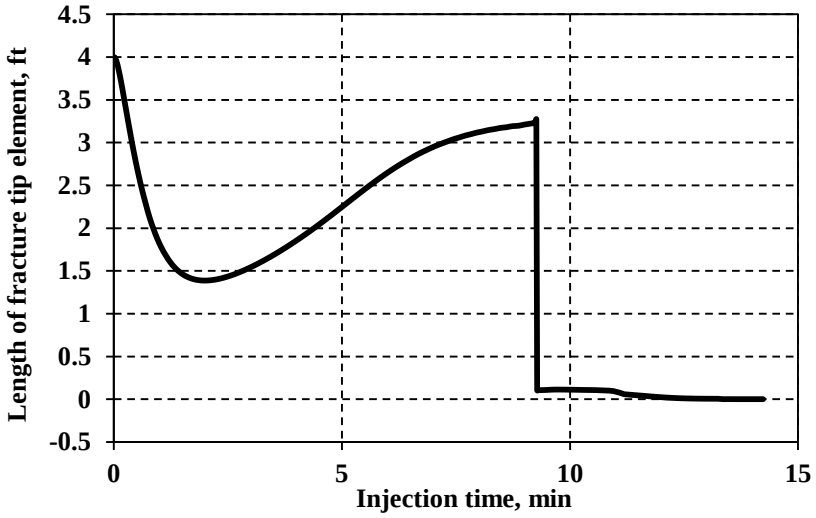

Figure 5.25: Length of fracture tip element of interior fractures vs. injection time.

5.3.3 Discussion

Simultaneous multiple fracture propagation is dominated by both mechanical and pressure interaction between multiple fractures. A challenging problem of multiple fracture propagation is to deal with the intersection of two hydraulic fractures connected to the same injection source. In our model, based on the analysis in Section 5.3.2, when a tip of a hydraulic fracture is very close to another hydraulic fracture for simultaneous multiple fracture propagation, it is assumed that the wing of the approaching fracture will stop extending. The reasonability of this assumption is required to be further verified. It is difficult to give an accurate description of tip behavior at the intersection point in our model due to the rough assumption of linear elastic fracture mechanics. In addition, our model does not consider the effects of proppant transport on fracture propagation. Fracture width is greatly restricted at the intersection point based on stationary analysis. It is possible that proppant screen-out would be induced at the intersection points, stopping fracture growth.

5.4 CONCLUSIONS

In this chapter, the Simplified Three-dimensional Displacement Discontinuity Method (S3D DDM) was tested and applied for multiple fracture problems under static and dynamic conditions. The results for stationary cracks demonstrate the accuracy and efficiency of S3D DDM for describing rock deformation. Opening fractures exert additional stresses on adjacent fractures and greatly reduce the width of the fracture approaching to the non-parallel opening fractures. For simultaneous multiple fracture propagation, both mechanical interaction and fluid flow interaction dominate fracture propagation. Mechanical interaction plays an important role in fracture geometry, resulting in non-planar fracture and width restriction. Fluid flow interaction is to maintain pressure equilibrium between fractures through horizontal wellbore and affects flow rate distribution into fractures. Propagation of interior fractures is restricted by stress shadow effects from exterior fractures, while pressure within interior fractures cannot build up to counteract the restriction if all fractures are coming from a common injection source. This causes the exterior fractures to dominate multiple fracture propagation, resulting in immature development of interior fractures.

CHAPTER 6: INTERACTION BETWEEN HYDRAULIC FRACTURE AND NATURAL FRACTURES[3]

In the previous chapters, a complex hydraulic fracture development model was derived, validated and tested to simulate multiple fracture propagation by coupling fluid mechanics and rock mechanics. A Simplified Three-Dimensional Displacement Discontinuity Method (S3D DDM) was proposed and incorporated into the model to describe rock deformation. Some interesting physical insights and mechanisms were drawn from the simulation results. However, natural fracture interaction was not taken into account, which can further complicate fracture geometry and plays a significant role in the effectiveness of hydraulic fracture treatment designs.

This chapter focuses on analyzing a single hydraulic fracture interacting with natural fractures. Fracture width is restricted on the segment of activated natural fractures. Additional pressure is required to start fluid deflecting into a natural fracture. The effects of the relative angle between the hydraulic and natural fracture, the length of activated natural fractures, differential stress and natural fracture configuration on HF/NF interaction are investigated. Detailed pressure and aperture distributions provide critical insights into fracture propagation mechanisms under the complex conditions.

[3]Parts of this chapter have been presented in the following conference: Wu, K. and Olson, J. E. 2014. Mechanics analysis of interaction between hydraulic and natural fractures in shale reservoirs. URTeC 1922946, presented at the Unconventional Resources Technology Conference held in Denver, Colorado, USA, 25-27 August. This paper was supervised by Jon Olson.

6.1 INTRODUCTION

Many experimental and field studies reveal that the effects of natural fractures on hydraulic fracture propagation include arrest of the fracture propagation, formation of multiple fractures, fracture offsets, and high net pressures. (Medlin and Fitch, 1983, Jeffrey et al., 2009). When the hydraulic fracture is arrested by a pre-existing natural fracture, pressure within the fracture will continue to increase at the point of intersection until either deflection into the natural fracture or crossing the natural fracture occurs (Blanton, 1986). An interaction criterion is used to determine the fracture propagation direction after intersecting with a natural fracture. After the hydraulic fracture is diverted along the pre-existing path of the natural fracture, fracture geometry and pressure responses will be significantly distinct from conventional bi-wing fractures.

In this chapter, two crossing criteria (Section 6.2) are described to determine the crossing/arresting behavior of a hydraulic fracture under the influence of frictional interfaces and cemented discontinuities. The two criteria are incorporated in our complex hydraulic fracture development model and used to determine fracture propagation direction when the hydraulic fracture encounters a natural fracture. After that, the model is use to investigate how fracture propagation geometry and injection pressure are affected by geometric configuration of the hydraulic and natural fractures as well as the in-situ differential stress in Section 6.3. Finally, the stress distribution on the natural fractures is analyzed to study the mechanisms of HF/NF interaction.

6.2 CROSSING CRITERIA

6.2.1 A crossing criterion for a frictional interface

Renshaw and Pollard (1995) developed a criterion predicting whether a growing fracture will arrest or cross a frictional interface at the right angle based on the linear elastic fracture mechanics, and Gu and Weng (2010) then extended the criterion to a fracture crossing frictional interfaces at non-orthogonal angles. This criterion analyzes stresses near a fracture tip only considering fracture propagation of mode I (opening mode). Since both modes I (opening mode) and II (sliding mode) could be induced when multiple fractures grow simultaneously, we incorporate both opening and sliding modes to analyze stress field and modify the criterion.

The condition for causing slip of a frictional surface is to satisfy a linear friction law; on the other hand, the condition for reinitiating the fracture on the opposite side of the interface is the tensile stress induced by the approaching fracture equal to the rock tensile strength T_o. The criterion is to analyze whether slip occurs along the interface when the tensile stress on the opposite side of the interface reaches the tensile strength T_o. The stresses near the tip within the fracture can be approximately calculated by:

$$\begin{Bmatrix}\sigma_{xx}\\ \sigma_{yy}\\ \tau_{xy}\end{Bmatrix} = \begin{Bmatrix}S_{H\max}\\ S_{h\min}\\ 0\end{Bmatrix} - \frac{K_I}{\sqrt{2\pi r}}\begin{Bmatrix}\cos(\frac{\theta}{2})[1-\sin(\frac{\theta}{2})\sin(\frac{3\theta}{2})]\\ \cos(\frac{\theta}{2})[1+\sin(\frac{\theta}{2})\sin(\frac{3\theta}{2})]\\ \sin(\frac{\theta}{2})\cos(\frac{\theta}{2})\cos(\frac{3\theta}{2})\end{Bmatrix} - \frac{K_{II}}{\sqrt{2\pi r}}\begin{Bmatrix}-\sin(\frac{\theta}{2})[2+\cos(\frac{\theta}{2})\cos(\frac{3\theta}{2})]\\ \sin(\frac{\theta}{2})\cos(\frac{\theta}{2})\cos(\frac{3\theta}{2})\\ \cos(\frac{\theta}{2})[1-\sin(\frac{\theta}{2})\sin(\frac{3\theta}{2})]\end{Bmatrix}, \tag{6.1}$$

where compression is positive, (r, θ) are polar coordinates with the origin at the fracture tip, S_{Hmax} is the maximum horizontal stress, S_{hmin} is the minimum horizontal stress, K_I and K_{II} are stress intensity factor of modes I and II, respectively.

Since compression is positive, the maximum tensile stress induced by the fracture on the opposite side of the interface is the minimum principle stress (Gu and Weng, 2010),

$$\sigma_3 = \frac{\sigma_{xx}+\sigma_{yy}}{2} - \sqrt{(\frac{\sigma_{xx}-\sigma_{yy}}{2})^2+\tau_{xy}^2}\ . \tag{6.2}$$

To reinitiate the fracture, σ_3 should be equal to $-T_o$ as

$$\frac{\sigma_{xx}+\sigma_{yy}}{2} - \sqrt{(\frac{\sigma_{xx}-\sigma_{yy}}{2})^2+\tau_{xy}^2} = -T_o\,. \tag{6.3}$$

Eq. 6.3 can be re-written as

$$(\frac{\sigma_{xx}+\sigma_{yy}}{2}+T_0)^2 = (\frac{\sigma_{xx}-\sigma_{yy}}{2})^2+\tau_{xy}^2\,. \tag{6.4}$$

Substituting Eq. 6.1 into Eq. 6.4 and setting $\theta = \beta$ or $\theta = \beta - \pi$ yield

$$A(\sqrt{2\pi r_c})^2 + 2B\sqrt{2\pi r_c} + C = 0\,. \tag{6.5}$$

Where

$$A = (\frac{S_{H\max}-S_{h\min}}{2})^2 - (\frac{S_{H\max}+S_{h\min}}{2}+T_o)^2$$

$$B = K_I\cos(\frac{\theta}{2})((\frac{S_{H\max}-S_{h\min}}{2})\sin(\frac{\theta}{2})\sin(\frac{3\theta}{2}) + (\frac{S_{H\max}+S_{h\min}}{2}+T_o))$$
$$+ K_{II}\sin(\frac{\theta}{2})((\frac{S_{H\max}-S_{h\min}}{2}) + (\frac{S_{H\max}-S_{h\min}}{2})\cos(\frac{\theta}{2})\cos(\frac{3\theta}{2}) - (\frac{S_{H\max}+S_{h\min}}{2}+T_o))$$

$$C = -{K_I}^2\cos^4(\frac{\theta}{2}) + 4K_IK_{II}\sin(\frac{\theta}{2})\cos^3(\frac{\theta}{2}) - 2{K_{II}}^2\sin^2(\frac{\theta}{2})\cos^2(\frac{\theta}{2}) + {K_{II}}^2\cos^2(\frac{\theta}{2})$$

Eq. 6.3 can be satisfied by solving for r_c in Eq. 6.5, where r_c is the critical radius where the maximum tensile stress on the other side of the interface reaches the tensile strength of rock. The next step is to analyze whether slip occurs along the interface at $r = r_c$. If the

stresses at $r = r_c$ can induce a slip, the fracture will be arrested and cannot reinitiate on the other side of the interface, because the fracture tip stresses cannot be transmitted across the interface. On the other hand, if the slip cannot occur at $r = r_c$, the fracture will propagate across the interface.

For a frictional surface (Figure 6.1), slip along the interface will not occur whenever:

$$\left|\tau_\beta\right| < S_o + \mu\sigma_{n\beta} \ , \tag{6.6}$$

where μ is the coefficient of friction for the interface, S_o is the cohesion of the interface, τ_β and $\sigma_{n\beta}$ are the shear and normal stresses acting on the interface. The stress state near a fracture tip is described in Eq. 6.1. τ_β and $\sigma_{n\beta}$ can be calculated by projecting the stresses onto the interface:

$$\tau_\beta = -\frac{\sigma_{xx} - \sigma_{yy}}{2}\sin 2\beta + \cos 2\beta\sigma_{xy} \ , \tag{6.7}$$

$$\sigma_{n\beta} = \frac{\sigma_{xx} + \sigma_{yy}}{2} - \frac{\sigma_{xx} - \sigma_{yy}}{2}\cos 2\beta - \sin 2\beta\sigma_{xy} \, . \tag{6.8}$$

Substituting Eq. 6.1 into Eqs. 6.7 and 6.8 and simplifying, we have new formulas for normal and shear stresses,

$$\begin{aligned}\tau_\beta = &-\frac{S_{H\max} - S_{h\min}}{2}\sin 2\beta - \frac{K_I}{\sqrt{2\pi r_c}}\cos(\frac{\theta}{2})\sin(\frac{\theta}{2})\cos(2\beta - \frac{3\theta}{2}) \\ &-\frac{K_{II}}{\sqrt{2\pi r_c}}[\cos(2\beta - \frac{\theta}{2}) + \sin(\frac{\theta}{2})\cos(\frac{\theta}{2})\sin(2\beta - \frac{3\theta}{2})]\end{aligned} \ , \tag{6.9}$$

$$\begin{aligned}\sigma_{n\beta} = &\frac{S_{H\max} + S_{h\min}}{2} - \frac{S_{H\max} - S_{h\min}}{2}\cos 2\beta + \frac{K_I}{\sqrt{2\pi r_c}}\cos(\frac{\theta}{2})[\sin(\frac{\theta}{2})\sin(2\beta - \frac{3\theta}{2}) - 1] \\ &+\frac{K_{II}}{\sqrt{2\pi r_c}}[\sin(\frac{\theta}{2}) + \sin(2\beta - \frac{\theta}{2}) - \sin(\frac{\theta}{2})\cos(\frac{\theta}{2})\cos(2\beta - \frac{3\theta}{2})]\end{aligned} \ . \tag{6.10}$$

The crossing condition in Eq. 6.6 can be determined by using the normal and shear stresses of Eqs. 6.9 and 6.10 with r_c solved from the Eq. 6.5 at $\theta = \beta$ or $\theta = \beta - \pi$.

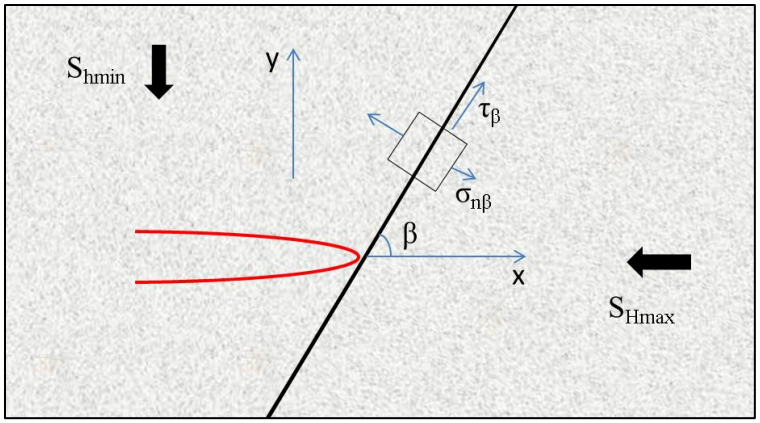

Figure 6.1: Schematic of a hydraulic fracture approaching a frictional interface.

For most angles of β, the above algorithm cannot be solved analytically and requires adopting a computer routine for evaluation. For 90^o, following Renshaw and Pollard (1995), an explicit equation can be obtained for crossing condition in Eq. 6.6:

$$\frac{\frac{S_o}{\mu} + S_{H\max}}{T_o + S_{h\min}} > \frac{(K_I - 3K_{II}) + \frac{|-K_I + K_{II}|}{\mu}}{3K_I - K_{II}}. \tag{6.11}$$

When there is no sliding mode stress intensity factor (Mode II), Eq. 6.11 simplifies to the extended criterion developed by Gu and Weng (2010). When neither the mode II stress intensity factor nor cohesion are considered, Eq. 6.11 reduces to the original criterion given by Renshaw and Pollard (1995). To discuss the impacts of K_I and K_{II} on the crossing condition, we set

$$K_r = \frac{(K_I - 3K_{II}) + \frac{|-K_I + K_{II}|}{\mu}}{3K_I - K_{II}}. \tag{6.12}$$

A large value for K_r implies less likelihood for crossing, while a small value of K_r means more likelihood for crossing.

6.2.2 A crossing criterion for fully cemented natural fractures

Dahi-Taleghani and Olson (2009) developed a crossing criterion for hydraulic fracture intersection with fully cemented natural fractures based on the energy release rate method for mixed mode fracture (Palaniswamy, 1972). The hypothesis of this method is that (1) a crack propagates at the crack tip in a radial direction along which the energy release is a maximum; and (2) the crack begins to propagate when the energy release rate reaches some critical value G_c. The predicted direction of crack propagation by this method is the same as the direction calculated by the maximum circumferential stress criterion (Erdogan and Sih, 1963).

When a crack propagates in its own plane, the energy release rate is given by (Sih and Liebowitz, 1968)

$$G_0 = \frac{K_I^2 + K_{II}^2}{E^*}, \tag{6.13}$$

where K_I and K_{II} are the stress intensity factors for mode I and II, E^* is Young's modulus E for plane stress, and is $E/(1-\nu^2)$ for plane strain (ν is the Possion's ratio). In some situations, the crack does not propagate in its own plane. The energy release rate in a specific orientation, θ, (Figure 6.2) (Nuismer, 1975), is

$$\begin{aligned} G_\theta &= \frac{K_{I\theta}^2 + K_{II\theta}^2}{E^*} \\ K_{I\theta} &= \frac{1}{2}\cos(\frac{\theta}{2})[K_I(1+\cos\theta) - 3K_{II}\sin\theta] \\ K_{II\theta} &= \frac{1}{2}\cos(\frac{\theta}{2})[K_I\sin\theta + K_{II}(3\cos\theta - 1)] \end{aligned} \tag{6.14}$$

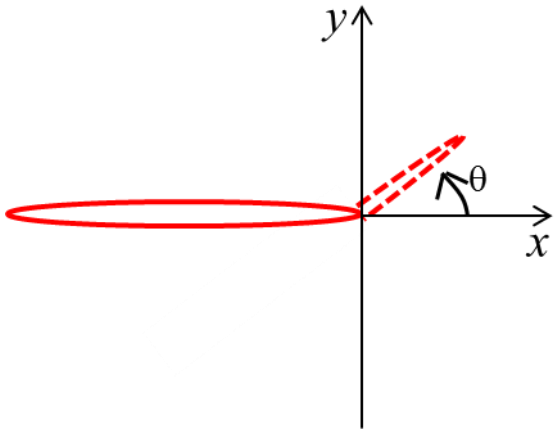

Figure 6.2: Geometry and coordinate systems for the crack.

For pure mode I, K_{II} is zero. The Eq. 6.14 is simplified as

$$K_{I\theta} = \frac{K_I}{2}\cos(\frac{\theta}{2})(1+\cos\theta)$$
$$K_{II\theta} = \frac{K_I}{2}\cos(\frac{\theta}{2})\sin\theta \quad . \qquad (6.15)$$
$$G_\theta = \frac{K_I^{\,2}}{E^*}\frac{1}{2}\cos^2(\frac{\theta}{2})(1+\cos\theta)$$

The normalized energy release rate (divided a constant K_I^2/E^*) as a function of angle (Figure 6.3) illustrates that the energy release rate reaches its the maximum value when θ is 0^o. The energy release rate decreases when fracture directions deviate away from in-plane propagation.

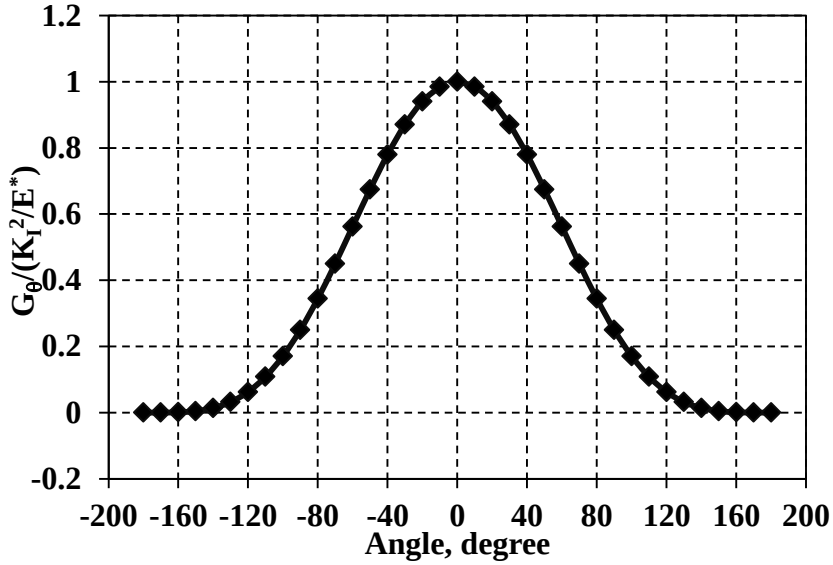

Figure 6.3: $G_\theta/ (K_I^2/E^*)$ in different directions for pure mode I.

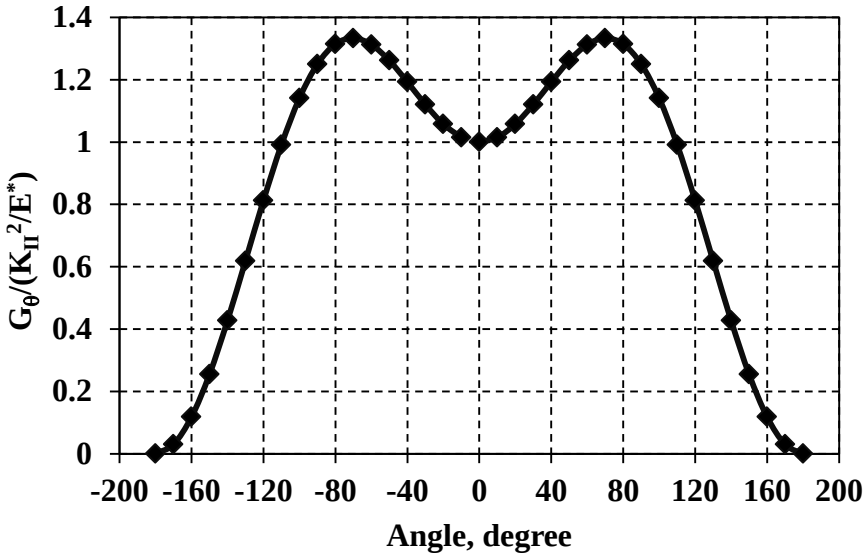

Figure 6.4: $G_\theta/ (K_{II}^2/E^*)$ in different directions for pure mode II.

For pure mode II, K_I is zero. Eq. 6.14 can be simplified as

$$K_{I\theta} = \frac{-3K_{II}}{2}\cos(\frac{\theta}{2})\sin\theta$$
$$K_{II\theta} = \frac{K_{II}}{2}\cos(\frac{\theta}{2})(3\cos\theta - 1) \quad . \tag{6.16}$$
$$G_\theta = \frac{K_{II}^{\ 2}}{E^*}\frac{1}{2}\cos^2(\frac{\theta}{2})(5 - 3\cos\theta)$$

The normalized energy release rate (Figure 6.4) reaches a maximum value when θ = $\pm 70.5^o$. The angles are identical to the angles predicted by the maximum circumferential stress criterion.

When a hydraulic fracture encounters a weak plane, such as a cemented natural fracture, the hydraulic fracture will have more than one path to follow as shown in Figure 6.5. The final path utilized by the fracture is determined by magnitudes of the relative energy release rate $G_m/G_c^{\ rock}$ and $G_\theta/\ G_c^{\ frac}$ (Dahi-taleghani, 2009). If $G_\theta/G_c^{\ frac}$ is less than $G_m/G_c^{\ rock}$, named G_θ/G_m is less than $G_c^{\ frac}/\ G_c^{\ rock}$, the fracture will cross, otherwise, the fracture will deflect into the natural fracture. G_m is the maximum energy release rate at the fracture tip, and G_θ is the energy release rate in an orientation θ. $G_c^{\ rock}$ is critical energy release rate of rock, and $G_c^{\ frac}$ is the energy required to open the unit area of the cement in the fracture or cement-matrix interface.

The ratio of G_θ and G_m is compared with the ratio of $G_c^{\ frac}$ and $G_c^{\ rock}$ for pure mode I and II (Figures 6.6 and 6.7). The ratio of $G_c^{\ frac}$ and $G_c^{\ rock}$ is the property of rock and cement. As shown in Figures 6.6 and 6.7, the fracture will deflect into the natural fracture if the relative angle of the hydraulic and the natural fractures is between the two green lines.

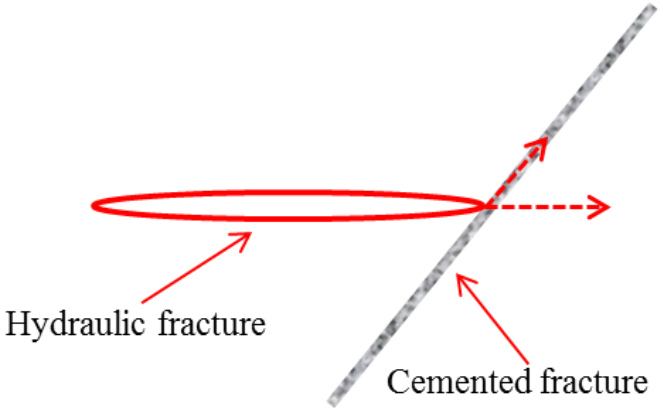

Figure 6.5: Intersection of a hydraulic fracture with a cemented fracture, two potential growth directions have been shown in red dash lines.

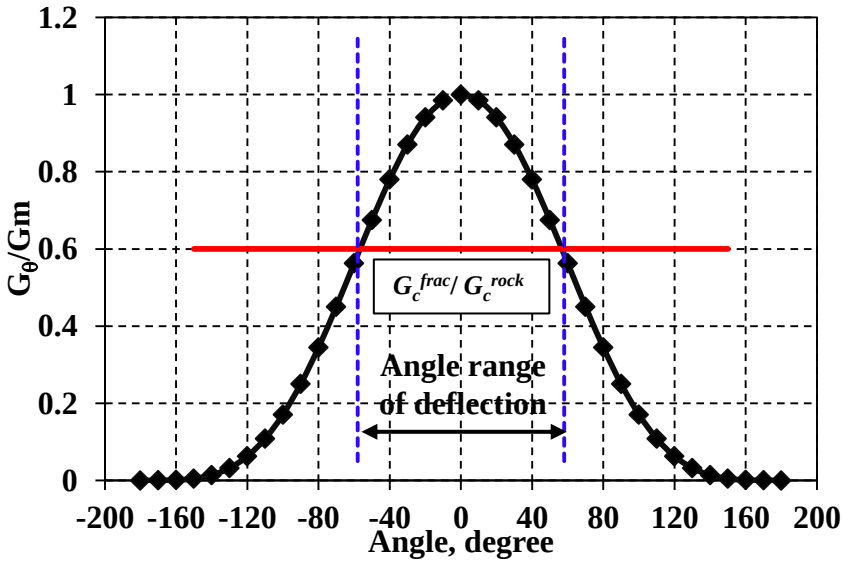

Figure 6.6: The angle range of deflection for pure mode I.

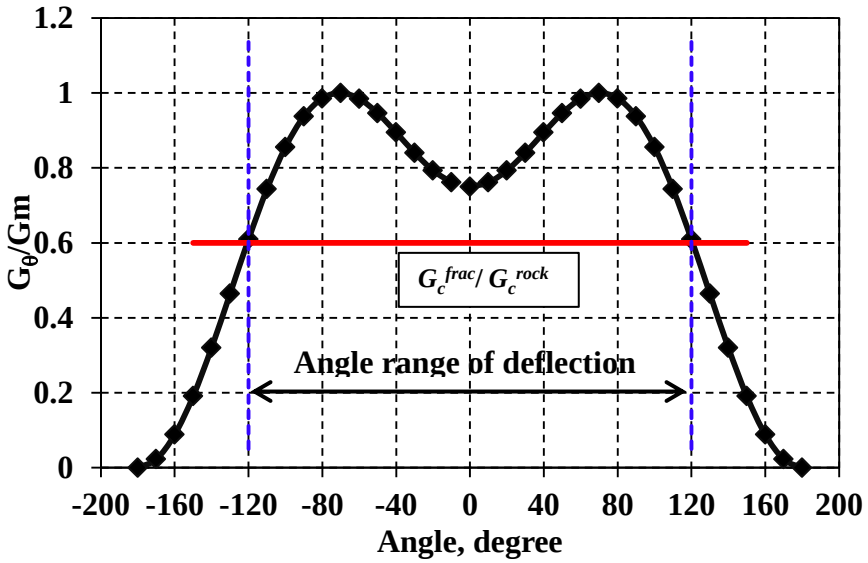

Figure 6.7: The angle range of deflection for pure mode II.

6.3 EFFECTS OF NATURAL FRACTURES ON HYDRAULIC FRACTURE PROPAGATION

To investigate the effects of natural fractures on hydraulic fracture propagation, we performed numerical experiments based on the configuration shown in Figure 6.8, using our complex fracture development model with extended Gu and Weng's criterion (Section 6.2.1). The parameters (Table 6.1) are prescribed based on the published data for the Barnett shale. The relative angle between the hydraulic and natural fracture, the length of activated natural fractures, differential stress and natural fracture configuration are varied. Most importantly, the orientations of the natural fractures and S_{Hmax} have been arranged such that the hydraulic fracture will intersect the natural fractures. The base case of fracture growth is examined under an isotropic remote stress field with two symmetric natural fractures at the distance of 100 ft away from the hydraulic fracture.

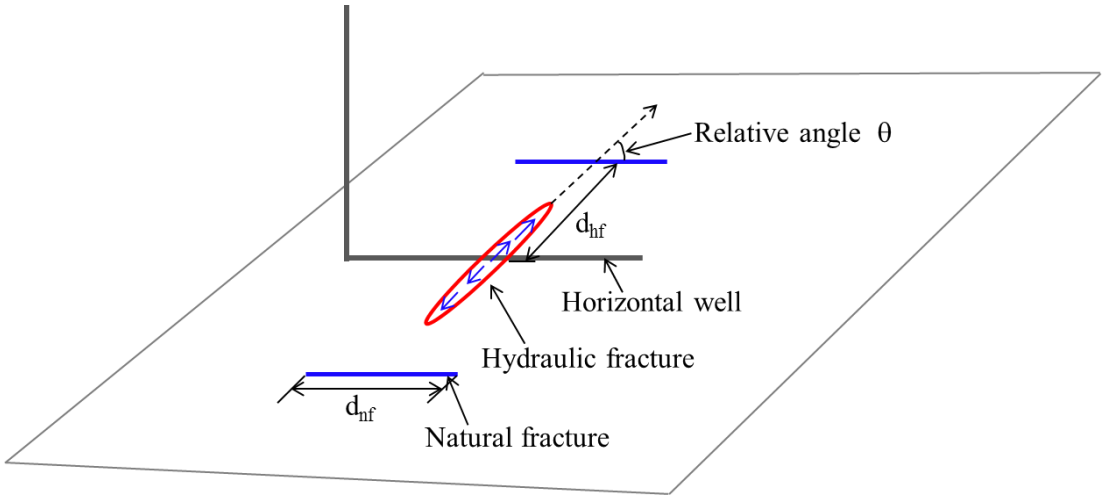

Figure 6.8: Schematic of a hydraulic fracture approaching pre-existing natural fractures.

Layer height	100 ft
Minimum horizontal stress	4,450 psi
Fluid Leak-off Coefficient	0.00001 ft/min$^{0.5}$
Injection Rate	20 bpm
Viscosity, cp	1.0
Young's Modulus	6.53×10^{6} psi
Poisson's Ratio	0.2
No. of Perforations	60
Density of Slurry	1.2 g/cm^{3}
Density of Water	1.0 g/cm^{3}
Diameter of Perforations	16 mm
Diameter of Wellbore	0.1 m
Tensile strength of rock	1305 psi
Cohesion of NF	0
Friction coefficient of NF	0.6

Table 6.1: Input parameters for case study.

6.3.1 The effects of relative angle between HF and NF

Natural fractures can occur at a variety of orientations within the reservoir, not necessarily parallel to the present day maximum horizontal stress (Laubach et al., 2004). In the Barnett shale, the dominant natural fractures are nearly normal to the maximum horizontal stress (Gale et al., 2007). We have performed some simulations to study the effects of relative angle between HF and NF on a hydraulic fracture intersecting with natural fractures (Figure 6.9). When the hydraulic fracture approaches natural fractures at a right angle, the natural fractures could be activated in both sides and fluid will divert

equally into the two branches (Figure 6.10 (a)). If the intersection is non-orthogonal, the natural fractures could only be activated in one side and fluid will flow into the branch, as shown in Figures 6.10 (b) and (c). Fracture width is shown in Figure 6.11, indicating that width restriction is more pronounced with the increasing relative angle. The fracture with two branches has a much smaller aperture than the other fractures, because total fluid volume is the same for all the cases. The net pumping pressure with time is plotted in Figure 6.12, which illustrates that an elevation of pumping pressure is required for fluid penetrating into natural fractures, and larger relative angles require higher elevation in pumping pressure. Indeed, the pressure elevation was observed in the HF/NF interaction experiments (Alabbad, 2014). Some field observations have also suggested that elevation of pumping pressure is probably due to fracture branching (Medlin and Fitch, 1983).

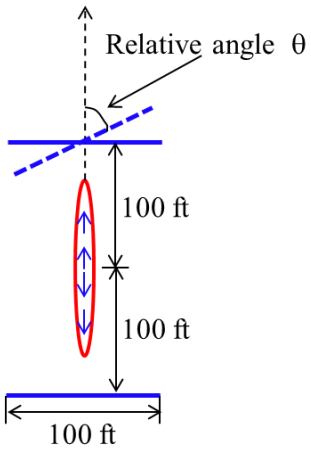

Figure 6.9: Schematic of a hydraulic fracture approaching natural fractures with different intersecting angles.

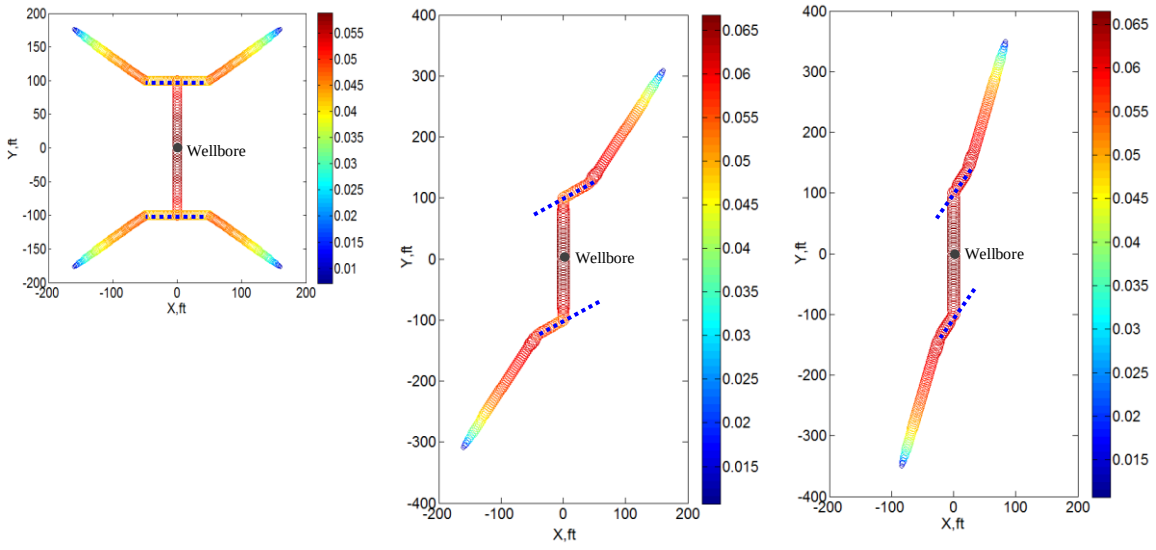

(a) $\theta = 90^{o}$ (b) $\theta = 60^{o}$ (c) $\theta = 30^{o}$

Figure 6.10: Width profile at the end of injection for different relative angles between HF and NF.

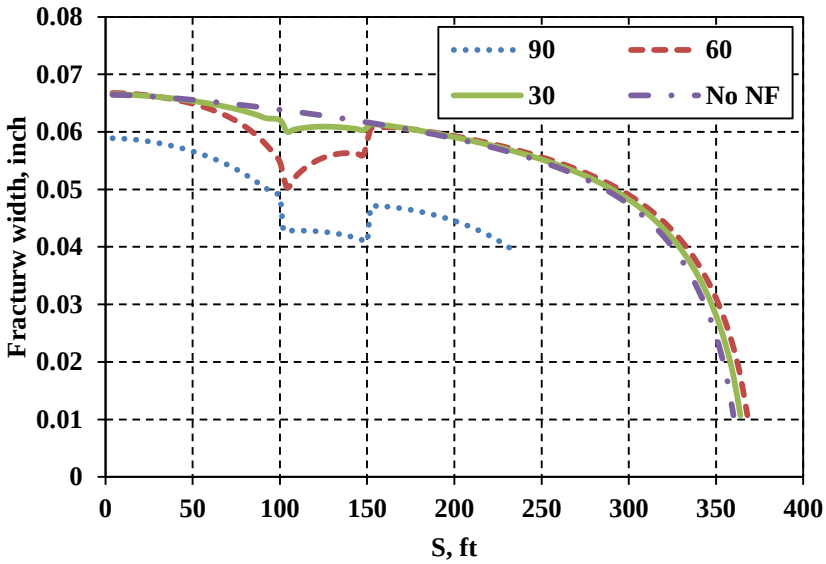

Figure 6.11: Fracture width profile for different relative angles between HF and NF.

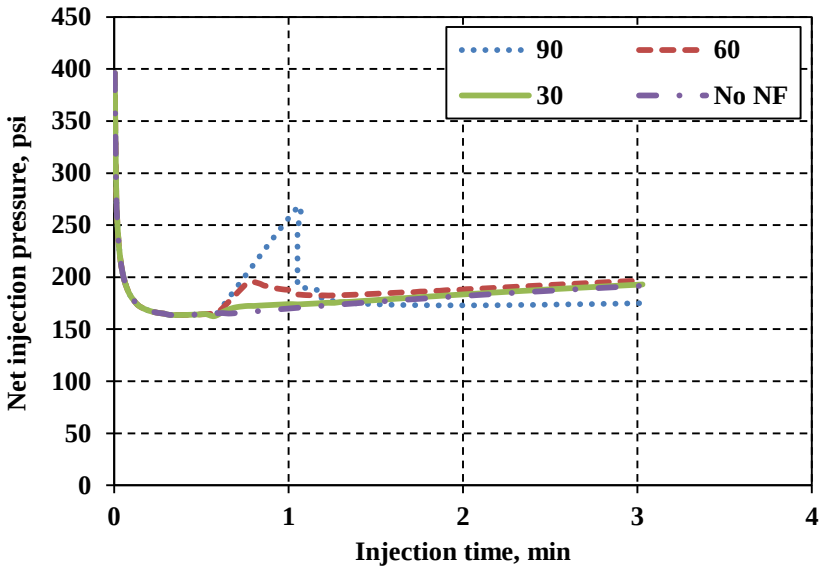

Figure 6.12: Variations of the net injection pressure at the injection point with time for different relative angles between HF and NF.

6.3.2 The effects of the length of activated natural fractures (d_{nf})

Fracture geometry is also influenced by the length of activated natural fractures. A hydraulic fracture propagates along the natural fracture until it comes to its tip. From there, the fracture propagation will kink back toward the original orientation of the hydraulic fracture or S_{Hmax}. In some cases this reorientation is gradual, and in some cases it is more abrupt. This angle is defined as kink angle, as shown in Figure 6.13. Fracture propagation was simulated in an isotropic stress reservoir. Figure 6.14 shows fracture geometry for different length of activated natural fractures and indicates that the longer diversion lengths along the natural fractures, and the smaller the kink angle. From Figure 6.15, it is evident that the kink angle decreases with increasing the length of activated nature fractures. This is because stress shadow effects from the hydraulic fracture segment gradually vanish as being far away from the segment. For an extreme case, if a natural fracture is very long and the effects of stress shadow disappear at the points far

away from the hydraulic fracture segment, the fracture would propagate along the original direction of natural fractures after kinking back toward isotropic stress reservoirs. If in-situ stresses in the reservoirs are anisotropic, the kink angle will also be influenced by the differential stress (S_{Hmax} - S_{hmin}). Both induced stresses and differential stress affect the kink angle after the fracture comes out from a natural fracture.

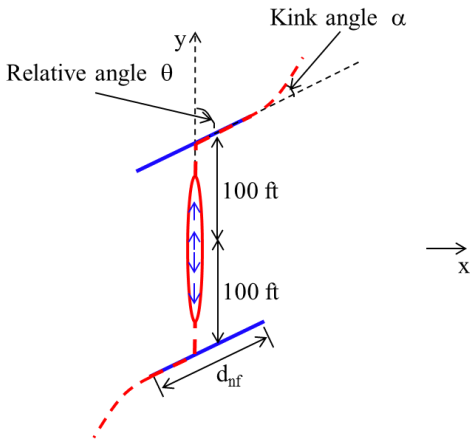

Figure 6.13: Schematic of a hydraulic fracture breaking out from the tips of natural fractures.

In Figure 6.13, the non-planar fracture has been divided into hydraulic fracture segments with a length of 200 ft, two natural fracture segments and two anti-symmetric fracture wings. Olson (1995) proposed that opening displacement discontinuity on the hydraulic fracture segments and fracture wings can lead to a shear offset of the natural fracture segments because of geometric continuity. Based on the purely geometric constraints, the width for natural fracture segments, w_{nf}, is related to relative angle between HF and NF, θ, and the width of the other two segments, w_{hf}, as

$$w_{nf} = w_{hf} \cos\theta \,. \tag{6.17}$$

The percentage of width reduction, R, can then be expressed as

$$R = 100\frac{w_f - w_w}{w_f} = 100(1-\cos\theta). \tag{6.18}$$

The purely geometric constraints are applicable only when hydraulic fracture segments and two fracture wings dominate the fracture geometry and the differential stress (S_{Hmax} - S_{hmin}) is zero. This relationship is plotted in Figure 6.16 (solid line) along with data from fracture propagation simulations in an isotropic reservoir for different activated natural fracture lengths. It is evident from this figure that width reduction is dependent on the length of natural fractures segment, which is in contrast to conclusions obtained by Olson (1995) and is consistent with previously published relationships (El Rabaa and Rogiers, 1990). As the length of activated natural fractures decreases, width reduction increases approaching to the purely geometric constraints (1 - cosθ). For a planar fracture, $\theta = 0^{o}$, there is no width restriction. As θ increases, the width reduction increases.

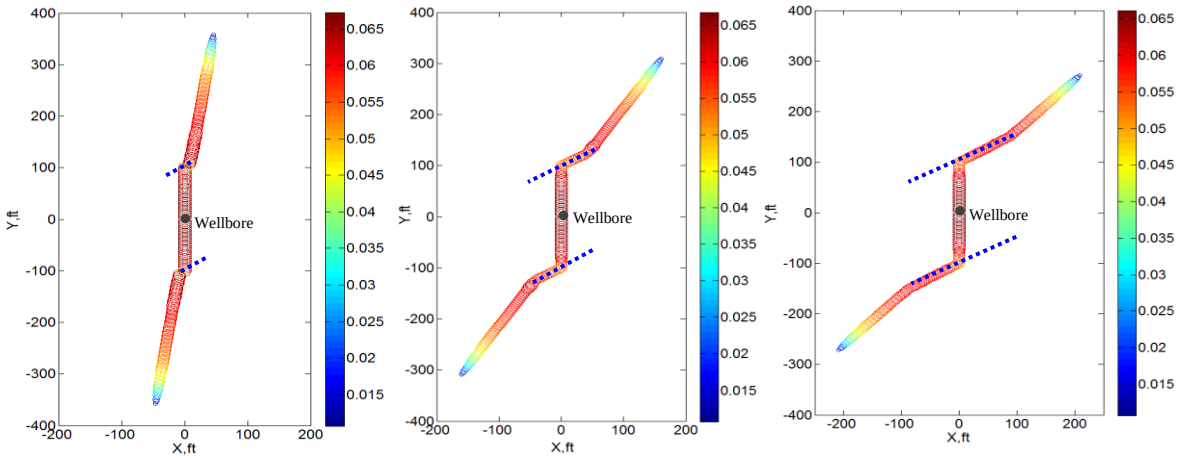

(a) d_{nf} = 20 ft (b) d_{nf} = 100 ft (c) d_{nf} = 200 ft

Figure 6.14: Width profile at the end of injection for different natural fracture length.

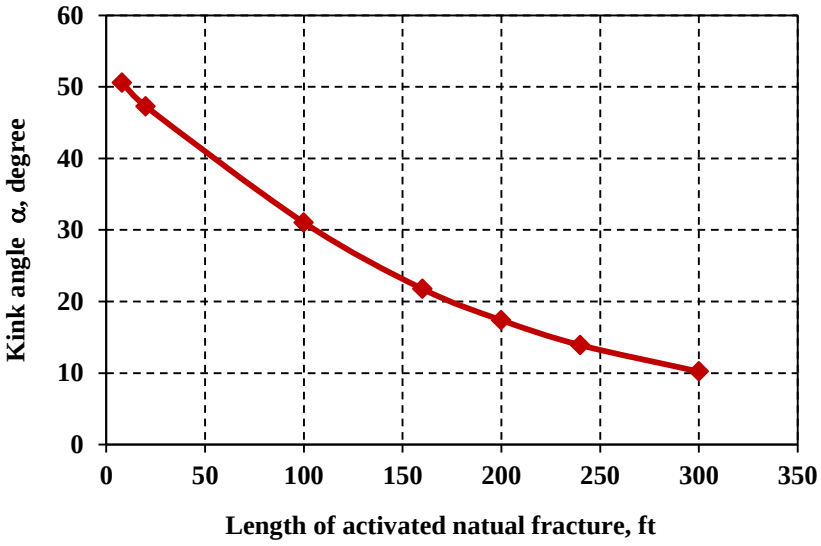

Figure 6.15: Disparity in orientations of the hydraulic fracture.

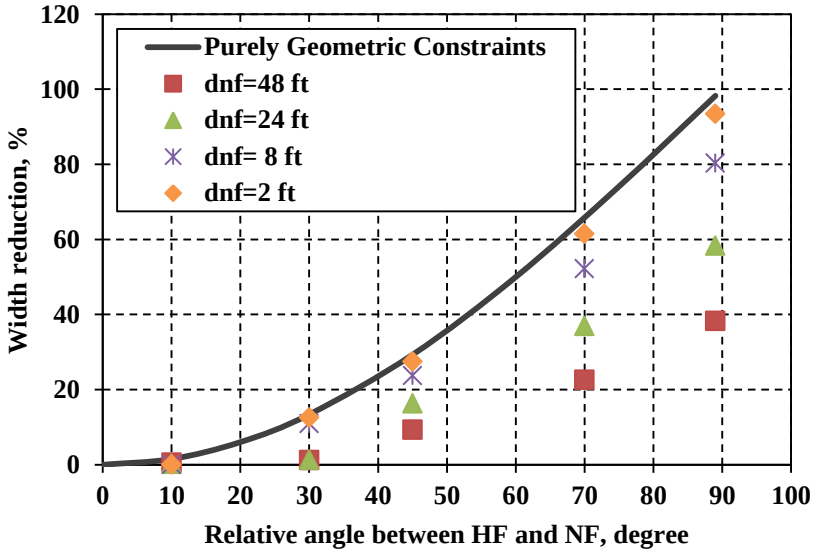

Figure 6.16: Width reduction of the natural fracture segment.

6.3.3 The effects of differential stress (S_{Hmax} - S_{hmin})

In this study, in an attempt to study the effects of stress shadow and differential stress (DS) separately, we simulate all the cases discussed above in an isotropic reservoir. In this subsection, the effects of differential stress on fracture geometry are investigated through studying the cases (Figure 6.8) with relative angle of 60^o and different differential stresses. Width profiles at the end of injection of the three cases are shown in Figure 6.17, which illustrates that width restriction in natural fracture segments is more severe for higher differential stress. After coming out from natural fractures, the fracture tends to propagate along the direction of the maximum horizontal stress and the kink angle is about 60^o when the differential stress is 100 psi or 200 psi. This is because for these two cases differential stress is greater than stresses induced by hydraulic fracture segment, and dominates fracture propagation direction. In addition, differential stress also has a great influence on injection pressure. Figure 6.18 presents the variations of net injection pressure with time and shows that higher elevation in injection pressure is required to start fluid penetration into the natural fractures for higher differential stress.

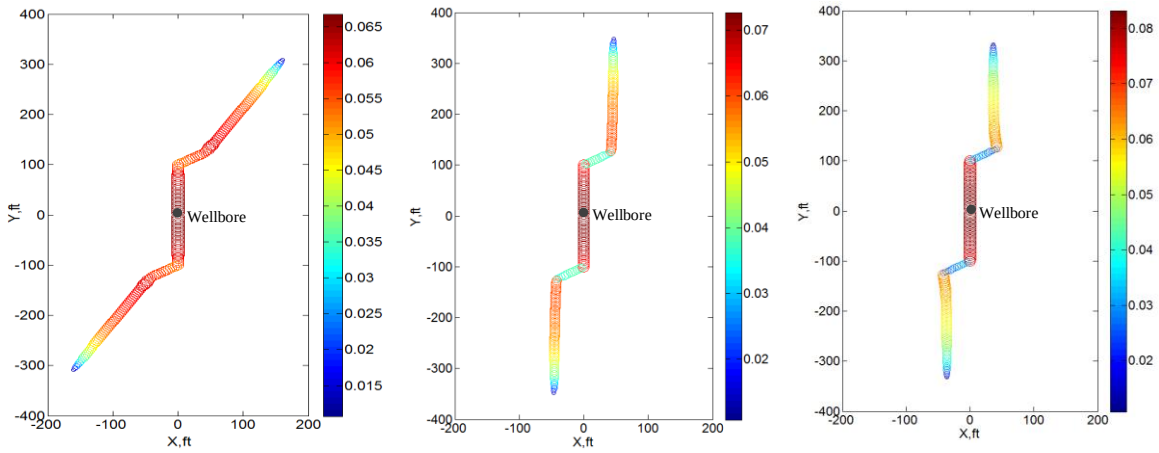

(a) DS = 0 psi (b) DS = 100 psi (c) DS = 200 psi

Figure 6.17: Width profile at the end of injection for different differential stresses.

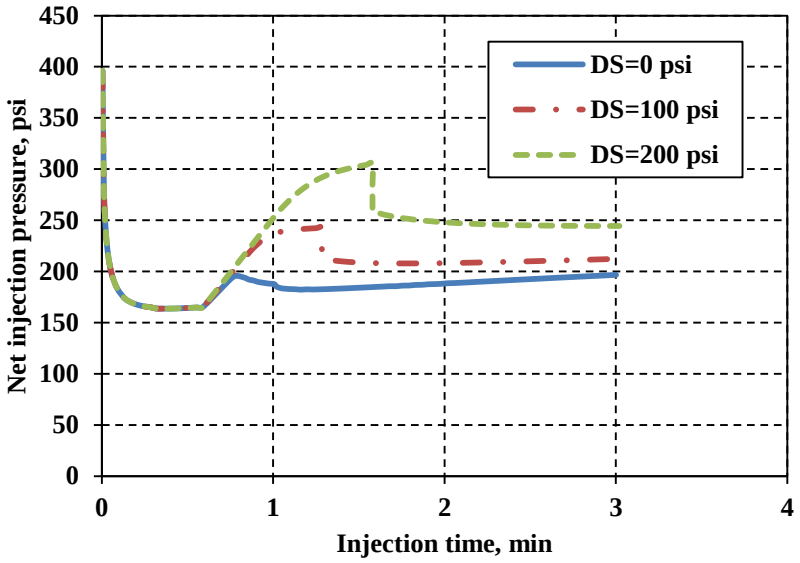

Figure 6.18: Variations of the net injection pressure at the injection point with time for different differential stresses.

6.3.4 The effects of natural fracture configurations

We simulate three cases with different schematics shown in the Figure 6.19. The symmetric case is the base case. The only difference between cases a and b is the position of two natural fractures relative to the hydraulic fracture, as shown in Figure 6.19 (a) and (b). Case c (Figure 6.19 (c)) only has one natural fracture. All the other parameters are kept the same for these three cases and listed in the Table 6.1. The injection point is located at (0, 0). The hydraulic fracture propagates and intersects two natural fractures simultaneously or sequentially, or only intersects one natural fracture at one side, resulting in different fracture geometry (Figure 6.20) and injection pressure (Figure 6.21).

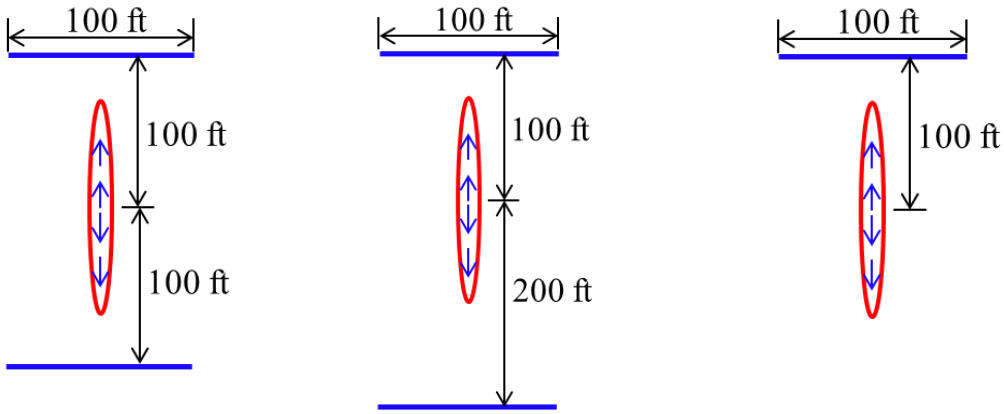

(a) Symmetric case (b) Non-symmetric case (c) One NF case

Figure 6.19: Three different schematics of a hydraulic fracture approaching natural fractures.

For the symmetric case (Case (a)), fracture geometry are symmetric, as shown in Figure 6.20(a). Fracture width at the segment of natural fractures is restricted. For the non-symmetric case (Case (b)), the hydraulic fracture intersects with natural fractures sequentially. When one wing of hydraulic fracture encounters a natural fracture, the propagation for this wing is greatly slowed down while the non-intersected tip propagates faster. When the other wing also meets a natural fracture, fluid rate is re-distributed and fluid flows into both wings. An unsymmetrical fracture geometry is formed (Figure 6.20(b)). For the case with only one natural fracture (Figure 6.20(c)), the propagation velocity of the hydraulic fracture decelerates on the natural fracture side and most of fluid flow and propagation occurs at the side fracture (Figure 6.20(c)).

The net injection pressure at the injection point is shown in Figure 6.21. Additional pressure is required to start fluid deflecting into a natural fracture. Magnitude of pressure elevation is dependent on many factors, including natural fracture configuration, approaching angles, differential stress. Based on cases shown in Figure 6.19, we can find that higher additional pressure is required for deflecting into natural

fractures simultaneously than sequentially. Injection pressure cannot greatly build up when one wing of the hydraulic fracture intersects with a natural fracture. This is because injection fluid can still flow into the other wing of the hydraulic fracture to avoid the impediment of the natural fracture. When the fracture tip at the other side also hit a natural fracture, pressure within the fracture will build up and propagation in this side will be slowed down.

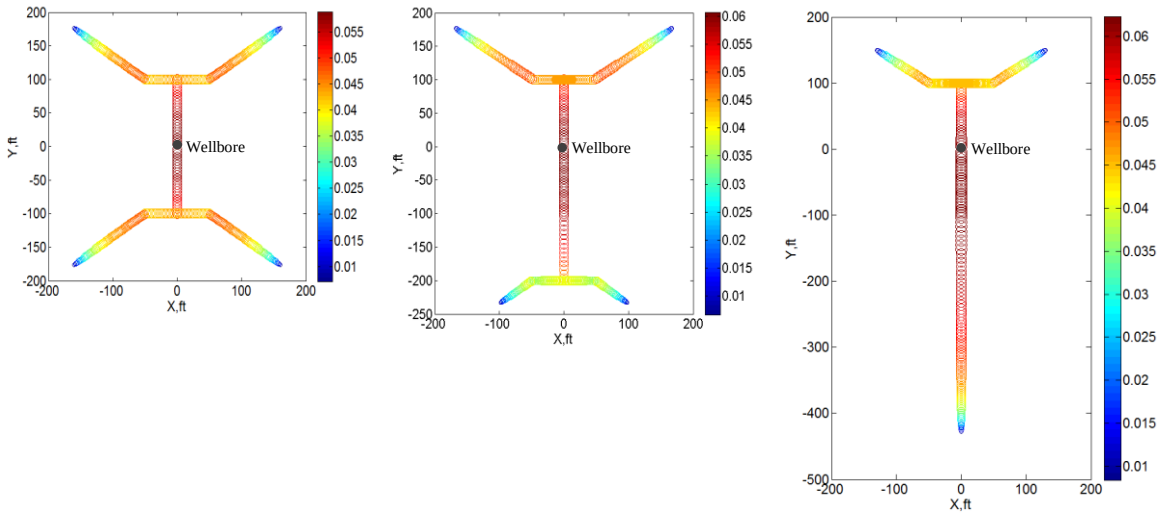

(a) Symmetric case (b) Non-symmetric case (c) One NF case

Figure 6.20: Width profile at the end of injection for the three cases in an isotropic stress reservoir.

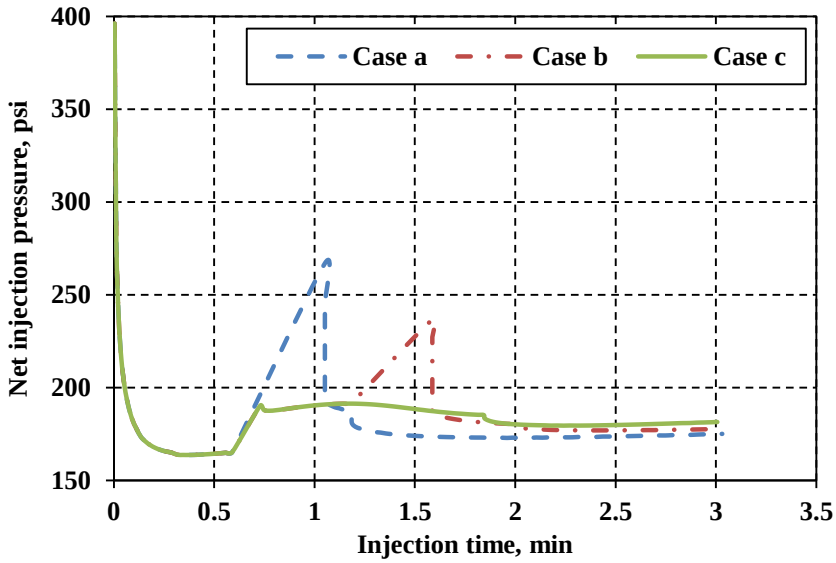

Figure 6.21: Variations of the net injection pressure at the injection point with time for the three cases in an isotropic stress reservoir.

6.4 ANALYSIS OF PHYSICAL MECHANISMS

From analyzing the effects of different parameters, it can be concluded that deflection into natural fractures requires additional injection pressure and cause fracture width restriction in natural fracture segments. Also, if differential stress is not zero, it causes higher elevation in injection pressure, more severe width restriction and larger kink angle. All these might be as results of higher closure stress acting across misaligned natural fractures and stress shadow effects from the hydraulic fracture segments. Higher closure stresses can be derived from in-situ stresses and the angle of natural fractures and are constant values along natural fractures. In this study, only induced stresses are analyzed through simulating a case with natural fractures of 400 ft in an isotropic stress reservoir (Figure 6.22).

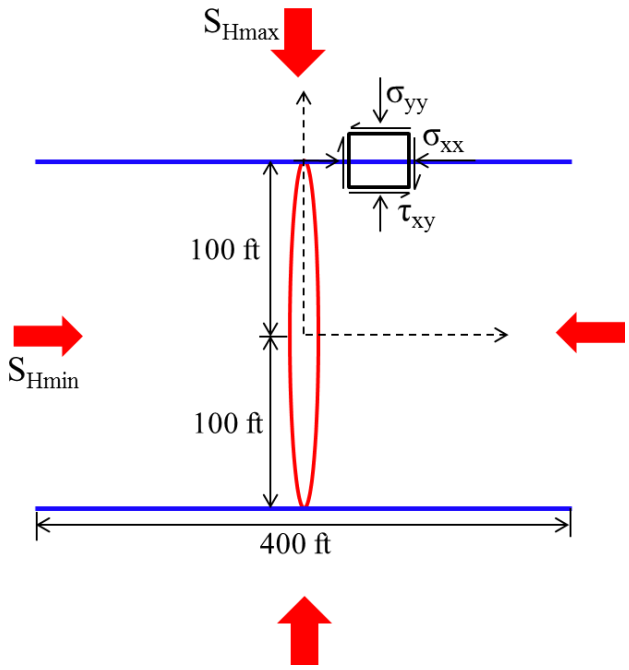

Figure 6.22: Schematic of stress field of a hydraulic fracture with two natural fractures.

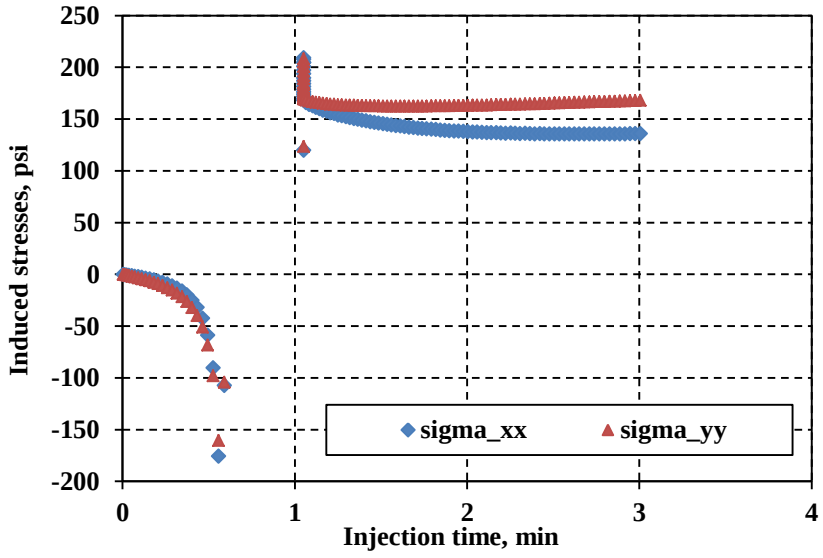

Figure 6.23: Induced normal stresses in x and y direction at the point (1, 100) in Figure 6.22.

The induced stresses on the natural fractures are changing as the hydraulic fracture propagates approaching to the natural fractures. Figure 6.23 shows induced normal stresses at the point (1, 100) beside the intersection point with injection time. It can be seen that there is a discontinuity once the hydraulic fracture encounters the natural fractures. Before intersection, tensile stresses at that point are induced and gradually increase as the tips approach the natural fractures. However, once the hydraulic fracture touches natural fractures, stresses acting on natural fractures switch from tension to compression. As the fracture propagates along the natural fractures, the induced compressional stresses achieve a constant value (Figure 6.23). Induced compressional stress in the y direction is higher than that in the x direction. These are additional stresses acting across the natural fracture segments, resulting in elevation in injection pressure and width reduction.

Figure 6.24 shows induced normal stress σ_{yy} distribution along the natural fracture segment at different time steps, illustrating that a large tensile stress is induced around the fracture tip and moves forward with fracture growth. Almost constant compressional stress is induced behind the fracture tip. In addition, there is no shear stress along the natural fractures for this case before fracturing. Figure 6.25 illustrates that after fracturing shear stress is induced around the fracture tip and gradually decreases as the tip moves forward. This is because the effects of stress shadow from hydraulic fracture segment gradually vanish as the fracture propagates away from the segment. The decrease in shear stress gives an explanation of the kink angle decreasing with the increment of the length of activated natural fractures shown in Figure 6.15.

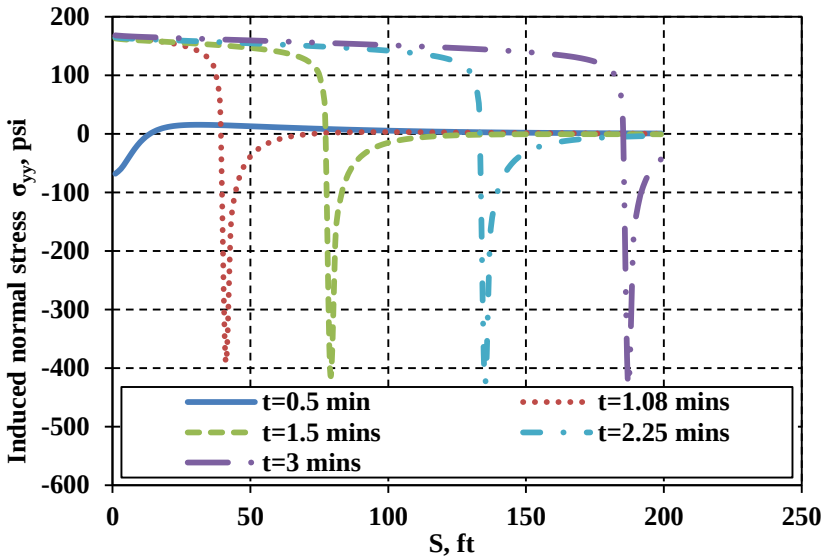

Figure 6.24: Induced normal stress in y direction from point (0, 100) along the natural fracture at different time steps.

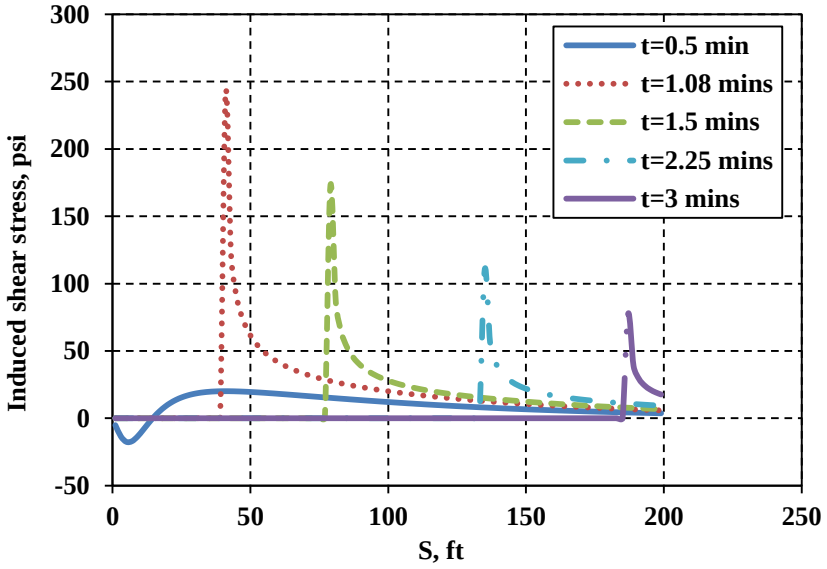

Figure 6.25: Induced shear stress from point (0, 100) along the natural fracture at different time steps.

6.5 DISCUSSION

When a hydraulic fracture propagates in a naturally fractured reservoir, the fracture might sequentially intersect with many natural fractures. A hydraulic fracture intersecting with multiple natural fractures is simulated in an anisotropic stress reservoir with differential stress of 100 psi. The purpose of running this case is to provide some insights into features of fracture geometry and injection pressure of a hydraulic fracture growing in a naturally fractured reservoir (Figure 6.26(a)). Fracture width is greatly restricted on the offsets (Figure 6.26(b)). There are big discontinuities of fracture width between its offsets and fracture segments. The width restriction and this sudden change in fracture path might increase fluid friction and impede proppant transport, resulting in high risk of screen-out. Net pumping pressure at the injection point is plotted in Figure 6.27, showing an up-and-down trend. The hydraulic fracture intersects with natural fractures sequentially, causing an increase of net pressure at the wellbore each time and dropping down when propagating along the natural fractures. This might be one of reasons that abnormal treating pressures are observed during fracturing treatments in the field (Medlin and Fitch, 1983). In practical applications, observation of the abnormal elevation in injection pressure could be taken as evidence of intersection with natural fractures, which might imply complex fracture networks. Jeffrey et al. (2009) adopted a two dimensional model to simulate a hydraulic fracture growing along natural fractures with offsets and obtained similar results about treating pressure and fracture width distribution.

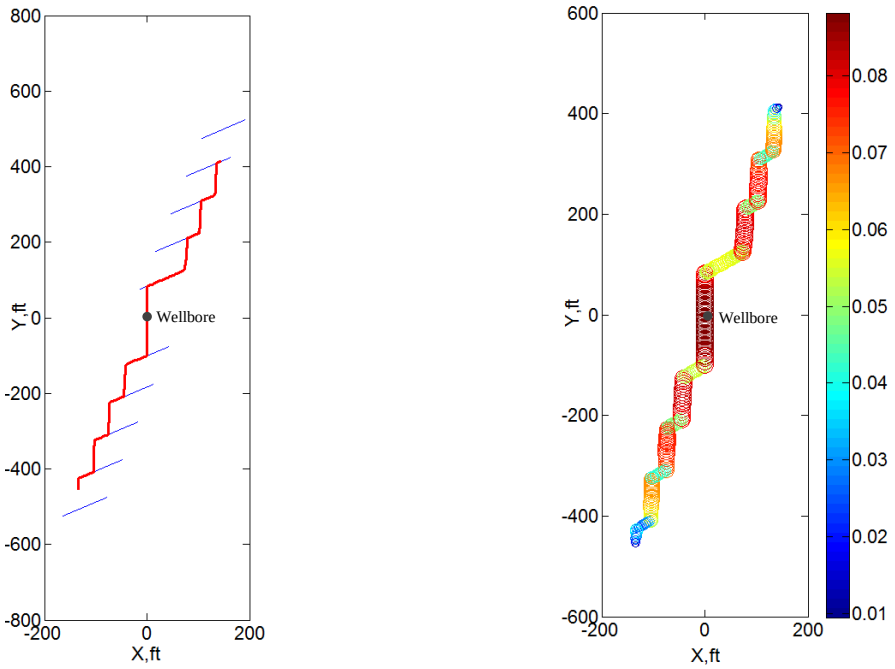

(a) Fracture trajectory (b) Width profile

Figure 6.26: Fracture trajectory and width profile at the end of injection.

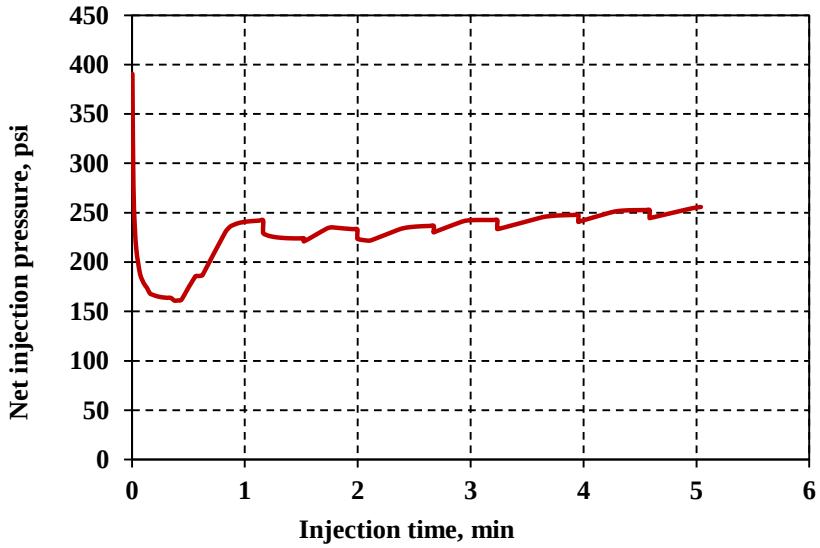

Figure 6.27: Variations of the net injection pressure at the injection point with time.

Our current model is able to simulate fracture propagation with constant fracture height, but cannot analyze the effects of height growth on fracture geometry and injection pressure response. Analytical models of PKN (Perkins et al., 1961; Nordgren et al., 1972) and KGD (Geertsma et al., 1969; Danaeshy et al., 1973) imparts the effects of fracture height on injection pressure. For the PKN model with an assumption of fracture height much less than fracture length, injection pressure increases as the fracture propagating; on the other hand, for the KGD model with an assumption of fracture height much greater than fracture length, injection pressure decreases as the fracture growing. For hydraulic fracturing in naturally fractured reservoirs, fracture length and height growing simultaneously as well as deflection into natural fractures result in different responses of injection pressure. Fracture height growth causes a decrease of injection pressure; on the contrary, deflection into natural fractures requires an elevation in injection pressure. If these two processes coincidently occur at the same time, response of injection pressure will depend on both of them. It is a big challenge to determine magnitude of the elevation in pressure which is affected by many factors. In some cases the elevation is easily observed from injection pressure history, while in some cases there is no obvious change of injection pressure. We reserve studying injection pressure of three-dimensional hydraulic fracturing in naturally fractured reservoirs in our future work.

6.6 CONCLUSIONS

Natural fractures play a significant role in hydraulic fracture growth and pressure response. Intersection with natural fractures can change fracture propagation trajectory, flow rate distribution and fluid flow pathways, resulting in abnormal pressure response and width restriction. In this Chapter, our complex hydraulic fracture development model

incorporating two crossing criteria is employed to study the physical mechanisms of a hydraulic fracture intersecting with natural fractures. A summary of the major conclusions is given below:

i. When both wings of a hydraulic fracture encounter natural fractures simultaneously and cannot cross them, pressure inside the hydraulic fracture builds up until natural fractures fail. When one wing of a hydraulic fracture encounters a natural fracture, the growth of this wing is retarded and fluid is re-directed to the other wing, and pressure within the fracture slightly increases. When the other wing also intersects a natural fracture afterwards, the pressure increases again and fluid flows into both sides of the fracture.

ii. The relative angle between HF and NF has a great influence on fracture geometry and pressure response. The larger the relative angle, the more severe width restriction and the higher elevation in injection pressure.

iii. Fracture geometry of intersection is also affected by the length of activated natural fractures. If activated natural fractures are very short, fracture width on the natural fracture segments will be greatly restricted, in particular for the relative angle of 90^{o}. In addition, after the hydraulic fracture come out from the tip of a natural fracture, the kink angle decreases as increasing the length of activated natural fractures.

iv. Differential stress worsens fracture width restriction and lead to high elevation in injection pressure. This is because of additional compressional stresses exerting on misaligning natural fracture segments.

v. Except additional closing stresses from in-situ stress field, stress shadow effects from the hydraulic fracture segment is another reason for width

reduction and pressure elevation. Compressional normal stresses and shear stress are induced on the natural fracture segments.

vi. The offset fracture geometry might be created when a hydraulic fracture propagates in a naturally fractured reservoir. Fracture width at the offsets is greatly restricted. Besides, wellbore injection pressure might aid in diagnosing whether complex fracture networks are created.

CHAPTER 7: COMPLEX FRACTURE NETWORK ANALYSIS

Chapter 6 investigated the effects of natural fractures on hydraulic fracture propagation and analyzed the physical mechanisms of the interaction between hydraulic and natural fractures. After understanding the interaction process, complex fracture networks generated in naturally fractured reservoirs are studied in this chapter.

To simulate hydraulic fracture growing in the naturally fractured reservoirs, we need to characterize natural fracture distribution. This chapter begins with an introduction to generating natural fracture patterns using a stochastic realization method. After that, we discuss how to provide reliable complex fracture geometry through combining our numerical model and diagnostic techniques. Microseismicity and fiber-optic sensing (distributed temperature sensing and distributed acoustic sensing) can be used to calibrate and validate the partitioning of flow rate and hypothetical microseismic event patterns calculated by our numerical model, respectively. In the last section, a series of sensitivity analyses is studied to examine the influence of perforation cluster spacing, differential stress and natural fracture patterns on fracture geometry complexity.

7.1 INTRODUCTION

Numerical fracture propagation models provide a critical link between fracture geometry and optimization of stimulation treatments. Hydraulic fracture propagation in naturally fractured reservoirs often develops complex fracture geometry. The complexity of fracture geometry results in significant uncertainty in fracturing treatment designs and field development optimization and is greatly affected by natural fracture patterns (Cipola et al., 2008; Olson et al., 2009; Dahi-Taleghani et al., 2009; Kresse et al., 2013). However, characterization of natural fracture distribution is a very challenging task based on limited available information. The reliability of the complex fracture geometry provided by numerical models has been challenged due to uncertain input parameters, such as natural fracture distribution. Therefore, more information given by diagnostic tools needs to be integrated and used to calibrate and constrain the fracture geometry from numerical models. The combination of diagnostic approaches and a hydraulic fracture model can greatly enhance the overall confidence in modeling and describing the complex fracture geometry in naturally fractured reservoirs.

Diagnostic techniques play an important role in providing detailed information about the fracturing process, fracture geometry and proppant placement in the fracture (Barree, 2002). However, none of diagnostic techniques can give the exact details of fracture geometry and full understanding of stimulation behaviors. Microseismicity and fiber-optic sensing can be used to provide more information about the fracturing process for calibrating numerical results and aid the fracture propagation model to predict accurate fracture geometry (Holley et al., 2010).

7.1.1 Microseismicity

Microseismic monitoring is one of the primary methods to indirectly assess the size and shape of generated hydraulic fracture in the far field, which provides the

information about fracture geometry for an entire stimulated region. Microseisms are very small-scale earth movements triggered by shear failure on bedding planes or natural fractures during hydraulic fracturing treatments. The shear failure is induced by stress changes during the fracturing process. There are two main mechanisms inducing the stress changes which could trigger the microseismicity (Warpinski, 1994; Warpinski et al., 2001; Warpinski et al., 2014; Garcia-Teijeiro and Rodriguez-Herrera, 2014). One is the leak-off of fracturing fluid. Pore pressure around the fracture is increased due to the leak-off of the high-pressure fracturing fluid, resulting in the reduction of effective stresses. The decrease of the effective stresses could activate the weakness planes and generate the source of microseismic events. The other mechanism is the mechanical effects of opening fractures. The dilation of an opening fracture induces additional compressive stress to the side of the fracture behind the tips and additional tensile stress near and ahead of the fracture tips, as discussed in Chapter 3. In the compressive zone, principal stresses are increased and the stability of weak planes in this zone is enhanced. In the region near the fracture tips, the stresses are tensile and the shear failure of weak planes is likely generated.

From the microseismic mapping, fracture geometry, such as orientation, length and height, can be estimated. But microseismicity cannot predict the fracture width distribution and provide the information about where the proppant is located in the far field after fracturing (Warpinski et al., 2014).

7.1.2 Fiber-optic sensing

Fiber-optic sensing in recent years has become a vital diagnostic tool for real-time monitoring of hydraulic fracturing treatments. It can be used to reliably observe the change of temperature, strain, and pressure as well as acoustics along the wellbore during

completion operations. Two fiber optic diagnostic tools primarily applied are distributed temperature sensing (DTS) and distributed acoustics sensing (DAS) (Sierra et al., 2008; Ugueto et al., 2014). DTS measures the temperature profile along the wellbore for estimating the distribution of the fluid and proppant into the fractures through wellbore temperature models (Seth et al., 2010; McCullagh et al., 2014; Yoshida et al., 2014). However, it is difficult for DTS to provide the actual injection rates of fracturing fluid (Molenaar et al., 2012). DAS is a relatively new technique which is able to quantify actual injection rates and proppant volume by analyzing the acoustic signal distribution along the wellbore (Molenaar et al., 2011). The resolution of both DTS and DAS is about 3 ft (1 m). The information from DAS and DTS can assess the fracture initiation points, fluid and proppant distribution among fractures, and the effectiveness of isolation tools in the near the wellbore region.

7.2 NATURAL FRACTURE CHARACTERIZATION

Two aspects of natural fractures should be understood to predict their effects on hydraulic fracture treatments, the mechanical properties of the natural fractures and their spatial distribution. The first aspect controls the hydraulic fracture propagation direction when the hydraulic fracture intersects a natural fracture. The second aspect contributes to the complexity of fracture geometry. In this chapter, natural fractures are assumed as frictional interfaces in the model. A crossing criterion, based on the extended Renshaw and Pollard criterion (Renshaw and Pollard, 1995; Gu and Weng, 2010), is used to determine the hydraulic fracture propagation direction after intersecting with a natural fracture (Figure 7.1). The detail of this criterion was analyzed in the Chapter 6.

Hydraulic fracture propagation upon intersecting a natural fracture is affected by the strength of natural fractures, relative angle between the natural and hydraulic fracture and the remote in-situ stress ratio. Figure 7.2 was given by Gu and Weng (2011), indicating the crossing condition for different in-situ stress ratios and a number of the relative angles with the condition of zero tensile strength and cohesion for the rock. The region to the right of each curve indicates the crossing condition. It is clear that the size of this region decreases with decreasing the relative angle. When the relative angle is 90^o, the hydraulic fracture can cross natural fractures with the friction coefficient greater than 0.4 for any in-situ stress ratio. Virtually no crossing is possible when the relative angle is 15^o or less.

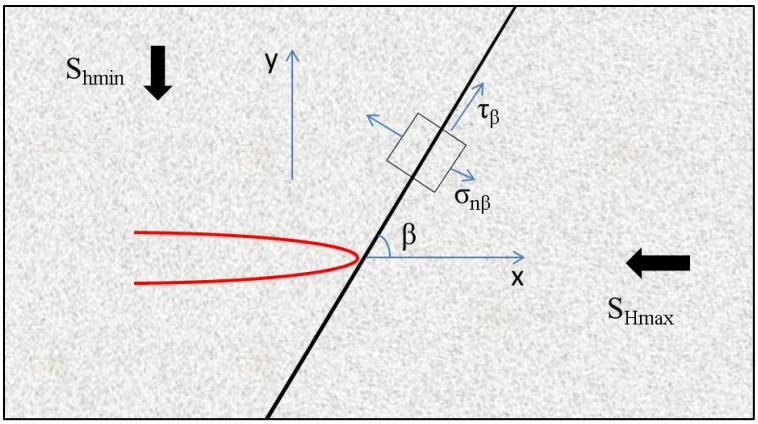

Figure 7.1: Schematic of a hydraulic fracture approaching a frictional interface.

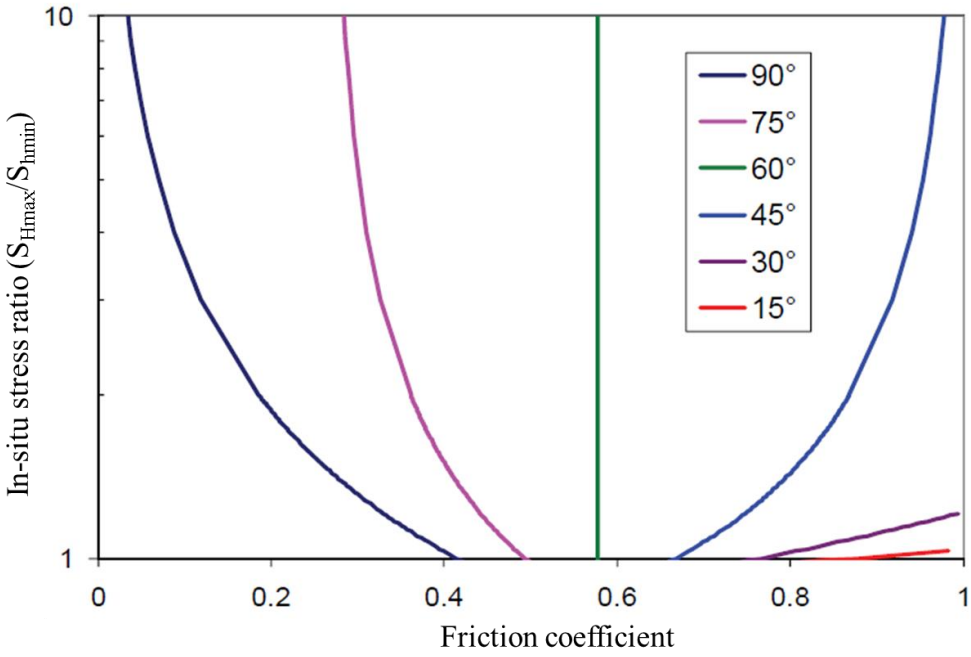

Figure 7.2: A crossing criterion for in-situ stress ratio between 1 to 10 and several intersection angles (Tensile strength $T_o = 0$ and cohesion $S_o = 0$). The region to the right of each curve is the crossing condition (Gu and Weng, 2011).

Based on the mechanical and geometric characterization of natural fractures, two types of methods are often used to describe natural fracture patterns, mechanical propagation models (Olson, 1993, 2007) and stochastic realization methods (Dershowitz and Einstein, 1988; Kulatilake et al., 1993; Bour et al., 1997; Bour et al., 2002; Darcel et al., 2003; Gale, 2004; Kim, 2007; Schultz et al., 2013; Hooker et al., 2013). Mechanical propagation models simulate the growing process of natural fractures, incorporating mechanical and fluid flow boundary conditions as well as rock properties and fractured bed thickness. According to the genesis of natural fractures (Pollard, 1988; Dahi Taleghani et al., 2013), there are four types: (1) tensile fractures due to compressive stresses; (2) shear fractures due to compressive stresses; (3) tensile fractures due to unloading of compressive stresses; (4) natural hydraulic fractures. Olson (1993, 2007)

developed a mechanical model to identify the important processes controlling propagation of joints in reservoirs. The model was based on a displacement-discontinuity, boundary-element numerical method incorporating an approximate correction factor for bed thickness effects. The results from the model indicated that boundary conditions and rock properties systematically affect final joint patterns observed from outcrops. Fracture length distributions might be described as power-law functions. The area distribution and lengths of joints are controlled by the subcritical growth law of propagation velocities between fractures.

The growth of a wide range of geologic structures is controlled by basic mechanical conditions, which make statistical analysis possible to investigate and understand the geometric attributes of the structures. Bonnet et al. (2001) reviewed the scaling of fracture systems in geological media and stated that power laws and fractal geometry provide applicable tools for characterizing fracture systems. They also introduced some methods to estimate exponents and fractal dimensions for fracture systems and provided a compilation of magnitudes of these properties. Bour and Davy (1997) applied power law fault length and random spatial distributions to study the connectivity of fault networks. Bour et al. (2002) developed another statistical scaling model for fracture network geometry and validated with a multi-scale mapping of a joint network. This model employed a power law in both fracture positions and lengths with three main parameters. Darcel et al. (2003) also applied stochastic fractal correlations to generate fracture networks for studying the connectivity properties of two-dimensional fracture networks. Kim (2007) developed stochastic fractal models in two and three dimensions to characterize fracture networks and estimated fracture porosity of naturally fractured reservoirs. Fractal theories were adopted to generate fracture center positions, fracture length and width. Schultz et al. (2013) adopted maximum likelihood estimation

methods for the distribution of length and displacement of opening-mode fractures, and then statistically evaluated the relationship between length and displacement. Hooker et al. (2013) described fracture-aperture-size distributions, spacing and tendency to be bed bounded in Cambrian Meson group, NW Argentina and summarized that fracture opening-displacement size distributions tend to follow a power law when fracture growth is unequally partitioned among variably cemented fractures; when growth is not influenced by cementation, the opening displacement follows a characteristic size distribution.

Two fracture characteristics contribute especially to the network complexity: fracture center location and fracture length distribution. In this section, we adopt random distribution in space or along one dimension to describe fracture-center positions. Fracture lengths are drawn from a power law probability distribution (Segall and Pollard, 1983; Davy, 1993; Gale et al., 2007; Olson, 2007):

$$n(l)dl = \alpha l^{-a}, \tag{7.1}$$

where $n(l)dl$ is the number of natural fractures having a length in the range [l, $l+dl$], α is a coefficient of proportionality, and a is an exponent varying between 1 and 3. As shown in Figure 7.3, the probability to introduce large fractures is much smaller than that of having small fractures. The relative abundance of small versus large fractures is inversely proportional to the magnitude of the exponent a (Figure 7.3).

Natural fractures are divided into sets based on common orientation. In Barnett shale, the dominant trend of natural fractures is west-northwest, and another set trends north-south (Gale et al., 2007). To investigate the sensitivity of the created geometry of fracture networks, we generated a single set of vertical natural fractures with a strike orientation of 45^{o} in a 1000 ft × 1000 ft square reservoir (Figure 7.4). Fracture spacing

was varied from random (Figure 7.4(a)) to regular (Figure 7.4(b)). Both patterns were created using exponent of power law $a = 2$ (Figure 7.5).

In our current model, all natural fractures are potential deformation locations. They are not discretized (no boundary elements are assigned) until the hydraulic fracture tip intersects the natural fracture and the interaction criterion indicates the fluid will be diverted along it. Only then is the natural fracture actually included into the deformation model. It is also assumed that once a hydraulic fracture diverts along the pre-existing path of a natural fracture, it must propagate to the end of the natural fracture before kinking back into the matrix.

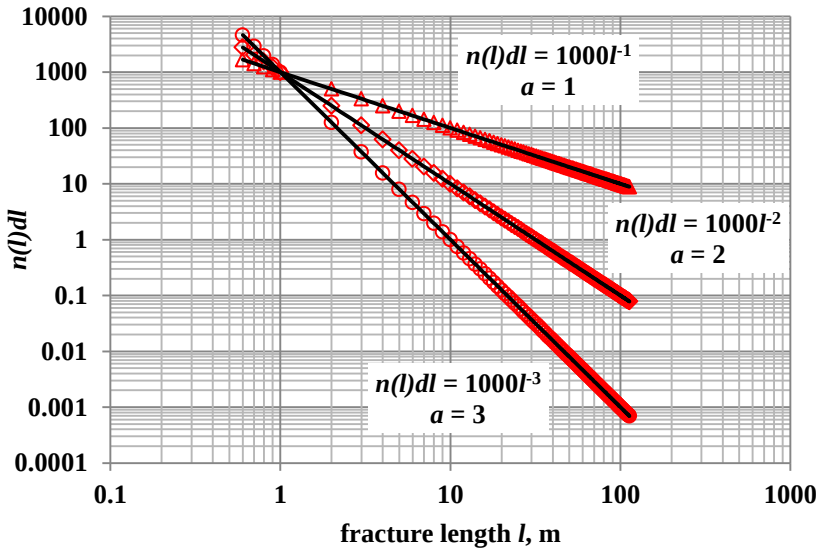

Figure 7.3: Illustration of the density $n(l)$ for power law population with exponent $a = 1$, 2 and 3.

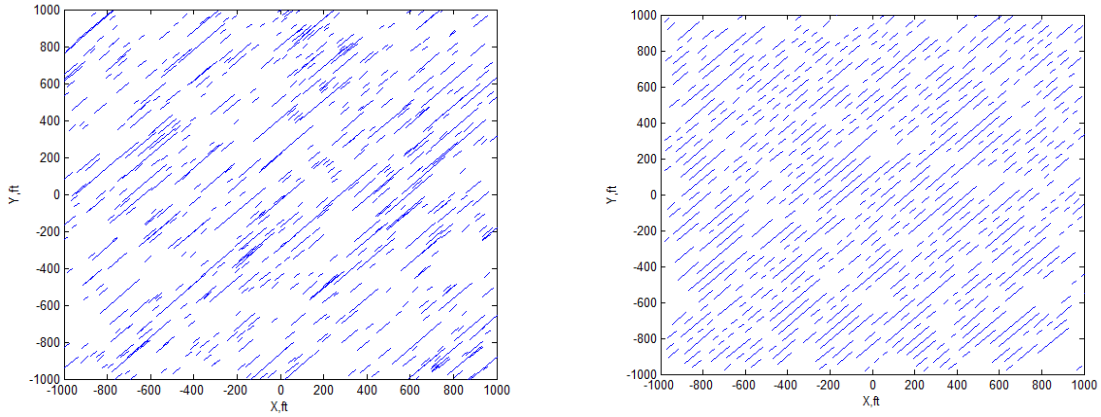

(a) (b)

Figure 7.4: Natural fracture patterns with power law fracture lengths distribution ($n(l)dl = \alpha l^{-a}$): (a) random distribution in space of fracture centers; (b) regular spacing of fracture centers.

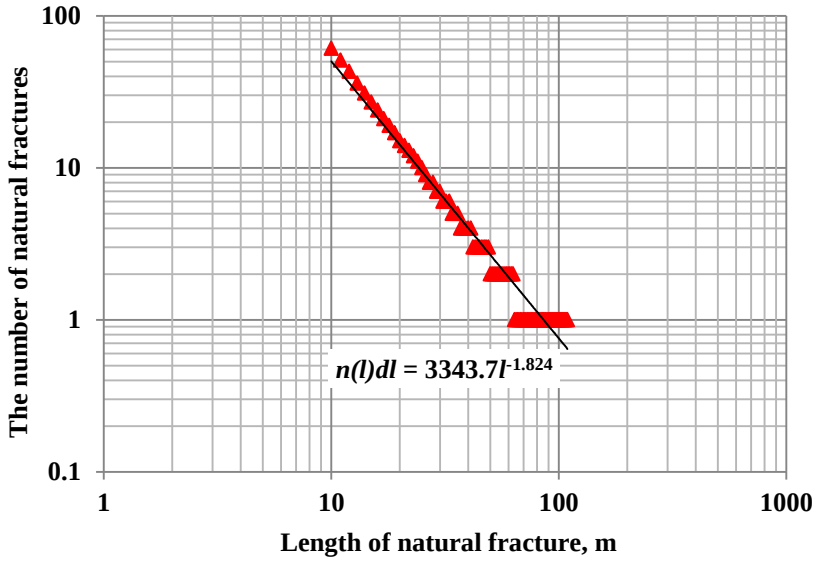

Figure 7.5: Fracture length distribution in Figure 7.4.

7.3 INTEGRATION OF DIAGNOSTIC TECHNIQUES FOR CALIBRATING FRACTURE MODELING

In this section, we run several cases to show how to relate our numerical model to diagnostic techniques. Microseismicity can provide an overall image of assessing where the fracture is likely to be created in the far-field, while DTS and DAS can provide almost immediate updates of the near-wellbore fluid rate into the fractures. Microseismicity operates at coarse resolution over a large area, and DTS and DAS offer fine resolution in the meter range near the wellbore. The information available through microseismicity and fiber-optic sensing is complementary and provides a complete picture of fracture stimulation for validating and constraining numerical results. We run cases of four fractures in a single stage growing simultaneously (Figure 7.6) and calculate the split of the fluid between different perforation clusters and a hypothetical microseismic event pattern which can be used to compare and validate with information offered by DTS and DAS and microseismicity, respectively. All the input parameters are listed in Table 7.1.

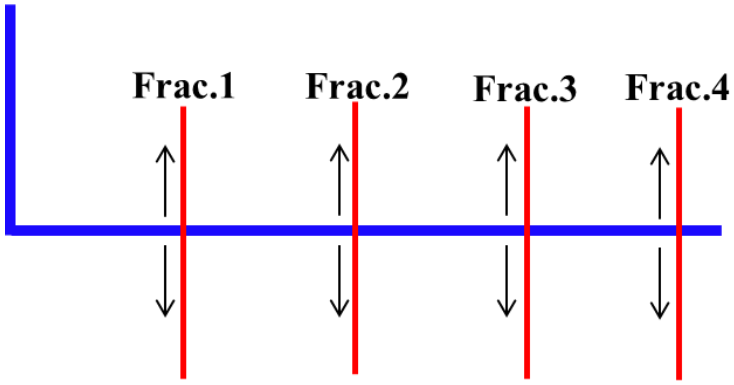

Figure 7.6: Illustration of four fractures propagating simultaneously.

Injection rate	60 bpm
Length of a stage	300 ft
Layer height	100 ft
Minimum horizontal stress	4450 psi
Fluid leak-off coefficient	0.00001 $ft/min^{0.5}$
Viscosity	1 cp
Young's Modulus	6.53×10^{6} psi
Poisson's Ratio	0.2
No. of perforations	60
Density of Slurry	1.2 g/cm^3
Diameter of perforations	16 mm
Diameter of wellbore	0.1 m
Proppant	40/70 Mesh
Proppant diameter	0.0124 inch
So	0 psi
To	900 psi
μ	0.6

Table 7.1: Input parameters for multiple fractures propagating simultaneously.

7.3.1 Modeling without natural fractures

The partition of flow rate entering a fracture approximately corresponds to the partition of the amount of proppant located in the fracture. Hence, the variation of flow rates can indirectly reflect fracture conductivity from the proppant distribution. One output of our model is the split of flow rate between various fractures in a stage. To

clearly show the partition of flow rates between different perforation clusters, we study four fractures growing simultaneously without the influence of natural fractures in this section. Two cases with different perforation cluster spacing and differential stresses are studied. Cluster spacing for case (a) is 100 ft and differential stress is 100 psi, while cluster spacing for case (b) is 70 ft and differential stress is 1000 psi. The influence of wellbore friction can be ignored because the distance between perforation clusters is small. Perforation friction pressure for each fracture is almost identical and small relative to the pressure within the fractures. Hence, fractures 1 and 4 have the same fracture geometry, and fractures 2 and 3 also have the same dimensions as shown in Figure 7.7. The stress shadow effects in case (b) are greater than the effects in case (a) because of closer cluster spacing. Also, it is harder for fractures in case (b) to turn away from each other to alleviate strong fracture interaction because of higher differential stress. It is clear from Figure 7.7 that fractures of case (b) are more planar that fractures of case (a).

Figure 7.8 shows the percentage of flow rate entering into fractures 1 and 2 for case (a) and (b), indicating that the exterior fractures receive more fluid and tend to dominate the propagation. The total volume taken by an exterior fracture is 39% for case (a) and 46% for case (b), as shown in Figure 7.9. For the case (b) with strong stress shadow and greater differential stress, the interior fractures almost cannot grow and the exterior fractures take the majority of the fluid volume, which has also been observed in the field by DTS and DAS (Wheaton et al., 2014).

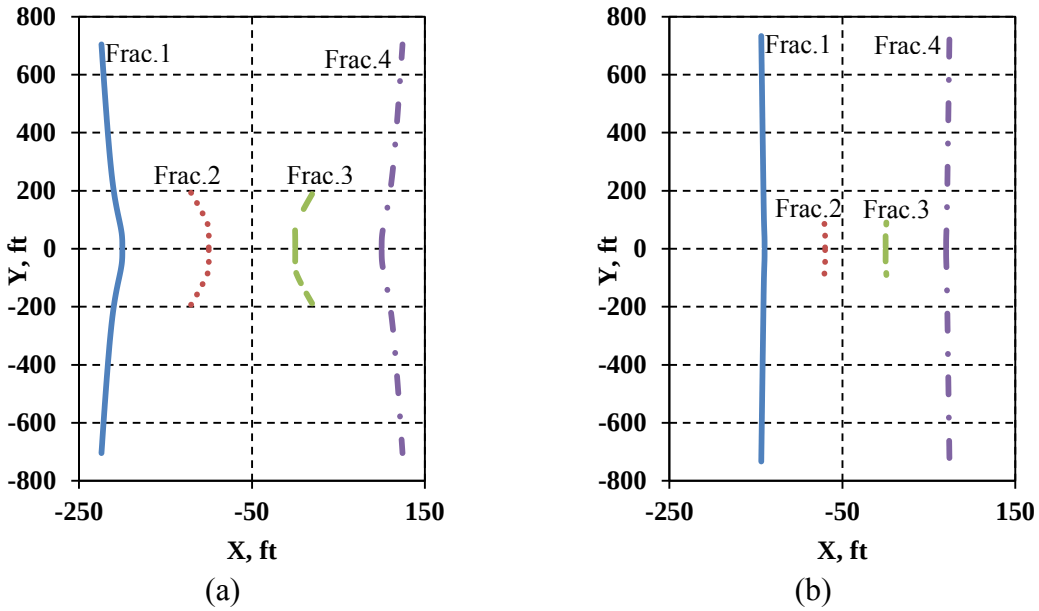

Figure 7.7: Fracture trajectory at the end of injection for case (a) with 100 psi differential stress and 100 ft cluster spacing and case (b) with 1000 psi differential stress and 70 ft cluster spacing.

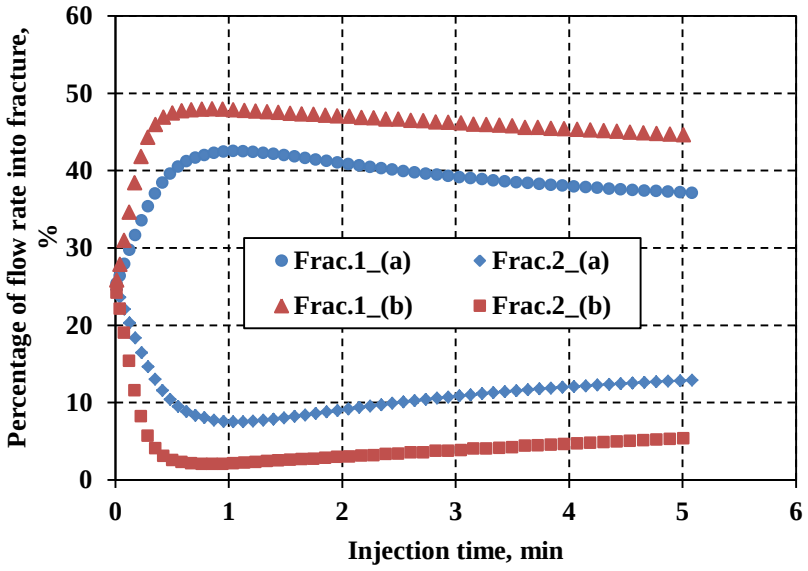

Figure 7.8: Percentage of flow rate splitting into each fracture vs. injection time for case (a) and case (b).

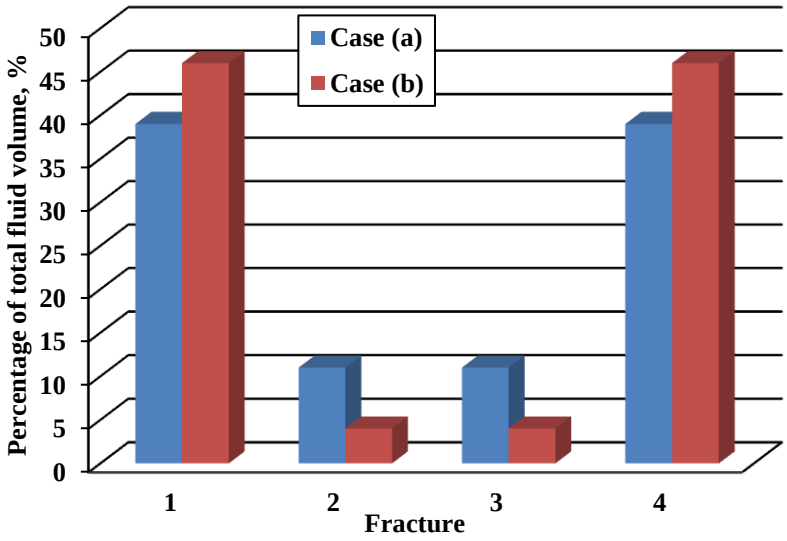

Figure 7.9: Percentage of total fluid volume splitting into each fracture at the end of injection for case (a) and (b).

7.3.2 Modeling with natural fractures

In this section, we run case (a) discussed in section 7.3.1, with the addition of natural fractures. Figure 7.10 shows fracture width distribution for four fractures, which illustrates that the fractures intersect natural fractures, propagate along the pre-existing paths of natural fractures and then come out from the tips. Fracture width is restricted on the natural fracture segments. The geometry of the two fracture wings is not symmetric because of a heterogeneous natural fracture distribution. The percentage of flow rate for each fracture wings is plotted in Figure 7.11, showing an obvious decrease of flow rate when a wing encounters a natural fracture and an increase of flow rate when the wing comes out from the tip of the natural fracture. Natural fractures can retard the growth of hydraulic fractures and vary the partitioning of flow rate between multiple fractures. In other words, sudden variations in flow rate observed by DTS and DAS might indicate the intersection with natural fractures. Besides, it is possible to infer the location of natural

fractures through combining fracture path provided by our model with real time data from DTS and DAS. The partitioning of total fluid volume at the end of injection is shown in Figure 7.12, illustrating that intersecting with natural fractures can change the distribution of fluid and make interior fractures receive more fluid. When the exterior fractures intersect natural fractures, the propagation of the interior fractures is enhanced to a certain degree. Comparison of Figures 7.9 and 7.12 indicate that natural fractures can change the fluid volume distribution between multiple fractures and alleviate the uneven development of multiple fractures.

Figure 7.13 shows a hypothetical microseismic event pattern based on shear failure of natural fractures induced by hydraulic fractures. Shear failure is determined by the linear friction law (Eq. 6.6) based on induced stresses from hydraulic fractures. Our model only captures the shear failure generated by mechanical effects from opening fractures. Poroelasticity induced by leakoff is not considered in the model. Figure 7.13 shows the hypothetical microseismic maps can approximately reflect fracture geometry.

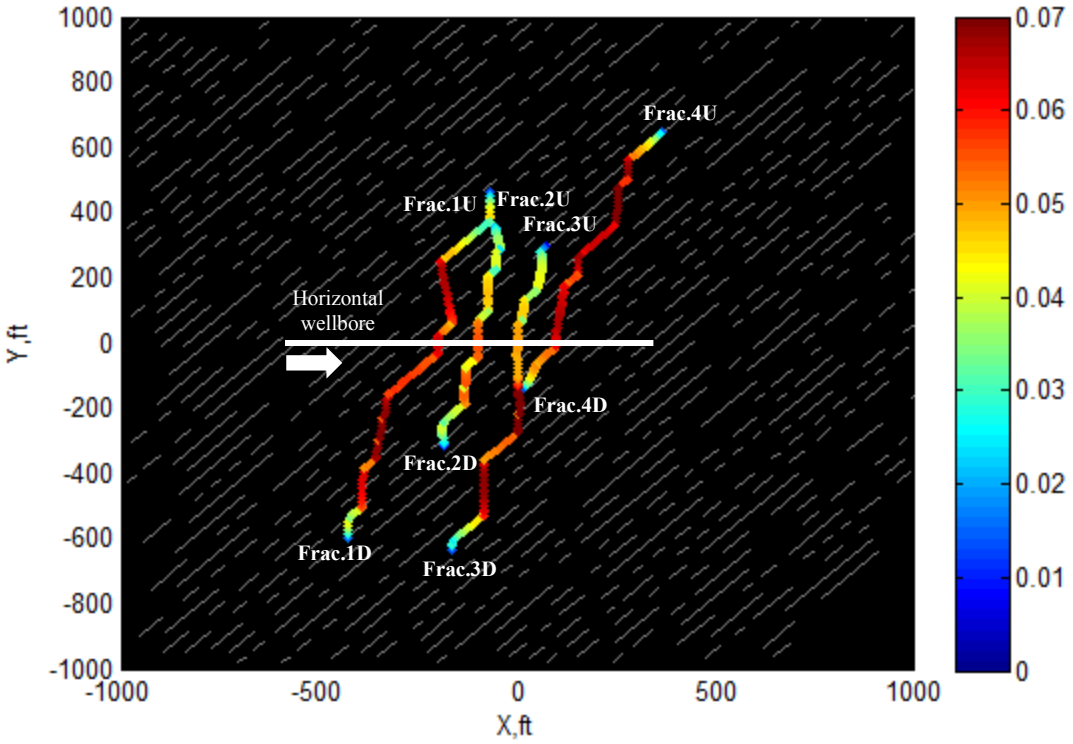

Figure 7.10: Fracture width distribution for four fractures propagating in a naturally fractured reservoir.

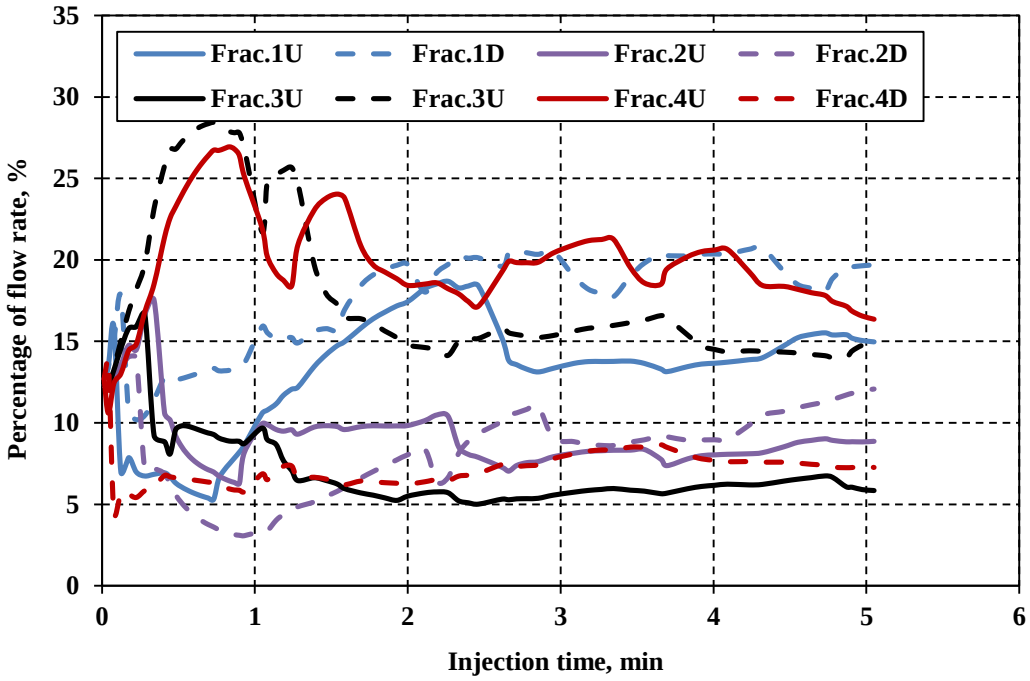

Figure 7.11: Percentage of flow rate splitting into each fracture vs. injection time.

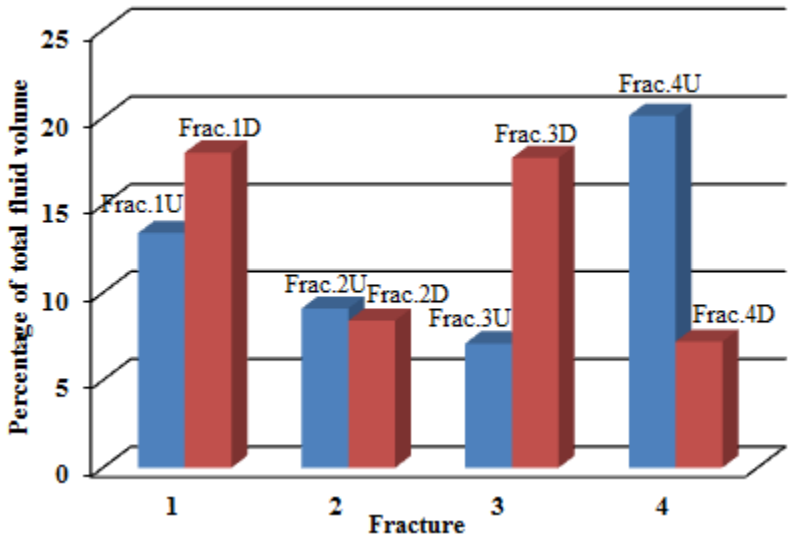

Figure 7.12: Percentage of total fluid volume splitting into each fracture wings at the end of injection.

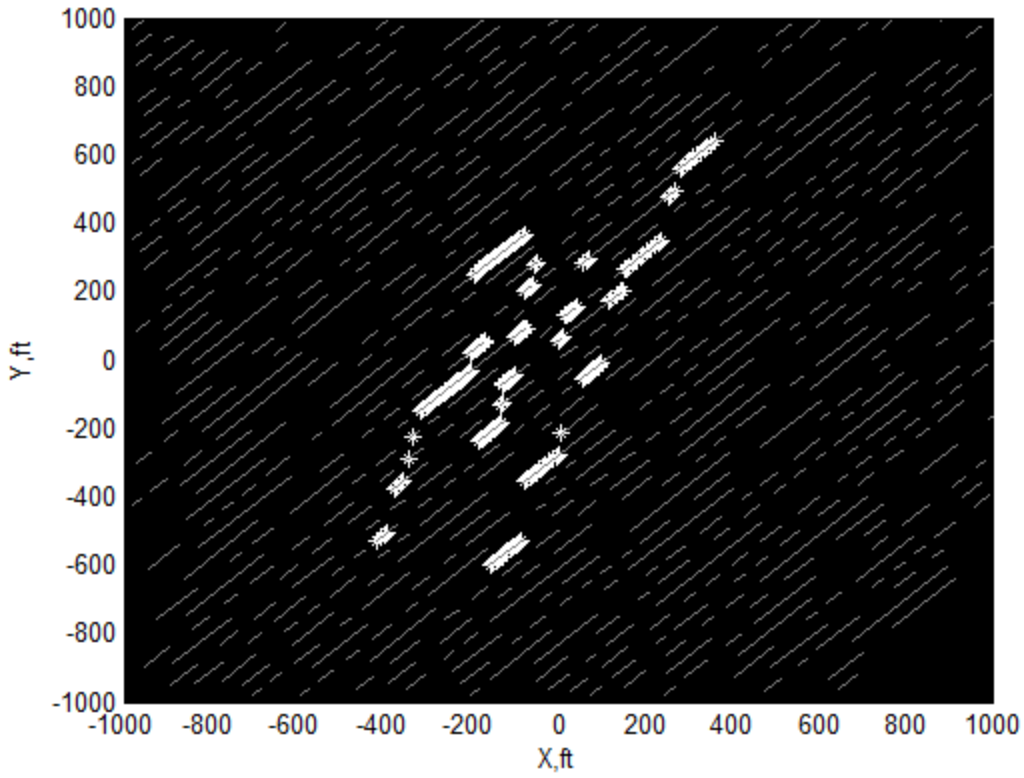

Figure 7.13: Hypothetical microseismic event pattern ('*': microseismic activity).

7.4 SENSITIVITY ANALYSIS OF COMPLEX FRACTURE NETWORKS

A series of simulations was performed using our fracture propagation model to illustrate the impact of perforation cluster spacing and differential stress (DS = S_{Hmax} - S_{hmin}) on fracture geometry and injection pressure in the naturally fractured reservoirs. The parameters (Table 7.1) are prescribed based on the published data for shale reservoirs. Fracture height is constant and equal to the thickness of the reservoir formation. Hence, fracture surface area is dependent on the effective length of hydraulic fractures. The effective fracture length is determined by proppant transport in the

complex fracture networks which is relative to proppant diameter. Cipolla et al. (2011) stated that the effective length is fracture length with aperture of 2.5 times greater than the average proppant diameter, which can allow proppant to enter a fracture.

7.4.1 The effects of perforation cluster spacing

Perforation cluster spacing is a very important factor that can be optimized to maximum oil/gas production. The cluster spacing affects oil/gas production, in two ways - pressure interference from production and fracture interaction between multiple fractures (Yu and Sepehrnoori, 2014; Yu et al., 2014). We solely focus on studying the fracture interaction. The stress shadow effects of simultaneous multiple fractures can result in uneven fracture growth (Olson, 2008; Roussel and Sharma, 2011; Wu and Olson, 2013). Furthermore, natural fractures also affect fracture growth and might generate complex fracture networks (Olson and Dahi-Taleghani, 2009; Dahi-Taleghani and Olson, 2009; Kresse et al., 2013; Wu and Olson, 2014(a)). The goal of stimulation designs is to expose as much fracture surface area as possible at the least amount of cost, because it is believed that drainage area is directly related to the surface area.

The total effective fracture length for four cases with different perforation cluster spacing is as shown in Figure 7.14 for a stage with a length of 300 ft. Changing the perforation cluster number from 3 to 6 changes cluster spacing from 150 ft to 60 ft. Previous work on stress shadows (Wu and Olson, 2013) suggests that when fractures have a spacing equal to or less than their height, fracture width will be hindered in the interior fractures of a multi-cluster stage. The widest spacing case in Figure 7.14 (S/H = 1.5) would consequently be considered a mild interaction case, and the 6 fracture case would be strong (S/H = 0.6). With decreasing perforation cluster spacing, the variability of growth between the fractures of a given stage increases. In the strong interaction case,

the exterior fractures have longer effective lengths than the interior ones. The larger the number of fractures, the more uneven effective fracture length distribution. The results also show that increasing the number of perforation clusters in fixed length stage does not necessarily result in increased total fracture length. For the range of input examined, the maximum total fracture length was for the case of 4 fractures. The greatest penetration away from the wellbore, however, was achieved for the closest spaced case which had the strongest mechanical interaction. Only 2 of the 6 fractures grew, allowing those that did grow to penetrate furthest away from the wellbore.

Figure 7.15 shows fracture extent and width profiles at the end of injection for each case. The grey lines represent natural fractures and lines with different colors represent the hydraulic fracture width distribution. Fracture width profiles of the four cases illustrate that near the wellbore, fracture surface area for cases with small cluster spacing (e.g. the case with 6 fractures) is much larger than that for cases with large cluster spacing (e.g. the case with 3 fractures). Away from the wellbore, however, the cases with small cluster spacing have somewhat less surface area and smaller width. This might imply a horizontal well with small cluster spacing could have high production rates during early time, but decline rapidly during the late time (Khan, 2013).

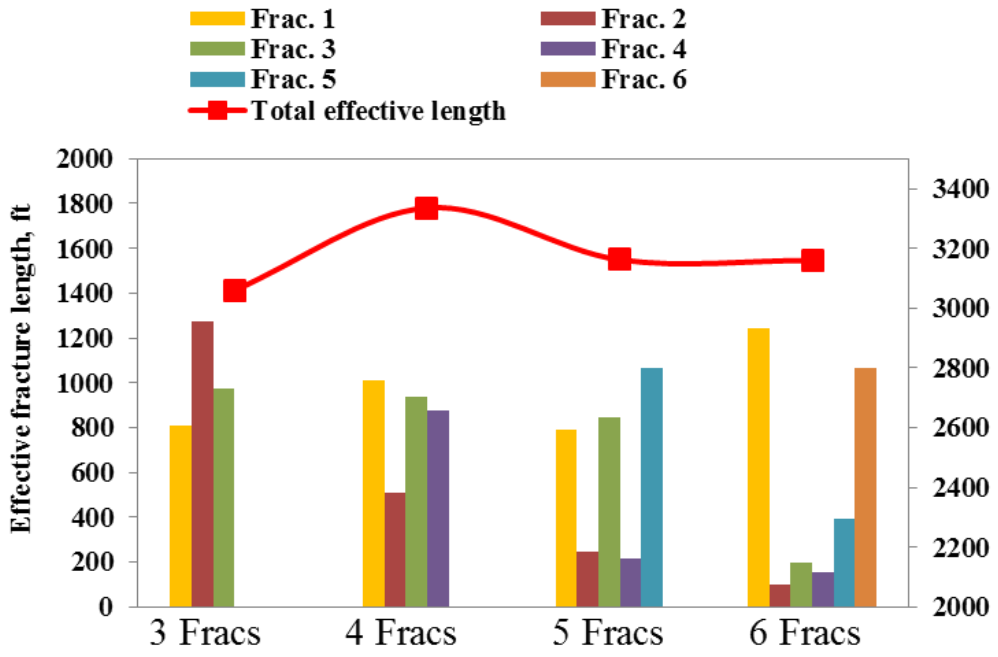

Figure 7.14: Effective fracture length distribution and total effective fracture length for four cases with different perforation cluster spacing (slickwater, injection rate = 60 bpm, DS = 100 psi, relative angle = 45^{o}, a = 2, NF spacing = 55 ft).

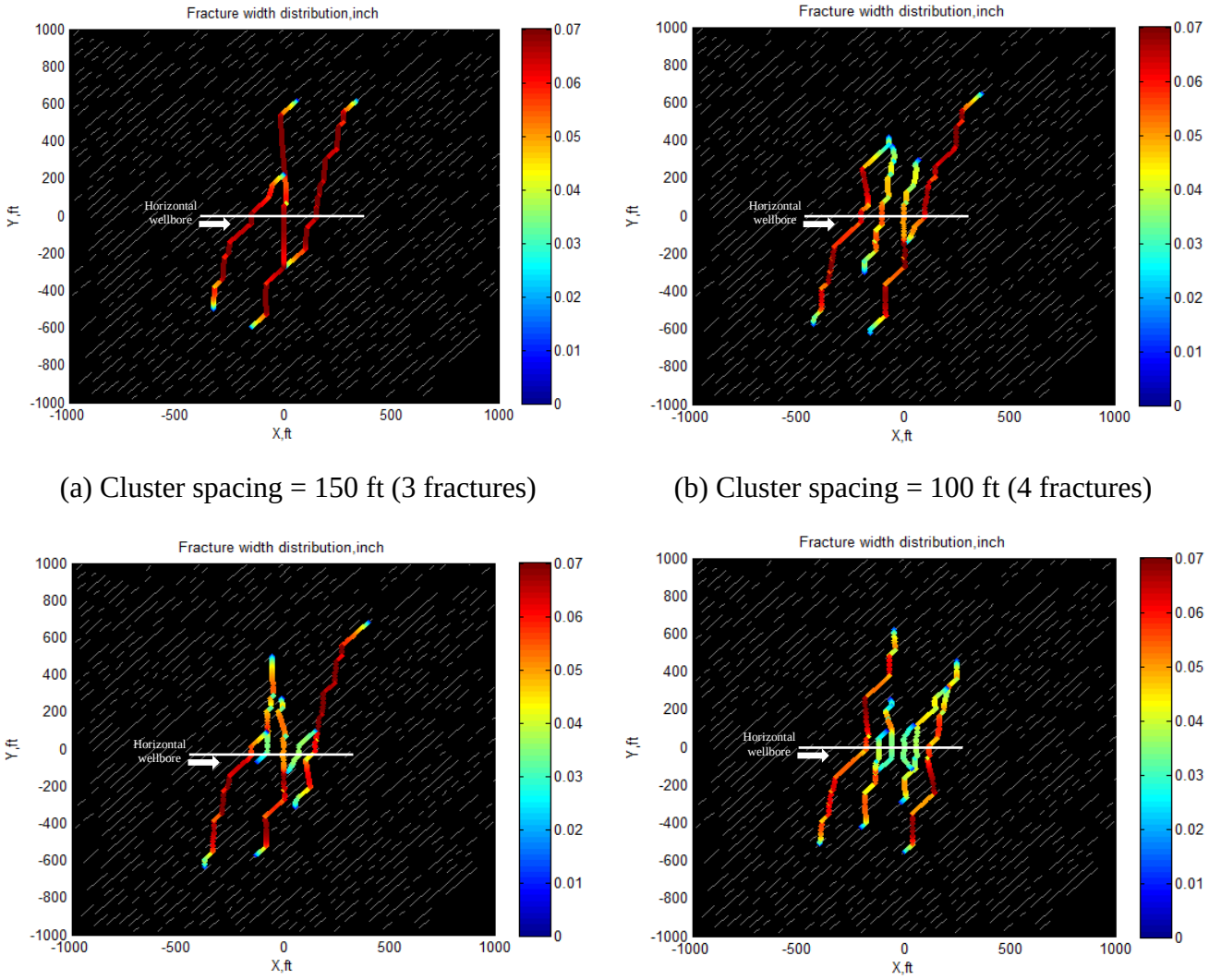

(a) Cluster spacing = 150 ft (3 fractures)

(b) Cluster spacing = 100 ft (4 fractures)

(c) Cluster spacing = 75 ft (5 fractures)

(d) Cluster spacing = 60 ft (6 fractures)

Figure 7.15: Width profile of fracture networks at the end of injection for four cases with different perforation cluster spacing (slickwater, injection rate = 60 bpm, DS = 100 psi, relative angle = 45^{o}, a = 2, NF spacing = 55 ft, '*': microseismic activity).

7.4.2 The effects of the remote differential stress

Remote differential stress also has a great impact on injection pressure and fracture complexity. Figure 7.2 indicates that the crossing condition is affected by the in-situ stresses ratio. Generally, the ratio is greater than 1 and less than 2. When the relative

angle of the hydraulic and natural fracture is 45^{o} and the friction coefficient is 0.6, it is evident from the figure that hydraulic fractures cannot cross natural fractures for any differential stresses. Furthermore, non-zero tensile strength of the rock makes it even harder to cross the natural fractures. Therefore, in this case hydraulic fractures will not cross natural fractures for three distinct differential stresses (0 psi, 100 psi, 300 psi). When a hydraulic fracture grows along a misaligned direction, additional stresses will act on the hydraulic fracture. Figure 7.16 shows net injection pressure at the wellbore with time and illustrates that the net pressure increases with increasing differential stress. In addition, the net pressure of the cases with different differential stresses exhibits distinct magnitudes of pressure change as intersecting with natural fractures, emphasizing that net pressure trend might be able to aid in characterizing complex fracture geometry.

Total fracture length and effective length are shown in Figure 7.17, illustrating that fracture growth is suppressed by high differential stress when hydraulic fractures divert along natural fractures. Fractures propagating in a reservoir with high differential stress have shallower reservoir penetration and wide fracture aperture (Figure 7.18) because fracture propagation is greatly slowed down when intersecting with natural fractures in the formation with high differential stress. The orientation histograms of fracture geometry are shown in Figure 7.19 by rose diagrams. Under isotropic stress conditions, hydraulic fractures have the tendency to continue growing along the direction of natural fractures after breaking out and have very small chance to grow in their original direction. Under anisotropic stress conditions, the chance of growing in the original direction increases and depends on the magnitude of differential stress. Figure 7.19(b) shows that fractures propagate along natural fractures, and then turn back to the original direction after coming out from the tips of natural fractures. As differential stress increases, Figure 7.19(c) indicates that hydraulic fractures mainly propagate along their

original direction. The complexity of fracture geometry is mitigated by high differential stress.

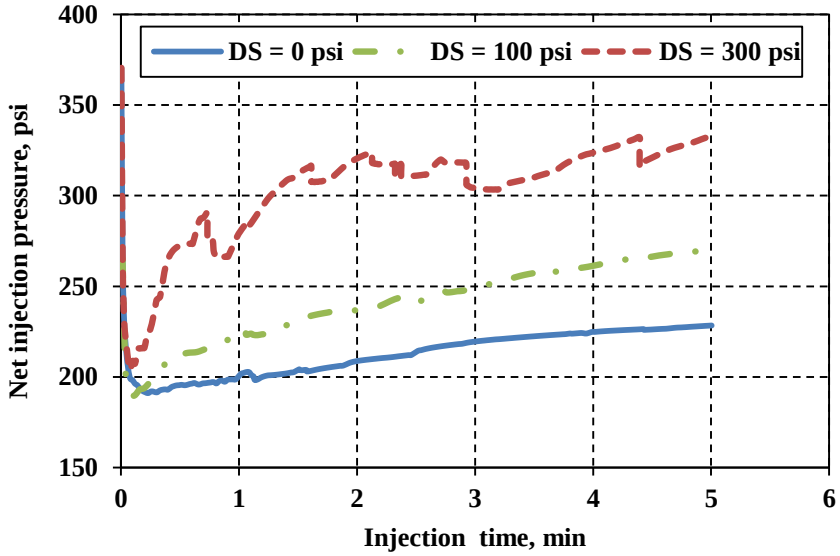

Figure 7.16: Variations of the net injection pressure at the heel of horizontal wellbore for three cases with different differential stresses (cluster spacing = 100 ft, slickwater, injection rate = 60 bpm, relative angle = 45^{o}, a = 2, NF spacing = 55 ft).

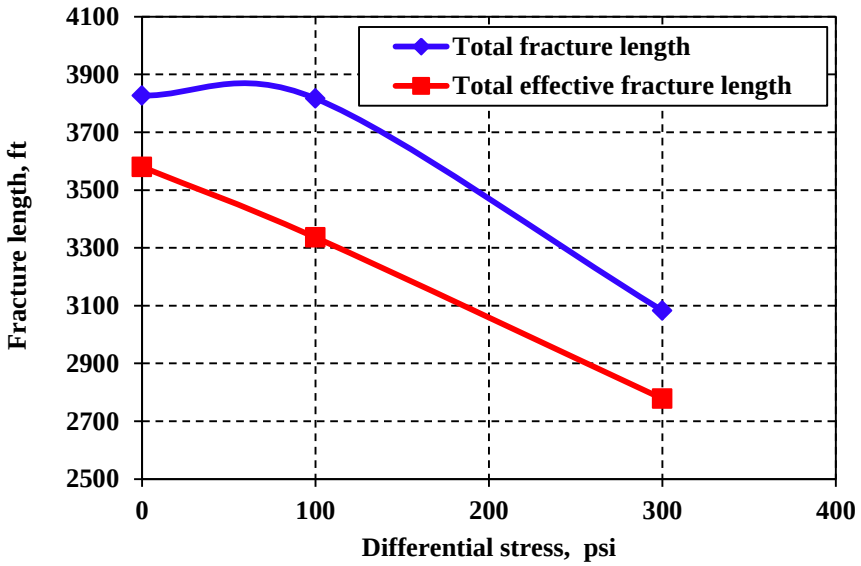

Figure 7.17: Effective and total fracture length of four fractures for three cases with different differential stresses (cluster spacing = 100 ft, slickwater, injection rate = 60 bpm, relative angle = 45^{o}, a = 2, NF spacing = 55 ft).

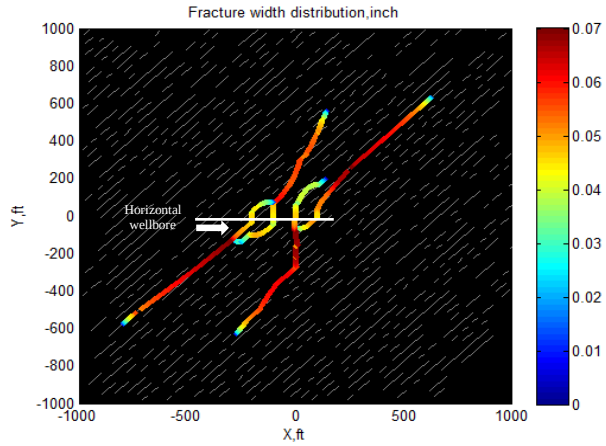

(a) DS = 0 psi

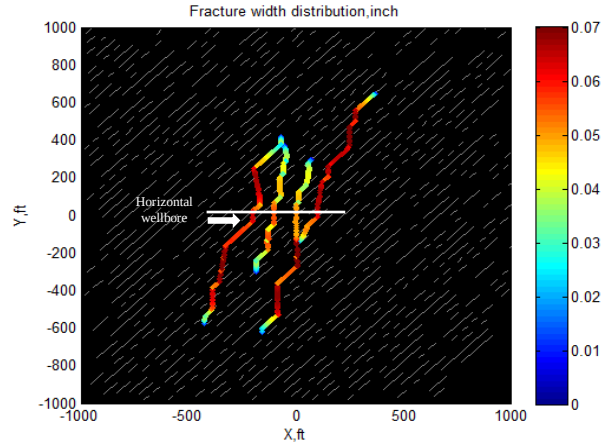

(b) DS = 100 psi

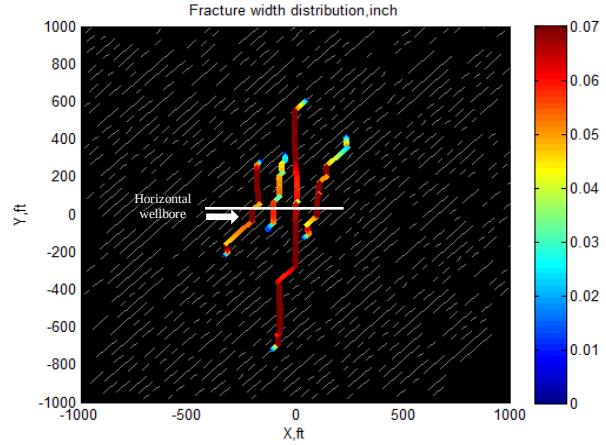

(c) DS = 300 psi

Figure 7.18: Width profile of fracture networks at the end of injection for three cases with different differential stresses (cluster spacing = 100 ft, slickwater, injection rate = 60 bpm, relative angle = 45^{o}, *a* = 2, NF spacing = 55 ft).

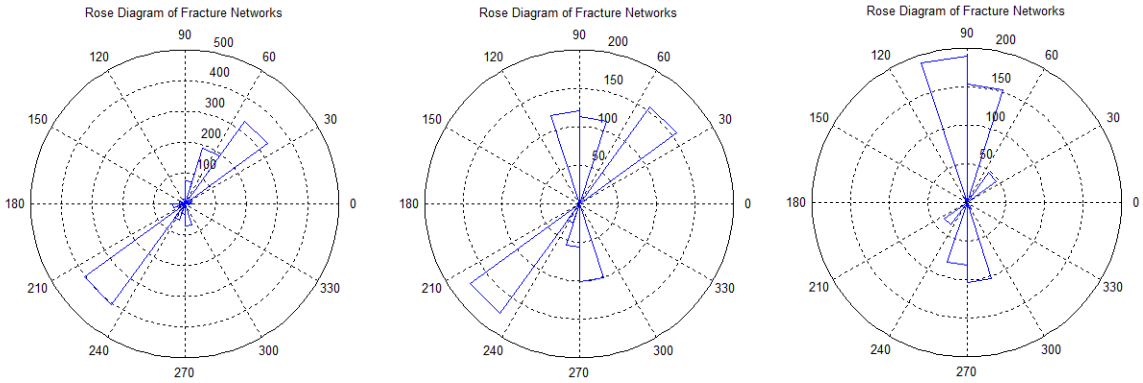

(a) DS = 0 psi (b) DS = 100 psi (c) DS = 300 psi

Figure 7.19: Rose diagrams showing fracture trends for associated three cases in Figure 7.18.

7.4.3 The effects of natural fracture patterns

Natural fracture patterns with different orientations, spacing, and lengths can significantly impact the shape of fracture geometry. In our model, a set of natural fractures with the same orientation and power law length distribution was created. Four hydraulic fractures propagating simultaneously were simulated to investigate the effects of the natural fracture orientation. Hydraulic fractures tend to cross natural fractures when the relative angle between HF and NF is 90^{o}, as shown in Figure 7.20 (a). Natural fractures with large relative angle to hydraulic fractures have less chance to alter propagation trajectory of the hydraulic fractures because hydraulic fractures have greater possibility to cross the natural fractures (Figure 2). As the relative angle decreases, the chance of hydraulic fractures crossing natural fractures decreases, which implies that more natural fractures are opened. Figure 7.20 (b) and (c) show more complex fracture geometries as a result from hydraulic fractures deflecting into natural fractures.

The results (Figure 7.21) of natural fracture patterns with different natural fracture lengths and spacing show a progression in hydraulic fracture geometry from a pattern with a preferential fracture trend in the direction of natural fractures (Figure 7.21 (a)), to

a pattern with through-going fractures roughly growing along their original direction (Figure 7.21(d)). The length of natural fractures are controlled by the exponent a of power law. The range of a is from 1 to 3 based on the geological observation from outcrops (Segall and Pollard, 1983; Davy, 1993). More large fractures can be generated with $a = 1$ than $a = 3$, as shown in Figure 13. Decreasing the exponent a tends to increase the likelihood to create long diversion length along the natural fractures, which enhances the possibility to control the trajectory of hydraulic fractures. Comparing Figure 7.21 (a) and (c), it is clear that the preferential trends of overall fracture trajectory are different, even though the direction of natural fractures is 45^o for both cases. The preferential fracture trend in case (a) with $a = 1$ is almost parallel to the natural fractures. Increasing the a causes more natural fractures with short length, which increases variation in width and orientation along the fractures, as shown in Figure 7.21 (c) and (d). The variations in fracture path might enhance the flow resistance and prevent proppant from flowing through fracture networks.

Natural fracture spacing also has great influence on fracture geometry. Natural fracture patterns with spacing 28 ft and 50 ft were created (Figure 7.21). The decrease in natural fracture spacing is a direct result of more and more natural fractures likely encountered and activated by the hydraulic fractures, which could trigger more microseismic activities. The preferential fracture trend is more likely to be parallel to the natural fractures when the fracture spacing decreases.

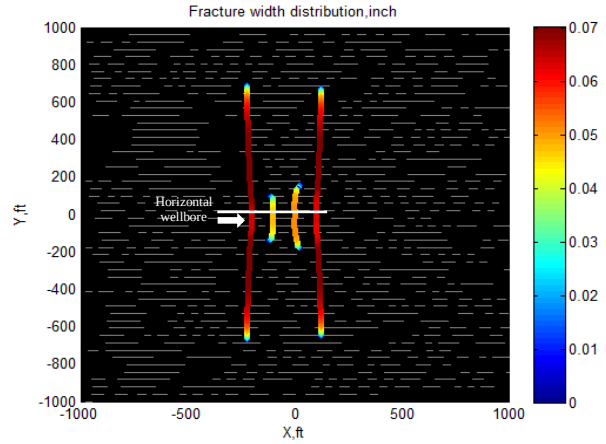

(a) Relative angle = 90^{o}

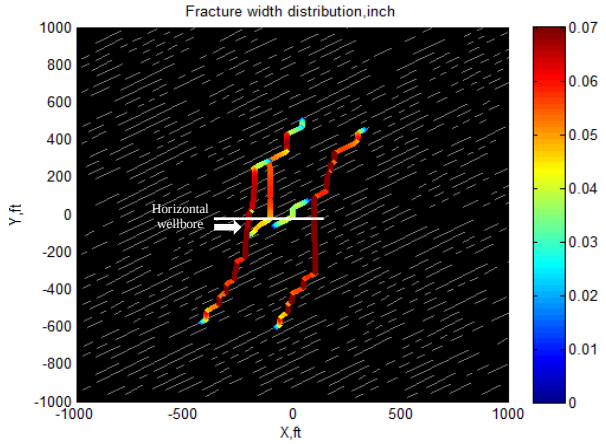

(b) Relative angle = 60^{o}

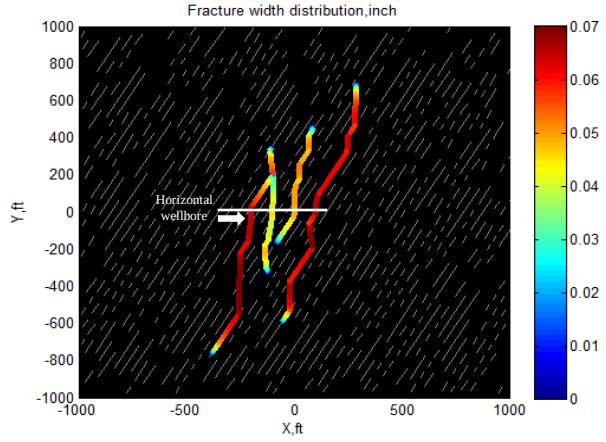

(c) Relative angle = 30^{o}

Figure 7.20: Width profile of fracture networks for three cases with different relative angles between HF and NF (cluster spacing = 100 ft, slickwater, injection rate = 60 bpm, DS = 100 psi, a = 2, NF spacing = 55 ft).

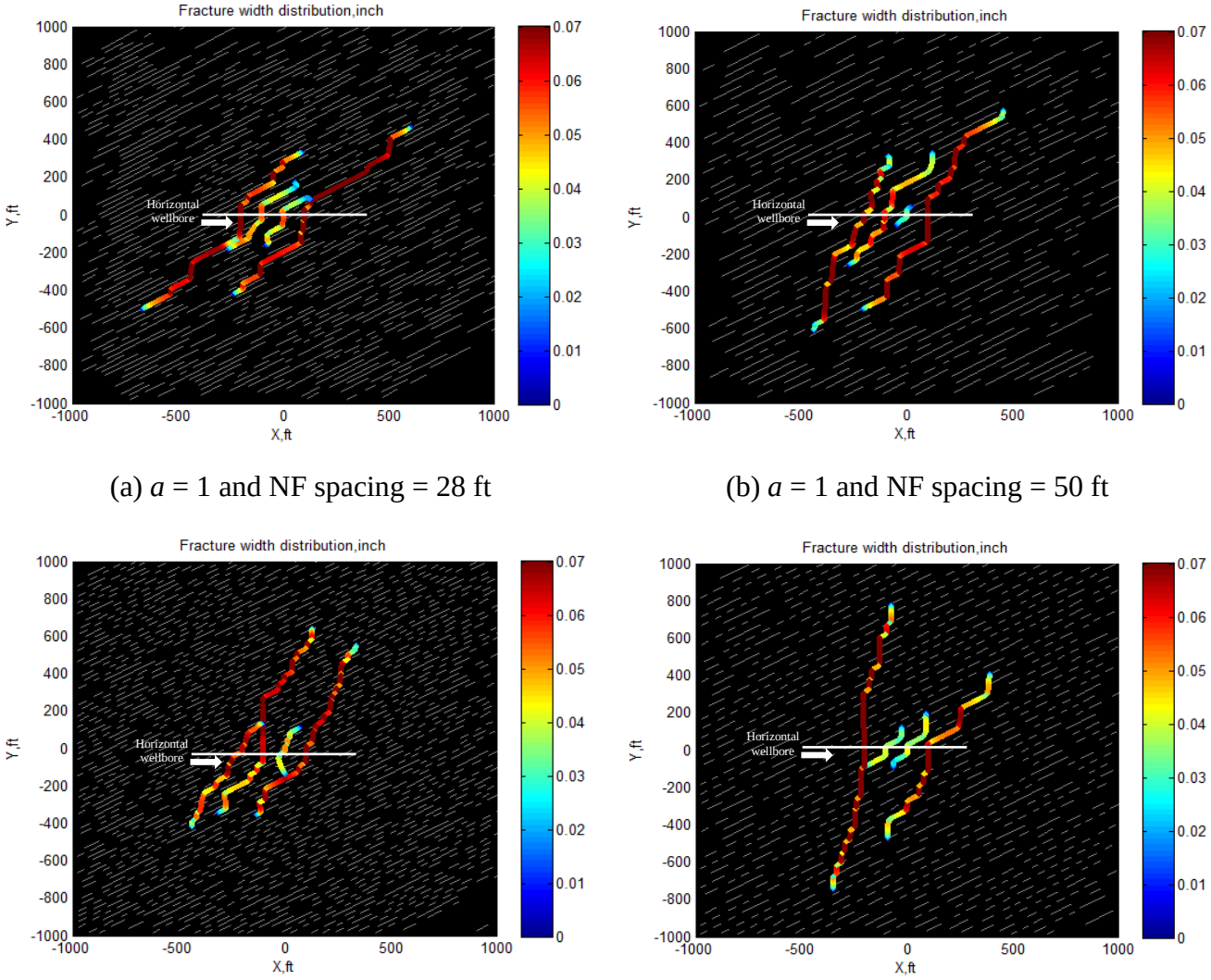

(a) a = 1 and NF spacing = 28 ft

(b) a = 1 and NF spacing = 50 ft

(c) a = 3 and NF spacing = 28 ft

(d) a = 3 and NF spacing = 50 ft

Figure 7.21: Width profile of fracture networks at the end of injection for four cases with different natural fracture patterns (cluster spacing = 100 ft, slickwater, injection rate = 60 bpm, DS = 100 psi, relative angle = 45^{o}, '*': microseismic activity).

7.5 CONCLUSIONS

This chapter studied complex fracture networks induced by multiple hydraulic fractures propagating in naturally fractured reservoirs. Natural fracture patterns were generated by a stochastic realization method. Flow rate distribution between multiple fractures is changed when fractures intersect with natural fractures. To accurately predict complex fracture geometry, the partition of flow rate between multiple fractures can be calibrated by DAS and DTS, and hypothetical microseismic event patterns can reflect fracture trajectory and be validated with microseismic results from the field. With validation and calibration of diagnostic results, the model has the potential to predict complex fracture geometry in naturally fracture reservoirs.

In addition, perforation cluster spacing, differential stress and natural fracture patterns have a great influence on fracture geometry. Close perforation cluster spacing causes immature development of interior fractures. High differential stress tends to increase injection pressure in naturally fracture reservoirs and reduces complexity of fracture geometry. Natural fracture patterns also play a significant role in controlling overall orientation of fracture path. The preferential trend of hydraulic fractures is more likely to be parallel to natural fractures with small relative angle to hydraulic fractures. Natural fracture patterns with a large length exponent a and close spacing tend to have a preferential fracture trend parallel to the direction of natural fractures.

CHAPTER 8: CONCLUSION AND FUTURE WORK

This chapter first summarizes main research work presented in the dissertation. The novel fracture propagation model was developed for multiple fractures propagating in a naturally fractured reservoir. Key physical mechanisms and insights for complex fracture propagation were drawn from the simulation results. After that, some extending topics are proposed for future research.

8.1 CONCLUSIONS OF THE COMPLETED WORK

8.1.1 The complex hydraulic fracture development model

A novel fracture propagation model was developed to simulate hydraulic fracture propagation from a horizontal wellbore in a naturally fractured reservoir. The model coupled rock mechanics and fluid mechanics together. The following is a list of theories of these two parts employed in the model.

For rock mechanics:

v. The Displacement Discontinuity Method (DDM) was used to describe rock deformation. A three-dimensional elastic correction factor, G (Olson, 2004), was used to consider the effects of finite fracture height.

vi. A Simplified Three-Dimensional Displacement Discontinuity Method (S3D DDM) was proposed to more accurately calculate displacements and induced stresses for multiple fractures, especially complex fracture networks in three dimensions. The computational efficiency of S3D DDM is improved by about one thousand times compared with 3D DDM.

vii. Linear elastic fracture mechanics was employed to determine fracture propagation. The propagation direction was determined by the maximum circumferential stress criterion.

viii. Stresses near fracture tips and energy release rate were described to predict crossing/arresting behavior of hydraulic fractures under the influence of frictional interfaces and cemented discontinuities, respectively.

For fluid mechanics:

v. Incompressible and non-Newtonian fluid flowing in the fractures was described by the lubrication theory.

vi. Fluid flow in the wellbore was analogous to the flow of electric current through an electrical circuit network, applying Kirchoff's first and second laws to determine the partition of flow rate between multiple fractures. The pressure equilibrium was maintained between horizontal wellbore and multiple fractures.

vii. The behavior of fluid leak-off from the fracture to formation was described by the Cater model.

Iteratively and fully coupled procedures were used to couple rock deformation and fluid flow. For iterative procedure, the Newton-Raphson method was used to solve a non-linear equation system of fluid mechanics, and then the Picard iteration method was employed to iteratively couple rock deformation and fluid flow. For the fully coupled procedure, rock deformation and fluid flow were solved together through the Newton Raphson method.

Compared with other complex fracture development models, our model has two distinguished advantages:

i. The model incorporates key physical mechanisms of complex fracture geometry, such as stress shadow effects, fluid rate distribution among multiple fractures, interaction of HF and NF.

ii. The model simulates complex fracture geometry in three-dimensions with high computational efficiency by using the Simplified Three-Dimensional Displacement Discontinuity Method (S3D DDM).

The model was developed for simulation of complex hydraulic fracture development. The primary capabilities of the model are:

i. Model non-planar single fracture propagation from a misaligned direction of the in-situ stress state.
ii. Model multiple fracture propagation from a stage or multiple stages simultaneously and sequentially.
iii. Model fracture propagation in naturally fractured reservoirs and analyze complex fracture geometry.

The model can be used to analyze the fracturing process and optimize stimulation designs. The main outputs from the model are:

i. Complex fracture geometry, such as fracture trajectory and fracture width distribution.
ii. Real time injection pressure in the horizontal wellbore and pressure distribution within the fractures.
iii. The real time partition of flow rate and total fluid volume distribution between multiple fractures.
iv. A hypothetical microseismic event pattern based on activated natural fractures.

8.1.2 Key points of complex hydraulic fracture propagation

One of the applications of a numerical fracture propagation model is to understand physical mechanisms of complex fracture propagation and provide insights for operators to design fracturing treatments and maximize the production. The following lists the key points for complex fracture propagation with and without the effects of natural fractures drawn from the results presented in the dissertation.

Fracture propagation without the effects of natural fractures:

i. Non-planar fracture geometry can be induced when the orientation of an initial fracture does not align with the direction of the maximum horizontal stress.

ii. Fracture width restriction of non-planar segments is more pronounced with larger misalignment angles.

iii. Reorientation of the fracture path is slower for weaker stress anisotropies. Extreme reorientation causes severe width restriction and high injection pressure.

iv. Non-planar geometry is induced for multiple fracture propagation with close spacing. Simultaneously propagating fractures will attract or repel each other due to stress shadow effects.

v. For multiple fractures propagating simultaneously in a stage, the exterior fractures generally dominate the propagation and take most of fluid, and the interior fractures are usually immaturely developed.

vi. Sequential versus simultaneous stimulation methods will cause distinctly fracture geometries.

vii. For simultaneous multiple fracture propagation, mechanical interaction and fluid flow interaction through the horizontal wellbore mutually affect each other, controlling simultaneous fracture propagation. Fracture propagation velocity rapidly decreases when a tip is close enough to an adjacent fracture.

Fracture propagation with the effects of natural fractures:

i. Natural fractures have a great influence on hydraulic fracture propagation and could change fracture propagation orientation, resulting in injection pressure elevation and fracture width restriction.

ii. Width reduction and pressure elevation can be caused by the additional closing stresses from in-situ stress field for misaligned fracture segments and stress shadow effects from nearby hydraulic fractures.

iii. Offset fracture geometry might be created when a hydraulic fracture propagates in a naturally fractured reservoir. Width restriction at offsets might increase the resistance to fluid flow within the fracture and the risk of screen-out.

iv. Complex fracture geometry in naturally fractured reservoirs could be accurately characterized by our numerical model combined with diagnostic methods.

v. Effective fracture surface area of complex fracture geometry is affected by perforation cluster spacing and differential stress. There is an optimal choice for the number of fractures per stage to maximize the surface area, beyond which increasing the number of fractures actually decreases effective fracture area.

vi. Fracture complexity is dependent on natural fracture patterns. Natural fractures with small relative angles to the hydraulic fracture trend are more likely to control fracture propagation path if intersected. Also, natural fracture patterns with more long fractures tend to increase the likelihood to dominate the preferential fracture trend of fracture trajectory.

vii. Our numerical model can provide physics-based complex fracture networks that can be imported into reservoir simulation models for production analysis.

8.2 FUTURE WORK

There are many topics which the work presented in the dissertation could be extended. These topics include (1) three-dimensional model development, (2) proppant transport, (3) and interaction between the natural and hydraulic fracture.

A hydraulic fracture extends not only in length but also in height. The current model assumes a constant height. The recent experimental work by Bahorich et al. (2012) suggests that bypass and mixed mode propagation are likely in hydraulic fracture intersections with cemented natural fractures when the height of natural fractures is less than the height of formations. This problem might be solved by the Three-Dimensional Displacement Discontinuity Method (3D DDM) coupling two-dimensional fluid flow. The future goal is to incorporate 3D DDM into our model and extend the fluid flow model to two dimensions.

In addition, the three-dimensional model can also be applied to hydraulic fracture propagation in the formations with multiple layers. Considering fracture propagation in multiple layers, the fracture geometry is much more complex than envisioned by the conventional models (Fisher and Warpinski, 2012). Out of zone growth is of great interest with regard to fracture treatment optimization.

Proppant transport in complex fracture networks is another important topic. The effectiveness of a hydraulic fracture treatment depends on proppant distribution at the end of pumping. However, the current model does not take into account proppant transport in complex fracture networks and its impacts on fracture geometry. Assessing proppant transport in fracture networks provided by the model might require adopting computational fluid dynamics modeling. One of possible approaches is to establish a relationship between proppant volumetric concentration and fracture geometry by using a commercial implementation of computational fluid dynamics. A modified viscosity of the

slurry could be applied to consider the effects of proppant concentration and their effect on fracture propagation, in particular examining fracture length and conductivity.

Finally, the interaction of natural and hydraulic fractures still requires more work. There are four physical mechanisms of mechanical activation of a natural fracture as a result of contacting a pressurized hydraulic fracture: (1) hydraulic fracture approach angle, (2) fracture coalescence, (3) fluid flow into the natural fracture, and (4) the subsequent initiation of secondary fractures from the natural fracture. The current model only considers the second and the third mechanisms. Future work will consider all four mechanisms theoretically and experimentally and estimate the effects on hydraulic fracture propagation. Recent work reported by Wang et al. (2013) indicates that the thickness of cemented natural fractures affects the interaction of natural and hydraulic fractures. However, this effect is ignored by existed interaction criteria. Future work could develop a new interaction criterion to determine fracture coalescence and subsequent initiation of a secondary fracture from cemented natural fractures. Energy release rate might be a potential parameter to be used as a criterion based on fracture mechanics, and some experimental tests also will be conducted to validate the criterion. The criterion could also be validated by numerical simulations, and the effects of these four mechanisms could be investigated by simulators. The criterion and results can then be used to enhance the current model.

Appendix A: Coordinate transform

A.1 Two dimensional coordinate transformation

Let X, Y be global coordinate, and (x, y) local coordinate. Transform to local coordinate from global coordinate:

$$\begin{bmatrix} x \\ y \end{bmatrix} = \begin{bmatrix} \cos\beta & \sin\beta \\ -\sin\beta & \cos\beta \end{bmatrix} \begin{bmatrix} X \\ Y \end{bmatrix}$$

$$A = \begin{bmatrix} \cos\beta & \sin\beta \\ -\sin\beta & \cos\beta \end{bmatrix}$$

Stress component from global coordinate to local coordinate:

$$\begin{bmatrix} \sigma_{xx} & \sigma_{xy} \\ \sigma_{yx} & \sigma_{yy} \end{bmatrix} = A \begin{bmatrix} \sigma_{XX} & \sigma_{XY} \\ \sigma_{YX} & \sigma_{YY} \end{bmatrix} A^T$$

$$\begin{bmatrix} \sigma_{xx} & \sigma_{xy} \\ \sigma_{yx} & \sigma_{yy} \end{bmatrix} = \begin{bmatrix} \cos\beta & \sin\beta \\ -\sin\beta & \cos\beta \end{bmatrix} \begin{bmatrix} \sigma_{XX} & \sigma_{XY} \\ \sigma_{YX} & \sigma_{YY} \end{bmatrix} \begin{bmatrix} \cos\beta & -\sin\beta \\ \sin\beta & \cos\beta \end{bmatrix}$$

$$\begin{bmatrix} \sigma_{xx} & \sigma_{xy} \\ \sigma_{yx} & \sigma_{yy} \end{bmatrix} = \begin{bmatrix} \cos\beta\sigma_{XX} + \sin\beta\sigma_{YX} & \cos\beta\sigma_{XY} + \sin\beta\sigma_{YY} \\ -\sin\beta\sigma_{XX} + \cos\beta\sigma_{YX} & -\sin\beta\sigma_{XY} + \cos\beta\sigma_{YY} \end{bmatrix} \begin{bmatrix} \cos\beta & -\sin\beta \\ \sin\beta & \cos\beta \end{bmatrix}$$

$$\begin{bmatrix} \sigma_{xx} & \sigma_{xy} \\ \sigma_{yx} & \sigma_{yy} \end{bmatrix} = \begin{bmatrix} \cos^2\beta\sigma_{XX} + \sin 2\beta\sigma_{YX} + \sin^2\beta\sigma_{YY} & -\sin\beta\cos\beta\sigma_{XX} + \cos 2\beta\sigma_{XY} + \sin\beta\cos\beta\sigma_{YY} \\ -\sin\beta\cos\beta\sigma_{XX} + \cos 2\beta\sigma_{YX} + \sin\beta\cos\beta\sigma_{YY} & \sin^2\beta\sigma_{XX} - \sin 2\beta\sigma_{YX} + \cos^2\beta\sigma_{YY} \end{bmatrix}$$

Stress component from local coordinate to global coordinate:

$$\begin{bmatrix} \sigma_{XX} & \sigma_{XY} \\ \sigma_{YX} & \sigma_{YY} \end{bmatrix} = A^T \begin{bmatrix} \sigma_{xx} & \sigma_{xy} \\ \sigma_{yx} & \sigma_{yy} \end{bmatrix} A$$

$$\begin{bmatrix} \sigma_{XX} & \sigma_{XY} \\ \sigma_{YX} & \sigma_{YY} \end{bmatrix} = \begin{bmatrix} \cos\beta & -\sin\beta \\ \sin\beta & \cos\beta \end{bmatrix} \begin{bmatrix} \sigma_{xx} & \sigma_{xy} \\ \sigma_{yx} & \sigma_{yy} \end{bmatrix} \begin{bmatrix} \cos\beta & \sin\beta \\ -\sin\beta & \cos\beta \end{bmatrix}$$

$$\begin{bmatrix} \sigma_{XX} & \sigma_{XY} \\ \sigma_{YX} & \sigma_{YY} \end{bmatrix} = \begin{bmatrix} \cos\beta\sigma_{xx} - \sin\beta\sigma_{yx} & \cos\beta\sigma_{xy} - \sin\beta\sigma_{yy} \\ \sin\beta\sigma_{xx} + \cos\beta\sigma_{yx} & \sin\beta\sigma_{xy} + \cos\beta\sigma_{yy} \end{bmatrix} \begin{bmatrix} \cos\beta & \sin\beta \\ -\sin\beta & \cos\beta \end{bmatrix}$$

$$\begin{bmatrix} \sigma_{XX} & \sigma_{XY} \\ \sigma_{YX} & \sigma_{YY} \end{bmatrix} = \begin{bmatrix} \cos^2\beta\sigma_{xx} - \sin 2\beta\sigma_{xy} + \sin^2\beta\sigma_{yy} & \sin\beta\cos\beta(\sigma_{xx} - \sigma_{yy}) + \cos 2\beta\sigma_{xy} \\ \sin\beta\cos\beta(\sigma_{xx} - \sigma_{yy}) + \cos 2\beta\sigma_{xy} & \sin^2\beta\sigma_{xx} + \sin 2\beta\sigma_{yx} + \cos^2\beta\sigma_{yy} \end{bmatrix}$$

A.2 Three dimensional coordinate transformation

A.2.1: Transform from local coordinate of j^{th} fracture element to local coordinate of i^{th} element

Let $\overset{i}{x}_1, \overset{i}{x}_2, \overset{i}{x}_3$ be local coordinate of i^{th} element, $\overset{j}{x}_1, \overset{j}{x}_2, \overset{j}{x}_3$ local coordinate of j^{th} element. For these two local coordinate systems, x_2 is the direction of the fracture height for both coordinates. Hence, we just need to make transformations of x_1 and x_3. Transform to local coordinate of i^{th} element from local coordinate of j^{th} element:

$$\begin{bmatrix} \overset{i}{x}_1 \\ \overset{i}{x}_2 \\ \overset{i}{x}_3 \end{bmatrix} = \begin{bmatrix} \cos\beta & 0 & \sin\beta \\ 0 & 1 & 0 \\ -\sin\beta & 0 & \cos\beta \end{bmatrix} \begin{bmatrix} \overset{j}{x}_1 \\ \overset{j}{x}_2 \\ \overset{j}{x}_3 \end{bmatrix}$$

$$A=\begin{bmatrix}\cos\beta & 0 & \sin\beta\\ 0 & 1 & 0\\ -\sin\beta & 0 & \cos\beta\end{bmatrix}$$

$$\begin{bmatrix}\overset{i}{\sigma}_{11} & \overset{i}{\sigma}_{12} & \overset{i}{\sigma}_{13}\\ \overset{i}{\sigma}_{21} & \overset{i}{\sigma}_{22} & \overset{i}{\sigma}_{23}\\ \overset{i}{\sigma}_{31} & \overset{i}{\sigma}_{23} & \overset{i}{\sigma}_{33}\end{bmatrix}=A\begin{bmatrix}\overset{j}{\sigma}_{11} & \overset{j}{\sigma}_{12} & \overset{j}{\sigma}_{13}\\ \overset{j}{\sigma}_{21} & \overset{j}{\sigma}_{22} & \overset{j}{\sigma}_{23}\\ \overset{j}{\sigma}_{31} & \overset{j}{\sigma}_{32} & \overset{j}{\sigma}_{33}\end{bmatrix}A^T$$

$$\begin{bmatrix}\overset{i}{\sigma}_{11} & \overset{i}{\sigma}_{12} & \overset{i}{\sigma}_{13}\\ \overset{i}{\sigma}_{21} & \overset{i}{\sigma}_{22} & \overset{i}{\sigma}_{23}\\ \overset{i}{\sigma}_{31} & \overset{i}{\sigma}_{23} & \overset{i}{\sigma}_{33}\end{bmatrix}=\begin{bmatrix}\cos\beta & 0 & \sin\beta\\ 0 & 1 & 0\\ -\sin\beta & 0 & \cos\beta\end{bmatrix}\begin{bmatrix}\overset{j}{\sigma}_{11} & \overset{j}{\sigma}_{12} & \overset{j}{\sigma}_{13}\\ \overset{j}{\sigma}_{21} & \overset{j}{\sigma}_{22} & \overset{j}{\sigma}_{23}\\ \overset{j}{\sigma}_{31} & \overset{j}{\sigma}_{32} & \overset{j}{\sigma}_{33}\end{bmatrix}\begin{bmatrix}\cos\beta & 0 & -\sin\beta\\ 0 & 1 & 0\\ \sin\beta & 0 & \cos\beta\end{bmatrix}$$

$$\begin{bmatrix}\overset{i}{\sigma}_{11} & \overset{i}{\sigma}_{12} & \overset{i}{\sigma}_{13}\\ \overset{i}{\sigma}_{21} & \overset{i}{\sigma}_{22} & \overset{i}{\sigma}_{23}\\ \overset{i}{\sigma}_{31} & \overset{i}{\sigma}_{23} & \overset{i}{\sigma}_{33}\end{bmatrix}=\begin{bmatrix}\cos\beta\,\overset{j}{\sigma}_{11}+\sin\beta\,\overset{j}{\sigma}_{13} & \cos\beta\,\overset{j}{\sigma}_{12}+\sin\beta\,\overset{j}{\sigma}_{23} & \cos\beta\,\overset{j}{\sigma}_{13}+\sin\beta\,\overset{j}{\sigma}_{33}\\ \overset{j}{\sigma}_{12} & \overset{j}{\sigma}_{22} & \overset{j}{\sigma}_{23}\\ -\sin\beta\,\overset{j}{\sigma}_{11}+\cos\beta\,\overset{j}{\sigma}_{13} & -\sin\beta\,\overset{j}{\sigma}_{12}+\cos\beta\,\overset{j}{\sigma}_{23} & -\sin\beta\,\overset{j}{\sigma}_{13}+\cos\beta\,\overset{j}{\sigma}_{33}\end{bmatrix}\begin{bmatrix}\cos\beta & 0 & -\sin\beta\\ 0 & 1 & 0\\ \sin\beta & 0 & \cos\beta\end{bmatrix}$$

$$\begin{bmatrix}\overset{i}{\sigma}_{11} & \overset{i}{\sigma}_{12} & \overset{i}{\sigma}_{13}\\ \overset{i}{\sigma}_{21} & \overset{i}{\sigma}_{22} & \overset{i}{\sigma}_{23}\\ \overset{i}{\sigma}_{31} & \overset{i}{\sigma}_{23} & \overset{i}{\sigma}_{33}\end{bmatrix}=\begin{bmatrix}\cos^2\beta\,\overset{j}{\sigma}_{11}+2\sin\beta\cos\beta\overset{j}{\sigma}_{13}+\sin^2\beta\,\overset{j}{\sigma}_{33} & \cos\beta\,\overset{j}{\sigma}_{12}+\sin\beta\,\overset{j}{\sigma}_{23} & -\sin\beta\cos\beta\,\overset{j}{\sigma}_{11}+\cos 2\beta\,\overset{j}{\sigma}_{13}+\sin\beta\cos\beta\,\overset{j}{\sigma}_{33}\\ \overset{j}{\sigma}_{12}\cos\beta+\overset{j}{\sigma}_{23}\sin\beta & \overset{j}{\sigma}_{22} & -\overset{j}{\sigma}_{12}\sin\beta+\overset{j}{\sigma}_{23}\cos\beta\\ -\sin\beta\cos\beta\,\overset{j}{\sigma}_{11}+\cos 2\beta\,\overset{j}{\sigma}_{13}+\sin\beta\cos\beta\,\overset{j}{\sigma}_{33} & -\sin\beta\,\overset{j}{\sigma}_{12}+\cos\beta\,\overset{j}{\sigma}_{23} & \sin^2\beta\,\overset{j}{\sigma}_{11}-2\sin\beta\cos\beta\,\overset{j}{\sigma}_{13}+\cos^2\beta\,\overset{j}{\sigma}_{33}\end{bmatrix}$$

$$\overset{i}{\sigma}_{33}=\sin^2\beta\,\overset{j}{\sigma}_{11}-2\sin\beta\cos\beta\,\overset{j}{\sigma}_{13}+\cos^2\beta\,\overset{j}{\sigma}_{33}$$

$$\overset{i}{\sigma}_{31}=-\sin\beta\cos\beta\,\overset{j}{\sigma}_{11}+\cos 2\beta\,\overset{j}{\sigma}_{13}+\sin\beta\cos\beta\,\overset{j}{\sigma}_{33}$$

$$\overset{i}{\sigma}_{32}=-\overset{j}{\sigma}_{12}\sin\beta+\overset{j}{\sigma}_{23}\cos\beta$$

A.2.2: Transformation between global coordinate and local coordinate of fracture elements (HF is normal to XY plane in global coordinate)

Let X, Y, Z be global coordinate, and (x_1, x_2, x_3) local coordinate. Transform to local coordinate from global coordinate:

$$\begin{bmatrix} \bar{x} \\ \bar{y} \\ \bar{z} \end{bmatrix} = \begin{bmatrix} \cos\beta & \sin\beta & 0 \\ -\sin\beta & \cos\beta & 0 \\ 0 & 0 & 1 \end{bmatrix} \begin{bmatrix} X \\ Y \\ Z \end{bmatrix}$$

$$B = \begin{bmatrix} \cos\beta & \sin\beta & 0 \\ -\sin\beta & \cos\beta & 0 \\ 0 & 0 & 1 \end{bmatrix}$$

$$\begin{bmatrix} x_1 \\ x_2 \\ x_3 \end{bmatrix} = \begin{bmatrix} 1 & 0 & 0 \\ 0 & 0 & 1 \\ 0 & 1 & 0 \end{bmatrix} \begin{bmatrix} \bar{x} \\ \bar{y} \\ \bar{z} \end{bmatrix}$$

$$C = \begin{bmatrix} 1 & 0 & 0 \\ 0 & 0 & 1 \\ 0 & 1 & 0 \end{bmatrix}$$

$$A = C * B = \begin{bmatrix} 1 & 0 & 0 \\ 0 & 0 & 1 \\ 0 & 1 & 0 \end{bmatrix} \begin{bmatrix} \cos\beta & \sin\beta & 0 \\ -\sin\beta & \cos\beta & 0 \\ 0 & 0 & 1 \end{bmatrix} = \begin{bmatrix} \cos\beta & \sin\beta & 0 \\ 0 & 0 & 1 \\ -\sin\beta & \cos\beta & 0 \end{bmatrix}$$

Stress component from local coordinate to global coordinate:

$$\begin{bmatrix} \sigma_{XX} & \sigma_{XY} & \sigma_{XZ} \\ \sigma_{YX} & \sigma_{YY} & \sigma_{YZ} \\ \sigma_{ZX} & \sigma_{ZY} & \sigma_{ZZ} \end{bmatrix} = A^T \begin{bmatrix} \sigma_{11} & \sigma_{12} & \sigma_{13} \\ \sigma_{21} & \sigma_{22} & \sigma_{23} \\ \sigma_{31} & \sigma_{32} & \sigma_{33} \end{bmatrix} A$$

$$\begin{bmatrix} \sigma_{XX} & \sigma_{XY} & \sigma_{XZ} \\ \sigma_{YX} & \sigma_{YY} & \sigma_{YZ} \\ \sigma_{ZX} & \sigma_{ZY} & \sigma_{ZZ} \end{bmatrix} = \begin{bmatrix} \cos\beta & 0 & -\sin\beta \\ \sin\beta & 0 & \cos\beta \\ 0 & 1 & 0 \end{bmatrix} \begin{bmatrix} \sigma_{11} & \sigma_{12} & \sigma_{13} \\ \sigma_{21} & \sigma_{22} & \sigma_{23} \\ \sigma_{31} & \sigma_{32} & \sigma_{33} \end{bmatrix} \begin{bmatrix} \cos\beta & \sin\beta & 0 \\ 0 & 0 & 1 \\ -\sin\beta & \cos\beta & 0 \end{bmatrix}$$

$$\begin{bmatrix} \sigma_{XX} & \sigma_{XY} & \sigma_{XZ} \\ \sigma_{YX} & \sigma_{YY} & \sigma_{YZ} \\ \sigma_{ZX} & \sigma_{ZY} & \sigma_{ZZ} \end{bmatrix} =$$

$$\begin{bmatrix} \cos\beta\sigma_{11} - \sin\beta\sigma_{31} & \cos\beta\sigma_{12} - \sin\beta\sigma_{23} & \cos\beta\sigma_{13} - \sin\beta\sigma_{33} \\ \sin\beta\sigma_{11} + \cos\beta\sigma_{31} & \sin\beta\sigma_{12} + \cos\beta\sigma_{32} & \sin\beta\sigma_{13} + \cos\beta\sigma_{33} \\ \sigma_{21} & \sigma_{22} & \sigma_{23} \end{bmatrix} \begin{bmatrix} \cos\beta & \sin\beta & 0 \\ 0 & 0 & 1 \\ -\sin\beta & \cos\beta & 0 \end{bmatrix}$$

$$\begin{bmatrix} \sigma_{XX} & \sigma_{XY} & \sigma_{XZ} \\ \sigma_{YX} & \sigma_{YY} & \sigma_{YZ} \\ \sigma_{ZX} & \sigma_{ZY} & \sigma_{ZZ} \end{bmatrix} =$$

$$\begin{bmatrix} \cos^2\beta\sigma_{11} - \sin 2\beta\sigma_{31} + \sin^2\beta\sigma_{33} & \sin\beta\cos\beta\sigma_{11} + \cos 2\beta\sigma_{13} - \sin\beta\cos\beta\sigma_{33} & \cos\beta\sigma_{12} - \sin\beta\sigma_{23} \\ \sin\beta\cos\beta\sigma_{11} + \cos 2\beta\sigma_{31} - \sin\beta\cos\beta\sigma_{33} & \sin^2\beta\sigma_{11} + 2\sin\beta\cos\beta\sigma_{31} + \cos^2\beta\sigma_{33} & \sin\beta\sigma_{12} + \cos\beta\sigma_{23} \\ \cos\beta\sigma_{21} - \sin\beta\sigma_{32} & \sin\beta\sigma_{21} + \cos\beta\sigma_{32} & \sigma_{22} \end{bmatrix}$$

$$\sigma_{XX} = \cos^2\beta\sigma_{11} - \sin 2\beta\sigma_{31} + \sin^2\beta\sigma_{33}$$

$$\sigma_{YY} = \sin^2\beta\sigma_{11} + 2\sin\beta\cos\beta\sigma_{31} + \cos^2\beta\sigma_{33}$$

$$\sigma_{ZZ} = \sigma_{22}$$

$$\sigma_{XY} = \sin\beta\cos\beta\sigma_{11} + \cos 2\beta\sigma_{31} - \sin\beta\cos\beta\sigma_{33}$$

$$\sigma_{XZ} = \cos\beta\sigma_{12} - \sin\beta\sigma_{23}$$

$$\sigma_{YZ} = \sin\beta\sigma_{21} + \cos\beta\sigma_{32}$$

References

Abass, H., Soliman, M., Al-Tahini, A., Surjaatmadja, J., Meadows, D. & Sierra, L. 2009. Oriented Fracturing: A New Technique To Hydraulically Fracture an Openhole Horizontal Well. SPE 124483, presented at in Proceedings SPE Annual Technology Conference and Exhibition. New Orleans, Louisiana, USA.

Abou-Sayed, A. S., Sinha, K. P. and Clifton, R.J. 1984. Evaluation of the influence of in-situ reservoir conditions on the geometry of hydraulic fractures using a 3-D simulator: Part I: technical approach. SPE 12877, presented at SPE/DOE/GRI Unconventional Gas Recovery Symp. Pittsburgh, PA, May 13-15.

Adachi, J., Siebrits, E., Peirce, A., Descroches, J., 2007. Computer simulation of hydraulic fractures. International Journal of Rock Mechanics & Mining Sciences 44(5): 739-757.

Advani, S. H. and Lee, J. K. 1982. Finite element model simulations associated with hydraulic fracturing. SPE 8941-PA. Society of Petroleum Engineering Journal 22(2): 209-218.

Alabbad, E. A. 2014. Experimental investigation of geomechanical aspects of hydraulic fracturing unconventional formations. Ph.D. thesis. The University of Texas at Austin.

Bahorich, B., Olson, J. E., Holder, J. 2012. Examining the effect of cemented natural fractures on hydraulic fracture propagation in hydrostone block experiments. SPE 160197, presented at the SPE Annual Technical Conference and Exhibition, San Antonio, Texas, USA, 8-10 October.

Barree, R.D., Fisher, M. K. and Woodroof, R.A. 2002. A practical guide to hydraulic fracture diagnostic technologies. SPE 77442, presented at the SPE Annual Technical Conference and Exhibition, San Antonio, Texas, 29 September - 2 October.

Barton, C. A., Zoback, M. D. 2002. Discrimination of natural fractures from drilling induced wellbore failures in wellbore data-implications for reservoir permeability. SPE 78599-PA. SPE Reservoir Evaluation & Engineering 5(3): 249-254.

Becker, A. A. 1992. The Boundary Element Method in Engineering. McGraw-Hill, London.

Beugelsdijk, L. J. L., de Pater, C. J., Sato, K. 2000. Experimental hydraulic fracture propagation in a multi-fractured medium. SPE 59419, presented at the SPE Asia Pacific Conference on Integrated Modelling for Asset management, Yokohama, Japan, 25-26 April.

Blanton, T. L. 1986. Propagation of hydraulically and dynamically induced fractures in naturally fractured reservoirs. SPE 15261, presented at the Unconventional Gas

Technology Symposium of the Society of Petroleum Engineering, Louisville, KY, May 18-21.

Bour, O., and Davy, P. 1997. Connectivity of random fault networks following a power law fault length distribution, water Resour. Res. 33(7): 1567-1583.

Bour O., Davy, P., Darcel, C. 2002. A statistical scaling model for fracture network geometry, with validation on a multiscale mapping of a joint network (Hornelen Basin, Norway). Journal of Geophsical Research, 107(B6): ETG 4-1- ETG 4-12.

Britt, L. K., Smith, M. B., Haddad, Z., Lawrence, P., Chipperfield, S., Hellman, T. 2006. Water-Fracs: we do need proppant after all. SPE 102227, presented at SPE Annual Technical Conference and Exhibition, San Antonio, TX, USA, 24-27 September.

Britt, L.K. and Smith, M.B. 2009. Horizontal well completion, stimulation optimization, and risk mitigation. Paper SPE 125526 presented at the 2009 SPE Eastern Regional Meeting, Charleston, September.

Budyn, E., Zi, G., Moes, N., Belytschko, T. 2004. A method for multiple crack growth in brittle materials without remeshing. International Journal for Numerical Methods in Engineering 61(10): 1741-1770.

Bunger, A. P., Zhang, X., Jeffrey, R .G. 2012. Parameters affecting the interaction among closely spaced hydraulic fractures. SPE 140426-PA. SPE Journal 17(1): 292-306.

Bunger, A. P., Jeffrey, R. G., Zhang, X. 2014. Constraints on simultaneous growth of hydraulic fractures from multiple perforation clusters in horizontal wells. SPE 163860-PA. SPE Journal 19(4): 608-620.

Castonguay, S. T., Mear, M. E., Dean, R. H., Schmidt, H. S. 2013. Predictions of the growth of multiple interaction hydraulic fractures in three dimensions. SPE 166259, presented at the SPE Annual Technical Conference and Exhibition held in New Orleans, Louisiana, USA, 30 September -2 October.

Carter, R. D.1957. Appendix to Optimum fluid characteristics for fracture extension. By G.C. Howard and C.R. Fast. Drill. And Prod. Prac, API 267.

Cheng, Y. 2009. Boundary element analysis of the stress distribution around multiple fractures: implications for the spacing of perforation clusters of hydraulically fractured horizontal wells. SPE 125769, presented at Eastern Regional Meeting held in Charleston, West Virginia, USA, 23-25 September.

Cipollar, C. L., Weng, X., Mack, M., Ganguly, U., Gu, H., Kresse, O., Cohen, C. 2011. Integrating microseismic mapping and complex fracture modeling to characterize fracture complexity. SPE 140185, presented at the SPE Hydraulic Fracturing Technology Conference and Exhibition held in The Woodlands, Texas, 24-26 January.

Cipollar, C. L., Warpinski, N. R., Mayerhofer, M. J. 2008. Hydraulic fracture complexity: diagnosis, remediation, and exploitation. SPE 115771, presented at the SPE Asia Pacific Oil & Gas Conference and Exhibition held in Perth, Australia, 20-22 October.

Chuprakov, D., Melchaeva, O, and Prioul R., 2013. Injection-sensitive mechanics of hydraulic fracture interaction with discontinuities. ARMA 13-252, presented at the 47th US Rock mechanics/ Geomechanics Symposium, San Francisco, CA, USA, 23-26.

Cipolla, C. L. 2000. State-of-the-art in hydraulic fracture diagnostics. SPE 64434, presented at the SPE Asia Pacific Oil and Gas Conference and Exhibition held in Brisbane, Austrilia, 16-18 October.

Cipolla, C. L. 2009. Modeling production and evaluating fracture performance in unconventional reservoirs. SPE 118536. Distinguished Author Series, Journal of Petroleum Technology 61(9): 84-90.

Clifton, R. J. and Abou-Sayed, A. S. 1981. A variational approach to the prediction of three-dimensional geometry of hydraulic fractures. SPE 9879, presented at SPE/DOE Low Perm. Symp., Denver, Co, May 27-29.

Crouch, S. L. 1976. Solution of Plane Elasticity Problems by the Displacement Discontinuity Method. International Journal for Numerical Methods in Engineering 10(2): 301-343.

Crouch, S. L. and Starfield, A. M. 1983. Boundary element methods in solid mechanics. London: George Allen & Unwin.

Crump, J. B. and Conway, M. W. 1988. Effects of perforation entry friction on bottom hole treating analysis. J. Pet Tech 40(8): 1041-1048.

Dahi-taleghani, A. 2009. Analysis of hydraulic fracture propagation in fractured reservoirs: an improved model for the interaction between induced and natural fractures. Ph.D. Dissertation. University of Texas at Austin.

Dahi-Taleghani, A., Olson, J. E. 2009. Numerical modeling of multistranded hydraulic fracture propagation: accounting for the interaction between induced and natural fractures. SPE 124884, presented at the SPE Annual Technical conference and Exhibition, New Orleans, 4-7 October.

Dahi-Taleghani, A., and Olson, J. E. 2013. How natural fractures could affect hydraulic-fracture geometry. SPE 167608-PA. SPE Journal 19(1): 161-171.

Dahi-Taleghani A., Ahmadi M. and Olson J. E. 2013. Secondary Fractures and Their Potential Impacts on Hydraulic fractures efficiency.Dr. Rob Jeffrey (ED.), ISBN: 978-953-51-1137-5, DOI: 10.5772/56360.

Danaeshy, A. A. 1973. On the design of vertical hydraulic fractures. SPE 3654-PA. J. Petroleum Technology 25(1): 83-97.

Daneshy, A.. 2011. Hydraulic Fracturing of Horizontal Wells: Issues and Insights. Paper SPE 140134, presented at the SPE Hydraulic Fracturing Technology Conference and Exhibition held in The Woodlands, Texas, USA, 24-26 January.

Darcel, C., Bour O., Davy, P., de Dreuzy J. R. 2003. Connectivity properties of two-dimensional fracture networks with stochastic fractal correlation. Water Resources Research 39(10):1272.

Davy, P., 1993. On the frequency-length distribution of the San Andreas fault system, J. Geophys. Res. 98(B7):12141-12151.

Desroches, J., Detournay, E., Lenoach, B., Papanastasiou, P., Pearson, J. R. A., Thiercelin, M., and Cheng, A. 1994. The crack tip region in hydraulic fracturing. proc. R. Soc. London, Ser. A, 447(1929): 39-48.

Dershowitz W. S., Einstein H. H. 1988. Characterizing rock joint geometry with joint system models. Rock Mech. Rock Eng. 21(1): 21-51.

Desroches, J., Lenoach, B., Papanastasiou, P., and Thiercelin, M. 1998. On the modeling of near tip process in hydraulic fractures. Int. J. Rock Mech. Min. Sci. Geomech. Abstr. 30(7): 1127-1134.

Detournay, E. 2004. Propagation regimes of fluid-driven fractures in impermeable rocks. International Journal of Geomechanics 4(1): 35-45.

Dong, C. Y., Peter C. J. de. 2001. Numerical implementation of displacement discontinuity method and its application in hydraulic fracturing. Comput. Methods Appl. Mech. Engrg. 191(8-10): 745-760.

Durst, D. G., Harris, T., Contreras, J. D., Watson, D. R. 2008. Improved single-trip multistage completion system for unconventional gas formations. SPE 115260, presented at SPE Tight Gas Completions Conference, San Antonia, TX, USA, 9-11 June.

Economides, M. and Nolte, K., eds. 2000. Reservoir stimulation, third editing, Chichester, UK: John Wiley & Sons.

Elbel, J. L., Piggott A. R. and Mack M. G. 1992. Numerical modeling of multilayer fracture treatments. SPE 23982, presented at SPE Permian Basin Oil and Gas Recovery Conference, March18-20.

El Rabaa, W.1989. Experimental Study of hydraulic fracture geometry initiated from horizontal wells. SPE 19720, presented at the SPE Annual Technical Conference and Exhibition held in San Antonio, TX, U.S.A., 8-11 October.

El Rabaa, W. and Rogiers, J. C. 1990. Potential rock response problems associated with horizontal well completions. Third South American Congress of the ISRM, Caracas, October 17-20.

Erdogan, F. and Sih, G. C., 1963. On the crack extension in plates under loading and transverse shear, Journal of Fluids Engineering 85(4): 519-527.

Fisher, M. K., Heinze, J. R., Harris, C. D., McDavidson, B. M., Wright, C. A., Dunn, K. P. 2004. Optimizing horizontal completion techniques in the Barnett Shale using Microseismic fracture mapping. SPE 90051, presented at the SPE Annual Technical Conference and Exhibition, Houston, TX, 26-29 September.

Fisher K. and Warponski, N. 2012. Hydraulic- fracture- height growth: real data. SPE 145949-PA. SPE Production & Operations 27(1): 8-19.

Fung, R. L., Vilajakumar S., Cormack D. E. 1987. Calculation of vertical fracture containment in layered fromations. SPE 14707-PA. SPE Formation Eval 2(4): 518-23.

Gale J. F. W. 2004. Self-organization of natural model-I fracture apertures into power-law distributions. ARMS/NARMS 04-488, presented at Gulf Rocks, the 6th North America Rock mechanics Symposium (NARMS): Rock Mechanics Across Border and Disciplines, held in Houston, Texas, June 5-9.

Gale, J. F. W., Reed, R. M., Holder, J. 2007. Natural fractures in the Barnett shale and their importance for hydraulic fracture treatments. AAPG Bulletin, 91(4): 603-622.

Gale, J., Holder, J. 2008. Natural fractures in shales and their importance for gas production. Tectonics Studies Group Annual Meeting, La Roche-en-Ardenne, Belgium, 8-10, January.

Garcia-Tijeiro, X. and Rodriguez-Herrera, A. 2014. Depdence of stress-induced Micro-seismicity on the natural fracture properties and in-situ stress. SPE 171632, presented at the SPE/CSUR Unconventional Resource Conference-Canada held in Calgary, Alberta, Canada, 30 September – 2 October.

Geertsma, J. and de Klerk, F. A. 1969. A rapid method of predicting width and extent of hydraulically induced fractures. J. Petroleum Technology 21(12): 1571-1781.

Germanovich, L. N., Astakhov, D. K. 2004. Fracture closure in extension and mechanical interaction of parallel joints. Journal of Geophysical Research 109(B2).

Germanovich, L. N., Astakhov, D. K. 2004. Stress-dependent permeability and fluid flow through parallel joints. . Journal of Geophysical Research 109(B9).

Grieser, B. Shellye, B., Soliman, M. 2009. Predicting production outcome from multi-stage, horizontal Barnett completions. SPE 120271, presented at the SPE Production Operations Symposium, Oklahoma City, OK, USA, 4-8 April.

Gu, H., Weng, X. 2010. Criterion for fractures crossing frictional interfaces at non-orthogonal angles, ARMA 10-198, presented at the 44th US Rock mechanics Symposium and 5th U.S.-Canada Rock mechanics Symposium, Salt Lake City, UT June 27-30.

Gu, H. Weng, X. Lund, J., Mack, M., Ganguly, U., Suarez-Rivera, R. 2011. Hydraulic fracture crossing natural fracture at non-orthogonal angles, a criterion, its validation and applications. SPE 139984, presented at the SPE Hydraulic Fracturing Technology Conference and Exhibition, The Woodlands, Texas, USA, 24-26 January.

Hooker, J. N., Laubach, S. E., Marrett, R. 2013. Fracture-aperture size-frequency, spatial distribution, and growth processes in strata-bounded and non-strata-bounded fractures, Cambrian Meson Group, NW Argentina. Journal of Structural Geology 54: 54-71.

Holley, E. H., Zimmer, U., Mayerhofer, M. J., Samson, E. 2010. Integrated analysis combining microseismic mapping and fiber-optic distributed temperature sensing (DTS). CSUG/SPE 136565, presented at the Canadian Unconventional Resrouces & International Petroleum Conference held in Calgary, Alberta, Canada, 19-21 October.

Jeffrey, R. G., Bunger, A. P., Lecampion, B., Zhang, X., Chen, Z. R., et al. 2009. Measuring hydraulic fracture growth in naturally fractured rock. SPE 124919, presented at SPE Annual Technical Conference and Exhibition, New Orleans, Louisiana, USA, 4-7 October.

Keshavarzi, R. 2012. Hydraulic fracture propagation in unconventional reservoirs: the role of natural fractures. ARMA 12-129, presented at the 46th US Rock Mechanics/Geomechanics Symposium held in Chicago, IL, USA, 24-27 June.

Ketter, A.. A., Daniel, J. L., Heinze, J. R. and Waters, G. 2006. A Field study Optimizing Completion Strategies for fracture initiation in Barnett shale horizontal wells. SPE 103232, presented at the SPE Annual Technical Conference and Exhibition held in San Antonio, Texas, U.S.A., 24-27 September.

Khan, A. 2013. Multi-frac treatments in tight oil and shale gas reservoirs: effect of hydraulic fracture geometry on production and rate transient. M.S. thesis. The University of Texas at Austin.

Khiristianovitch, S. A. and Zheltov, Y. P. 1955. Formation of vertical fractures by means of highly viscous fluid. WPC-6132. 4th World Petroleum Congress, 6-15 June, Rome, Italy.

Kim, T. H. 2007. Fracture characterization and estimation of fracture porosity of naturally fractured reservoirs with no matrix porosity using stochastic fractal models. Ph.D. dissertation. Texas A&M University.

King, G. E. 2010. Thirty years of Gas hale fracturing: what have we learned. SPE 133456, presented at the SPE Annual Technical Conference and Exhibition held in Florence, Italy, 19-22 September.

Kresse, O., Weng, X., Gu, H., Wu, R. 2013. Numerical modeling of hydraulic fracture interaction in complex naturally fractured formations. Rock Mech Rock Eng 46(4): 555-568.

Kulatilake P. H. S. W., Wathugala D.N., Stephasson O. 1993. Joint network modeling with a validation exercise in Stripa mine, Sweden. Int. J. Rock Mech. Min. Sci. & Geomech Abstr., 30(5): 503-526.

Laubach, S. E., Olson, J. E., Gale, J. F. W. 2004. Are open fractures necessarily aligned with maximum horizontal stress? Earth and Planetary Science Letters 222(1): 191-195.

Lecampion, B. and Desroches, J. 2014. Simultaneous initiation of multiple transverse hydraulic fractures from a horizontal well. ARMA 14-7110, presented at the 48th US Rock Mechanics/ Geomechanics Symposium held in Minneapolis, MN, USA, 1-4 June.

Li, Yi. 1991. On initiation and propagation of fractures from deviated wellbores. Ph.D. Dissertation. The University of Texas at Austin.

Love, A. E. H 1944. A Treatise on the Mathematical Theory of Elasticity. 4th ed. New York: Dover.

Mack, M. G., Elbel, J. L. 1992. Numerical representation of multilayer hydraulic fracturing. ARMA 92-0335, presented at the 33 th U.S. Symposium on Rock Mechanics (USRMS), 3-5 June, Santa Fe, New Mexico.

McClure, M. W. 2012. Modeling and characterization of hydraulic stimulation and induced seismicity in geothermal and shale gas reservoirs. Ph.D. Dissertation. Stanford University.

McCullagh, C. L., Tutuncu, A. N., Song, T. H. 2014. Coupling distributed temperature sensing (DTS) based wellbore temperature models with microseismic data for enhanced characterization of hydraulic fracture stimulation. ARMA 14-7623, presented at the 48th US Rock Mechanics/Geomechanics Symposium held in Minneapolis, MN, USA, 1-4 June.

Medlin, W. L. and Fitch J. L. 1983. Abnormal treating pressures in massive hydraulic fracturing treatments. SPE 12108, presented at the SPE 58th Annual Tech. Conf. & Exhib., San Francisco, October 5-8.

Meyer, B. R., Bazan, L. W. 2011. A discrete fracture network model for hydraulically induced fractures: theory, parametric and case studies. SPE 140514 presented at SPE Hydraulic Fracturing Technology Conference and Exhibition, Woodlands, Texas, 24-26 January.

Miller, C., Waters, G., Rylander, E. 2011. Evaluation of production log data from horizontal wells drilled in organic shales. SPE 144326, presented at SPE North

American unconventional gas conference and exhibition, the Woodlands, TX, USA, 14-16 June 2011.

Min, K. S., Zhang, Z., and Ghassemi, A. 2010. Numerical analysis of multiple fracture propagation in heterogeneous rock. ARMA 10-363, presented at 44th US Rock Mechanics Symposium, Salt Lake City, Utah, June 27-30.

Molenaar, M.M., Hill, D. J., Webster, P., Fidan, E., Birch, B. 2011. First downhole application of distributed acoustic sensing (DAS) for hydraulic fracturing monitoring and diagnostics. SPE 140561, presented at the SPE Hydraulic Fracturing Technology Conference and Exhibition held in The Woodlands, Texas, USA, 24-26 January.

Molenaar, M.M., Fidan, E., Hill, D. J. 2012. Real-time downhole monitoring of hydraulic fracturing treatments using fibre optic distributed temperature and acoustic sensing. SPE 152981, presented at the SPE/EAGE European Unconventional resources conference and exhibition held in Vienna, Austria, 20-22, March.

Muskhelishvili, N. I. 1919. Izv. (Bull.) Akad. Nauk SSSR 12, 663-686.

Mutalik, P. N. and Gibson, B. 2008. Case history of sequential and simultaneous fracturing of the Barnett shale in Parker County. Paper SPE 116124, presented at the 2008 SPE Annual Technical Conference and Exhibition held in Denver, Colorado, USA, 21-24 September.

Nagel, N., Gil, I., Sanchez-Nagel, M., and Damjanac, B. 2011. Simulating hydraulic fracturing in real fractured rock – Overcoming the limits of pseudo3d models. SPE 140480, presented at SPE Hydraulic Fracturing Technology Conference and Exhibition, The Woodlands, Texas, January 24-26.

Nordgren, R. P.1972. Propagation of a vertical hydraulic fracture. SPE 3009-PA. Society of Petroleum Engineering Journal 12(4): 306-314.

Nuismer, R. 1975. An energy release rate criterion for mixed mode fracture, International Journal of Fracture 11(2): 245-250.

Okada, Y. 1992. Internal deformation due to shear and tensile faults in a half-space. Bulletin of the Seismological Society of America 82(2):1018-1040.

Okada, Y. 1985. Surface deformation due to shear and tensile faults in a half-space. Bulletin of the Seismological Society of America 75(4):1135-1154.

Olson, J. E. and Pollard, D. D. 1989. Inferring paleostresses from natural fracture patterns: A new method. Geology 17(4): 345-348.

Olson, J.E. 1993. Joint pattern development: the effects of subcritical crack growth and mechanical interaction. J. of Geophysical. Research 98(B2): 12,251-12,265.

Olson, J. E. 1995. Fracturing from highly deviated and horizontal wells: Numerical analysis of non-planar fracture propagation. SPE 29573, presented at SPE Rocky

Mountain Regional/Low-Permeability Reservoirs Symposium, Denver, Colorado, March 20-22.

Olson, J. E. 2003. Sublinear scaling of fracture aperture versus length: an exception or the rule? Journal of Geophysical Research 108(B9): 2413.

Olson, J. E. 2004. Predicting fracture swarms- the influence of subcritical crack growth and the crack-tip process zone on joint spacing in rock. Geological society, London, Special Publications 231(1): 73-88.

Olson, J. E. 2007. Fracture aperture, length and pattern geometry development under biaxial loading: a numerical study with applications to natural, cross-jointed systems. Geological Society of London, Special Publications, v. 289: 123-142.

Olson, J. E. 2008. Multi-fracture propagation modeling: application to hydraulic fracturing in shales and tight gas sands. ARMA 08-327 presented at the 42nd US Rock Mechanics Symposum and 2nd U.S.-Canada Rock Mechanics Symposium, held in San Francisco, June 29-July 2.

Olson, J. E., and Dahi-Taleghani, A. 2009. Modeling simultaneous growth of multiple hydraulic fractures and their interaction with natural fractures. SPE 119739, presented at SPE Hydraulic Fracturing Technology Conference, The Woodlands, Texas, USA, 19–21 January.

Olson, J. E., Bahorich, B., Holder, J. 2012. Examining hydraulic fracture – natural fracture interaction in hydrostone block experiments. SPE 152618, presented at the SPE Hydraulic Fracturing Technology Conference, The Woodlands, Texas, USA, 6-8 February.

Olson, Jon E., Wu, K. 2012. Sequential versus Simultaneous Multi-zone Fracturing in Horizontal Wells: Insights from a Non-planar, Multi-frac Numerical Model, SPE 152602, presented at the SPE Hydraulic Fracturing Technology Conference in The Woodlands, Texas, USA 6-8 February.

Owens, K. A., Andersen, S. A., and Economides, M. J. 1992. Fracturing pressures for horizontal wells. SPE 24822, presented at 67th Annual Technical Conference and Exhibition of the SPE, Washington, D.C., October 4-7.

Palaniswamy, K. 1972. Crack propagation under general in-plane loading, Ph.D. dissertation, California Institute of Technology.

Pan, Feng. 2009. Development and application of a coupled Geomechanics model for a parallel compositional reservoir simulator. Ph.D. Dissertation. The University of Texas at Austin.

Pathak, H., Singh, A., Singh, I. V., Yadav, S. K. 2013. A simple and efficient XFEM approach for 3-D cracks simulations. Int J Fract. 181(2): 189-208.

Perkins, T. K. and Kern, L. R.1961. Width of hydraulic fractures. J. Petroleum Technology 13(9): 937-949.

Renshaw, C. E., Pollard, D. D. 1995. An experimentally verified criterion for propagation across unbounded frictional interfaces in brittle, linear elastic materials. Int. J. Rock Mech. Min. Sci. & Geomech. Abstr 32(3): 237-249.

Pollard, D. D. and Segall, P. 1987. Theoretical displacements and stresses near fractures in rock: With applications to faults, joints, veins, dikes and solution surfaces in Fracture Mechanics of Rock (edited by B.L. Atkinson), Academic Press, London: 277-350.

Pollard D. D., Atilla Aydin. 1988. Progress in understanding jointing over the past century. Geological Society of America Bulletin 100(8): 1181-1204.

Renshaw, C.E., Pollard, D.D. 1995. An experimentally verified criterion for propagation across unbounded frictional interfaces in brittle, linear elastic materials. Int. J. Rock Mech. Min. Sci. & Geomech. Abstr. 32(3): 237-249.

Rongved, L. 1957. Dislocation over a bounded plane area in an infinite solid. J. Appl. Mech. 24: 252-254.

Roussel, N. and Sharma, M. 2011. Optimizing fracture spacing and sequencing in horizontal-well fracturing. SPE 127986-PA. SPE Production & Operations 26(2): 173-184.

Roussel, N. and Sharma, M. 2011. Strategies to minimize frac spacing and stimulate natural fractures in horizontal completions. SPE 146104, presented at the SPE Annual Technical Conference and Exhibition held in Denver, Colorado, USA, 30 October-2 November.

Rungamornrat, J., Wheeler, M. F., Mear, M. E. 2005. A numerical technique for simulating nonplanar evolution of hydraulic fracture. SPE 96968, presentation at the 2005 SPE Annual Technical Conference and Exhibition, Dallas, Texas, U.S.A., 9-12 October.

Salamon, M. D. G. 1964. Elastic analysis of displacements and stresses induced mining of seam or roof deposits, Part IV. J. S. Afr. Inst. Min. Metall. 65: 319-338.

Sato K., Wright C. A. and Makoto I., 1999. Post-Frac Analyses indicating multiple fractures created in a volcanic formation, SPE 59097-PA. SPE Prod. & Facilities 14(4): 284-291.

Schlichting H. 1968. Boundary-layer theory, 6th Edn. McGraw-Hill. New York.

Schultz R. A., Klimczak, C., Fossen, H., Olson, J. E., Exner, U., Reeves, D. M., Soliva, Roger. 2013. Statistical tests of scaling relationships for geologic structures. Journal of Structural Geology 48: 85-94.

Segall, P., David, D. D. 1983. Joint formation in granitic rock of the Sierra Nevada. Geological Society of America Bulletin 94(5): 563-575.

Seth, G., Reynolds, A. C., Mahadevan, J. 2010. Numerical model for interpretation of distributed temperature sensor data during hydraulic fracturing. SPE 135603, presented at the 2010 APE Annual technical Conference and Exhibition held in Florence, Italy, 20-22 September.

Settari, A. and Cleary M. P. 1982. Development and testing of a pseudo-three-dimensional model of hydraulic fracture geometry (P3DH), SPE 10505-PA, SPE Production Engineering 1(6): 449-466.

Settari, A. and Cleary, M.P. 1984. Three-dimensional simulation of hydraulic fracturing. SPE 10504-PA. J. Petroleum Technology 36(7): 1177-1190.

Shin, D. H., Sharma, M. M. 2014. Fractors controlling the simultaneous propagation of multiple competing fractures in a horizontal well. SPE 168599 presented at the SPE Hydraulic Fracture Technology Conference held in The Woodlands, Texas, USA, 4-6 February.

Shou, K. J. 1993. A high order three-dimensional displacement discontinuity method with application to bonded half-space problems. Ph.D. dissertation. University of Minnesota.

Shou, K. J., Siebrits, E., Crouch, S. L. 1997. A high order displacement discontinuity method for three-dimensional elastostatic problems. Int. J. Rock Mech. Min. Sci. 34(2): 317-322.

Sierra, J., Kaura, J., Gualtieri, D., Glasbergen, G., Sarkar, D., Johnson, D. 2008. DTS monitoring data of hydraulic fracturing; experience and lessons learned. SPE 116182, presented at the SPE Annual Technical Conference and Exhibition held in Denver, Colorado, USA, 21-24 September.

Sih, G. C. 1964. Proc. 2nd Conf. Theoretical Appl. Mech. Pergamon, Oxford, 117-130.

Sih, G. C. 1966. J. Fracture Mech. 2:628-630.

Sih, G. C. and Liebowitz, H. 1968. Mathematical theories of brittle fracture, Fracture, An Advance Treatise, Vol. 2, Academic Press.

Sih, G. C., 1974. Strain energy density factor applied to mixed mode problems, International Journal of Fracture 10(3): 305-321.

Simonson E. R., Abou-Sayed A. S., Clifton R. J. 1978. Containment of massive hydraulic fractures. SPE 6089. SPE J 18(1): 27-32.

Siriwardane, H. J., Layne A. W., 1991. Improved Model for Predicting Multiple Hydraulic Fracture Propagation From a Horizontal Well. SPE 23448, presented at SPE Eastern Regional Meeting in Lexington, Kentucky, October 22-25.

Sneddon, I. N., Elliott, H. A. 1946. The opening of a Griffith crack under internal pressure. Quart. Appl. Math. IV, No.3, 262-267.

Sneddon, I. N. 1951. Fourier transforms. New York: McGraw-Hill.

Spence, D. A. and Sharp, P. W. 1985. Self-similar solution for elastohydrodynamic cavity flow, Proceedings of the Royal society of London, Series A 400(1819): 289-313.

Thomas, A. L. 1993 Ploy3D: A three-dimensional, polygonal element, displacement discontinuity boundary element computer program with applications to fractures, faults, and cavities in the earth's crust. M.S. Thesis, Standford University.

Tao, Q. F. 2010. Numerical modeling of fracture permeability change in naturally fractured reservoirs using a fully coupled displacement discontinuity method. Ph.D. dissertation. Texas A&M University.

Ugueto, G. A., Ehiwario, M., Grae, A., Molenaar, M. McCoy, K., Huckabee, P. Barree, B. 2014. Application of integrated advanced diagnostics and modeling to improve hydraulic fracture stimulation analysis and optimization. SPE 168603, presented at the SPE Hydraulic Fracturing Technology Conference held in The Woodlands, Texas, USA, 4-6 February.

Valko, P., Economides, M. J. 1995. Hydraulic fracture mechanics. John Wiley & Sons Ltd, Baffins Lane, Chichester, West Sussex PO19 IUD, England.

Van Eekelen, H. A. 1982. Hydraulic fracture geometry: fracture containment in layered formation. SPE 9261-PA. Society of Petroleum Engineering Journal 22(3): 341-349.

Veatch, R. W. 1986. An Overview of recent Advances in hydraulic fracturing technology. SPE 14085, presented at International Meeting on Petroleum Engineering, 17-20 March, Beijing, China.

Vulgamore, T., Clawson, T., Pope, C., Wolhart, S., Mayerhofer, M., Machovove, S. and Waltman, C. 2007. Applying hydraulic fracture diagnostics to optimize stimulations in the Woodford shale. SPE 110029, presented at SPE Annual Technical Conference and Exhibition, Anaheim, California, U.S.A., 11-14 November.

Wang, W., Olson, J. E., Prodanovic, M. 2013. Natural and hydraulic fracture interaction study based on semi-circular bending experiments. SPE 168714/URTeC 1576910, presented at The Unconventional Resources Technology Conference, Denver, Colorado, USA, 12-14 August.

Warpinski, N. R., Teufel, L. W. 1987. Influence of geologic discontinuities on hydraulic fracture propagation. SPE 13224. Journal of Petroleum Technology 39(2): 209-220.

Warpinski, N. R., and Branagan, P.T. 1989. Altered-stress fracturing. SPE 17533-PA. J. of Petroleum Technology 41(9): 990-997.

Warpiniski, N. R., Lorenz, J. C., Branagan, P. T., Myal, F. R. and Gall, B. L., 1991. Examination of a cored hydraulic fracture in a deep gas well. SPE 22876, presented at Annual Technical Conference and Exhibition, Dallas, Oct.6-9.

Warpinski, N. R. 1994. Interpretation of hydraulic fracture mapping experiments. SPE 27985, presented at the University of Tulsa Centennial Petroleum Engineering Symposium field in Tulsa, OK, U.S.A., 29-31 August.

Warpinski, N. R., Wolhart, S. L., Wright, C. A. 2001. Analysis and prediction of microseismicity induced by hydraulic fracturing. SPE 71649, presented at SPE Annual Technical Conference and Exhibition, New Orleans, Louisiana, 30 September-3 October.

Warpinski, N. R., mayerhofer, M.J., Davis, E.J., Holley, E.H. 2014. Integrating fracture diagnostics for improved microseismic interpretation and stimulation modeling. SPE/AAPG/SEG 1917906, presented at the Unconventional Resources Technology Conference held in Denver, Colorado, USA, 25-17 August. DOI 10.15530/urtec-2014-1917906.

Warpinski, N. R. 2014. A review of hydraulic-fracture induced microseismicity. ARMA 14-7774, presented at the 48th US Rock Mechanics/Geomechanics Symposium held in Minneapolis, MN, USA, 1-4 June.

Waters, G., Dean, B., Downie, R., Kerrihard, K., Austbo, L., McPherson, B. 2009. Simultaneous hydraulic fracturing of adjacent horizontal wells in the Woodford Shale. SPE 119635, presented at the SPE Hydraulic Fracturing Technology Conference, The Woodlands, TX, 19-21 January.

Watson, D. R., Durst, D. G., Harris, T., Contreras, J. D. 2008. One-trip Multistage completion technology for unconventional gas formations, SPE 114973, presented at CIPC/SPE Gas Technology Symposium Joint Conference, Calgary, Alberta, Canada, 16-19 June.

Weijers, L. and de Pater, C. J. 1992. Fracture reorientation in model tests. SPE 23790, presented at the SPE International Symposium on Formation Damage Control, Lafayette, LA, Feb. 26-27.

Weijers, L., de Pater, C. J. 1994. Interaction and link-up of hydraulic starter fractures close to a perforated wellbore. SPE 28077, presented at the SPE/ISRM Rock Mechanics in Petroleum Engineering Conference held in Delft, The Netherlands, 29-31 August.

Weijers L., Wright C. A., Sugiyama H., Sato K., Zhigang L. 2000. Simultaneous Propagation of Multiple hydraulic Fracture – Evidence, Impact and Modeling Implications, SPE 64772, presented at International Oil and Gas Conference and Exhibition in Beijing China, November 7-10.

Weng, X., Kresse, O., Cohen, C., Wu, R., and Gu, H. 2011. Modeling of hydraulic fracture network propagation in a naturally fractured formation. SPE 140253,

presented at SPE Hydraulic Fracturing Technical Conference and Exhibition, The Woodlands, Texas, January 24-26.

Westergaard, H.M. 1939. J. Appl. Mech. 6, A49-A53.

Wheaton, B., miskimins, J., Wood, D., Lowe, T., Barree, R. 2014. Inegration of distributed temperature and distributed acoustic survey results with hydraulic fracture modeling: a case study in the woodford shale. URTeC 1922140, presented at the Unconventional Resources Technology Conference held in Denver, Colorado, USA, 25-16 August.

Wiley, C., Baree, B., Eberhard, M., Lantz, T. 2004. Improved horizontal well stimulations in the Bakken formations. SPE 90697, presented at SPE Annual Technical Meeting and Exhibition, Houston, TX, USA, 26-29 September.

Wong, S. W., Xu, G.. 2013. Interaction of multiple hydraulic fractures in horizontal wells. SPE 163982, presented at SPE Middle East Unconventional Gas Conference and Exhibition, Muscat, Oman, January 2013.

Wu, Kan and Olson, Jon E. 2013. Investigation of critical in situ and injection factors in multi-frac treatments: Guidelines for controlling fracture complexity. SPE 163821, presented at SPE Hydraulic Fracturing Technology Conference in The Woodlands, Texas, USA 4-6 February.

Wu, R., Kresse, O.,Weng, X., Cohen, C.,and Gu, H., 2012. Modeling of interaction of hydraulic fractures in complex fracture networks. SPE 152052, presented at SPE Hydraulic Fracture Technology Conference, Texas, USA, 6-8 February.

Wu, K. and Olson J. E. 2013. Investigation of the impact of fracture spacing and fluid properties for interfering simultaneously- or sequentially- generated hydraulic fractures. SPE 163821-PA. SPE Production & Operations 28(4): 427-436.

Wu, K. and Olson, J. E. 2014. Simultaneous multi-frac treatments: fully coupled fluid flow and fracture mechanics for horizontal wells. SPE 167626-PA. SPE Journal. http://dx.doi.org/10.2118/167626-PA.

Wu, K. and Olson, J. E. 2014. Mechanics analysis of interaction between hydraulic and natural fractures in shale reservoirs. URTeC 1922946, presented at the Unconventional Resources Technology Conference held in Denver, Colorado, USA, 25-27 August.

Xu, W., Le Calvez, J. and Thiercelin, M. 2009. Characterization of hydraulically-induced fracture network using treatment and microseismic data in a tight-gas formation: a geomechanics approach. SPE125237, presented at SPE Tight Gas Completions Conference, San Antonio, Texas, USA, 15-17 June.

Xue, W. and Ghassemi, A. 2009. Poroelastic analysis of hydraulic fracture propagation. ARMA 09-129, presented at 43rd US Rock Mechanics Symposium, Asheville, North Carolina, June 28-July 1.

Yamamoto, K., Tatsuo S. and Shunichi S. 2004. Multiple fracture propagation model for a three-dimensional hydraulic fracturing simulator. International journal of geomechanics ASCE 4(1): 46-57.

Yew, Ching H. 1997. Mechanics of hydraulic fracturing. Gulf Publishing Company, Houston, Texas.

Yoshida, N., Zhu, D., Hill, A. D. 2014. Temperature-prediction model for a horizontal well with multiple fractures in a shale reservoir. SPE 166241-PA. SPE Production & Operations.

Yu, W., Sepehrnoori, K. 2014. Sensitivity study and history matching and economic optimization for Marcellus shale. URTeC 1923491, presented at the Unconventional Resources Technology Conference held in Denver, Colorado, USA, 25-27 August.

Yu, W., Huang, S., Wu, K., Sepehrnoori, K. 2014. Development of a semi-Analytical Model for simulation of gas production in shale gas reservoirs. URTeC 1922945, presented at the Unconventional Resources Technology Conference held in Denver, Colorado, USA, 25-27 August.

Zhang, X., Detournay, E., and Jeffery, R. 2002. Propagation of a penny-shaped hydraulic fracture parallel to the free-surface of an elastic half-space. International Journal of Fracture 115(2): 125-158.

Zhang, X., Jeffrey, R. G., and Detournay, E. 2005. Propagation of a hydraulic fracture parallel to a free surface. Int. J. Numer. Annual. Meth. Geomech. 29(13): 1317-1340.

Zhao, X. P. and Young, R. P. 2009. Numerical simulation of seismicity induced by hydraulic fracturing in naturally fractured reservoirs. SPE 124690, presented at SPE Annual Technical Conference and Exhibition, New Orleans, Louisiana, October 4-7.

Zimmerman, R. W. Kumar, S. and Bodvarsson, G.S. 1991. Lubrication theory analysis of the permeability of rough-walled fractures. International Journal Rock Mechanics Mine Science & Geomechanics. Abstr. 28(4): 325-331.